MOLECULAR DYNAMICS SIMULATIONS OF CONJUGATED SEMICONDUCTING MOLECULES

by

Jack Wildman

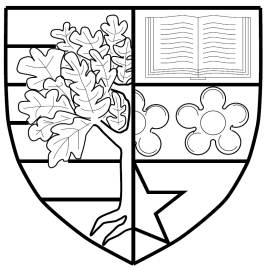

Submitted for the degree of
Doctor of Philosophy

Institute of Photonics and Quantum Sciences
School of Engineering and Physical Sciences
Heriot-Watt University

August 2017

Abstract

In this thesis, we present a study of conformational disorder in conjugated molecules focussed primarily on molecular dynamics (MD) simulation methods. Along with quantum chemical approaches, we develop and utilise MD simulation methods to study the conformational dynamics of polyfluorenes and polythiophenes and the role of conformational disorder on the optical absorption behaviour observed in these molecules. We first report a classical force-field parameterisation scheme for conjugated molecules which defines a density functional theory method of accuracy comparable to high-order *ab-initio* calculations. In doing so, we illustrate the role of increasing conjugated backbone and alkyl side-chain length on inter-monomer dihedral angle potentials and atomic partial charge distributions. The scheme we develop forms a minimal route to conjugated force-field parameterisation without substantial loss of accuracy. We then present a validation of our force-field parameterisation scheme based on self-consistent measures, such as dihedral angle distributions, and experimental measures, such as persistence lengths, obtained from MD simulations. We have subsequently utilised MD simulations to investigate the interplay of solvent and increasing side-chain lengths, the emergence of conjugation breaks, and the wormlike chain nature of conjugated oligomers. By utilising MD simulation geometries as input for quantum chemical calculations, we have investigated the role of conformational disorder on absorption spectral broadening and the formation of localised excitations. We conclude that conformational broadening is effectively independent of backbone length due to a reduction in the effect of individual dihedral angles with increasing length and also show that excitation localisation occurs as a result of large dihedral angles and molecular asymmetry.

Acknowledgements

It goes without saying (but deserves to be said anyway) that, while a thesis comes with one name attached to it, it is by no means a one-person effort. Without the help, support, and belief of those around me, I would not have been able to achieve the work presented here.

My foremost thanks go to Prof. Ian Galbraith, for without his help, support, patience, guidance, knowledge, and ideas (all of which in seemingly limitless quantities), I would not have been able to put together and submit this work. I cannot express my thanks enough for everything that he has done for me.

I would also like to express thanks to Dr. J.-C. Denis for his invaluable input to my work through his inspirational ideas and (often considerable) technical assistance. His willingness to receive questions, comments, and general nuisances in the years we worked in parallel is immensely appreciated. Also, I would like to thank Dr. Peter McDonald for his support and ideas during the early stages of my studies.

Our collaboration with the theoretical photochemistry group of Prof. Martin Paterson runs throughout this work and Martin's vast knowledge of molecular calculation and modelling has been vital in guiding and shaping it. Additionally, the contribution of Dr. Peter Repiščák, both in supporting me in getting started with molecular dynamics simulations and our close collaboration on our force-field parameterisation work, was both highly enjoyable and valuable. Also, I cannot thank Dr. Jeremy Coe enough for his continuous work in maintaining the hpc6 cluster and keeping it running, almost impossibly, consistently.

Our collaboration with the Organic Semiconductor Centre in St. Andrews has led to a number of highly interesting discussions which have informed much of the direction of this work. Both the opportunity to regularly receive an experimentalist's viewpoint of this work as well as to get a view of the experimental side of conjugated material research has been illuminating. Particularly, I would like to thank Dr. Gordon Hedley, Dr. Arvydas Ruseckas, Prof. Graham Turnbull, Prof. Ifor Samuel, and everyone else who was present at our meetings for their comments, ideas, and critiques.

I would also like to express my gratitude to the Scottish Centre for Doctoral Training in Condensed Matter Physics (CM-CDT) for funding my work. In addition, thanks to everyone who was a part of the CDT for making our get-togethers memorable and for sharing in the highs and lows of the PhD process. Also, special thanks to Julie Massey and Christine Edwards for the incredible job they do in co-ordinating everything.

Finally, I would like to thank all of my family and friends for their continuous support, patience, and love. I am fortunate enough that the list of names here is far too long to even begin individually acknowledging. You all know who you are.

(The chances are, though, that if I am showing you this thesis personally, you are certainly in the unfortunate position of being someone I hold truly dear to me.) I cannot express how much you all mean to me, I'm sorry that I've not been around much lately, and without you, I could not have accomplished this.

Contents

Chapter 1

Introduction

This introductory chapter provides an overview of organic semiconducting technology and the unique potential advantages and challenges associated with it. First, we provide a brief history of organic semiconducting materials and the physical concepts associated with both their semiconducting character as well as the processes of photo-excitation and charge transport in these disordered molecular systems. We then discuss the role of molecular morphology in recent breakthroughs in organic devices and the need to better understand material properties and processing techniques in order to optimise solution-based fabrication. From this, we discuss the basic principles of polymer physics before motivating the use of computational simulation techniques. This brings us to the core topic of this work: utilising molecular dynamics simulations as a means of modelling solution conformations of conjugated polymers.

1.1 Overview of organic semiconducting phenomena

Semiconductor technology has underpinned an ongoing technological revolution from the mid-20th century onwards. The invention of transistors, for example, gave birth to the modern computer which influences all aspects of 21st century life: from increasing the computational and analytical power of scientific and industrial disciplines to revolutionising the manner in which humanity communicates and accesses information. Alongside such logic-based devices, semiconductors also serve to combat current environmental issues from utilising light-emitting diodes (LEDs) for energy-efficient lighting to solar cells for renewable energy production [1–4].

The term 'organic semiconductor' typically applies to molecular materials which have conduction properties less than that of a typical conductor but greater than that of an insulator. The key point that differentiates them from conventional or 'inorganic' semiconductors is in the core building blocks of which they are comprised. Inorganic semiconductors, such as Si or Ge, are typically crystalline structures of atoms which could be considered as a single molecular block [2, 3]. Organic semiconductors, on the other hand, are typically mixtures of several molecules ranging

from low molecular weight (LMW) molecules to polymers. This crucial difference offers organic semiconducting technology a wealth of prospective benefits such as the ability to utilise solution processing techniques for large scale growth - as opposed to crystal growth techniques such as chemical vapour deposition [5] - as well as the light-weight and flexibility of these materials, when compared to inorganic and crystalline materials, allowing for the possibility of flexible electronics [1, 6, 7].

As with any emerging technology, the development of organic semiconducting materials comes with its share of challenges. While the multi-molecular nature of these materials leads to appealing properties such as mechanical flexibility and solution-based fabrication, molecular materials typically form amorphous or semi-crystalline morphologies with highly localised states which often lead to substandard device performance [1, 8, 9]. In this section, we shall discuss these advantages and challenges by first discussing the history and development of organic semiconducting materials and describing the basic physics and operation of organic semiconducting devices. In doing so, we highlight and focus on one particularly crucial challenge resulting from the molecular nature of these materials: the variety of disordered material morphologies typically adopted by organic semiconducting materials and its impact on device performance.

1.1.1 Molecular and macromolecular semiconductors

Given that the electronic structure of organic matter is typically composed of highly-localised electronic states, the majority of organic materials are insulative [9]. However, the work of Kallman and Pope demonstrated that, with the aid of halogen doping, it is possible to induce conductivity in crystals of anthracene [10, 11] and later demonstrated the material's electroluminescent properties [12]. Following these discoveries, the first semiconducting polymer - polyacetylene - was discovered by Shirakawa, MacDiarmid, and Heeger [13, 14] in 1977. In their pioneering work, they discovered that films of polyacetylene display conductivity which both increases with increasing temperature and is sensitive to the presence of dopant materials - two hallmark properties of a semiconductor [2]. While the technological revolution resulting from inorganic semiconductor technology was well underway by this point - with the discovery of the transistor occurring some thirty years earlier - this discovery was especially significant given the marked difference in the material properties of polymers compared to typical conductors and semiconductors.

In an almost parallel manner to the rise of inorganic semiconducting technology, the 20th century seen the discovery, development, and industrialisation of synthetic polymers commonly known as 'plastics' [15,16]. By definition, a polymer is a repeating structure of many (*poly*) units (*meros*) [16]. The long, repeating structure of polymer materials gives them many extraordinary properties, perhaps the foremost of which is the balance of strength and flexibility afforded by the tangling of individ-

ual polymer chains in a bulk material [15, 16]. Polymeric materials are abundant in the natural world with examples such as DNA molecules, and polyisoprene - the primary constituent of natural rubber [17]. The discovery of synthetic polymerisation and the remarkable mechanical properties of nylon led to mass-scale production and development of similar plastic materials which are now ubiquitous in modern life. As such, the key significance of the discovery of semiconducting polyacetylene lay in the possibility of fabricating semiconductors with the low-weight and flexibility of polymers. In this regard, organic semiconductors are sometimes referred to as components of 'plastic electronics' [1].

While the development of organic semiconductors was many years behind that of inorganic semiconductors, several landmark achievements were soon realised in the field of organic semiconductors. Electroluminescence in conjugated polymer films was discovered by Partridge in 1983 [18–21] in films of poly-vinylcarbazole. The first organic light emitting diodes (OLEDs) were developed in 1987 based on the the low-molecular weight Alq3 by Tang *et al* [22] which were soon followed by the first demonstration of an OLED device based on the conjugated polymer poly(*p*-phenylene-vinylene) (PPV) by Burroughes *et al* [23] in 1990. 1986 saw the development of the first organic photovoltaic (OPV) cell with a power conversion efficiency of 1% [24] while the first organic field-effect transistor (OFET), based on a poly-thiophene conjugated polymer, was developed shortly afterwards [25].

The discovery of semiconducting polymers and organic electronics was a surprising development due to the prevailing notion that organic materials were all insulators [9]. That materials like polyacetylene are semiconductors is due to one key molecular property: orbital conjugation [1, 26]. The principal component of any material labelled 'organic' is the carbon atom [27]. Consider two simple carbon-based molecules, ethane and ethene (shown in Figure 1.1), which are comprised of two bound carbon atoms with differing numbers of bound hydrogens. While each of these molecules are similar at face value, the resulting structure of their orbitals is substantially different. This is the result of orbital hybridisation [1, 27–29]. Orbital hybridisaton is essentially another manner of saying that that the bound pair of atoms have a different set of electronic eigenfunctions - 'hybrid' orbitals - comprised of a combination of the atomic eigenfunctions - atomic orbitals. The valence orbitals of carbon are the $2s$ and three $2p$ orbitals. As this shell is only half filled in carbon (four valence electrons), each of the carbons in ethane forms bonds with the opposing carbon and three other hydrogens which each result from doubling the occupancy of each orbital. The hybrid orbitals of the carbon atoms in this case are formed from four combinations of the $2s$ and three $2p$ orbitals which results in four hybrid sp_3 orbitals [26, 27]. The resulting bonding orbitals formed from sp_3 orbtials are four 'single' bonds referred to as σ orbitals. In ethene, the missing hydrogen leaves only three covalent bonding sites for each carbon. As such, the hybridisa-

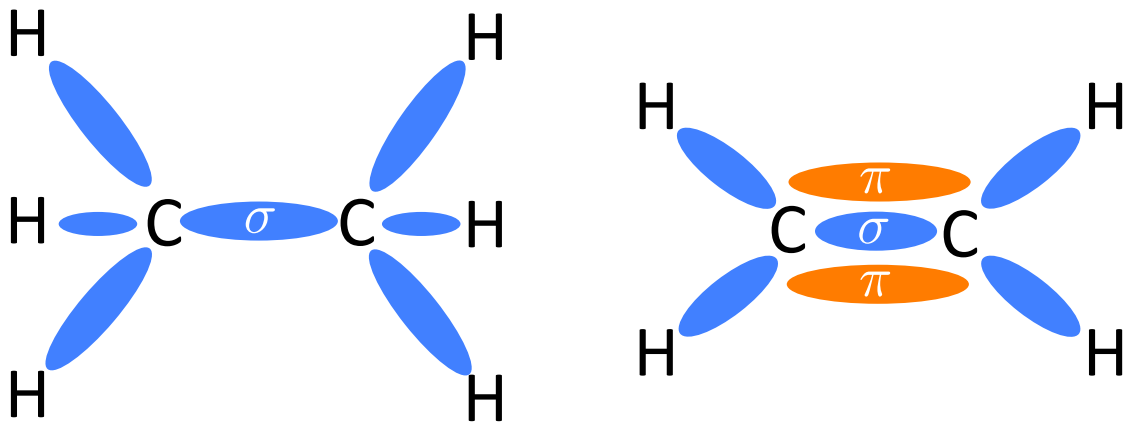

(a) Ethane (sp_3) (b) Ethene (sp_2)

Figure 1.1: Schematic of orbital hybridisation in (a) ethane (sp_3) and (b) ethene (sp_2) highlighting the difference between σ (blue) and π (orange) bonding orbitals. The σ bonds between C and H atoms are of equivalent length in both schematics and the π portion of (b) represents one orbital.

tion is sp_2 hybridisation - hybrid orbitals formed of one $2s$ and two $2p$ orbitals - with each hybrid orbital contributing to three σ bonds. In this case, the electronic structure is stabilised by the remaining $2p$ orbitals forming extra bonding orbitals called π orbitals. π orbitals, rather rather than being primarily localised between the two atoms, extend across each carbon. The π and σ bonding orbital combination between two carbons is often referred to as a 'double bond' [27] and is shown schematically in Figure 1.1.

The difference in orbital hybridisation has significant consequences when one considers an oligomer or polymer with analogues of these molecules as the repeating unit. Succesive extensions of ethane and ethene with extra carbons and hydrogens each lead to a continuing chain of hybridisation. Extending ethane (which, for a large number of carbons, N, leads to the polymer polyethylene) results in successive σ orbitals between each of the sp_3 hybridised carbons while extending ethene (polyacetylene for large N) leads to successive σ and π orbitals between each carbon. As opposed to σ orbitals, the π orbitals in ethene are delocalised across the pair of carbon atoms and this pattern of delocalisation extends across the formed polyacetylene chain. This leads to a delocalised electronic structure which extends across the entire polyacetylene chain. As this does not occur without the presence of π orbitals, the delocalised electronic structure of polyacetylene significantly distinguishes it from polyethylene.

As a chain of delocalised π electrons, one may expect that polyacetylene is metallic. However, it is known that one-dimensional metallic states are unstable [9]. If we consider polyacetylene as a chain of lattice sites of a spacing, a, its Brillouin zone ranges from $k = -\pi/a$ to π/a. If one then considers a perturbation, δ, of the lattice spacing occurring every second atom, the resulting dimerised lattice has a lattice

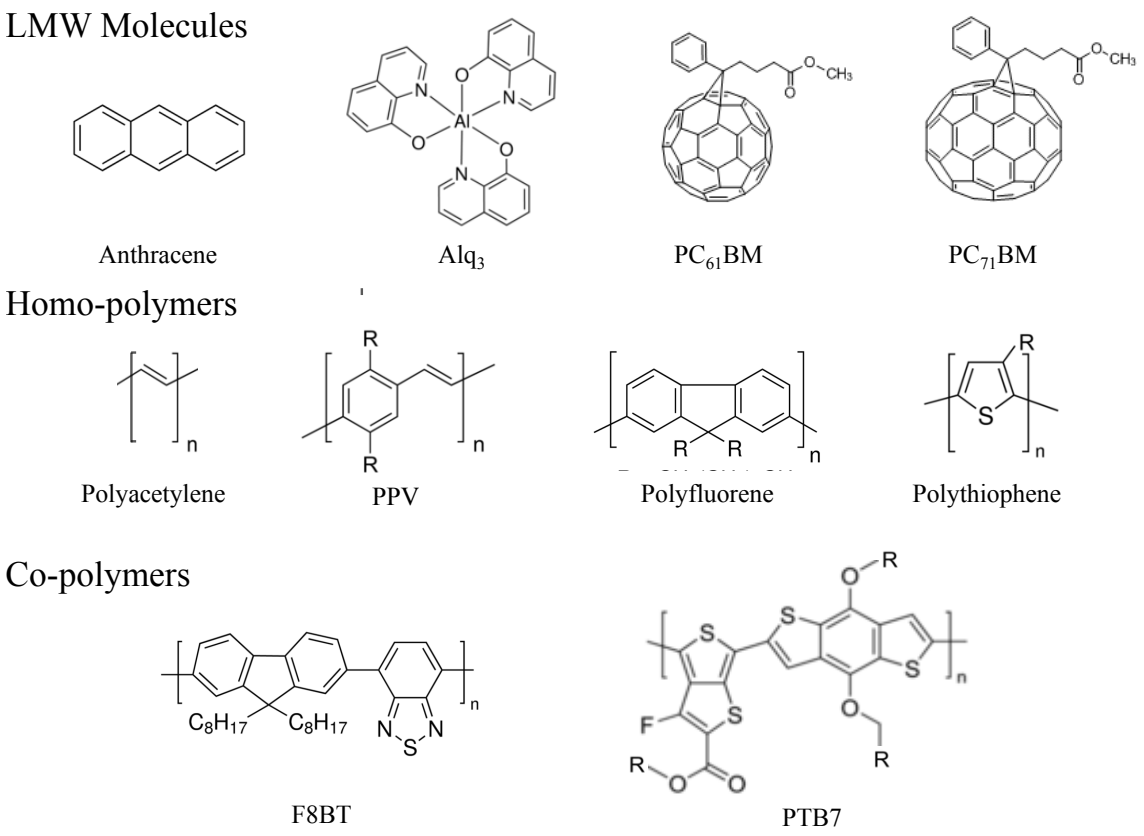

Figure 1.2: Examples of conjugated molecules ranging from low-molecular weight (LMW) molecules, homo-polymers (comprised of one repeat unit), and co-polymers (comprised of alternating repeat units). R represents positions to which side-chain groups are appended. In PTB7, R=ethyl-hexyl. Polyacetylene image reproduced from reference [30]. All other images reproduced from reference [31].

spacing of $2a$ and, thus, a reduced Brillouin zone of $k = \pi/2a$ which results in a band-gap. This band-gap reduces the energy of the valence electrons and, in a one-dimensional system, this reduction in energy is significant enough to stabilise the dimerised system with a bandgap. This effect is known as the Peierls instability [9] and results in π delocalised systems being characterised by a series of alternating bond lengths - the characteristic known as orbital conjugation. Furthermore, the emergence of this bandgap means that polyacetylene and many other conjugated molecules are, in fact, semiconductors [13].

Some common examples of conjugated molecules are shown in Figure 1.2 with each categorised as low molecular weight (LMW) or polymer. The distinction between the two is that the LMW molecules are typically much smaller than the polymers and consist of individual, non-repeating units as opposed to the repetitive structures of polymers. In all of the examples, the pattern of alternating conjugated double and single bonds can be seen.

Notable examples of LMW conjugated molecules are the acenes - such as napthalene and anthracene which each consist of two and three benzene-like rings, respectively [1, 32, 33]. These were among the first candidates for organic conduc-

tors [10–12]. Another notable example is Alq3 which was utilised in creating the first OLED device [22] and has since become a prototypical OLED active material [1, 33]. LMW conjugated molecules are often components of OLED devices due to their high-yield electroluminescence [33, 34] though many are promising components for OPV cells and OFETs due to the relative ease with which they form crystalline domains [6, 35]. A particularly common class LMW conjugated molecule for the purposes of OPVs is the fullerenes, particularly $PC_{61}BM$ and $PC_{71}BM$, which are efficient electron acceptors [36, 37] and are widely used acceptor materials in polymer-fullerene bulk heterojunction solar cells (which we discuss in Section 1.1.3). LMW conjugated molecules have also been theoretically considered for enhancing photochemical cells due to the well defined dipole-dipole interactions between dimer structures leading, in certain instances, to improved energy storage by relaxation to dark states [38].

Conjugated polymers are built of repeating structures of individual conjugated units such as polyacetylene described above. The archetypal conjugated polymers are those comprised of successive repeating structures of a single monomeric structure. These polymers, known as homopolymers, include polyacetylene as well as polymers consisting of planar structures such as PPVs [23, 39–44], polythiophenes [45–48], and polyfluorenes [49–53]. Another class of conjugated polymers are co-polymers which have monomer units consisting of combinations of individual conjugated monomers such as F8BT [54–56] (consisting of fluorene and benzothiadiazole monomers) or PTB7 [57–59] (consisting of a combination of benzo-bithiophene and thieno-thiophene monomers). Beyond polyacetylene, modern conjugated polymers can be functionalised extensively to allow for solution processing as well as enhanced efficiency and tuning of characteristics. [1, 37, 60–62]. These points will be discussed further in Section 1.1.4.

Conjugated polymers offer unique prospective benefits such as solution processability; low-cost fabrication with few environmental concerns; and mechanical flexibility which are not afforded by inorganic technologies [1, 26]. However, with conjugated polymers, it is often these same properties which lead to substandard performance. For example, their polymer nature and the disordered morphologies that lead to their flexibility and being solution processable also lead to a complicated energy landscape for charge transport and, ultimately, loss in efficiency [8]. To understand how these principles arise, we now present an overview of the basic photo-physics and charge transport properties of conjugated materials.

1.1.2 Photo-physics and charge transport in conjugated materials

Many of the basic operational concepts behind organic devices are similar to those of inorganic materials. For OLEDs, high-mobility transport of carriers (both electrons and holes) is required for optimal performance as well as the ability for electrons

and holes to meet in emissive regions and radiatively recombine [1, 26, 32–34]. For OPVs, it is required that the material is absorptive with photo-generated electron-hole pairs being separable and mobile across the device [6, 63] and OFETs require high carrier mobilities and which can be manipulated effectively by an applied gate voltage [6, 64–66]. While these concepts resemble those of inorganic semiconductors, the physical mechanisms of carrier transport and optical response in each differ quite significantly. In this section, we shall review the basic concepts of optical transitions, exciton formation, and carrier transport in organic materials.

Optical transitions from or to the molecular ground-state are transitions between occupied and unoccupied orbitals. In forming a covalent bonds, two singly occupied hybrid atomic orbitals form a doubly occupied bonding orbital comprised of a combination of the two. In addition, another higher energy, unoccupied orbital is formed. This orbital is known as an anti-bonding orbital which, for a π bonding orbital, is labelled as a π^* orbital. The equivalents of the valence band (VB) and conduction band (CB) in conjugated molecules are the π orbitals and the π^* orbitals respectively [1]. The highest and lowest energy orbitals in each band are known as the highest occupied molecular orbital (HOMO) and lowest occupied molecular orbital (LUMO) and the energy difference between the two is representative of the molecular band gap. Typically, the HOMO-LUMO gap is $\simeq$ 1-3 eV in conjugated molecules [60].

In order for any optically induced transition to occur, an overlap between the orbitals in the π and π^* bands is required. Often, for a given transition this occurs on particular segments of the molecule which are known as chromophores [26]. A typical, simplified picture of the transitions involved in optical absorption and emission processes between the molecular ground state, S_0, and, in this case, the molecular first excited singlet state, S_1, is given in Figure 1.3 and highlights key features of molecular absorption and emission. The first of these is the additional vibronic transitions which occur along with the direct transitions. These result from the intrinsic vibrations of each molecule which, in turn, lead to phonon coupling of the optical transitions. These can often be described by considering the molecular geometry to have a harmonic oscillator response with a set of additional, vibrationally-accessible energy levels [26] which, in planar conjugated structures, are often linked to the vibrational modes of conjugated rings [67]. As such, in absorption there are direct transitions from the S_0 vibrational ground-state to one of the vibrational states in the S_1 space with secondary states resulting from vibrational excitation (from phonons) in the S_0 state and subsequent optical absorption. The converse also occurs for emission from the S_1 to S_0 states. Secondly, there is typically a red-shift in emission energies when compared to absorption energies. This shift, known as a Stokes shift, results from the molecular geometry reorganising to accomodate for an excited state (S_0-S_1 relaxation) or a change to the ground state

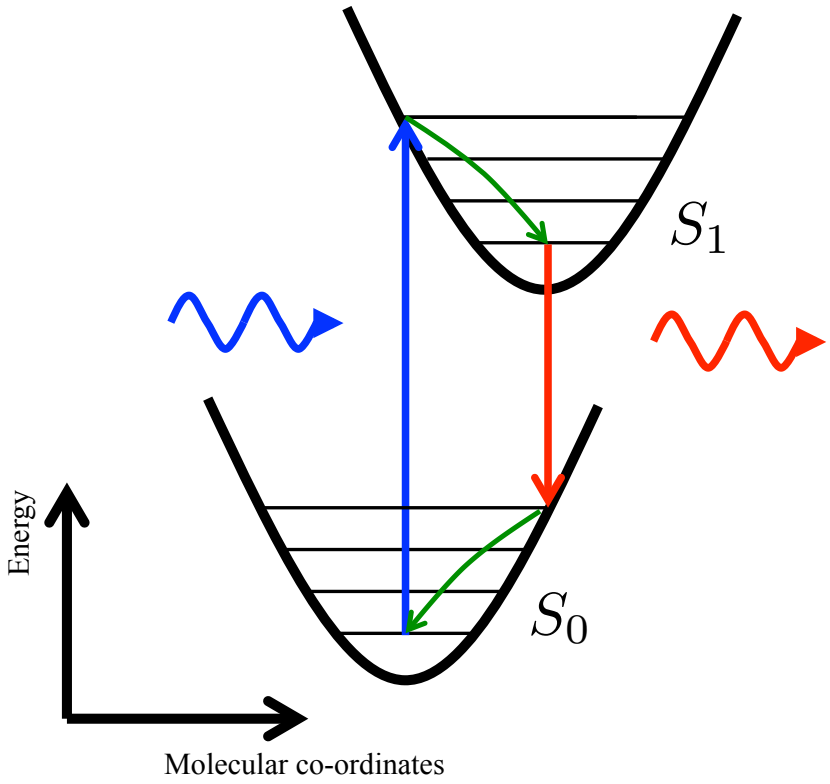

Figure 1.3: Diagram representing singlet absorption (blue arrow) and emission (red arrow) in a molecule from the S_0 manifold to the S_1 manifold and vice versa. Relaxation (green arrows) occurs after each process with energy dissipated to the surrounding environment.

(S_1-S_0 relaxation) [68]. Direct transitions from S_0 are to states above the relaxed S_1 state and vice-versa. As such, the absorption transition can have a notably higher energy than the emission transition.

Due to the relatively low relative permittivity of organic materials ($\epsilon \simeq 3$ as opposed to $\epsilon \simeq 11$ in inorganic materials), optical absorption typically leads to the creation of bound electron-hole states known as excitons [8]. As the electronic ground-state of a molecule consists of electron pairs with anti-parallel spins, the excitons formed immediately upon optical absorption are singlets (denoted by the notation S_n above). These excitons are typically localised to individual chromophores (known as Frenkel excitons) [1]. The generation of other excited states, such as triplet excitons and polarons, is possible. These excited states often have a significant role in device performance. For instance, free carriers forming excitons will, from spin statistics, form triplets and singlets in a ratio of 3:1, respectively [1]. Radiative recombination in triplets is generally far slower than that in singlets due to the the triplet recombination requiring an additional change of spin [1,69]. As such, OLED performance can be significantly reduced by triplet formation. In OPVs, the converse is true in that recombination of photo-generated carriers is a loss mechanism and, as such, triplet excitons formed from free-carriers may dissociate again before recombination mechanisms occur [70]. Polarons occur from ionisation and

strong carrier-phonon interactions which result in a combined lattice distortion and excited state [1, 7–9, 71]. Polarons also exhibit sub-gap absorption [7, 9] as well as self-trapping [1] which, in turn, can have a significant impact on conduction and carrier dynamics.

Excitons in organic materials typically have large ($\sim$ 0.5-1 eV) binding energies [1]. These excitons are difficult to separate and, for OPV materials in particular, transport of excitons is crucial in order to reach charge separation sites [7, 57, 72] (as we discuss in the following section). Excitons diffuse by mechanisms such as Förster transfer [73] and Dexter transfer [74]. Förster transfer involves virtual photon emission between adjacent chromophores and is sensitive to chromophore spacing and alignment as well as the emission and absorption spectral overlap of the donor and acceptor chromophores, respectively [75, 76]. Dexter transfer results from a two-electron tunnelling process and typically occurs only at very short inter-chromophoric separations [77, 78].

In addition to the strongly-bound excitons typical to organic semiconductors, the inherent conformational disorder in multi-molecular systems leads to a different notion of charge transport than that of inorganic materials [8]. The highly-regular nature of crystalline inorganic materials leads to effectively continuous bands. Although it is convenient to consider the HOMO and LUMO levels as constituting bands in organic semiconductors, fundamentally these bands are a collection of disordered and localised states. As such, transport in these systems is described by discrete hops over a semi-random distribution of states with hopping integrals typically determined by the electron/hole affinities of acceptor/donor units as well as their spatial separation [9]. This type of transport results in carriers which are far less mobile [8, 79] than those in a continuous band of states. Hopping transport is often described by models which incorporate a description of state disorder within bands. A review of these models can be found in reference [8]. From the basic picture, we note that the discrete, disordered landscape will hinder charge transport. Furthermore, band disorder leads to the emergence of numerous trap states which can effectively halt charge transport [8, 9]. Thus, to fully understand, theoretically, the charge transport properties of organic semiconductors, it is necessary to understand how disorder arises. This forms the primary motivation for the work presented in this thesis.

In this section, we have given a brief overview of the basic principles governing optical response and charge/exciton transport in conjugated systems. In discussing transport, we have alluded to the disordered nature of charge transport expected from these molecular materials. In the following section, we shall discuss how the physical concepts of transport and photo-electric interactions are closely related to molecular conformation at the single molecule and bulk molecular morphology levels and demonstrate the significance of each of these in optimising organic devices. In

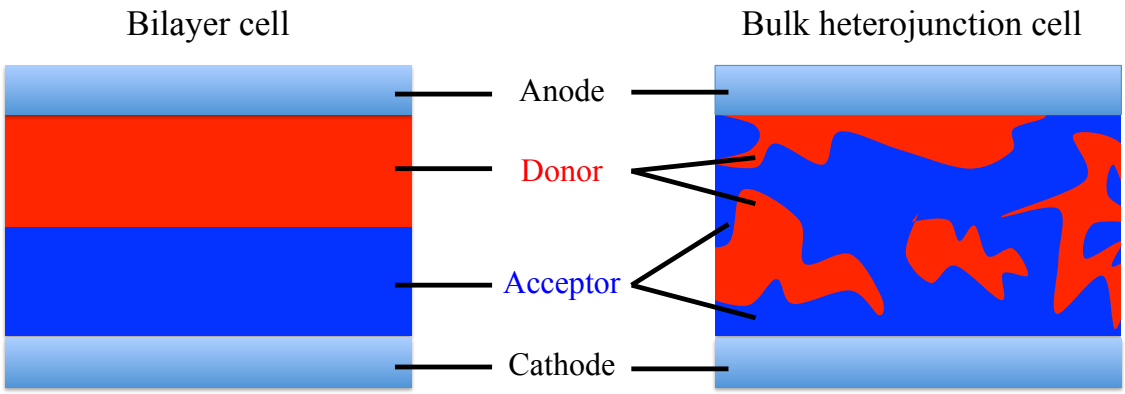

Figure 1.4: Sketches of photovoltaic cells made of a donor (red) and acceptor (blue) materials. The bilayer cell is comprised of a layer of each material while the bulk heterojunction cell has the donor and acceptor media interspersed throughout the active layer.

this regard, we highlight the need to better understand and model the properties of molecular conformation and morphology in order to further the development of these technologies.

1.1.3 Influence of material morphology on electronic characteristics

Organic materials typically offer a wide variety of possible morphologies spanning crystalline, semi-crystalline, and amorphous configurations. As discussed in the previous section, highly disordered transport systems have typically lower carrier mobility and are prone to carrier traps. The disorder in these systems is closely related to the disorder in the overall material morphology which can be treated on two scales: the macro-scale material morphology, which concerns the formation of molecular domains and transport channels; and the discrete molecular conformations, which contribute to on-chain disorder in polymeric systems.

Across organic devices, there are numerous examples of the impact of morphology on the charge and exciton transport properties of a given device. To illuminate the impact of morphology on organic device performance, we shall discuss the notable example of the bulk heterojunction (BHJ) OPV cell. Considerations of morphology for charge transport optimisation are of a similar nature for OLEDs [32, 33] and OFETs [6,66]. The BHJ OPV cell has been the subject of much of the research and many breakthroughs in OPV devices in recent years [6,32,36,37,57,62,63,70,80,81]. The utility of these composite device layers, typically composed of a blend of conjugated polymer and fullerene materials, was discovered by Kraabel *et al* [36] who demonstrated that C_{60} fullerene works as an excellent electron acceptor for separating photo-generated excitons on the conjugated poly(3-octyl-thiophene) (P3OT) polymer leading to a factor of 10 increase in photo-conductivity. A sketch of a BHJ OPV cell is shown in Figure 1.4. This differs from a conventional, crystalline bilayer photovoltaic cell (also shown in Figure 1.4) in that the donor and acceptor media

(the conjugated polymer and fullerene, respectively) are interspersed throughout the active layer as opposed to in effectively separate p-type and n-type regions. In a BHJ device, charge separation occurs throughout the active layer and the resulting photo-current progresses along the channels formed by each material.

Control over bulk heterojunction morphology is crucial to the overall device perfomance. While charge separation at a polymer-fullerene boundary is an efficient process [36,37], photo-generated excitons must first diffuse across the polymer region. Exciton diffusion lengths in conjugated polymers are typically $\sim$ 10-20 nm [82–85] which imposes a limit on the width of electron-donating polymer regions. Furthermore, the alignment of π-π stacked layers with the cathode has been shown to also have a significant effect on device performance by promoting hole transport [62, 81].

Proper control of BHJ morphology has been shown to lead to solar cells with near 100% internal quantum efficiency (IQE) - the efficiency of photo-current generation based on the number of formed excitons [37]. Many works have studied the emergence of optimal BHJ morphology [57, 62, 81, 86, 87] and typically conclude that optimal cells are comprised of fibrous networks of polymer-rich and fullerene rich domains with widths $\simeq$ 10-50 nm [37, 57] which allow excitons to diffuse to separation interfaces while maximising channel length so as to promote carrier transport upon separation.

Recently, Liu *et al* [80] showed that a set of thiophene and benzodiathiazole based co-polymers formed BHJ cells with efficiencies of $\sim$ 10%. A crucial aspect of the formation of these cells was in the temperature-dependent solution aggregation of the polymers which was utilised to form precursor aggregated domains prior to spin-casting. This in turn led to enhanced crystallinity of the polymer domains and, therefore, greater hole transport. This work was further expanded in the same group by Zhao *et al* [81] who, using the polymer PffBT4T-2OD fabricated the record-setting 11.7% efficient OPV cell. They noted that, by optimising both the material and fabrication techniques (which we discuss in greater detail in the following section), their optimal solar cells, when compared to their poorer performing samples, had enhanced crystallinity within the semi-crystalline domains as well as a greater degree of face-on packing at the hole-transport interface.

In terms of optical properties, device morphology and, at the discrete molecular level, molecular conformation have significant effects beyond that of transport properties alone. The majority of modern conjugated polymers consist of planar units connected by π-conjugation. As such, a twist or 'dihedral' angle can be defined between two given units (as shown schematically in Figure 1.5). As orbital conjugation is typically spread across the planar sub-units, the twist between two planes disrupts conjugation and leads to an increase in the HOMO-LUMO gap [88]. This can be rationalised by considering the reduction in the overlap of adjacent π orbitals shown schematically in Figure 1.5(b). For dihedral angles close to 90°,

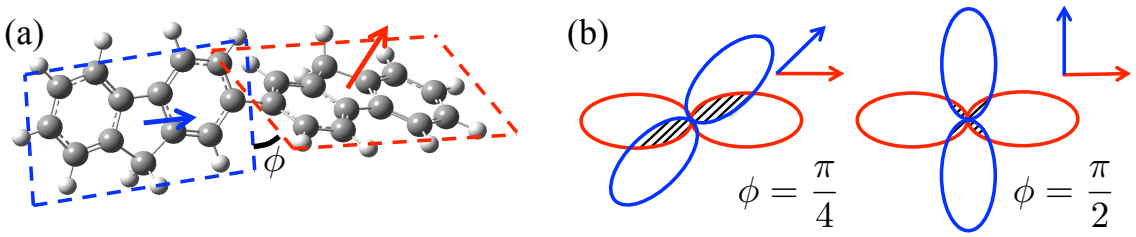

Figure 1.5: (a) Inter-monomer dihedral angle, ϕ, in a fluorene 2mer formed between the fluorene monomer planes. (b) Simplified diagram of how π orbital overlap between monomers changes are function of dihedral. The red and blue bubbles represent an effective π orbital between one monomer unit and the next (blue and red respectively) with the overlap shown by the shaded regions. The vectors signify the normals to the corresponding planes.

the orbital overlap is at a minimum which results in minimised electronic coupling between adjacent monomers. In turn, large distortions of these kind disrupt the overall conjugation and lead to increases in the HOMO-LUMO gap and localisation behaviour [89]. Furthermore, it has been theorised that, by distorting or 'breaking' conjugation, the occurence of large dihedral angles can be treated as conjugation breaks and this notion is often used as a one means of identifying the chromophores of a polymer [88,90–93] (though it is to be noted that this definition of chromophore is contested in the literature [89, 94–96] and we shall discuss this point in greater detail in Chapter 5).

In the ground state, dihedral angle dynamics are governed by the competing effects of conjugation, which prefers planarity, and steric conflicts, which typically lead to energy penalties for planar conformations. Thus, the majority of conjugated oligomers and polymers have energetic minima corresponding to dihedral angles in the region of 30°-60° [44,93,97,98]. Molecules in the excited state typically planarise due to the enhanced effect of the excited conjugated orbitals [98]. This is one of the major relaxation mechanisms responsible for the Stokes shift discussed in Section 1.1.2.

Of course, other environmental factors can influence dihedral angle behaviour in certain circumstances. One notable example is the emergent planarisation of polyfluorenes known as β-phase [50–52, 98–100]. This phase is characterised by a sharp absorption peak in the region of 440 nm and a clear vibronic progression in emission [49] and emerges upon aggregation in films and in poor quality solvents [50, 51]. These features are attributable to extend segments of planarised dihedral angles and has been shown to be linked to the choice of alkyl side-chain [100] and solvent [99] (which we discuss further in Section 1.1.4).

Given the planar stability of conjugated monomers afforded by π conjugation, variations in inter-monomer dihedral angles are a primary source of local, along-chain conformational disorder in conjugated oligomers and polymers. As with morphological disorder between adjacent chromophores, disorder along the polymer

chain can have significant localising effects on molecular orbitals and can lead to exciton self-trapping [98, 101–106]. One clear example of this behaviour was observed by Montgomery *et al* [103, 104] in which optically induced exitons in a star-shaped oligofluorene-truxene complex were found to localise on one oligofluorene arm due to favourable dihedral distortions. This lead to the otherwise C_3 rotationally-symmetric molecules having fluorescence behaviour akin to rod-like molecules.

Conformation and morphology are responsible for a myriad of effects in the optical response and charge transport properties of organic semiconducting materials. It is evident that morphology optimisation and material design are both crucial to improving device performance. Furthermore, the wide scope of molecular conformations also leads to the attractive potential of tunability to desired behaviour given a full understanding of how to control molecular behaviour and material processing. With this in mind, we turn to the key features of material design and solution processing and how they are utilised to enhance desired properties.

1.1.4 Relating material properties and processing to morphology

Along with the mechanical properties of organic materials, one of the attractive prospects of organic semiconductors is the use of solution processing techniques which lend themselves to low-cost, large-area fabrication. However, these techniques themselves present a number of significant challenges. For example, fully dissolving molecules in a solvent will destroy crystalline or semi-crystalline formations. Furthermore, conjugated molecules require functionalisation to be soluble in the first place by, typically, appending highly-soluble branched molecules known as 'side-chains' to conjugated units. Side-chains introduce disorder to conjugated molecules which, in turn, enhances solubility. However, by this same mechanism, side-chains also lead to disorder in the solid sample. Both the choice of solvent and side-chains, along with the conjugated component ('backbone') itself, lead to a vast array of variables which require effective engineering so as to best suppress the intrinsic undesirable properties and optimise performance. This is exemplified by the work of Yuan *et al* [35] in which control over solution processing techniques and polymer design were utilised to design highly-ordered LMW OFET devices with hole mobilities of 43 $\mathrm{cm^2V^{-1}s^{-1}}$ - a record for OFET devices - as well as that of the record-setting OPV devices of Zhao *et al* [81] discussed in the previous section. Both these works, along with many others on organic device research [37, 57, 62, 63, 66, 80, 107], demonstrate how the engineering of these features can yield breakthroughs in device optimisation. To conclude this section, we give an overview of the influence of molecular design, side-chains, and solvents on material properties, photo-physical response, and aggregate formation.

As the semiconducting properties of conjugated materials emerge from the conjugated backbone, it follows that the design of these portions is crucial to optimising

device behaviour. For instance, incorporating heavy atoms into conjugated backbones has been successfully utilised to enhance intersystem crossing as a means of harvesting singlets or triplets for enhanced phosphorescence or fluorescence in OLEDs [32,33]. (An example is the Al atom in Alq_3 shown in Figure 1.2.) Utilising combinations of different conjugated moieties in a polymer, for example, in donor-acceptor co-polymers such as F8BT and PTB7, is a widely adopted strategy for decreasing the HOMO-LUMO gap [6,60]. Donor-acceptor co-polymers are typically comprised of electron-rich (D) and electron-deficient (A) conjugated moieties in alternating structures (such as those shown in Figure 1.2) and have lower band gaps than conventional homopolymers ($\simeq$ 1-1.5 eV compared to $\simeq$ 2-3 eV) [60]. This has been shown to lead to significant increases in OPV performance by enhancing the efficiency of solar absorption [60]. As such, these materials have become commonplace in these devices and in conjugated material research [57, 80, 81, 108].

Conjugated molecules are typically insoluble and require solubilising side-chain groups for solution processing [61]. The most commonly used side-chains are alkyl side-chains which consist of hydrocarbon branches of several (often six to twelve) methylene groups [61]. Side-chains often have the effect of inhibiting the formation of planar-stacked structures and, thus, the desirable semi-crystalline domains discussed in the previous section, as a result of their flexible and disordered nature. Side-chains have also been shown to enhance orbital localisation in amorphous materials [44] and, thus, reduce the charge tranfer character of devices. It is clear that careful tuning of the side-chain length is required so as to allow for solvation without compromising on forming suitable morphologies. However, side-chains can also lead to a number of potentially desirable effects. For instance, utilising hexyl side-chains on polythiophenes (poly(3-hexyl-thiophene), P3HT) optimises solution crystallisation as a result of inter-molecular interactions between neighbouring side-chains [46,97,109]. Also, the β-phase of poly-fluorene has been shown to be strongly side-chain dependent and can be most readily formed utilising octyl side-chains (poly(9,9-dioctyl-fluorene), PF8) [100].

Alkyl side-chains are formed of sp_3 carbons and, as such, typically do not greatly affect the sp_2 orbital conjugation properties at the intra-molecular level. However, various other functional forms of side-chains may be used to directly manipulate the properties of the conjugated backbone orbitals. These include electron donating and accepting groups or conjugated branches. A comprehensive review of the various forms of side-chains can be found in reference [61].

Given their purpose, it follows that side-chains interact strongly with the solvent medium. The example of β-phase PF8 has been suggested to result from the side-chains effectively locking the inter-monomer dihedral angles in the planar position and a sufficiently low solvent quality so as to aid solution aggregation and further stabilise this configuration [52,99,100]. Solvents are often considered based on their

ability to solvate a system and are often classified as 'good' or 'poor' solvents which roughly denote whether solvent-polymer interactions are favourable - leading to enhanced polymer solvation - or polymer-polymer and solvent-solvent interactions are favourable - which lead to reduced polymer solvation and aggregation. If a solvent is too 'poor', then no solvation can happen. However, if a solvent is too 'good', it becomes very unfavourable for any sort of ordered aggregates to form upon casting. As such, for the purposes of polymer device fabrication, solvent tuning is required to strike a delicate balance between these two contrasting principles.

Often, solvent properties are tuned by utilising otherwise 'good solvents' with a small concentration of an additive [57, 58, 80, 81, 86, 87, 110, 111]. Returning to the example of the BHJ cell, a commonly used additive is 1,8-di-iodo-octane (DIO) [57,58,80,81,86,87,110,111]. As demonstrated by Peet *et al* [86], a similar additive (octane-dithiol) greatly improved the efficiency of BHJ cells of PCPDTPT:$PC_{61}BM$ solar cells by around a factor of two. This improvement was compounded through the use of DIO by Lee *et al* [87] who showed that the solvent additive had the effect of selectively dissolving the fullerene layer and, thus, leading to domain formation upon aggregation. Since then, DIO has become a ubiquitous solvent additive for BHJ fabrication. However, other viable alternatives exists such as phenyl-napthalene, Zhao *et al* [81] which, for the polymer PffBT4T-2OD, was found to greater enhance polymer-interface alignment and domain crystallinity when compared to DIO.

So far, we have discussed the basic principles underlying organic semiconductor behaviour. By first discussing the basic principles of conjugation, followed by those of photo-physics and charge transport in conjugated materials, we have formed an understanding of how material morphology has a significant impact on device performance. Furthermore, it has been shown by numerous works that the multi-faceted nature of material design and solution-processing leads to a number of significant problems as well as potential opportunities for controlling and tuning emergent device characteristics. So far, the bulk of the work we have discussed has been experimental and has shown the great progress which has been made at the laboratory level. However, we have hinted at the complex nature of the interactions which lead to the resulting material properties. Particularly, the nature of polymers and the complex relationship between polymers, side-chains, and solvents are crucial components of effectively modelling these materials. As such, the following section is devoted to the concepts of polymer physics and how they may be related to a conjugated polymer framework.

1.2 Polymer statistical mechanics

In the previous section, we discussed the sensitivity of device characteristics and performance to the morphology of their discrete molecular constituents. We noted the complex morphologies which are formed from conjugated polymer based devices.

The complexity involved in polymers follows directly from the large scale of the molecules (often referred to as 'macromolecules' in this respect). Beyond the typical molecular interactions - van der Waals forces, covalent bonding, etc. - polymers have a large number of possible conformations which requires a statistical mechanical treatment.

We devote this section to the basic formulations of polymer statistical mechanics. This allows us to build up the language of polymer conformation as well as the guiding principles which we utilise in the analyses throughout this thesis. Initially, we discuss the idealised, freely-jointed chain (FJC) [15] of uncorrelated, discrete monomer units. In this model, polymer conformations of a given length are akin to the paths of Brownian particles over a given time. We then discuss models with a notion of polymer stiffness: the discrete freely-rotating chain (FRC) [15], and its continuum analogue, the wormlike chain (WLC) [112].

1.2.1 Freely-jointed chains

In its simplest conception, a polymer conformation of N units each of a fixed length l may be considered as one possible path of a discrete random walk of N steps of length l. This simple model is commonly known as the freely-jointed chain (FJC) [15] and allows for the definition of the idealised i.e. completely unrestricted dynamics of a polymer which, in turn, permit the determination of reference quantities such as the idealised end-to-end length and radius of gyration.

To each bond i, we assign a unit tangent vector, $\mathbf{v}_i$ and assume a fixed monomer length, l. The chain is thus characterised by the set of bond angles, θ_i, and bond-bond dihedral angles, $\tilde{\phi}_i$. (The distinction $\tilde{\phi}$ and the term 'bond-bond dihedral angle' is in place to distinguish between the dihedral angle between two conjugated planes which we refer to as the dihedral angle, ϕ, throughout this work.) These are shown schematically in Figure 1.6.

For polymers, the typical convention for the dihedral angles is setting the *trans* bond-bond dihedral to $\tilde{\phi} = 0°$ such that a chain of succesive bond-bond dihedrals of $\tilde{\phi}_i = 0°$ and a finite bond angle is zig-zagged and is curved for succesive $\tilde{\phi}_i = 180°$. This is known as the polymer convention [15] and is used throughout this work both for bond-bond dihedrals and the intermonomer dihedral angles.

The molecular end-to-end vector, $\mathbf{r}$, of a particular conformation is given by:

$$\mathbf{r} = \sum_{i=1}^{N} \mathbf{v}_i. \tag{1.1}$$

As the polymer environment is assumed isotropic, the average over the end-to-end vector, $\langle \mathbf{r} \rangle$, vanishes. The mean-squared end-to-end vector is the more meaningful

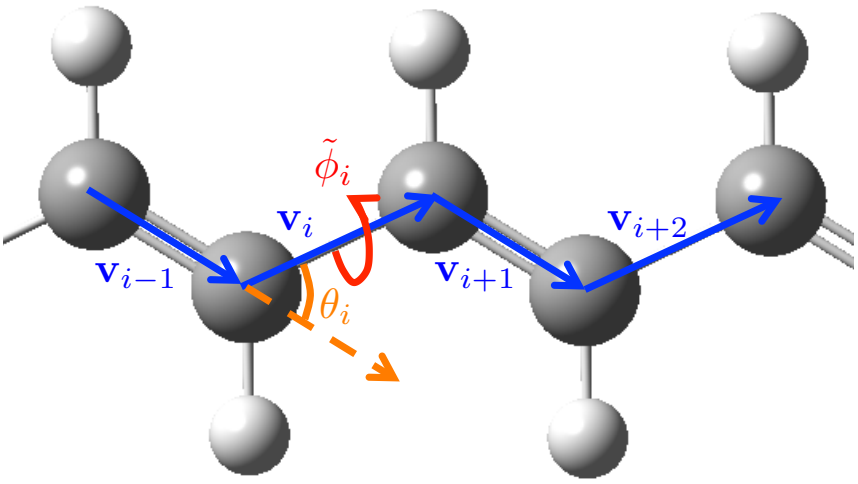

Figure 1.6: Labelling convention of a linear polymer chain (polyacetylene). The labels i, θ_i and $\tilde{\phi}_i$ referencing the i-th bond in the chain (represented by the vector $\mathbf{v}_i$ shown in blue) refer to: the bond angle between bond i and $i+1$ (shown in orange) and the bond-bond dihedral angle between the plane formed by bonds i and $i+1$ and that formed by bonds i and $i-1$ (shown in red), respectively.

quantity:

$$\left\langle r^2 \right\rangle = \sum_{i,j} \left\langle \mathbf{v}_i \cdot \mathbf{v}_j \right\rangle = l^2 \left[N + 2 \sum_{i=1}^{N-1} \sum_{j=i}^{N} A(|j-i|) \right]. \tag{1.2}$$

Above, we have defined a tangent-vector correlation function, $A(|j-i|) = \langle \mathbf{v}_i \cdot \mathbf{v}_j \rangle$. This form of mean-squared end-to-end length is valid for any linear molecular system with a fixed monomer length. For the FJC model, it is assumed that there is no correlation between any two tangent vectors. As such, $A(\Delta n) = \delta_{0,\Delta n}$ where $\delta_{i,j}$ is the Kroenecker delta measure. Then, Eq. 1.2 reduces to:

$$\left\langle r^2 \right\rangle = Nl^2 \equiv \left\langle r^2 \right\rangle_0 . \tag{1.3}$$

The quantity $\langle r^2 \rangle_0$ forms a base length scale for a polymer herein referred to as the ideal length scale. In the limit of a very long polymer such that $Nl \gg l$, the distribution of end-to-end lengths is subject to the central limit theorem. As with Brownian motion [113], the distribution is Gaussian with a variance of $\langle r^2 \rangle_0$. Using the standard definition of a $d = 3$ normalised Gaussian distribution:

$$P_N(\mathbf{r}) = \left(\frac{3}{2\pi \left\langle r^2 \right\rangle_0} \right)^{\frac{3}{2}} \exp\left(\frac{-3r^2}{2\left\langle r^2 \right\rangle_0} \right) = \left(\frac{3}{2\pi N l^2} \right)^{\frac{3}{2}} \exp\left(\frac{-3r^2}{2Nl^2} \right). \tag{1.4}$$

Rigorous derivations of this distribution may be found in references [15] and [114].

While this idealised model assumes no correlations between monomers, this behaviour emerges in real polymer systems of very large N such that the polymer may be subdivided in blocks of N_b units of length b such that $N_b \gg 1$ and $Nl = N_b b$ [115].

In this regime, Eq. 1.3 takes the form:

$$\left\langle r^2 \right\rangle = N_b b^2. \tag{1.5}$$

The length b is known as the Kuhn length [15, 17, 115] and forms an effective length over which the molecule may be represented as rigid and, thus, provides a measure of molecular rigidity applicable to large molecular weight systems.

Another important measure of polymer conformation which may be extracted from this model is the radius of gyration, R_g [15]. R_g is, by definition, a mean-squared quantity that measures the average squared distance of each mass in the molecule from the centre of mass point:

$$R_G^2 \equiv (N+1)^{-1} \sum_{i=0}^{N} |\mathbf{r}_i - R_{CM}|^2, \tag{1.6}$$

with

$$R_{CM} \equiv \frac{\sum_{i=0}^{N} m_i \mathbf{r}_i}{\sum_{i=0}^{N} m_i} = \frac{1}{N+1} \sum_{i=0}^{N} \mathbf{r}_i. \tag{1.7}$$

In the above, as we are considering a model of point masses connected by bond vectors, the system of N bond vectors contains $N+1$ point masses which leads to the appearance of the pre-factors $(1/N+1)$ in the definitions.

The importance of this quantity can be seen, first of all, as it, along with the the end-to-end length, serves as a measure of polymer folding. Each quantity provides insight into how close-packed a polymer is on itself when compared to the total arc-length, Nl. The radius of gyration, however, is particularly useful as it is experimentally quantifiable using light scattering techniques [45, 51] and is a commonly measured quantity for polymers. Measurement of end-to-end lengths is possible but, in most cases, requires the creation of polymers with 'end-marked' terminal units [116]. We discuss both of these points further in Section 4.3.

In discussing the freely-jointed chain model, we have established the idealistic behaviour of a macromolecular chain which has uncorrelated freedom. As mentioned, this behaviour may be observed in very long chains which can be split into effectively uncorrelated segments. However, if one wishes to build models with control over the microscopic details which govern the dynamics on a more intermediate scale, one has to introduce terms which represent these correlations. A simple extension is to introduce a notion of stiffness or 'persistence' to the model by either fixing bond angles or having an energy penalty associated with bends.

1.2.2 Freely-rotating and wormlike chains

Freely-rotating models are based on the notion that bond angles are often more restricted than bond-bond dihedral angles [15]. This step towards more realistic

polymer descriptions enforces a restriction on the bond angle - either by means of an energy penalty as in the Kratky-Porod model [112] or by fixing the bond-angle in the freely-rotating chain (FRC) model - while allowing bond-bond dihedral angles free rotation.

A simple way of manipulating discrete freely-rotating models is utilising a transformation matrix representation of the tangent vectors [15]. By assigning a coordinate frame (i) to the vector $\mathbf{v}_i$ such that $\mathbf{v}_i^{(i)}$ is aligned along the x axis, the transformation matrix, T_i, for translating the vector $\mathbf{v}_{i+1}^{(i+1)}$ to the (i) co-ordinate frame is defined by:

$$\mathbf{v}_{i+1}^{(i)} = T_i \mathbf{v}_{i+1}^{(i+1)} = \begin{bmatrix} \cos\theta_i & \sin\theta_i & 0 \\ \sin\theta_i \cos\phi_i & -\cos\theta_i \cos\phi_i & \sin\phi_i \\ \sin\theta_i \sin\phi_i & -\cos\theta_i \sin\phi_i & -\cos\phi_i \end{bmatrix} \mathbf{v}_{i+1}^{(i+1)}. \tag{1.8}$$

The dot products of each bond vector may be computed in terms of the elements of the tranformation matrix:

$$\mathbf{v}_i^{(i)} \cdot \mathbf{v}_j^{(i)} = (\mathbf{v}_i^i)^T \left(\prod_{k=i}^{j-1} T_k \right) \mathbf{v}_j^{(j)} = l^2 \left[\prod_{k=i}^{j-1} T_k \right]_{11}. \tag{1.9}$$

Eqs. 1.8 and 1.9 can be formulated for any linear, fixed-length model. As is to be expected, in increasingly non-idealised models, complexity arises in computing the products of T_i and, particularly, in formulating averages in systems where next-nearest neighbour correlations are considered. However, the assumption of free rotation simplifies this considerably. In this regime, the averaged transformation matrices $\langle T_i \rangle = \langle T \rangle \ \forall \ i$ with:

$$\langle T \rangle = \begin{bmatrix} \langle \cos\theta \rangle & \langle \sin\theta \rangle & 0 \\ 0 & 0 & 0 \\ 0 & 0 & 0 \end{bmatrix}. \tag{1.10}$$

Due to the simple form of the averaged matrix, the 11 element of the product matrix will be given by the 11 element of the averaged matrix raised to the power of the number of successive products. As such, the tangent-correlation function of this model can be simply defined as:

$$A(\Delta n) \equiv \left\langle \mathbf{v}_n^{(n)} \cdot \mathbf{v}_{n+\Delta n}^{(n)} \right\rangle = \left[\langle T \rangle^{\Delta n} \right]_{11} = \alpha^{\Delta n}(\theta). \tag{1.11}$$

With $\alpha \equiv \langle \cos(\theta) \rangle$.

A realistic condition is that $\theta \in [0, \pi/2]$, and, thus, α is positive and less than one for any choice of restrained bond angle. As such, Eq. 1.11 may be re-written as:

$$A(\Delta n) = \alpha^{\Delta n} \equiv \exp(-\Delta n / n_p) \equiv \exp(-\Delta n l / l_p), \tag{1.12}$$

with:

$$n_p \equiv -\frac{1}{\ln(\alpha)} \tag{1.13}$$

The quantities n_p and $l_p \equiv n_p l$ are the 'persistence length' [15] expressed in number of monomers and absolute length, respectively. This quantity gives an intuitive measure of the rigidity of a polymer or, equivalently, how long a straight segment 'persists' for. As such, the lack of correlation in the FRC model is equivalent to a persistence length of 0. Similarly, perfectly straight chains ($\langle\alpha\rangle = 0$) have $l_p \to \infty$.

From Eq. 1.11 and Eq. 1.2, the mean-squared length of the polymer is:

$$\left\langle r^2 \right\rangle = Nl^2 \left(\frac{1+\alpha}{1-\alpha} + \frac{2\alpha}{N} \frac{(1-\alpha^N)}{(1-\alpha)^2} \right) \xrightarrow{N\to\infty} Nl^2 \left(\frac{1+\alpha}{1-\alpha} \right). \tag{1.14}$$

The ideal length of Eq. 1.3 appears in this expression as a scaling factor though the functional form of the equation is lost. In the thermodynamic limit, $N \to \infty$, however, this form reduces to that of a constant factor, dependent on α, of the ideal length. As such, the Kuhn form of the mean-squared length is recovered with a Kuhn length of $b = [(1+\alpha)/(1-\alpha)]l$.

Energetically, such a chain may be considered with an energy penalty or bending modulus, κ associated with deviations from the rigid case. This model, the Kratky-Porod model [112], can be expressed by the Hamiltonian:

$$\mathcal{H}_{KP} \equiv -\frac{\kappa}{l} \sum_{i=1}^{N-1} \mathbf{v}_i^{(i)} \cdot \mathbf{v}_{i+1}^{(i)} = -\frac{\kappa}{l} \sum_{i=1}^{N-1} \cos(\theta_i). \tag{1.15}$$

The partition function, Z, of the system is defined by:

$$Z = \prod_{i=1}^{N} \left(\int_0^{\pi} d\theta_i \sin(\theta_i) \exp\left[\frac{\beta\kappa}{l} \cos(\theta_i) \right] \right) \equiv Z_1^N, \tag{1.16}$$

with $\beta \equiv (k_B T)^{-1}$. As each angle is assumed independent, the above definition is given in terms of the single angle partition function, Z_1, defined as:

$$Z_1 = \int_0^{\pi} d\theta \sin(\theta) \exp\left[\frac{\beta\kappa}{l} \cos(\theta) \right] = \frac{2l}{\beta\kappa} \sinh\left(\frac{\beta\kappa}{l} \right). \tag{1.17}$$

This allows for the definition of $\alpha \equiv \langle\cos(\theta)\rangle$:

$$\alpha = \frac{1}{Z_1} \frac{\partial Z_1}{\partial(\beta\kappa l^{-1})} = \coth\left(\frac{\beta\kappa}{l} \right) - \frac{l}{\beta\kappa}, \tag{1.18}$$

which has the limiting behaviour of $\alpha \to 1$ or 0 as $\kappa \to \infty$ or 0, respectively.

For sufficiently long polymers, it is often convenient to express the KP model in its continuum limit variety: the wormlike chain (WLC) model [115]. In the continuum limit, the model is amenable to descriptions of force extension [115, 117] and path integral methods [118, 119]. Taking the continuum limit of Eq. 1.15

(equivalent to $N \to \infty$, $l \to 0$) leads to the WLC Hamiltonian:

$$\mathcal{H}_{WLC} = \frac{\kappa}{2} \int_0^L ds \left|\mathbf{v}'(s)\right|^2 . \tag{1.19}$$

As opposed to a series of links, the chain represented by this Hamiltonian is a continuous curve of arc-length L parameterised by the arc-length parameter s. Likewise, the continuum limit of Eq. 1.13 and Eq. 1.18 results in:

$$l_p = -\frac{l}{\ln(\alpha)} \to \frac{l}{1-\alpha} \to \beta\kappa. \tag{1.20}$$

As such, the persistence length is directly proportional to the bending modulus. By utilising the continuum limit correlation function (obtained from Eq. 1.11), one obtains the mean-squared end-to-end length by:

$$\langle r^2 \rangle = \int \int_0^L ds ds' \exp(-|s-s'|/l_p) = 2l_p \left[L + l_p(1 - \exp(-L/l_p))\right] . \tag{1.21}$$

In the limit of $L \gg l_p$, $\langle r^2 \rangle \to 2l_pL$. As the continuum chain may still be arbitrarily subdivided into segments i.e. $N_b b = L$ may still be defined, in this limit we once again recover the ideal length factor based on the Kuhn length:

$$b = 2l_p. \tag{1.22}$$

Thus, the persistence length may obtained in relation to the Kuhn length in the large N limit. Furthermore, given that radii of gyration may be probed experimentally, measurements of persistence length may be used both as an empirical parameter for WLC simulations as well as reference for validation of other polymer models and simulations.

The FRC and WLC models give a basic idea of the behaviour of polymers which have an associated stiffness. We see that the quantity l_p - the persistence length - is a useful means of characterising the overall flexibility of a molecule which may be related to the Kuhn length in the thermodynamic limit. These examples give an overview of the basic concepts of polymer dynamics and statistical mechanics. While the models described are idealised in that they are governed entirely by the entropic freedom of the polymer, they also have bearing in modelling the dynamics of a wide range of molecules including conjugated polymers [120, 121] and biomolecules such as proteins [122] and DNA [117]. Analytical techniques can be used to manipulate these models e.g. path integrals [118, 119] (which we return to in Section 4.3.2) and normal mode analysis. These models also serve as the basis for simulation schemes such as Monte-Carlo [118, 123]. However, it is often the case that the interactions and form of polymers of interest (such as conjugated polymers) have a dynamical complexity which make them more amenable to simulation approaches.

1.3 Computational approaches to molecular modelling

In the above models, there has been no treatment of interactions other than those assumed to result in polymer stiffness. As such, they do not account for polymer chains self-avoiding or the effect of a solvent. In this sense, these models are highly idealised. There exists a vast number of extensions of these models which can account for such effects. One example is the Flory-Huggins model which treats the system volume as comprised of elements either occupied by the polymer or solvent [16, 17, 124]. This model allows for both self-avoidance and the definition of solvent-solvent, monomer-solvent, and monomer-monomer interaction terms. This model has recently been used as the basis of simulations domain formation in polymer/fullerene blends based on empirically-determined interaction parameters [125].

In most instances, these polymer models are at their most powerful in systems which can be described in an overall, coarse-grained manner i.e. when the microscopic details of the inter- and intra-molecular interactions and interactions with solvent may described *en masse*. While the general results of these models emerge, in certain instances, from a full treatment of the microscopic details of the system, as will be demonstrated throughout this thesis, there are numerous subtleties in the microscopic dynamics which play a large role in the overall macroscopic dynamics and in the light-matter interactions of a given system.

Much of modern theoretical research in conjugated polymers is performed using numerical calculations and simulations. These range from quantum mechanical calculations at the atomistic level - quantum chemical methods - which are often employed to probe excited state behaviour based on static conformations [75, 88, 89, 95, 96, 98, 108, 126, 127]; to parametric calculations and simulations, such as Monte-Carlo [128–131], Bloch equations [76], and molecular dynamics methods [46, 47, 97, 109, 132–134]. These latter methods rely on parameters obtained either empirically or from quantum chemical calculations to calculate and simulate properties for which a fully quantum chemical treatment is computationally infeasible e.g. dynamical conformations of polymers [46, 47, 97, 109, 132–134] or carrier transport dynamics in molecular devices [128–131]. Given the scale of a typical conjugated oligomer of, for example, 32 repeat units ($\sim 10^2$ - 10^3 non-hydrogen atoms or $\sim 10^3$ - 10^4 electrons) and the highly entropic nature of polymeric systems (leading to the necessity of many material configurations for analysis), the former class of methods is currently intractable for understanding polymer dynamics. As such, the latter class of methods must be employed in order to obtain insight into the problem of understanding molecular conformation and morphology.

In this section, we discuss parametric modelling techniques for dynamical simulations of molecular morphology. We focus particularly on the classical molecular dynamics approach given its ability to provide a description of computationally large ($\sim 10^6$ atoms) systems with resolution at the individual atomic level. In doing so,

we highlight two key areas which must be addressed: mapping quantum mechanical behaviour to classical mechanical simulations in the context of conjugated polymers; and the possibility of employing a two step procedure of, first, performing classical mechanical simulation, and, secondly, quantum mechanical calculations methods in order to probe conformational disorder and its role in excited-state behaviour.

1.3.1 Simulations of molecular conformation

The behaviour of polymer molecules and molecular ensembles are statistical in their nature: the typical quantities of interest are distributions and expectation values of given thermodynamic or configurational properties. These properties are amenable to simulation methods. With the aim of simulating polymer conformations and molecular morphologies, the two major approaches are those based on Monte-Carlo modelling and molecular dynamics. Monte-Carlo methods generate ensembles of possible configurations based on an underlying physical description of a system's energetic landscape by taking an initial configuration and varying it over the course of several steps [135, 136]. At each step, the change in configuration or 'move' is permitted with a probability corresponding to the Boltzmann factor $\exp(-\Delta E/k_B T)$ where ΔE is the change in energy resulting from the move. Statistical ensembles of possible geometries are obtained by performing several runs over a sufficient number of steps. Molecular dynamics, on the other hand, is a dynamical simulation regime which simulates real-time dynamics based on a set of configurational co-ordinates and a description of the potentials governing these co-ordinates. If a dynamical system can be assumed to be in a state of thermodynamic equilibrium and is sampled over sufficiently long time steps so as to avoid correlated samples, a set of 'snapshots' is obtained which are built into a statistical ensemble [135].

Each of these simulation methods requires parameterisation based on the interactions between atoms and molecules. How this parameterisation is performed can be described either as atomistic or coarse-grained with the former covering parameterisation which assigns a physical description to individual atoms and the latter to groups of atoms or blocks in a system [135]. In this work, we focus on molecular dynamics approaches at the atomistic level. Utilising atomistic simulations offers several notable advantages over coarse-grained simulations. Atomistic simulations can capture the microscopic detail underpinning phenomena such as the role of alkyl side-chains in conjugated polymers and the nature of solvent-polymer interactions which have contributions from solvent molecule shape, polarity, as well as van der Waals terms. Also, conformations resulting from atomistic simulations may be directly utilised in quantum chemical calculations (which require the specification of individual atomic co-ordinates) in addition to the possibility of being mapped to coarse-grained models. For polymer dynamical simulations, Monte Carlo methods are often coarse-grained to some extent, e.g. by considering block solvent-monomer

interactions [131]. In fully atomistic cases, different atomic motions are specified with different rates at which moves are performed corresponding to the different time scales of different degrees of freedom e.g. backbone moves occurring on longer time scales than side-chain moves [137].

Molecular dynamics simulations require a description of potentials which, in the atomistic regime, means a description of the interactions between covalently bound atoms and non-covalently paired atoms (Van der Waals (VdW) forces). Essentially, this is a Born-Oppenheimer simulation regime in that the electronic motion is considered to be sufficiently fast as to be separable from nuclear motion. The potentials in the simulation govern the nuclear co-ordinates and are representative of the quantum mechanical behaviour of the molecular electrons. Thus, the simulation itself is of the effective Newtonian dynamics of the nuclei.

The manner in which the basic potentials are described form two distinct methodological regimes. First, a realistic scenario would involve calculating an effective force-field utilising a fully quantum mechanical representation of the electronic states. This regime involves incorporating quantum chemical methodology following a basic algorithm of: defining the electronic energy landscape for a given molecular configuration using quantum chemistry; calculating effective forces on the nuclei based on the energy landscape and allowing these forces to act on the nuclei over a given timestep; and recalculating the energy landscape based on the new molecular configuration. Approaches which fall into this category are often referred to as *ab-initio*-molecular dynamics (*ai*MD) [106, 138, 139]. Secondly, in a system where it can be assumed that there is zero probability of the occurence of high-energy phenomena, such as the breaking of bonds, molecular ionisation or, indeed, photon absorption, one may make the approximation that each molecular configuration corresponds exactly to a given potential energy i.e. that, for a given temporal resolution, the electronic structure for a given molecular configuration closely corresponds to the ground state electronic structure of said configuration. Invoking this approximation leads essentially to a classical description of the dynamics. This regime is known as classical molecular dynamics [135].

Currently, the utility of *ai*MD methods is limited to very small molecules [106, 139] due to the fully quantum mechanical treatment embedded in the method. However, as we discuss in Section 1.3.3, the development of these methods offers numerous possibilities for observing excited-state behaviour in a dynamical environment. For dynamical simulations of systems of large molecules (i.e. $L \gg l_p$) in a fully atomistic manner, classical MD (herein referred to simply as MD) is the only viable option of the two.

Provided an appropriate description of the set of interaction potentials (referred to as a 'force-field'), which we discuss in the following subsection, MD simulation methods are capable of modelling large volumes of molecules in solvents or aggre-

gates of molecules with each treated with explicit interactions. As such, it is an ideal candidate for understanding the subtle behaviour of conjugated material conformation and morphology and its scope has been recognised in numerous works ranging from studies of crystalline and amorphous aggregate structures [44,46,132,140–143], the formation of single molecule ordering in solution [144], and the role of solvent additives on aggregation in fullerenes [145]. The ability to directly implement the results of MD simulations for quantum mechanical calculations has also been recognised in studying the formation of trap states due to conformational disorder [44], the effect of conjugated molecule stacking on absorption spectra and excitonic coupling [142, 143], and variations in absorption spectra between different phases of P3HT [47].

The scope of MD simulation for understanding conformation and morphology in conjugated materials is apparent from the above and is the focus of the work presented. As is to be expected, there are a number of technical considerations for carrying out these simulations which are discussed in greater detail in Chapter 2. One key consideration, which we introduce in the following, is forming a set of force-field parameters for conjugated molecular systems.

1.3.2 Classical force-fields for conjugated polymers

The key working principle of MD simulation lies in the ability to construct a classical force-field as a description of inherently quantum mechanical bodies. As one may expect, this is a non-trivial task and has been the subject of much work [146–154] which has primarily targeted simulations of biomolecules. Concurrently, the ongoing development of these force-fields has led to MD simulation becoming a vital tool in understanding biological molecular systems [146,155]. Conjugated polymers, given their synthetic origins, are not well described by these force-fields. As such, it is necessary to re-parameterise available force-fields for simulating conjugated molecules and the manner of doing so requires careful consideration so as to obtain an accurate force-field representation in an optimal manner.

In Section 2.1, we give a detailed discussion of the various potential terms in the force-field and how they are utilised in the conjugated polymer framework. To briefly summarise, arguably the most important term to be considered are the potential terms governing the inter-monomer dihedral angles in a conjugated system. Accurate modelling of the dihedral profile and energy barriers between conformers is of utmost importance as the excited-state landscape and optical properties of conjugated molecules are strongly dependent on these angles [156]. This is echoed by the majority of methodological approaches [47, 93, 132, 140, 144]. As any force-field potential is intrinsically a representation of quantum mechanical, electronic behaviour, obtaining dihedral potentials requires quantum chemical calculations. In addition, treatment of inter-molecular interaction terms (due to dispersion forces

and electrostatic interactions) must be properly assessed so as to accurately account for e.g. π-π-stacking interactions when modelling aggregation effects [132].

For conjugated polymers, force-fields have been parameterised in a number of works [47, 93, 132, 140, 144]. However, it is often the case that there are conflicting results on the details of each (which we review in greater detail in Chapter 3 and Section 4.1). One notable example of such a conflict is in the level of quantum chemical theory required to accurately model dihedral potentials. Recently, Bloom and Wheeler [157] have performed highly accurate calculations of the dihedral potentials of thiophene 2mers. The calculation method used in their work is infeasible for larger molecules (e.g. fluorene, PTB7 or molecules longer than 2mer) though the result provides a benchmark by which to compare computationally tractable methods. As such, it is possible to determine an optimal methodology for obtaining potentials which can shed light on the level of theory required for these calculations.

As we discussed in Chapter 1.1.4, there is a wide-scope for molecular engineering based on the variety of conjugated moieties and their side-chain branched analgoues. Understanding the role of these variants is crucial to realising the potential of MD simulation framework for material design and, given the recent progress made in utilising computational chemistry methods in steps towards massively parallelising high-throughput material screening [158], it follows that optimising the transferability and functionality of conjugated molecular force-fields could play a vital role in further developing these approaches. An optimal force-field parameterisation scheme is one which, along with utilising optimal calculation methods, can be generalised as far as possible to different backbones and side-chain groups so as to enhance the transferability and, thus, efficiency of the modelling process. So far, exploration of this generalisability has been neglected in the majority of works. Both the work of DuBay *et al* [93] and Jackson *et al* [144] have presented methods for calculating dihedral potentials which, based on self-referential calculations, are similarly accurate across several types of backbone. The role of side-chains on dihedral potentials and other force-field parameters has not had a comprehensive treatment to date. Also, the effect of extending backbone length has not been adequately treated. While the work of Darling and Sternberg [159] has treated both extending backbones and alkyl side-chains, as well as that of Bhatta *et al* [97], both works utilise an approximation by which the conjugated backbone is assumed to have no significant relaxation with regards to dihedral rotations. We have found this approximation to be invalid and, thus, leads to dihedral potentials with clear dependence on initial conditions. Furthermore, the conclusion of backbone length dependent torsional potentials obtained by both works has been contested by Jackson *et al* [144] for a variety of conjugated molecules.

It is clear that there is a need for a study of the generalisability of calculation schemes and, thus, the development of an optimal parameterisation method. These

points are the focus of the work in Chapter 3 and Section 4.1 and reviews and discussions of the body of associated literature are given throughout the chapters.

1.3.3 Excited-state phenomena from classical simulations

Modelling excited state phenomena, e.g. light-matter interactions, ionisation, polaron formation, etc. requires a quantum mechanical treatment. Furthermore, understanding these phenomena is crucial to molecular characterisation and design. Often, quantum chemical methods are utilised to this end. However, as discussed in Chapter 1.1, conformational disorder is known to have a significant effect on optical response and other excited-state behaviour. Given that quantum chemical calculations are performed on individual geometries, accounting for disorder must be done by implementing distortions to molecular geometries *ad hoc* [88, 103] or by modifying results based on known effects e.g. adding an inhomogeneous broadening linewidth to calculated spectra representative of conformational broadening [76]. Certain quantum mechanical treatments, particularly density matrix renormalisation group (DMRG) methods, can be modified to include intrinsic disorder parameters which, in turn, permit the study of disorder-dependent effects such as exciton localisation [89, 95, 96]. However, while these methods are succesful in studying the phenomenology of disorder-dependent behaviour, the nature of particular variants of conformational disorder cannot be directly obtained.

On the other hand, MD simulation offers the ability to simulate conformational disorder but cannot simultaneously obtain excited state behaviour based on these sources of disorder. As we have discussed above, MD simulation, of its own accord, is a useful tool for determining conformational properties and material morphologies of conjugated molecular systems. With the view of optimising device performance, if one knows the desirable conditions, e.g. the formation of semi-crystalline domains discussed in Section 1.1.3, then the results of MD can be used directly to guide the process of material design. However, if one wishes to directly probe the relationship between molecular conformation and morphology and the resulting charge transport or optical response behaviours, the results of MD simulation may be utilised as input for quantum mechanical calculations.

One such way would be to use simulation configurations as input for further calculation methods based on empirical or calculated parameters e.g. hopping rates and spectral overlaps. This approach is exemplified by that of Frost, Nelson *et al* [128–131, 134]. In several of their works, they have used Monte Carlo methods in conjunction with morphologies obtained from MD to determine, for example, electron and hole mobilities in Alq_3 films [128] and C_{60} fullerene films [129, 130] as well as utilising a tight-binding model approach to calculate the HOMO density of states in amorphous P3HT [134].

As opposed to utilising MD simulation output as input for other parameter-based

models, it is possible to utilise MD simulations as the basis for direct quantum chemical calculations. This is one of the advantages of atomistic as opposed to coarse-grained simulations. Utilising atomistic simulation geometries, one can perform calculations of ground state (e.g. electronic densities, total energies, and HOMO and LUMO orbitals) and ground-to-excited state (e.g. linear absorption, vertical ionisation, excitation densities) properties of molecular samples. These properties may then be related to the array of conformational disorders generated over the course of the simulation.

One example of such an approach is the work of Kilina, Tretiak *et al* [44]. Utilising simulation geometries of amorphous and crystalline solids of conjugated polymers (PPV, polyfluorene, and derivatives) in conjunction with ground state density functional theory (DFT), they performed calculations of distributions of electronic states. In doing so, they calculated the density of states of the HOMO and LUMO bands and, by mapping each state to a number of participant molecules, determined the localisation behaviour of these states. They found that conformational disorder leads to an emergence of trap states which is amplified by the presence of side-chains. Recently, Bockmann *et al* [47] utilised such an approach (with TD-DFT methods) to obtain absorption spectra for P3HT-based oligomers of 32 units in crystalline, amorphous, and solution phases based on their force-field paramterisation scheme discussed previously. This allowed for a partial study of the impact of conformational disorder on the resulting spectra. The work of Haverkort *et al* [142, 143] has also exemplified this approach by utilising MD simulations of cyanine dyes in conjunction with a quantum-chemically parameterised Hamiltonian to calculate absorption spectra in various aggregated complexes. Additionally, Barford *et al* [89] (utilising Monte-Carlo based dynamics as opposed to classical force-field dynamics for geometry generation) have studied exciton localisation based on generated configurations and a configuration interaction calculation scheme.

Utilising combined classical MD and quantum mechanical approaches has limitations. Namely, it is not possible to obtain real-time quantum dynamics and, thus, an understanding of geometry relaxation and phenomena associated with that (e.g. charge transfer, optical emission). To this end, the *ai*MD regime is best suited to this task. One particular method is the non-adiabatic excited state MD (NA-ESMD) method developed by Tretiak *et al* [138] which, while still being computationally limited to very small molecules [139] and rings [106], has shown promising results in novel predictions such as the dynamics of ultrafast torsional relaxation in excited states. However, these methods cannot currently capture the full extent of conformational disorder in near-polymeric molecules (with $L \gg l_p$) due to their high computational demand..

In the above, we have given a brief summary of methods for calculating excited state behaviour utilising the MD simulation regime. In this work, we focus on

utilising DFT and TD-DFT methods for the purpose of understanding optical absorption phenomena based on single conjugated molecules in solution. The manner in which this is performed is discussed further in Section 2.3.4 with our results given in Chapter 5.

1.4 Aim and outline of thesis

Conjugated semiconducting materials offer unique possibilities for realising a new generation of low-cost, light-weight, flexible semiconductor devices. As we have discussed in this chapter, there are significant challenges which must be overcome in order to realise full commercialisation of these materials. Particularly, developing a better theoretical understanding of the drivers of molecular morphology from solution processing by the engineering of the core materials and solvent environments is crucial to further development. This requires a deeper understanding of both the dynamics of polymers in the dilute and semi-dilute solution regimes as well as how thin-film devices form upon solvent evaporation. Furthermore, it is also necessary to study how the multitude of possible molecular conformations in each of these regimes affects the optical and excitonic properties of devices so as to inform the design of individual molecules for devices. For this purpose, MD simulation is a clear candidate for a theoretical methodological framework capable of encompassing the wide range of molecular interactions, and material and environmental conditions in a computationally tractable and effective manner.

The aim of this work is to develop a classical force-field parameterisation scheme which is generalisable to a wide range of conjugated molecules and, by utilising MD simulations, simulate conjugated molecules in dilute solutions to both validate our parameterisation framework and develop a picture of the microscopic phenomena which lead to macroscopic polymer conformations and variations in optical absorption phenomena. To do so, we utilise oligomers of fluorene and thiophene and their alkyl-branched analogues as test molecules - both of which, as we briefly discussed in Section 1.1, are widely characterised experimentally both in terms of their optical response, and conformational and morphological properties as well as being currently relevant device materials.

In Chapter 2, we begin with a more detailed discussion of classical force-fields for conjugated polymers, MD simulation protocols, and quantum chemical calculations which form the basis of the results presented.

In Chapter 3, we perform a quantum chemical examination of dihedral potentials and partial charge distributions in fluorene and thiophene. In doing so, we determine a density functional theory (DFT) methodology for obtaining dihedral potentials which is comparable to high-level quantum chemical calculations (such as those of Bloom and Wheeler [157]); and we analyse how varying backbone length and side-chain length affect the potentials and atomic charges. Thus, we develop a

novel calculation regime for force-field parameterisation which avoids unnecessary computational expense without compromising on accuracy.

In Chapter 4, we develop an implementation scheme for implementing dihedral potentials and discuss methods of improving the correspondence of the classical force-field potential fitting to the expected quantum chemical potentials. This is followed by a series of simulations in dilute solutions which serve as a means of validating the force-field parameterisation scheme as well as highlighting the conformational properties of each molecule both at the small scale (2mer) and large scale (up to 32mer).

In Chapter 5, we utilise the molecular conformations obtained from MD simulation in conjunction with time-dependent density functional theory (TD-DFT) to calculate absorption spectra from conformation ensembles. This allows us to understand the conformational distortions which play a significant role in conformational broadening and how they scale with backbone length. This is followed by a study of excitation localisation and its dependence on conformational disorder.

Finally, in Chapter 6, we draw conclusions and outline a number of routes for application and extension of the presented work.

Chapter 2

Molecular dynamics and quantum chemical methodology

In this chapter, an overview is given of the details of the quantum chemistry (QC) and molecular dynamics (MD) algorithms used throughout this thesis. We begin by expanding on the MD simulation regime described at the end of the previous chapter and focusing on a number of aspects of running simulations and parameterising classical force-fields for use with conjugated polymers. This is followed by the introduction of numerous QC algorithms, focusing on density functional theory (DFT) approaches which are the primary QC calculations used in this work. Throughout, we lay out our framework for parameterisation, performing and processing simulations, and absorption calculations which pertain to the Chapters 3, 4, and 5 respectively.

2.1 Molecular classical force-fields

A general force-field for a molecular system of N atoms is of the form:

$$V_{ff} = V_{cov} + V_{non-cov}. \tag{2.1}$$

The potentials V_{cov} and $V_{non-cov}$ represent sums over contributions from two families of potentials: interactions resulting from covalent bonding, and all other atomic interactions (non-covalent interactions), respectively. In essence, the total V_{cov} potential enforces the basic molecular structure by controlling the bond lengths, bond angles, and dihedral angles and the intrinsic vibrational properties of the system while the $V_{non-cov}$ potential governs, primarily, intermolecular effects such as polymer-solvent interactions as well as, for long or branched molecules, intramolecular interactions between parts of a molecule which are separated by a number of covalent bonds.

Denoting a full set of atomic pairs in a system by $\{ij\}$, the set of covalent bonds, $\{ij\}_{\text{cov.}}$, is defined as a subset of $\{ij\}$ comprised only of pairs which are covalently

bound. From this set, the set of bonds angles between groups of three successively bound atoms, $\{ijk\}_{\text{cov.}}$, and dihedral angles between groups of four bound atoms, $\{ijkl\}_{\text{cov.}}$, are defined. For each group of atoms in these sets, a potential, $V_{b,ij}$, $V_{\theta,ijk}$, and $V_{\phi,ijkl}$ for bonds, bond angles, and dihedral angles, respectively, is specified which may, in principle, be unique for any given degree of freedom. As such, the potential V_{cov} is expressed as a sum over these sets of variables:

$$V_{cov} = \sum_{\{ij\}_{\text{cov.}}} V_{b,ij}(b_{ij}) + \sum_{\{ijk\}_{\text{cov.}}} V_{\theta,ijk}(\theta_{ijk}) + \sum_{\{ijkl\}_{\text{cov.}}} V_{\phi,ijkl}(\phi_{ijkl}), \tag{2.2}$$

with b_{ij}, θ_{ijk}, and ϕ_{ijkl}, representing the values of a given bond length, bond angle, and dihedral angle, respectively.

Non-covalent contributions are specified first by defining a subset of pairs, $\{ij\}_{\text{non-cov.}}$, and ascribing potentials, V_{ij}, to these pairs. Thus:

$$V_{non-cov} = \sum_{\{ij\}_{\text{non-cov.}}} V_{ij}(r_{ij}). \tag{2.3}$$

The potentials V_{ij} are typically split into components which account for dispersion forces, close-range repulsion, and electrostatic interactions between atoms. We discuss these potential forms as well as how the subset $\{ij\}_{\text{non-cov.}}$ is defined in Section 2.1.2.

There are numerous [147, 148, 153, 154, 160–163] force-fields to be chosen from when performing MD simulations. Given the nature of force-field methods, it is necessary to obtain parameters semi-empirically by fitting to certain properties. These include probing the agreement of resultant molecular structures with X-ray diffraction measurements [161, 163], densities [132, 147, 148, 153, 162], and thermodynamic properties such as free enthalpies of solvation [154] and heats of vaporisation [147, 148, 153, 162]. Furthermore, force-fields differ in the functions natively applied to different potential terms. For example, the OPLS (Optimised Potential for Liquid Simulations) force-field utilises a fourth-order Fourier expansion for dihedral angle terms whereas the GROMOS force-field utilises a single cosine-based function. A good review of available force-fields can be found in reference [160].

Parameters in almost all classical force-fields have been developed for biomolecular simulation, and parameters for even the simplest of conjugated monomers are not typically known. Similarly, parameters for organic solvents are not widely available. For our purposes, a given force-field may be restrictive when aiming to probe a variety of molecules and solvents of varying complexity.

With the above in mind, we choose, as a starting point, the OPLS force-field [147, 148, 153, 162] due to its provision of parameters for many atoms in a multitude of different molecular frameworks as well as its use in previous works to parameterise conjugated polymers [47, 93, 97, 133, 140, 145, 164]. We have not widely explored the possibility of utilising other force-fields. However, the parameterisation scheme we

have set up is done so using a methodology which is, in principle, force-field independent due to its explicit inclusion of the effect of the force-field (as we shall discuss in greater detail in Section 2.1.4 and Chapter 4). As such, we believe that our results would be, to some extent, transferable to similar force-fields, e.g. GROMOS [154] or AMBER [163], with the provision of similarly accurate solvent parameters. Furthermore, as is shown in Chapter 4, the results obtained from our parameterisation scheme in conjunction with the OPLS force-field yield good agreement with experimental results. It may be the case, however, that other properties not covered in this thesis may be better described using other force-fields.

For a system of N atoms with co-ordinates $\mathbf{r}_i$ for an atom i, the basic form of the OPLS force-field is:

$$\begin{aligned} V_{\text{opls}}(\mathbf{r}_1, \mathbf{r}_2, \ldots \mathbf{r}_N) = & \frac{k_{ij}}{2}(r_{ij} - r_{ij}^{(0)})^2 && \text{(Bonds)} \\ & + \frac{k_{ijk}}{2}(\theta_{ijk} - \theta_{ijk}^{(0)})^2 && \text{(Bond angles)} \\ & + \sum_{n=0}^{5} c_{n,ijkl} \cos^n(\phi_{ijkl}) && \text{(Proper dihedrals)} \\ & + k_{ijkl}[1 - \cos(2\phi)] && \text{(Improper dihedrals)} \\ & + \frac{e^2 q_i q_j}{4\pi\epsilon_r\epsilon_0} + 4E\left[\left(\frac{\sigma}{r_{ij}}\right)^{12} - \left(\frac{\sigma}{r_{ij}}\right)^{6}\right] && \text{(Non-covalent terms).} \end{aligned} \tag{2.4}$$

In the above, the summations over the relevant combinations of atoms is omitted for clarity of presentation. The remainder of this section focuses on each of the potential terms in this expression and their function. In addition, we shall discuss terms which are beyond this pair-wise force-field definition (i.e. N-body non-covalent interactions), the difficulties posed by them, and how pair-wise force-fields typically account for them. Following these discussions, we detail our approach to parameterisation which is the basis for the work carried out in Chapter 3 and Section 4.1.

2.1.1 Force-field terms for covalent interactions

The 'covalent bond' between two atoms is a description of the bound state of two atoms occuring due to each of the atoms effectively sharing electrons in order to stabilise each other. Relative to long-range binding forces (Van der Waals forces), covalent bonds are typically very stable. Assuming the Born-Opppenheimer approximation is valid, the bound atoms can be conceptualised by considering each nuclear mass to be connected by a spring system with one or more fundamental vibrational modes. In terms of the nuclear co-ordinates, this leads to an effective quantum

oscillator description.

In utilising a classical force-field, one essentially approximates each local quantum oscillator by a form of classical oscillator. If we consider harmonic oscillators, the quantum harmonic oscillator has an energy spacing of $h\nu$ where ν is the fundamental frequency mode of the associated harmonic potential. If one is to approximate a system of states with a continuous, dynamical system, a first requirement is that a superposition of states is possible. For a system of temperature T, the thermally populated superposition of states is governed by k_BT in the Bose-Einstein distribution. If $k_BT \ll h\nu$, the oscillator system will be restricted to its ground state and, as such, is not well described by a classical oscillator. Satisfying this requirement is a key consideration for being able to ascribing a classical molecular force-field to covalently-bound degree of freedom.

We now discuss the potential forms for bonds, bond angles, and dihedral angles in molecular force-fields as shown. In most cases, we follow the conventions given in OPLS shown in Eq. 2.4 but also review the scope and potential of other methods.

Bond-stretching

The most straight-forward of covalent force-terms is that governing the rectilinear oscillation of two atoms which we refer to as *bond-stretching* terms. These terms are assigned based on the atomic separation, r, between two atoms as shown schematically in Figure 2.1(a).

Quantitatively, bond-stretching is often well described by a Morse potential [165]:

$$V_M^{(b)}(r) = E_D \left[1 - \exp\left(-\frac{r - r_0}{a}\right)\right]^2. \tag{2.5}$$

This potential both accounts for the oscillation of two bound nuclei, defined as a potential well centred at r_0 with width defined by a, while also containing a dissociation energy, E_D, which sets the energy required to break the bond. In a low-energy limit, the vibrational character of a Morse potential is well characterised by a simple harmonic oscillator:

$$V_H^{(b)}(r) = \frac{k}{2}(r - b)^2, \tag{2.6}$$

where $k = E_D/a^2$ is the effective spring constant on the bond.

Bond-stretching terms are the highest frequency terms in any molecular system. Typically the vibrational frequency is $\sim 100\,\mathrm{THz}$ and $\sim 50\,\mathrm{THz}$, for C-H σ bonds, and C-C π bonds respectively [166]. At room temperature, these frequencies are far larger than $k_BT/h \simeq 6\,\mathrm{THz}$ and, as such, approximating these vibrations with a classical oscillator is likely to be very poor even for vibrations involving heavy atoms. As can be seen from the harmonic potential shown in Figure 2.1(b), taken from the OPLS model of the bond between a pair of thiophene carbon atoms, the potential is

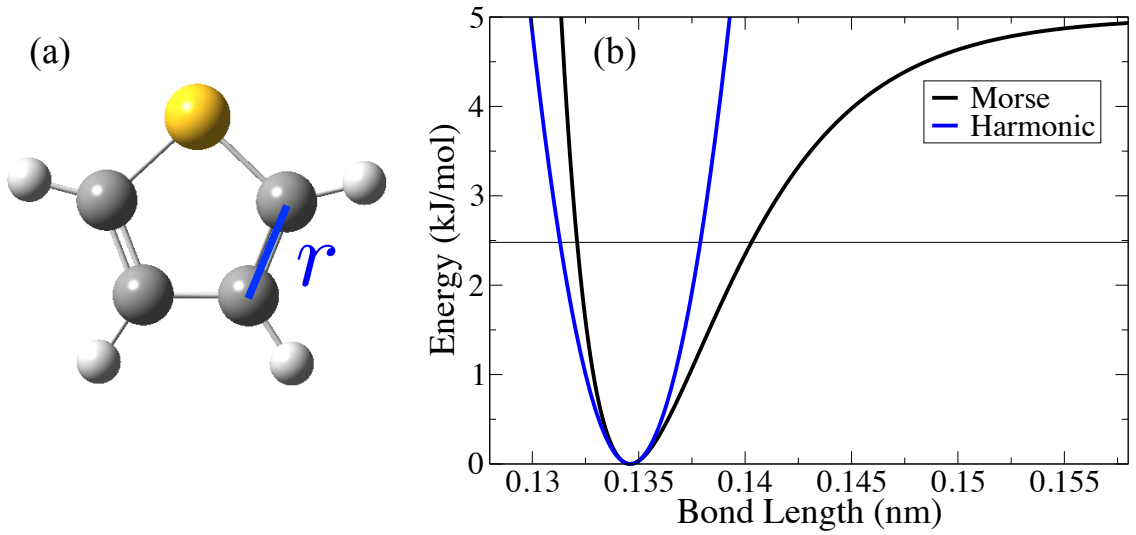

Figure 2.1: (a) A C-C bond in a thiophene unit. (b) The same bond modelled by a harmonic bond potential (Eq. 2.6, $k = 456,892\,\mathrm{kJ/mol\,nm^{-2}}$, $r_0 = 0.1346\,\mathrm{nm}$) taken from the OPLS force-field and a similar morse bond potential (Eq. 2.5, $E_D = 5\,\mathrm{kJ/mol}$, $a = \sqrt{2E_D/k}$, $r_0 = 0.1346\,\mathrm{nm}$). The horizontal line shows $RT = 2.479\,\mathrm{kJ/mol}$.

highly restrictive - allowing for stretching of $\sim \pm 0.03\,\text{Å}$ when assuming that the full extent of the motion will occur at $\sim RT = 2.479\,\mathrm{kJ/mol}$ (where $R = N_A k_B$ is the gas constant and T is the system temperature). As opposed to using such highly restrictive potentials, one widely utilised method [46, 133, 140, 142, 143, 145, 164] is to freeze the bond lengths directly using constraint algorithms [166–168]. As well as forming a conformationally equivalent description of the otherwise effectively frozen bond length, these algorithms also lead to a significant increase in simulation efficiency by allowing for larger integration steps in the Newtonian dynamics solvers (discussed further in Section 2.2.2). Thus, we utilise these constraint algorithms for all bond lengths in all of our simulations.

Angle-bending

The next covalent degree of freedom to consider involves the motion of groups of three atoms. By defining vectors between each of the outer atoms and the central one, as shown in Figure 2.2(a), an angle known as the bond angle can be defined.

A basic potential for the angular degree of freedom is analogous to the harmonic potential for bond-stretching with the angle, θ:

$$V_H^{(\theta)}(\theta) = \frac{k}{2}(\theta - \theta_0)^2, \tag{2.7}$$

where k is the effective angular spring constant and θ_0 is the equilibrium bond angle. This potential is simply motivated by symmetry about the equilibrium bond angle, θ_0. However, as is the case for bonds and the use of the Morse potential, one cannot always assume this symmetry. As a basic extension, a cosine harmonic potential

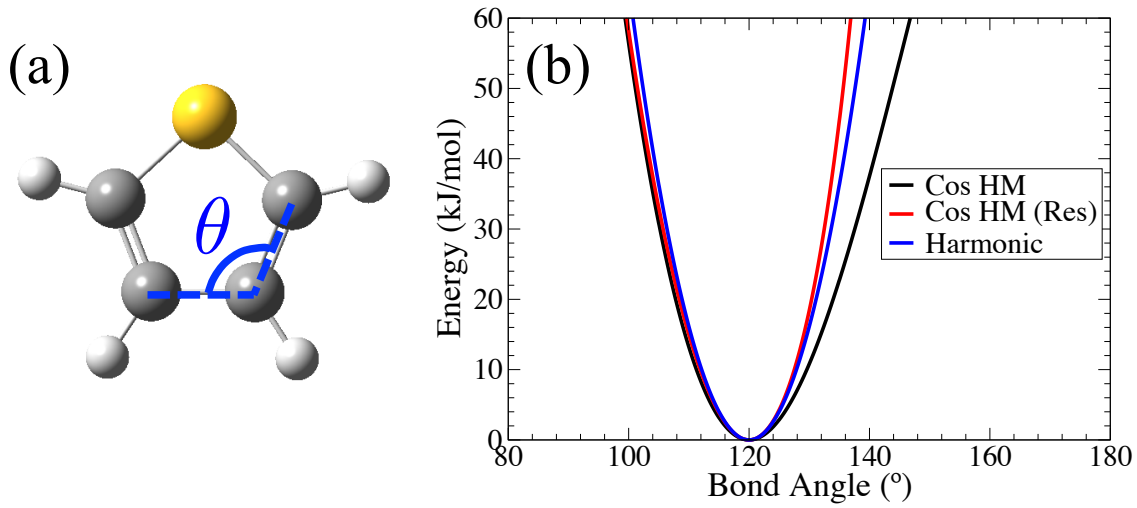

Figure 2.2: (a) Schematic of a bond angle modelled in a thiophene unit. (b) An example of a harmonic (Eq. 2.7), cosine harmonic (Eq. 2.8), and restricted cosine harmonic (Eq. 2.9) angle potential each with $k = 530\,\text{kJ mol}^{-1}\,\text{rad}^{-2}$ and $\theta_0 = 120°$.

may be defined:

$$V_{CH}(\theta) = \frac{k}{2}(\cos(\theta) - \cos(\theta_0))^2, \tag{2.8}$$

where k is a spring constant (different from that of Eq. 2.7). As the argument of the harmonic term is the cosine of the angle, this potential is softer towards one direction in θ in comparison to the harmonic potential in Figure 2.2(b). For particularly weak potentials, this potential requires further modification so as to assure that the angle is restricted from reaching the 0° and 180° points. If this were to happen, the definiton of a dihedral angle fails as the plane formed by three colinear points is undefined. To combat this, a restricted cosine harmonic potential can be formed:

$$V_{RCH}(\theta) = \frac{k}{2}\frac{(\cos(\theta) - \cos(\theta_0))^2}{\sin^2(\theta)} \tag{2.9}$$

The frequencies of angular vibrations are typically on the scale of ~ 20 THz [166]. At these frequency scales, the validity of using angular vibrational terms becomes questionable as does the assumption of a fixed ground state. The harmonic potential of Figure 2.2(b) is that which describes the angle between 3 carbon atoms in a conjugated ring structure from the OPLS force-field. From this potential, it is clear that the angles have been parameterised to have a freedom of around 5° on either side of θ_0 (again, taking the energy RT as a reference). As such, the OPLS force-field forms a strong but not entirely rigid restriction on angular degrees of freedom. In following the OPLS parameterisation, we do not constrain in angular terms in our simulations and utilise the harmonic angular terms available in the force-field.

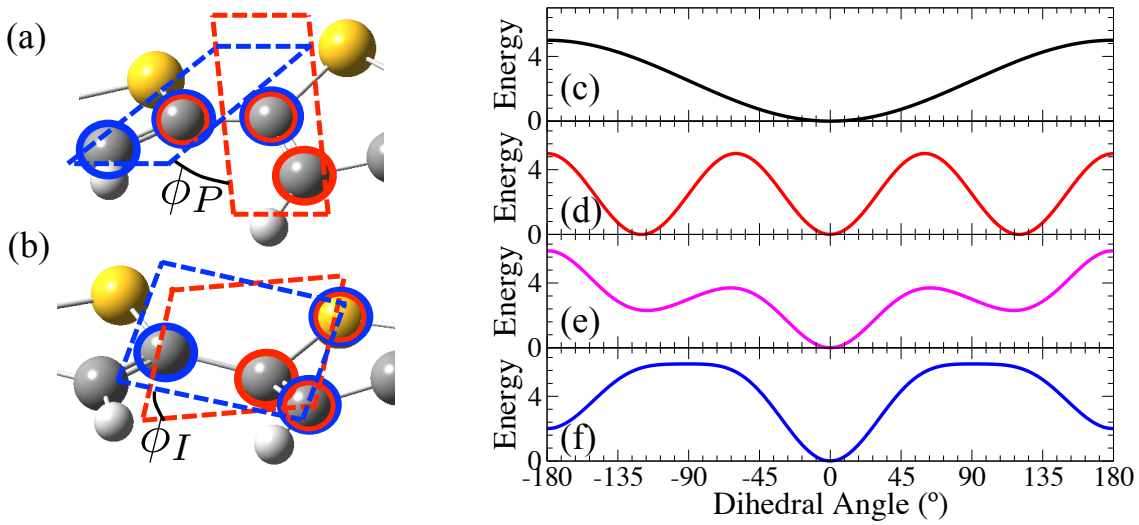

Figure 2.3: Schematic of a (a) proper and (b) improper dihedral angle at and intermonomer junction of a thiophene oligomer. (c)-(f) Examples of Ryckaert-Bellemans (RB) functions (Eq. 2.12) displaying a number of different potential forms. (The coefficients, $\{c_n\}$ are (a) $\{2.5, -2.5, 0, 0, 0, 0\}$, (b) $\{2.5, 7.5, 0, -10, 0\}$, (b) $\{3, -2.25, 0, 3, 0, -2.25\}$, and (d) $\{6, 0, -0.3, -1, -4.7, 0\}$ and energies are given in kJ/mol.)

Dihedral torsion

The final family of covalent bonding terms we discuss are those governing the relative motion of groups of four atoms. For a group of four points, it is possible to define two distinct planes which are at an angle to each other. This angle is the dihedral angle. As discussed in Section 1.1.3, an appropriate description of dihedral torsion in conjugated molecules is particularly crucial due to the role of the intermonomer dihedral angle between planar conjugated units on the conjugated orbital structure and, thus, optical absorption and emission. Dihedral terms are generally split into two classes: *proper* and *improper* dihedrals. As shown schematically in Figure 2.3 (a) and (b), the difference between the two classes is in the ordering of the atoms which define the planes. By definition, each plane must share two atoms. For a proper dihedral, the four atoms are identified by a linear series of bonds which allow for the middle two atoms to be shared by both planes. As a result, a potential in terms of this angle governs a torsion of the four atoms around the axis of the central two. On the other hand, an improper dihedral is specified by one atom which is bound to another three. By defining a plane from the outer three atoms and another from two of the outer three atoms and the central atom, the angle formed between the planes is a measure of how out-of-plane the central atom is with respect to the outer atoms.

Normally, improper dihedral terms serve to re-enforce planarity in rigid, planar systems such as conjugated rings. In the OPLS force-field (Eq. 2.4), improper

dihedrals are treated using the potential:

$$V_I^{(\phi)}(\phi) = k[1 - \cos(2\phi)]. \tag{2.10}$$

with $k = 4.6\,\mathrm{kJ/mol}$ for conjugated structures.

Proper dihedrals are the primary dihedral terms in a force-field. As torsional motion is, at times, complex, so too are the functional representations required with respect to those of bonds and bond angles. In certain cases, such as in the planar proper dihedrals along the conjugated planar rings, it is possible to utilise the simple potentials described for bond angles. In other cases, such as the dihedral term governing intermonomer dihedral motion, these descriptions are insufficient.

One possible description is a periodic dihedral function centred around an equilibrium value ϕ_0:

$$V_P^{(\phi)}(\phi) = k_c[1 - \cos(n\phi - \phi_0)]. \tag{2.11}$$

This potential is useful for dihedrals which have a high degree of symmetry or, if a high value of k_c is chosen, for dihedrals which are restricted to values near ϕ_0 (though, in this form, this potential is essential reduced to something akin to the cosine harmonic in Eq. 2.8).

For more complex dihedrals, it is often the case that either a Fourier expansion or, for dihedral rotations symmetric about 180°, the equivalent cosine polynomial expansion is required. One common example is the 5th-order cosine polynomial known as the Ryckaert-Bellemans (RB) function [166]:

$$V_{RB}^{(\phi)}(\phi) = \sum_{n=0}^{5} c_n[\cos(\phi)]^n. \tag{2.12}$$

A variety of RB functions are shown in Figure 2.3(c)-(f). The 5th order expansion is capable of producing a number of complex potential forms.

The standard dihedral term varies from force-field to force-field. For instance, the GROMOS force-field is parameterised using cosine harmonics natively. The OPLS force-field natively uses a 4th order Fourier cosine expansion which is straightforwardly mapped to the RB function. As will be demonstrated in Chapter 4, accurate fitting of the intermonomer dihedral term requires a function of the order of the RB function. As such, we utilise the RB function throughout our force-field parameterisation.

The majority of dihedral terms in conjugated planar molecules are those governing proper dihedrals in planar structures. Given that conjugated units themselves are effectively constrained to be planar, these are typically straightforward in parameterisation and in OPLS there is a single, general parameter for conjugated inner-ring proper dihedral terms (which is essentially Eq. 2.10 with $k \simeq 15\,\mathrm{kJ/mol}$). In

contrast, the potential governing intermonomer dihedral rotation is neither parameterised nor strictly straightforward in parameterisation for any conjugated oligomer. This is primarily due to the number of component interactions (such as Van der Waals interactions between atoms on opposing units) which have large additional contributions to the overall potential. Also, the relative freedom of this dihedral angle (relative to all other covalent degrees of freedom) requires the potential to be specified accurately over the entire range of rotation as opposed to within a highly-confined region. As we discussed in Section 1.3.2, obtaining an appropriate description of this dihedral term is one of the primary focuses of this thesis. We shall revisit the methodological approaches for parameterising these rotations later in Section 2.1.4 and outline an approach for their calculation and implementation based on QC calculations in Section 2.3.4.

2.1.2 Force-field terms for non-covalent interactions

The second class of interaction terms shown in Eq. 2.4 are non-covalent interaction terms. These terms consist of all interactions which do not result directly from covalent bonding between atoms. These types of interactions are collectively known as *Van der Waals (VdW) forces* and are responsible for the interactions between separate molecules and the self-interaction of parts of a molecule which are, in terms of covalent links, well-separated but may, in the course of the dynamics, interact.

In an atomistic simulation, the simplest manner of simulating VdW is to simulate interactions between pairs. This leads to three types of interaction. First, there is the electrostatic interaction between two atoms resulting from the average local charge density around individual atoms. Secondly, there are forces which result from variations in the electronic densities of atoms as a result of the presence of another atom and its electron cloud. These are known as *dispersion* forces [169]. Finally, there exists a term which accounts for the repulsion of atoms at close separations which forms a hard barrier to atoms becoming infinitesimally close.

Generally, non-covalent interactions are not included between atoms which are separated by one, two or, in some cases, three covalent bonds. In these cases, the effect of the non-covalent terms are accounted for by their associated covalent terms. In certain force-fields, such as OPLS, non-covalent interactions are included for the end atoms of proper dihedrals to account for the relative freedom of the interatomic separation of these atoms relative to that of atoms separated by one or two covalent bonds. These interactions are calculated in the same manner as other non-covalent interactions and then scaled by a constant factor (0.5 in OPLS) [162].

In the following, we give an account of the different potential forms used for non-covalent interactions, their applicability, and how they are parameterised. We also give a brief discussion of extensions beyond pair-wise interactions, which can account for e.g. molecular polarisation. Finally, we discuss the use of interaction

cut-off radii for reducing the number of calculated pairs and interaction terms and how this leads to the necessity of introducing methods to account for long-range electrostatic phenomena (particularly, the emergence of dielectric screening).

Electrostatics

Electrostatic phenomena between atomic pairs arises due to the non-uniform molecular electronic density. In the local vicinity of a given atom, the proportion of the total electronic density combined with the corresponding nuclear charge can be considered to be an effective atomic charge. This is known as a *partial charge*. For two atoms, i and j, with partial charges q_i and q_j, respectively, the electrostatic interaction, as a function of the inter-atomic separation r_{ij}, is mediated by the Coulomb interaction:

$$V_C(r_{ij}) = \frac{e^2 q_i q_j}{4\pi\epsilon_0\epsilon_r r_{ij}}, \tag{2.13}$$

with the constant $(4\pi\epsilon_0)^{-1} \equiv 138.935\,\mathrm{kJ/mol\,nm}\,e^{-2}$, ϵ_r is the relative permittivity of the medium, and q_i and q_j given in units of electronic charge, e. This potential forms the basis of all pair-wise electrostatic interaction with a force-field provided that one can ascribe a suitable value of q_i to atom i.

Partial charges are typically determined by fitting the electronic density, calculated quantum mechanically, to the nuclear centres and determining the net charge of the atomic centre and its local electronic cloud. Techniques for obtaining partial charges are discussed in Section 2.3.

In contrast to covalent forces, partial charge values are known to change significantly depending on their host molecular environment. Indeed, even for similar combinations of atoms in the same molecule, for which covalent potential terms may be effectively 'borrowed', there are often substantial differences in the partial charge distributions. As such, in generating a force-field for a molecule, one must re-parameterise the partial charges by performing quantum chemical calculations of the molecular electronic density (discussed in Section 2.3). Determining an optimal manner of performing this parameterisation forms the subject of the work presented in Section 3.3

Dispersion and short-range repulsion

The dispersion force refers to the attractive force felt between a pair of atoms at small separations. As derived by London [169], the dispersion force arises from the influence of neighbouring atoms on each others electron clouds. Due to the repulsion of electrons, electric multipoles are formed across the electron cloud which result, to first non-vanishing order, in an effective potential, $V_D(r)$, in terms of the internuclear

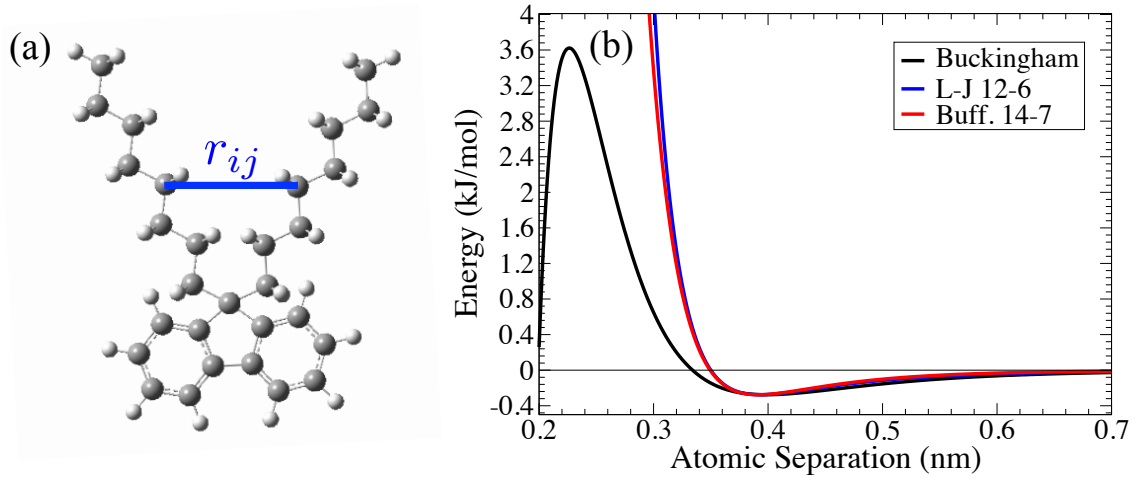

Figure 2.4: (a) Schematic of a long-range interaction between two side-chain carbons in dioctyl-fluorene monomer. (b) Examples of a repulsive-dispersive interaction potentials: Lennard-Jones 12-6 potential (Eq. 2.15, $E = 0.276\,\mathrm{kJ/mol}$, $\sigma = 0.35\,\mathrm{nm}$), a Buffered 14-7 potential (Eq. 2.17, $E_{14-7} = E$, $\sigma_{14-7} = \sigma/2^{1/6}$) and a Buckingham potential (Eq. 2.16, $A = 5000\,\mathrm{kJ/mol}$, $B = 23\,\mathrm{nm}^{-}1$, $C = 0.0032\,\mathrm{kJ/mol\,nm^6}$)

separation, r, of the form:

$$V_D(r) \propto -\frac{1}{r^6}. \tag{2.14}$$

The dispersion force becomes infinitely attractive with decreasing r. However, at very small separations, the dispersion force is overcome by atomic repulsion. This repulsion occurs as a result of Coulomb repulsion as well as the Pauli exclusion principle - which prevents two electrons of equal spin occupying the same state. Unlike the dispersion force, the spatially resolved forms of these repulsion phenomena are not known. From the previous description, it may be inferred that the potential governing this interaction should consist of an effectively hard wall for some r greater than 0. However, the choice in casting such a function is very much context dependent and requires experimental validation.

In force-fields, repulsion and dispersion forces are generally combined as two terms in a single potential. In Figure 2.4(a), a schematic is given of an example in which these interactions are modelled. For a pair of atoms i and j of internuclear separation r_{ij}, a first, and most prominent, example of a dispersion-repulsion potential is the Lennard-Jones 12-6 (LJ) potential [170]:

$$V_{LJ}(r_{ij}) = 4E\left[\left(\frac{\sigma}{r_{ij}}\right)^{12} - \left(\frac{\sigma}{r_{ij}}\right)^{6}\right]. \tag{2.15}$$

Here, E is the energy at the minimum of the potential which occurs at $r_{ij} = 2^{\frac{1}{6}}\sigma$. In this potential, the repulsive contributions are modelled by the r_{ij}^{-12} term. The main motivation in this choice is it being the square of the r_{ij}^{-6} dependence of the dispersion force which means that, computationally, it is more efficient than most

potential forms. An example of the LJ function is given in Figure 2.4(b) using the OPLS parameters for the interaction between two alkyl chain carbon atoms.

LJ functions are currently the most common representation of dispersion-repulsion forces due both to their computational simplicity and the extent to which they have been parameterised. However, it is also known that the hard-wall of the LJ potential is not the most accurate representation of the exclusion interaction and, as a result, the LJ potential fails to accurately describe systems with a high degree of close-packed, non-covalent interactions. As such, it is often necessary to consider alternative functional forms.

One such form is the Buckingham potential [171], which proposes a mono-exponential decay term as a more realistic representation of the repulsive exclusion:

$$V_{exp-6}(r_{ij}) = A\exp(-Br_{ij}) - \frac{C}{r_{ij}^6}. \tag{2.16}$$

This potential form, while having been shown to have advantages over the LJ function [132, 171, 172], has two significant drawbacks. First, the computational ease afforded by the LJ function is lost in including an exponential term and, as a result, forms a limitation on the scale of a simulation. Secondly the limiting behaviour as $r \to 0$ is a divergence to infinite attraction as opposed to infinite repulsion (as can be inferred from the potential shown in Figure 2.4(b)). With a suitably large exponential component, a sufficiently large barrier can be formed so as to make it very highly improbable that two atoms could ever reach such small values of r. However, its existence causes an ever-present risk of simulation instability.

A final example, which addresses the failings of LJ and Buckingham potentials, is the Buffered 14-7 potential (B14-7) of Halgren [173]:

$$V_{B14-7}(r_{ij}) = E_{14-7}\left(\frac{1+\delta}{r_{ij}/\sigma_{14-7}+\delta}\right)^7\left(\frac{1+\gamma}{(r_{ij}/\sigma_{14-7})^7+\gamma}-2\right). \tag{2.17}$$

This potential, with buffer terms $\delta = 0.07$ and $\gamma = 0.12$ for increased stability for small r_{ij} values, reduces to a 14-7 potential for $\delta, \gamma = 0$. As with the LJ potential, E_{14-7} is the depth of potential at the minimum which is given by σ_{14-7}. The rationale for this potential is that, although the r_{ij}^{-14} term represents a stronger repulsive barrier, modifying the dispersive component to an r_{ij}^{-7} dependence means that, for $r_{ij} \sim \sigma$, the barrier is shallower. This may be seen by comparison of equivalent LJ and B14-7 potentials in Figure 2.4(b).

The r_{ij}^{-7} dependence of the B14-7 potential is, by considering the analytical form of the dispersion interaction, unphysical. However, in allowing for a form which allows for a more realistic repulsion term while also preserving (partially) the computational ease of the LJ potential, this potential has been utilised successfully for a number of systems [93, 172, 174, 175]. As a particularly relevant example, the

B14-7 potential has been used successfully as part of a parameterisation scheme for conjugated polymers [93] in which the close proximity of neighbouring units in a chain often leads to unphysical repulsion between neighbouring units.

As mentioned, the OPLS force-field, and most others, are natively LJ force-fields. As such, using different potential terms would either require a translation of LJ parameters to parameters suitable for another functional form, re-parameterisation of the force-field, or utilising a different, less well documented force-field. Both of the latter instances would require extensive parameterisation, particularly if one wishes to utilise numerous explicit solvent environments and non-biological molecules. The translation of LJ parameters is perhaps valid though it is unclear whether this would lead to substantially different physics in test systems and, thus, an invalidation of the force-field. As we discuss in Section 4.1, the difficulties in using LJ functions can be overcome with the appropriate use of a force-field subtraction procedure (which is outlined in Section 2.1.4).

As a brief note, the OPLS force-field parameters for LJ interactions are listed as a value σ_i and E_i for a given atom i. For the interaction of two atoms of type i, these are the values used correspondingly in Eq. 2.15. For two atoms of different types, i and j, the parameters, Eij and σ_{ij}, for the LJ interaction are formulated using geometric average combination rules [162]:

$$\sigma_{ij} = \sqrt{\sigma_i \sigma_j}; \quad E_{ij} = \sqrt{E_i E_j} \tag{2.18}$$

Induction/Polarisation

Both the electrostatic and dispersion-repulsion force-field terms described previously are pair-wise potentials. However, the full treatment of molecular interaction consists of forces which can involve large sections of a molecule which span several atoms and are dependent on the configuration of each atom within a given interacting structure. These types of interaction are an extension of the dispersive interactions to multi-atomic systems and are, as before, a function of the molecular polarisability. This is dependent on the configuration of the atoms and individual atomic polarisabilities and not simply the interactions between each individual atomic pair. This is an especially important phenomenon when considering the aggregation of multiple conjugated molecules as this effect is crucial to π-π stacking of parallel structures [142, 143, 176, 177].

In practice, these interactions are difficult to treat. One approach to doing so would be in defining interactions based on individual groups of atoms. This is essentially intractable given the number of possibile unique groups in any simulation system. One practically applied approach is in forming an approximation to the polarisation effect based on individual polarisabilities by attaching Drude oscillators to each atom, which represent small shifts in the partial charge of the atom. This

technique - which has proven succesful in simulating highly polar systems [174,175] and low molecular weight conjugated molecules [142, 143] - has not been, to date, examined substantially for conjugated polymers.

The standard approach of pair-wise force-fields such as OPLS is to modify the repulsion-dispersion interactions to account for these missing interaction terms. As such, this leads to a loss of generality in LJ parameters. For example, the LJ parameters for a carbon atom in a conjugated structure generally have a far larger attractive component than in an alkyl structure. This is due, in the first instance, to the greater polarisability afforded by the π electron delocalisation of conjugated carbon atoms but also due to an increase in the attractive interaction energy required to mimic, for example, the many-body effect of π-π stacking between conjugated rings.

In parameterising a dioctyl-fluorene octamer, Marcon *et al* [132] found that, using the MM3 force-field, the conjugated atoms in the system required rescaling the attractive interactions by a factor of 4/3 so as to obtain the correct molecular densities. This strategy may also be necessary with the OPLS force-field as an extension of our parameterisation work. However, as the work of this thesis deals entirely with conjugated molecules in solution, the effects of π-π stacking are seen in very few instances. As such, in adopting the OPLS force-field, we make no further modifications to the attractive interactions responsible for this stacking but note that, in extending this work to multi-molecular systems, this may require a more thorough analysis.

2.1.3 Interaction cut-offs and long-range electrostatics

For a system of N atoms with a full force-field as in Eq. 2.4, it is clear the pair-wise, non-covalent force terms account for the majority of simulation processing. If each atom has pair-wise forces between them, this results in a simulation which scales $\sim O(N^2)$. However, the pair-wise interactions considered all have the feature of converging to near zero after $\sim$ 1-2 nm. As such, if one were only to consider particles within a nearby, and, thus, strongly interacting, volume, this scaling can be reduced, in principle, to somewhere closer to $O(N)$. As such, a cut-off radius, r_c, is generally defined in simulations beyond which non-covalent forces are set to zero.

While offering significant improvements in simulation scalability, introducing interaction cut-offs has a number of implications. First, for fluid systems, interaction cut-offs facilitate the need for algorithms which determine which interactions are to be calculated i.e. to track atoms or groups which diffuse beyond the cut-off radius of others. A common scheme for this is the Verlet scheme [166,178]. Further details of this algorithm may be found in the associated references.

In terms of effects on the simulation physics, it must be noted interaction terms are very unlikely to be identically zero at the cut off radius. As such, applying a

cut-off will lead to a step-like change in energy at the cut-off radius and, thus, an undefined force. However, as only relative differences in energy are important to any dynamics, this problem is easily remedied by simply shifting a given potential, $V(r)$, by its value at the cut-off radius: $V(r) \rightarrow V(r) - V(r_c)$. In doing so, the first derivative is again well-defined.

In utilising a cut-off radius, particularly with the above scheme, it is important that $V(r_c)$ is near zero before applying a shift. Generally, $r_c = 1.4$ nm is sufficient to ensure this. However, when considering the Coulomb interaction, while the potential scales as r^{-2}, the number of atoms at a distance r from any particular atom (assuming an effectively isotropic system) scales as r^2. Thus, electrostatic interactions have a substantial long-range component which, in using an interaction cut-off, is neglected. This has the major implication of removing the emergence of dielectric screening from the system meaning that the effect of atomic charges will be overstated without proper treatment.

One method for treating dielectric screening is known as the *Reaction-Field* (RF) method [179]. In utilising RF, one defines two dielectric constants: ϵ_r, which describes the dielectric behaviour within a volume defined by the cut-off radius; and ϵ_{RF}, which defines the dielectric effect within the cut-off volume due to the electrostatics of the surrounding system. This then results in a simple modification of the Coulomb potential:

$$V_{RF}(r_{ij}) = f\frac{q_i q_j}{\epsilon_r r_{ij}}\left[1 + \frac{\epsilon_{RF} - \epsilon_r}{2\epsilon_{RF} + \epsilon_r}\frac{r_{ij}}{r_c}\right]. \tag{2.19}$$

In the above, the constant term which ensures $V_{RF}(r_c) = 0$ has been omitted for clarity. This method is the simplest in dealing with long-range electrostatic phenomena and, in being simply a linear modification to the potential, has no significant effect on the simulation scaling. In practice, this method is used with $\epsilon_r = 1$, representing a vacuum dielectric environment with local dielectrics emerging from the explicit short-range electrostatics, and ϵ_{RF} defined by the solvent used in the simulation.

Another commonly utilised method for computing long-range electrostatics is the *Ewald summation* [180] or, in its more modern and widely utilised formulation, *Particle-Mesh Ewald* (PME) [181]. In computing the entire electrostatic behaviour of a system, one must sum over the paired interactions of all N atoms in the system and, in principle, all their periodic images which, as before, is computationally labourious and can be reduced by restricting this summation to within a cut-off radius. In recovering the long-range component, the Ewald summation is essentially applying this technique to treat the long-range electrostatics by first splitting the summation over all atoms into a short-range sum (defined with $r < r_c$) and a remaining long-range sum. The long-range sum may then be calculated in reciprocal space utilising a Fourier transform and, given that the dominant high spatial frequency components are treated within the real-space r_c, this summation may then be trun-

cated to over a small subset of low-frequency components. In practice, the PME variant of the Ewald summation is used. This variant calculates the Fourier sum by generating a discrete mesh over reciprocal space and utilising the Fast Fourier Transform algorithm to increase efficiency.

RF and PME both have significant advantages and disadvantages. The chief advantage of the RF protocol is that it incurs effectively no excess run-time beyond standard methods while PME, although a substantial improvement over a direct Ewald sum, still incurs an, at best, $O(N \ln(N))$ scaling. However, PME is a more direct and precise treatment which takes into account the actual dynamics of the system as opposed to an assumption of a uniform dielectric environment.

The choice of each method and the precise domain of applicability is still widely discussed within MD fields [182–184]. As such, it is not clear *a priori* which method is best suited to our work. As the choice of each method cannot be determined immediately, due to the possibility of effects resulting from different polarities of solvent, we have performed tests, based on the simulations discussed in Chatper 4, of each method in a variety of solvents. Generally, we find that PME has no significant effect on the results we obtain. Therefore, we have used the RF protocol throughout this work. The full details of our tests are provided in Appendix B.

2.1.4 Our approach to parameterisation

A significant portion of the work in this thesis is in establishing a suitable set of force-field parameters for conjugated molecules. Using polyfluorene and polythiophene as our test examples, we build a parameterisation scheme based on an accurate representation of the dihedral angle potentials and the partial charge distributions of each molecule. In this subsection, we detail the individual aspects which require parameterisation and the general scheme for implementing a dihedral potential into the force-field which we build upon in Chapter 3 and Section 4.1, respectively.

The first stage of parameterisation is to incorporate appropriate parameters already available within the OPLS parameter set. For fluorene, the parameters of the individual monomer unit are approximated using the available parameters for biphenyl. The parameters for a monomer of thiophene are available directly from the virtualchemistry.org database [185, 186].

From the basic monomer, the force-field for oligomers is built up using the monomer parameters. This leaves only the bonds, angles, and dihedrals associated with the inter-monomer junction between the two units and partial charges to be parameterised. These dihedrals are shown in Figure 2.5 for a thiophene 2mer with those of fluorene following analogously.

For fluorene, the inter-monomer bond and angle terms may be taken from the corresponding OPLS biphenyl parameters. There is no such analogue available for thiophene. Given the relative rigidity of these degrees of freedom, we utilise the

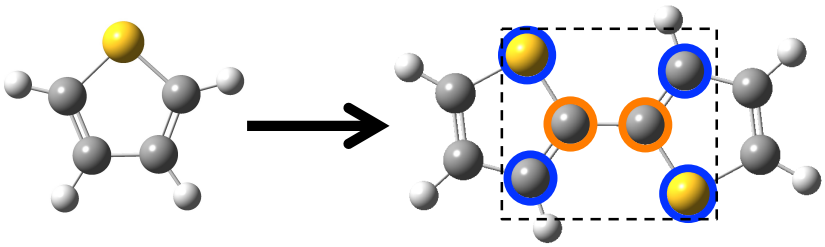

Bonds (r_{ij})	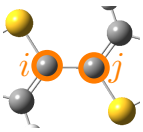
Angles (θ_{ijk})	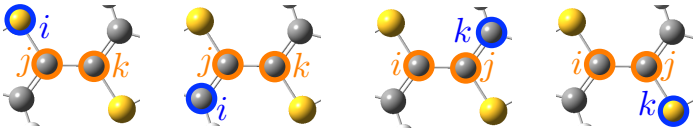
Proper dihedrals (ϕ_{ijkl})	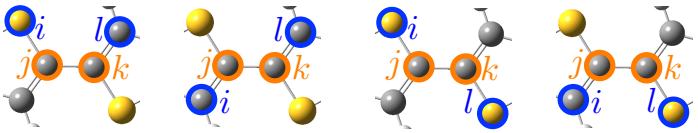
Improper Dihedrals (ϕ_{ijkl})	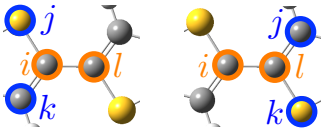

Figure 2.5: Sketch and table of degrees of freedom requiring parameterisation when going from a parameterised thiophene 1mer to a thiophene 2mer (or, analogously, longer oligomers).

biphenyl parameters also for these terms. As we shall discuss in Chapter 4, these parameters can be reliably used by modifying the equilibrium angles of these potentials to correspond to minimal values obtained using quantum chemical (QC) calculations. The improper dihedral terms are taken from the OPLS standard parameters for improper dihedrals involving conjugated ring carbons.

The required dihedral potential is determined in several stages. The first stage is to calculate, using QC methods, the total dihedral potential at intervals of 10° spanning the range 0° to 180°. We denote this as $V(\phi)$. This procedure is discussed in greater detail along with our discussions of QC methods in Section 2.3.4. This calculation forms a reference potential for the parameterisation. However, this potential also accounts for terms already described within the force-field, given by an effective potential $V_{FF}(\phi)$ which includes, for example, the contributions from bond angle terms and long-range interactions within the molecule. As such, $V(\phi)$ is composed of the force-field contribution and the contribution which is to be parameterised from the four dihedral functions, $V_S(\phi)$, such that $V(\phi) = V_{FF}(\phi) + V_S(\phi)$. In order to isolate $V_S(\phi)$, it is necessary to calculate the contribution from the rest of the molecular force-field and evaluate the difference between the two. This pro-

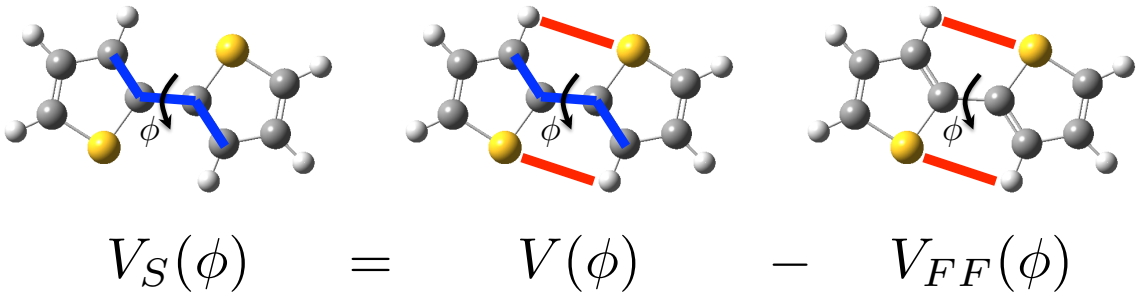

Figure 2.6: The stages of the subtraction procedure for implementing a dihedral angle potential, $V(\phi)$, into an otherwise established force-field. The contribution from the force-field, $V_{FF}(\phi)$, must be subtracted from $V(\phi)$ in order to isolate the required potential for the dihedral terms, $V_S(\phi)$. In the diagrams, blue lines depict (one of) the inter-monomer dihedral angle terms and red lines are examples of energetic terms accounted for by the force-field (non-covalent interactions in this case).

cedure, which has been utilised successfully in other force-field works [132,142,187], is referred to herein as the "subtraction" procedure and is shown in Figure 2.6.

Before the subtraction procedure can be performed, it is necessary to obtain partial charges for the molecular system. Again, these are calculated from QC calculations which allow the electronic density to be ascribed to the atomic centres. The methods for performing these calculations are discussed in Section 2.3.4 and, along with our calculations of dihedral potentials, a discussion of the results and a general implementation of these procedures to conjugated polymers forms a significant portion of the work presented in Chapter 3. For the subtraction procedure, the partial charges are required so as to represent the Coulomb contribution to the force-field potential, $V_{FF}(\phi)$.

With partial charges in place, the subtraction procedure is carried out by generating dihedral potentials for the molecule which is fully parameterised apart from the four dihedral potential terms which are set to zero. From this force-field, we calculate the force-field dihedral potential, $V_{FF}(\phi)$, by, as when calculating $V(\phi)$ from QC, restraining the given dihedral angle at intervals of 10° between 0° and 180° and performing an energy minimisation (discussed in Section 2.2.2) at each step. The resulting 'subtracted' potential, $V_S(\phi) = V(\phi) - V_{FF}(\phi)$, is then fit to the Ryckaert-Bellemans function (Eq. 2.12).

Further details of the subtraction procedure and its results are discussed in Section 4.1 and a schematic overview is shown in Figure 2.6. This process generates the full set of parameters required for MD simulations.

2.2 Performing molecular dynamics simulations

All of our MD simulations and force-field calculations are performed using the Gromacs 4.6.3 suite of programs [188,189]. This choice was made due to the wide-variety

Table 2.1: Table of the phases of an MD simulation: four phases of equilibration - energy minimisation, NVT equilibration, restrained NPT equilibration, and unrestrained NPT equilibration - and the full production run. For each phase, the typical run times are given in terms of simulation time and the run time (on a GPU node with 12 CPU cores) for thiophene (T) 2mers and 16mers, and fluorene (F) 32mers. (The former and latter are the smallest and largest systems considered in this work.)

Simulation phase	Simulation time (ns)	Run time (hours)		
		T 2mer	T 16mer	F 32mer
Minimisation	N/A	$\simeq 0.02$	$\simeq 0.1$	$\simeq 6$
NVT equilibration	0.5	$\simeq 0.03$	$\simeq 0.2$	$\simeq 10$
Res. NPT equilibration	0.5	$\simeq 0.03$	$\simeq 0.2$	$\simeq 10$
Unres. NPT equilibration	10	$\simeq 0.5$	$\simeq 4$	$\simeq 200$
Production	100	$\simeq 5$	$\simeq 40$	$\simeq 2\times10^3$

of available force-field options (such as those listed in Section 2.1) and its wide use in MD simulation of numerous materials including conjugated molecules [47, 141, 145]. Particularly, Gromacs is optimised for massively-parallel GPU simulation and is considered to be one of the fastest available MD packages for GPU-accelerated clusters (which our primary simulation hardware is). It is worth noting that, as before regarding the choice of force-fields, many works in MD simulations of conjugated polymers have also been performed using other simulation suites such as TINKER [44,93,190] and LAMMPS [140]. The force-fields and methods used throughout this work are in common with most of these packages and, as such, we believe that the results we have obtained may be replicable using these packages.

For reference, Table 2.2 gives a breakdown of the various stages of a full MD run which we discuss in the remainder of this section. Before this, we first describe our methodology for building conjugated oligomeric geometries and solvated periodic boxes for simulations. We then go on to discuss key algorithms within Gromacs for performing simulations such as dynamics integrators, and temperature and pressure controls. This is followed by an outline of the process of equilibration required to bring a system to a reasonable equilibrium (which comprises the first four phases shown in Table 2.2). From here, we discuss the manner in which we generate results from MD calculations both in establishing appropriate simulation sampling times and extracting conformational features from output molecular trajectories.

2.2.1 Simulation pre-processing

For both simulations and, as we shall discuss in Section 2.3, quantum chemical calculations, input geometries are generated using a set of polymer generating scripts which create duplicates of an input monomer translated along the chain axis and add in dihedral angles and, if necessary, side-chains. Where possible (typically, for molecules $<$ 16mer in length), these molecules are optimised quantum mechani-

cally to remove any possible problem forces e.g. those resulting from atoms being unphysically close together initially.

Simulations are built using the Gromacs functions for generating periodic boxes and introducing solvent molecules. The former defines the type of box and the distance between the edge of the box and the molecule. In all simulations, we use cubic boxes. The distance between the solute and the box is set to 0.7 nm - half of the cut-off radius $r_c = 1.4\,\text{nm}$ discussed in Section 2.1.3 - to ensure that no self-interaction between adjacent periodic images is possible. The only exception to this is in simulating 2mer molecules in which this distance must be increased to 1.2 nm. This is due to the parallelisation algorithms failing for very small boxes and very few atoms.

Solvent molecules are introduced to the box using an algorithm which, utilising a pre-defined, sufficiently large ($\sim$ 1000 molecules), and well equilibrated box of a given solvent, fills in solvent molecules around the solute. By using a pre-equilibrated solvent box (see Sections 2.2.3 and 2.2.4), this procedure yields a box close to the expected solvent density with as few unnatural crystalline features as possible. As with our algorithm for generating molecules, this generated box serves only as a starting point for simulation and, by the equilibration methodology we shall describe in Section 2.2.3, the minor conformational defects which remain following this procedure are quickly removed.

Following these procedures, an MD simulation is ready to be carried out. Before continuing to discuss this procedure, it is imperative that we first determine which of the variety of MD algorithms available are best suited to our simulation.

2.2.2 Simulation algorithms

An idealised MD simulation in an isolated environment needs only, with an appropriate force-field, to numerically solve Newtonian dynamics for an entire molecular ensemble. As such, the basic algorithm underpinning MD simulation is, first, calculating forces and, thus, velocities based on the force-field and the system coordinates, then translating the coordinates over a discrete time step according to the calculated velocities, and repeating. Of course, the key practical difficulties in a production simulation are in the amount of computational power required and the intrinsic inadequacy of a classical representation of a quantum mechanical system. With the additional caveat of simulating a system in equilibrium with a constant temperature and pressure environment, these points lead to a series of necessary modifications to this basic MD algorithm.

Arguably, the most crucial algorithm and variable is the integrator method and timestep, Δt, for the Newtonian dynamics. Any numerical differential equation solver requires a time integration step-size, Δt, small enough to provide an accurate description of the dynamics. On the other hand, decreasing Δt leads to a

proportional decrease in simulation efficiency. Furthermore, there are several integration methods for the dynamics which, similarly, can be optimised for balancing simulation efficiency and accuracy.

Beyond the basic MD algorithm, there are a wide variety of algorithms for implementing temperature and pressure coupling. As with integration methods, the most efficient algorithms can come at the expense of accuracy and identifying how, if at all, this loss of accuracy manifests in the simulations we perform and, thus, the optimal algorithm is key to improved performance.

Numerous other algorithms are utilised in a production MD run such as the long-range electrostatic treatments discussed in Section 2.1.3, algorithms for maintaining bond lengths such as the LINCS and P-LINCS algorithms [167,168], and algorithms, such as the Verlet algorithm [178], for maintaining and updating interacting neighbour lists. Along with the references listed, an overview of these and the many other algorithms often utilised in MD simulations can be found in reference [166]. In this section, we focus on the integrator and environmental coupling algorithms and present an overview of the basic principles underlying these algorithms and the optimisation and testing procedures we have carried out.

Integrators for Newtonian dynamics

Of the integrators for Newtonian dynamics available in Gromacs, we use the default leap-frog algorithm [191]:

$$\dot{\mathbf{r}}_i(t + \frac{1}{2}\Delta t) = \dot{\mathbf{r}}_i(t - \frac{1}{2}\Delta t) + \frac{\Delta t}{m_i}\mathbf{F}_i(t), \tag{2.20}$$

$$\mathbf{r}_i(t + \Delta t) = \mathbf{r}_i(t) + \Delta t\dot{\mathbf{r}}_i(t + \frac{1}{2}\Delta t). \tag{2.21}$$

This integrator, as can be seen from the above, has positions and velocities specified at different times in all iterations. This may have consequences in systems in which very tightly controlled energetics are required. In such systems, the Verlet integrator [192], which recasts the leap-frog algorithm so that the positions and velocities are specified at the same time step and, therefore, provides a more consistent input to temperature and velocity scaling, is often required. This integrator is given by:

$$\dot{\mathbf{r}}_i(t + \Delta t) = \dot{\mathbf{r}}_i(t) + \frac{\Delta t}{m_i}(\mathbf{F}_i(t) + \mathbf{F}_i(t + \Delta t)), \tag{2.22}$$

$$\mathbf{r}_i(t + \Delta t) = \mathbf{r}_i(t) + \Delta t\dot{\mathbf{r}}_i(t) + \frac{\Delta t^2}{2m}\mathbf{F}_i(t). \tag{2.23}$$

While the Verlet integrator step incurs approximately the same processing cost as the leap-frog algorithm, the additional terms in the integration step mean that around

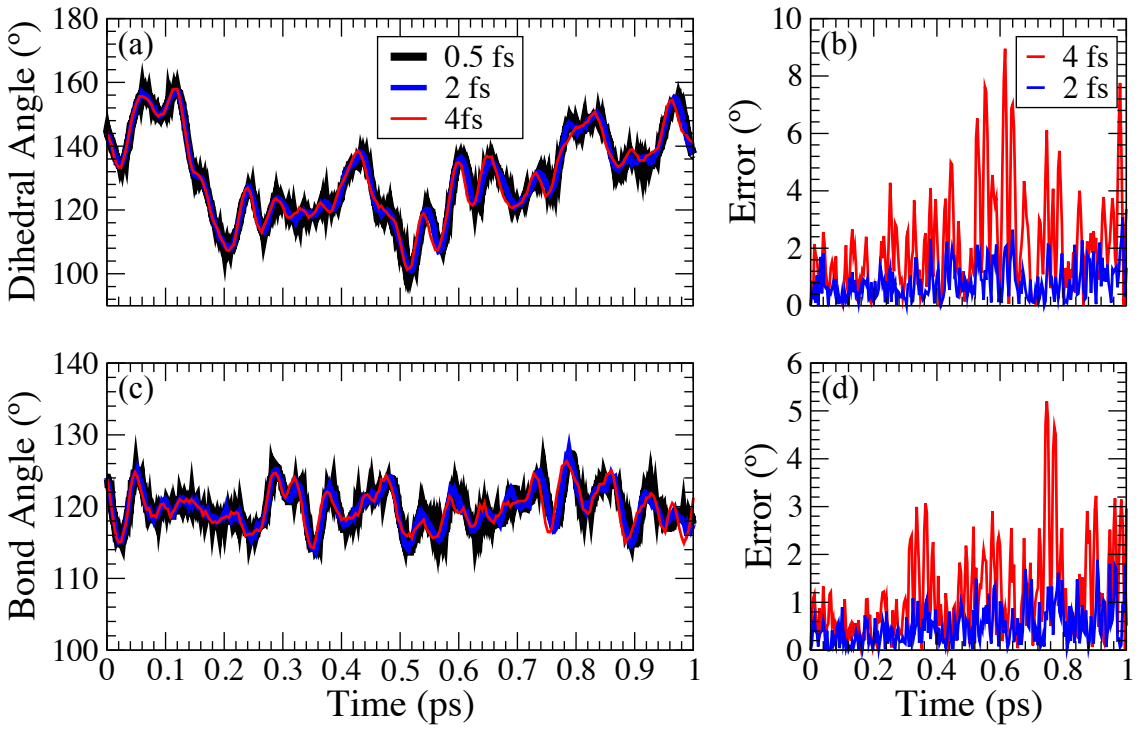

Figure 2.7: Comparison of time traces of (a) a dihedral angle and (c) a bond angle between carbons at the intermonomer junction of a dioctyl-fluorene 2mer simulated in chloroform for integrator step-sizes of $\Delta t = 0.5$, 2, and 4 fs. In (b) and (d), the absolute error, with respect to the 0.5 fs trace, is given for the dihedral angle and bond angle, respectively. (Legends in (a) and (b) apply to (c) and (d), respectively.)

twice as many communication calls are required [166] which, for large and highly parallelised simulations such as ours, is a significant disadvantage. Furthermore, as the fine details of thermodynamics are not a primary aim of our simulations and, also, given its succesful use in other MD works of a similar nature [46, 93, 141, 193], we find the leap-frog algorithm to be the optimal compromise.

Due to the implementation of constraints on bond-stretching terms (typically of vibrational period $T \sim 10$ fs), the highest frequency vibrations present in a simulation are the bond angle terms ($T \sim 50$ fs). As such, it follows that a suitable integration timestep would be $\Delta t \sim 1$ fs with values of 1 fs and 2 fs common in other MD works [46, 47, 93, 141–143]. In order to obtain an optimal value of Δt, we performed simulations with no temperature or pressure coupling (NVE ensemble simulations) with varying values of Δt. With no external coupling, the simulation dynamics are entirely deterministic and lead to comparable trajectories. In Figure 2.7, it is seen that the trajectories for an example dihedral angle and bond angle, each taken at the intermonomer junction of a dioctyl-fluorene 2mer, are near-identical over the course of 1ps with absolute errors in the range of 1°-2° between each trace. In contrast, an integrator step of 4 fs leads to the propagation of significant errors which are 3°-4° after 0.5 ps and as high as 5° for the bond angle and 10° for the dihedral angle after 1 ps.

Note that a typical simulation run is over 100 ns so the correspondence of these trajectories over only 1 ps is not fully indicative of the stability of the integrator over simulations of 10-100 ns in length. However, in production simulations with temperature and pressure coupling (as discussed later in this subsection), consistency is only required over this time-scale due to, in particular, the randomisation of velocities over a temperature coupling step ~ 0.1 ps. Therefore, fully deterministic dynamics only ever occur over this timescale. With this point and the results shown in Figure 2.7 in mind, it is evident that 2 fs is a sufficiently small and accurate integration timestep.

Temperature and pressure scaling

In order to bring into effect any temperature or pressure scaling, one must first form a definition of each which can be extracted from the simulation state. The instantaneous, simulation temperature, T, is defined based on the relationship between kinetic energy, E_K, and temperature in analogy with the equipartition of energy [194]:

$$E_K = \frac{1}{2} N_d k_B T = \frac{1}{2} \sum_i^N m_i |\dot{\mathbf{r}}_i|^2, \tag{2.24}$$

with N the number of atoms in the simulation and N_d the number of degrees of freedom available. Eq. 2.24 reduces immediately to the standard definition of ensemble temperature upon averaging over all states. In defining temperature in this way, it follows that an external source of heat may be coupled to the system via modification of a suitable sample of the system velocities.

To mediate the modification of velocities, we use the velocity-rescale thermostat [195]. This is a modified version of the Berendsen thermostat [194] whose basic operation is in modifying the simulation temperature T to the reference temperature T_0 after an an interval τ_T as:

$$\frac{dT}{dt} = \frac{T - T_0}{\tau_T}. \tag{2.25}$$

The modifying interval τ_T can be viewed as a coupling constant which controls the influence of the external environment over the simulated system. The modification of the system temperature is performed by a uniform scaling of all velocities in the system. With the velocity rescale thermostat, the basic scaling of Eq. 2.25 is used along with an additional stochastic noise term so as to avoid suppressing fluctuations entirely. (For a full discussion of this point, see reference [195].)

This simple form of thermostat, even with the modification of preserving the kinetic energy distribution, is not fully capable of perfectly describing the internal thermodynamics of all systems. The failing of this method is in controlling temperature often too tightly and not allowing for the natural thermal fluctuations in the

system. Examples of approaches which can improve this are thermostats are the Nosé-Hoover (NH) [196, 197] and Andersen [198] thermostats. The NH thermostat is often used in simulations of conjugated polymers though we find that adding this additional complexity to temperature control yields insignificant differences in our results. However, it is, as with the choice of integrator algorithm, noted that this may not be true if one is interested in strictly thermodynamic properties.

Given the definition of a system boundary, the simulation pressure can be defined using an instantaneous version of the virial equation [194].

$$P = \frac{1}{3V}\left(\sum_{i}^{N} m_i|\dot{\mathbf{r}}_i|^2 + \sum_{i}^{N}\sum_{j<i}^{N} \mathbf{r}_{ij}\cdot\mathbf{F}_{ij}\right). \tag{2.26}$$

The first term on the R.H.S. of this definition is related to the kinetic energy and, therefore, the simulation temperature. The second term is the virial of the system. Again, averaging over Eq 2.26 returns the usual definition of the virial equation [113]. The definition given here is also simplified due to our use of isotropic systems. Also, this definition is a modified variant for use with a pair-wise force-field in which $\mathbf{r}_{ij} \equiv \mathbf{r}_j - \mathbf{r}_i$ and $F_{ij} \equiv \partial V_{ij}(r_{ij})/\partial \mathbf{r}_{ij}$ are easily accesible.

The variable used for rescaling pressure is the system volume which is controlled by rescaling the box vectors accordingly. This is mediated by the Berendsen barostat [194], which, as its name suggests, performs in an analogous manner to the thermostat of Eq. 2.25 for a simulation pressure, P, reference pressure, P_0, and coupling interval, τ_P. For an isotropic system, the box vectors are scaled uniformly in order to return the system pressure to its equilibrium value.

As with the Berendsen and velocity-rescale thermostats, the Berendsen barostat is a simplified barostat which suppresses fluctuations in the system. However, as with the simplified thermostat, we find this barostat equivalent in accuracy to, as an example, the Parrinello-Rahman barostat [199, 200] with fewer complications (such as simulations crashing in the equilibration phase).

In all our simulations, we use a $\tau_T = 0.1$ ps and $\tau_P = 0.4$ ps. These values are recommended by the Gromacs program in combination with our choice of integrator step-size and neighbour searching frequency though, given our choice of thermostat and barostat, varying them has little effect on the resulting accuracy or efficiency. Further details of our tests of the velocity-rescale and Nosé-Hoover thermostats, and Berendsen and Parrinello-Rahman barostats are provided in Appendix B.

Having discussed our use of thermostats and barostats in controlling temperature and pressure, and, thus, controlling the system equilibrium, we can now proceed to detail the process of achieving equilibrium in a simulation: the process of equilibration.

2.2.3 System equilibration

A full production MD simulation aims to simulate a molecular system such that the system's temperature and pressure are in equilibrium with an external environment. As an MD algorithm is based on solving the exact Newtonian dynamics, an additional conserved quantity is the particle number. As such, a simulated system is an NPT ensemble: a constant particle Number, Pressure, and Temperature ensemble. Other than N, these quantities are not conserved intrinsically by Newtonian dynamics, where the dynamics are instead representative of an NVE ensemble. With the temperature and pressure coupling techniques described above, it is possible to modify the dynamics so as to simulate an effective pressure and temperature. However, this does not automatically qualify an NPT ensemble. To do so, the system must be brought to an equilibrium within the NPT ensemble. This process, a necessary requirement in utilising MD simulations, is known as *equilibration*.

The primary function of an equilibration procedure is to allow dynamics to run in an NPT setting for a period of time before performing a full MD run. If this time is long enough, the system dynamics will naturally progress towards an equilibrium state. This equilibrium state is thus representative of a natural system and, as a result, statistical properties may be reliably extracted.

The process of equilibration is not quite as simple as that described previously. An initial condition generated for a simulation, even if generated in a 'sensible' manner, is not necessarily a stable arrangement in an NPT ensemble. If one were to immediately switch on pressure and temperature coupling, the simulation may immediately breakdown as a result of dealing with potentially unphysical forces and trying to balance both temperature and pressure simultaneously. It is, therefore, necessary to treat equilibration more carefully.

Equilibration is generally split up into four stages. The first is an energy minimisation process. This process aims to remove 'bad' forces and local configurations from the initial system by finding, ideally, an energetic minimum or, more often, a local minimum or near-minimum.

The second stage involves restraining the solute molecule (in our case, the conjugated oligomer) and applying temperature coupling; thus generating an NVT ensemble and beginning the restrained NVT equilibration phase. This is followed by a restrained NPT equilibration phase with pressure coupling applied. In these phases, the solute restraints allow the solvent to find a stable equilibrium gradually without the added complication of the solute dynamics.

Removing the solute restraints brings the procedure into the final stage: unrestrained NPT equilibration. Over the course of this phase, the solute is free to assume a more stable and statistically likely conformation. This is generally the longest equilibration phase and, upon stabilisation, forms a fully equilibrated dynamical system.

Energy minimisation

The first step in an MD run is an energy minimisation step. This step ensures that the initial configuration of molecules in an energetically stable configuration and won't, upon initiating dynamics, enter into any unphysical configuration. Two basic algorithms available in Gromacs are the steepest-descent and conjugate gradients algorithms; details of which are available in the Gromacs manual [166].

For our pre-simulation energy minimisation, we use the steepest-descents algorithm, which is formulated by evaluating forces on each atom at each step and shifting the atomic coordinates in the direction of the force. A tolerance of $10\,\mathrm{kJ/mol\,nm^{-1}}$ on the maximum force was used with an step size 0.01 nm. For the majority of simulations, this resulted in a minimisation which converged to machine precision.

For force-field minimisations on individual geometries, for the use in comparison with quantum chemically obtained geometries (Chapter 4), the steepest descent method was not always capable of providing sufficiently converged geometries. For these minimisations, we utilised the conjugate-gradients approach with the same tolerance and step size as with the steepest descents approach.

Restrained NVT Equilibration

In defining NVT equilibration, we observe the stability of temperature over the course of a restrained NVT run based observation of the temperature trace. In the case of our longest simulations, 32mers of thiophene and fluorene molecules, the simulation time required to stabilise temperature is $\simeq$100 ps with a standard deviation $\simeq$5 K ($\simeq$ 2%) based on a Gaussian fit to the temperature distribution. For absolute certainty, we use an NVT equilibration time of 500 ps in all runs.

Restrained NPT Equilibration

NPT equilibration can be gauged using two metrics: The first is, in analogy with NVT equilibration, obtaining a trace of the simulation pressure. However, pressure fluctuations are often large (with a standard deviation of $\sim$ 200 bar based on a Gaussian fit to the pressure distribution) even for a well equilibrated system and can only be properly analysed by performing running averages. We find that a more intuitive method is using the time-trace of the box volume. As the pressure of the system is scaled primarily through rescaling the box, the convergence of the box volume is an indicator of stability of pressure.

As an example, the the leftmost columns of Figure 2.8 depict the traces of the box volume in the restrained NPT equilibration step of a 2mer, 16mer, and 32mer (Figure 2.8(a), (c), and (e), respectively) of hexyl-thiophene in chloroform. In all cases, there is a considerable decrease in box volume in the initial ($\sim$ 50 ps) phase of the run which becomes effectively, but not perfectly, stabilised. Regardless, this

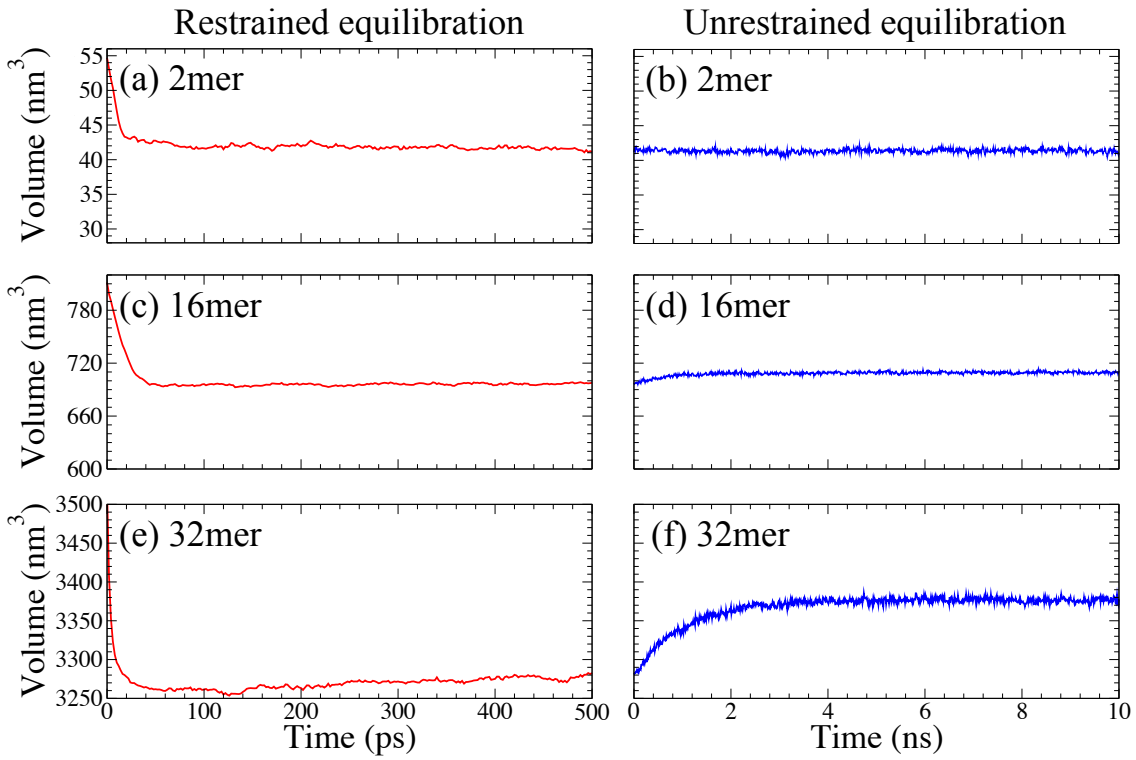

Figure 2.8: Scaling of box volume as a function of time for a 2mer ((a) and (b)), 16mer ((c) and (d)), and 32mer, ((e) and (f)) of hexyl-thiophene in chloroform. The left panels are taken from restrained NPT equilibration and the right from unrestrained NPT equilibration.

initial rapid decaying phase is the most crucial element of this procedure as it eliminates the major remnants of the solvation procedure (see Section 2.2.1). Given that further NPT equilibration is performed with a relaxed solute, an initial phase of 500ps is satisfactory and ensures proper running of a production simulation.

Unrestrained equilibration

The final phase of equilibration, unrestrained equilibration, is another phase of NPT equilibration with restraints removed from the solute molecule. This phase allows the molecule to find an appropriate starting configuration and fully equilibrates the molecule-solvent system. Following the minimisation procedures, the solute effectively always starts in a low-entropy, minimised state - a fully-extended, straight molecule - and tends to a more statistically-probable disordered conformation over the course of unrestrained dynamics. In doing so, the solvent itself continually re-adjusts around each succesive change in the solute conformation. As such, both the solvent and solute are equilibrating with each other and the environment. As is seen from the rightmost panels of Figure 2.8, this results in a slow component of convergence in the box volume.

As demonstrated in Figure 2.8, the convergence of the 32mer (f) is considerably longer ($\sim$ 5 ns) than for the 16mer (d) ($\sim$ 2 ns) and the 2mer (e), which is converged

from the restrained equilibration. This follows intuitively from considering that the minimal (straight) configuration of a longer molecule, with greater conformational freedom, is far less representative of a physically realistic, dynamical conformation than that corresponding to a shorter molecule. That the restrained 2mer requires effectively no further equilibration serves as an example of this point given that a 2mer system does not exhibit any notable conformational freedom beyond dihedral rotation.

Based on this analysis, we deem that 10 ns of unrestrained equilibration is sufficient to ensure, after energy minimisation and 500 ps of both restrained NVT and NPT equilibration, a fully equilibrated system. With this procedure in place, we now go on to briefly discuss the use of solvents as the final requirement for performing full production MD simulations.

2.2.4 Solvent parameters

Due to its major application area being in biomolecular simulation, the default solvent of Gromacs is water and has a number of built in models for water solvation. Water, however, is not a relevant solvent for organic electronics. Water, as is shown as an extreme example in our simulations in Section 4.2.2, is a very poor solvent for conjugated polymers. Commonly used solvents for these materials are generally organic solvents with significantly lower polarity than water such as chloroform, tetrahydrofuran (THF), and toluene. In this work, we utilise these three solvents along with methanol and water. Barring water, these solvents are simulated using the parameters available from the virtualchemistry.org database [185, 186]. Each of these solvent molecules has been parameterised independently based on calculations of quantities such as density, surface tension, and isothermal compressibility and compared with experimental values.

As a confidence check, we have reproduced the densities of these solvents, as calculated by Caleman *et al* [185], utilising our own simulation methodology. These, along with the experimental values available from Yaw [201], are displayed in Table 2.2.4. In all cases, there is very good agreement between our values and the others.

All of the above solvents are utilised in probing solvents effects in 2mers. In approaching longer chains, it becomes computationally prohibitive to use any solvent other than chloroform. Chloroform, while having a higher mass density than the other solvents listed, has a lower density of atoms in total. As such, solvation with chloroform yields a decrease in required computation time of a factor of $\simeq 2$ due to the reduction in the number of differential equations which are required to be solved. As THF is, to a certain extent, a more common solvent for conjugated polymers and, particularly, the solvent of choice in our experimental comparisons in Chapter 4, we also utilise THF for longer molecules wherever possible though for a system as large as a fluorene 32mer (with $\sim 2 \times 10^5$ solvent molecules required for dilute

Table 2.2: Comparison of solvent density, ρ, computed using our simulation methodology, computed by Caleman *et al* [185] using the same parameters, and experimental values taken from reference [201]

	ρ (kg m^{-3})		
	This work	Caleman *et al* [185]	Experiment [201]
chloroform	1401.6±3.9	1372.8±0.3	1479.5±0.5
THF	862.1±1.0	858.5±0.1	881.9±2.6
toluene	870.8±0.8	863.0±1.7	871.8±0.1
methanol	779.1±0.4	786.9±0.3	776.5±0.2

simulation) doing so is unfeasible.

2.2.5 Sampling intervals and simulation lengths

A final point to be analysed for running simulations is the required sampling interval, τ_S, which allows us, in turn, to formulate an idea of how long a simulation is required to run. If τ_S is too small, the statistics generated from a simulation would contain highly correlated data points. This correlation implies that each point is not statistically independent and, as such, a large proportion of the output data will be superfluous. As such, the choice of τ_S should be made so as to minimise both the computational expense of over-sampling the simulation as well as the total run-time by avoiding under-sampling.

We determine τ_S by calculating the auto-correlations, $A(\tau)$, of time traces of a given property, $P(t)$, from a simulation:

$$A(\tau) = \frac{\int_\tau^T dt\, p(t)p(t-\tau)}{\int_\tau^T dt\, (p(t))^2}; \qquad p(t) \equiv P(t) - \langle P(t)\rangle, \tag{2.27}$$

where T is the total time of the simulation, τ is the lag-time, and the angle brackets denote an average over all time frames of a given simulation. As with tangent-correlation functions (discussed in Sections 1.2 and 2.2.6), a correlation time can be defined based loosely on a monoexponential decay. In Figure 2.9, this correlation time can be characterised by the values at which $A(\tau) \simeq e^{-1}$. The properties displayed are the total energy, end-to-end length, and intermonomer dihedral and bond angles calculated from a 16mer of hexyl-thiophene in chloroform.

The total energy has a short correlation time of $\sim 1\,\text{ps}$ which can be expected as it is a sum over the essentially random contributions of the $\sim 10^4$ atoms in the system. As such, in instances when energy sampling is important (which, in this work, is only in defining the temperature and pressure dynamics), τ_S must be of this order. Conformational properties display correlations which persist for around $20 - 40\,\text{ps}$. This defines an upper-bound on τ_S for production simulations. To avoid under-sampling, we choose $\tau_S = 10\,\text{ps}$ for a sampling interval. We also use this value of τ_S for thermodynamic sampling in production runs.

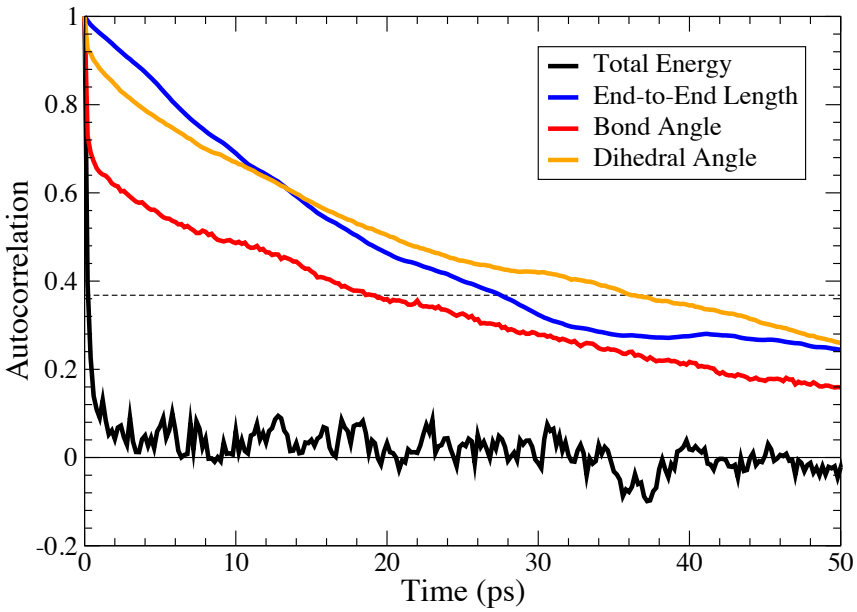

Figure 2.9: Autocorrelations of properties of a 16mer of hexyl-thiophene in chloroform. The black, dashed line indicates the value e^{-1}. The bond and dihedral angle autocorrelation functions are averaged over the 15 functions for each inter-monomer junction in the 16mer.

Based on an appropriate sampling rate, we determine the required run-time of simulations based on the convergence of distributions arising from the properties we detail in the following subsection. In almost all cases, distributions of geometrical properties are converged after 100 ns. The only exception to this is in the end-to-end length distribution of fluorene 32mers which we discuss in Section 4.3.2. Accordingly, we perform all simulations over the course of 100 ns unless otherwise noted.

2.2.6 Simulation post-processing

The first stage of simulation post-processing involves extracting the molecular conformation trajectory from the output binary files. This is performed using built-in Gromacs commands which remove all solvent atoms and reposition the molecule if it is spread over more than one periodic box for all frames. From this trajectory, all of the simulation results presented in Chapter 4 can be extracted and, in turn, the geometries used for ensemble spectra calculations in Chapter 5. What follows is a description of the methods used to extract these features.

Dihedral angles

We define the dihedral angle, ϕ_i, between units i and $i+1$ in a chain using the positions of four of the atoms at the intermonomer junction which are labeled in Figure 2.10(a) and (b) for 2mers of fluorene and thiophene respectively. As the conjugated monomers are near planar at all times, this measure is essentially the same as taking the dihedral angle between the actual planes of the entire monomer

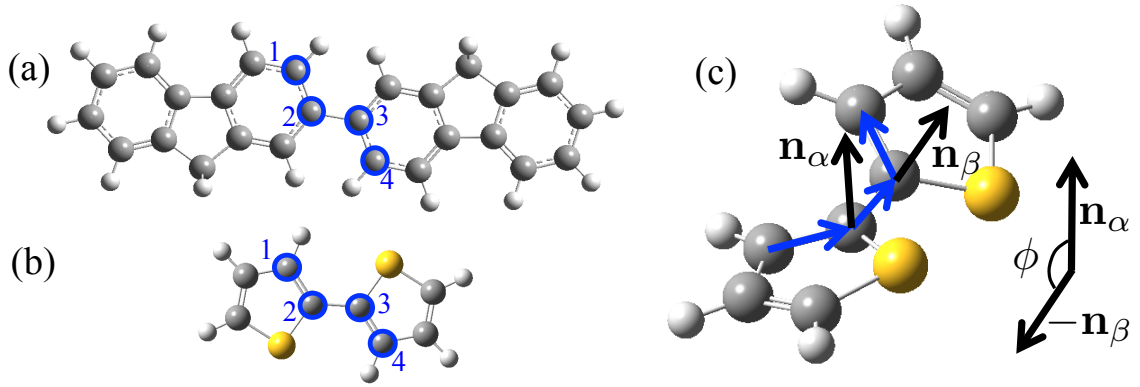

Figure 2.10: (a) and (b) Schematic of the four atoms used for dihedral angle calculations in 2mers of fluorene and thiophene respectively. (c) Schematic of the dihedral angle calculation for a thiophene 2mer.

units. With our full parameterisation in place (following the results Section 4.1), we find that any of four suitable combinations of four atoms is appropriate.

Figure 2.10(c) depicts the calculation of a dihedral. If each atom i of the four has a position $\mathbf{x}_i$ and atoms $\{1,2,3\}$ are assigned to the plane α and $\{2,3,4\}$ to plane β, the dihedral angle is formulated by taking finding the normal vector, $\mathbf{n}_\alpha$ and $\mathbf{n}_\beta$, for each plane:

$$\mathbf{n}_\alpha = (\mathbf{x}_2 - \mathbf{x}_1) \times (\mathbf{x}_3 - \mathbf{x}_2) \tag{2.28}$$

$$\mathbf{n}_\beta = (\mathbf{x}_3 - \mathbf{x}_2) \times (\mathbf{x}_4 - \mathbf{x}_3). \tag{2.29}$$

As the normals are both rotated by $\pi/2$ in the same direction from the orientation of their respective planes, the angle between them is equivalent to the dihedral angle in the standard convention. As such:

$$\cos(\phi) = -\frac{\mathbf{n}_\alpha \cdot \mathbf{n}_\beta}{|\mathbf{n}_\alpha||\mathbf{n}_\beta|}. \tag{2.30}$$

The negative sign on the R.H.S. is in place to return a dihedral in the polymer convention (as discussed in Sections 1.2). In obtaining ϕ by applying an inverse cosine function, we do not distinguish between dihedral angles of values ϕ and $\pi - \phi$ as, given the symmetry of each molecule about π, they are representative of an effectively identical conformation. This results in an effective doubling of the sample size of a given run. This procedure is used for all calculations of dihedral angle distributions presented in this work.

Bond angles

To calculate bond angles, we first assign a tangent vector, $\mathbf{v}_i$, to each unit, i, taken between the end carbons. This is shown for an example fluorene oligomer in Figure

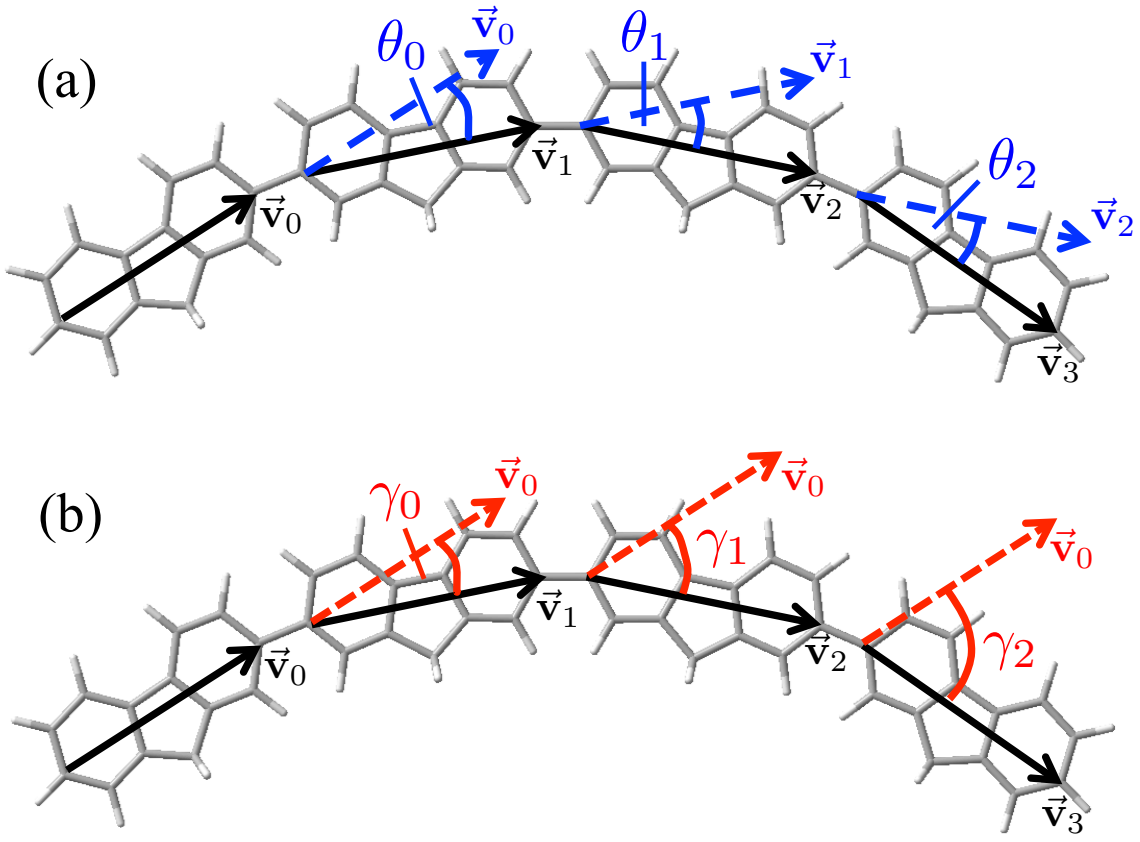

Figure 2.11: Schematics of the definitions of (a) the bond angles, θ_i, and (b) the tangent angles, γ_i, in a 4mer of fluorene.

2.11. For thiophene, this vector is defined in a similar manner using the 1 and 4 position carbons which are typically bound to the neighbouring units in the oligomer. We define the bond angle, θ_i, by the angle between $\mathbf{v}_i$ and $\mathbf{v}_{i+1}$. This is depicted schematically in Figure 2.11(a) and represented mathematically by:

$$\cos(\theta_i) = \frac{\mathbf{v}_{i+1} \cdot \mathbf{v}_i}{|\mathbf{v}_{i+1}||\mathbf{v}_i|}. \tag{2.31}$$

While this definition discards variations in the angle between the intermonomer bond and monomer vector, we believe this incurs no loss of generality while significantly simplifying the definition.

Tangent-correlation functions

As described in Section 1.2, tangent-correlation functions, $A(\Delta n)$ are generally formulated by averaging over the dot product of a given tangent vector and another tangent vector Δn units away. This is shown schematically in Figure 2.11(b). Using the same tangent vectors defined previously for bond angles in Eq. 2.31, we define the tangent-correlation function as:

$$A(\Delta n) = \frac{\langle\langle \mathbf{v}_n \cdot \mathbf{v}_{n+\Delta n} \rangle\rangle}{\langle\langle \mathbf{v}_n \cdot \mathbf{v}_n \rangle\rangle} = \langle\langle \cos(\gamma_{\Delta n}) \rangle\rangle. \tag{2.32}$$

In this definition, the double angular brackets denote an average over simulation time (i.e. over all samples) as well as an average over all possible n. In averaging over all n, we both eliminate the effects of the chain ends as well as significantly increasing the sample size. However, the increase in the sample size is skewed towards lower values of Δn due to the greater number of data points available for lower separations. For N units, the number of data points for a separation Δn scales as $N - \Delta n$. As such, smaller Δn values are significantly better represented than larger ones. Due to this, we generally truncate the correlation function at $\Delta n = N/2$ units. As we discuss in Section 4.3.1, in obtaining persistence lengths, which are effectively correlation lengths obtained by fitting $A(\Delta n)$ to a mono-exponential function, this procedure generally leads to better fitting and a clearer result.

End-to-end lengths

The end-to-end length, L, is calculated by taking the positions of the first and last carbons, $\mathbf{x}_f$ and $\mathbf{x}_l$ respectively, of the molecule for a given sample and finding the length of the vector between them:

$$L = |\mathbf{x}_l - \mathbf{x}_f|. \tag{2.33}$$

Often, the end-to-end length is scaled by the maximum possible chain length, $L_{max} = Nl$, to allow for comparisons of different molecules and chain lengths. We define l as the average length of a monomer from a simulation, l_m, based on the previously defined tangent vectors and the average length of the C-C bond between two monomers, l_b, which is effectively constant due to constraints. We then define the relative end-to-end length, r, as:

$$r = \frac{L}{Nl}. \tag{2.34}$$

This definition is is interpreted by noting that $r = 1$ represents a fully-extended chain; $r = 1/2$ is a significantly folded chain; and $r = 0$ is a closed-loop chain.

2.3 Quantum chemical calculations

As noted in Section 1.3, the MD simulation method is powerful due to its approximation of the quantum mechanical nature of matter by classical force-fields. However, as the simulations are classical, any fully quantum mechanical properties, such as those concerned with electronic dynamics, cannot be obtained using MD simulation alone. Particularly, one cannot obtain any insight into a simulated system's optical properties without invoking a quantum mechanical treatment. Furthermore, the classical force-fields which govern the nuclear motion cannot be derived without recourse to the quantum mechanical nature of electrons. In this section, we discuss a portion of the numerous quantum chemical (QC) calculation methods - methods

concerned with calculating molecular quantum mechanical properties - and how they are utilised in this work.

In all varieties of quantum chemistry, the primary objective is to solve the Schrödinger equation with a given Hamiltonian, $\hat{H}$, for a multi-electron wavefunction, Ψ, and electronic total energy, E:

$$\hat{H}\Psi = E\Psi. \tag{2.35}$$

In the Born-Oppenheimer approximation, which allows for the separation of the electronic and nuclear dynamics, the basic, general form of the electronic Hamiltonian, $\hat{H}_e$, for a system of M atomic nuclei and N electrons is stated as:

$$\hat{H}_e = \hat{T}_e + \hat{V}_{ne} + \hat{V}_{ee} + \hat{V}_{nn}, \tag{2.36}$$

$$\hat{T}_e \equiv -\frac{\hbar^2}{2m_e}\sum_{i=1}^{N}\nabla^2, \tag{2.37}$$

$$\hat{V}_{ne} \equiv -\frac{e^2}{4\pi\epsilon_0}\sum_{i=1}^{N}\sum_{A=1}^{M}\frac{Z_A}{|\mathbf{R}_A - \mathbf{r}_i|}, \tag{2.38}$$

$$\hat{V}_{ee} \equiv \frac{e^2}{4\pi\epsilon_0}\sum_{i=1}^{N}\sum_{j>i}^{N}\frac{1}{|\mathbf{r}_i - \mathbf{r}_j|}, \tag{2.39}$$

$$\hat{V}_{nn} \equiv \frac{e^2}{4\pi\epsilon_0}\sum_{A=1}^{M}\sum_{B>A}^{M}\frac{Z_A Z_B}{|\mathbf{r}_i - \mathbf{r}_j|}. \tag{2.40}$$

In the above, the $\hat{T}_e$ term denotes the electronic kinetic energy and the $\hat{V}_{ne}$, $\hat{V}_{ee}$ terms are the Coulomb potential energy terms for nucleus-electron, and electron-electron interactions; Z_m is the atomic number of atomic centre m; and $\mathbf{R}_m$ and $\mathbf{r}_n$ are the positions of atomic centre m and electron n, respectively. Contributions from the nuclear-only terms are constant for a given molecular geometry and the nuclear kinetic energy term, T_n, is neglected.

The task of directly solving the Schrödinger equation with such a Hamiltonian is practically impossible as soon as one starts to consider more than a handful of electrons. By contrast, even the smallest of molecules will contain upwards of 50 electrons. As such, even for very small molecules, attempting to find a complete solution of the Schrödinger equation is impossible.

The utility of QC algorithms is in the ability to address this problem in different, limited regimes which allow for approximative solutions. These range from *ab-initio* methods, such as expansions in perturbation and coupled-cluster theory, which classify the problem as a series expansion which may be truncated at the required level; to semi-empirical models, such as the Austin models; and density functional theory (DFT), which invokes the one-to-one correspondence of the ground-state

energy and electron density of a system [135]. Each of these is solved numerically by first defining an appropriate linear combination of electronic functions - a basis set - which spans a region of the space of all possible electronic states in the system.

The remainder of this section outlines the relevant aspects of QC methods which are utilised in this work. First, we discuss the basis set concept and the various ways in which basis sets are defined. We then go on to discuss how one approximates the Schrödinger equation by first discussing *ab-initio* methods and then focussing on DFT methods. Both of these classes of methods have found use in the field of conjugated polymers. While at certain stages, such as in Chapter 3, we utilise *ab-initio* methods, the majority of QC work carried out here utilises DFT. As such, we pay greater attention to discussing DFT algorithms and the various aspects involved with them.

2.3.1 Basis sets

Any solution of the Schrödinger equation for a molecular system yields a set of eigenfunctions known as molecular orbitals (MOs), which are occupied or unoccupied by the system's electrons, and their associated energy eigenvalues. To obtain the energy eigenvalues numerically, it is necessary to first obtain the MOs of the system. Taking a linear combination of atomic orbitals (LCAO) approach and including all possible atomic orbitals, it is, in principle, possible to determine the MOs exactly and, thus, the physics of the system. However, as the space of atomic orbitals is infinite, this is practically impossible. In practice, it is necessary to use a reduced combination of functions representative of the atomic orbitals with the number and type of functions used depending on the system and the physical properties in question. This reduced set is known as a *basis set*.

The completeness of a basis set is crucial in obtaining consistent results from QC methodology. A basis set which is so incomplete as to significantly under-represent the MOs involved in a given physical property will lead to large artefacts in a calculation. One prominent example of this is basis set superposition error (BSSE) [135, 202]. BSSE generally occurs as a result of an incomplete basis set failing to account for the higher-lying states which are important in describing the interaction between different parts of a molecule or two distinct, interacting molecules. In this instance, the under-representative basis set leads to these interactions being described by an effective sharing of basis set functions which, in turn, bring the interacting parts closer together and over-estimate the strength of the interaction. While there are means of approximating and correcting for this error (such as the Counterpoise procedure [135]) for cases where the necessary basis set would be computationally prohibitive, it is always best, in the first instance, to assess whether the use of a basis set which minimises these types of errors is feasible.

Molecular basis sets comprised of a combination of Gaussian-type functions cen-

tred around the atomic nuclei are widely used due to their relative ease of computation [135]. The most rudimentary of these types of sets is the STO-nG family of basis sets. These form a minimal basis set - a basis set which aims to define one MO per valence electron - and ascribes n functions to each MO by fitting to the more physically realistic Slater-type orbital (STO). Minimal basis sets are only of particular use in the simplest of systems, such as monatomic hydrogen, as it is almost always necessary to consider further extended basis sets which include a greater number of functions which can allow higher lying orbitals to enter into, for instance, molecular bonding [135]. Extended basis sets are known as n-tuple zeta sets where there are n times as many functions as the corresponding minimal basis set.

The Pople, or k-nm, basis sets form a practical double zeta (DZ) expanded basis set and are prevalent in quantum chemical work [203–212]. These split the increase in the number of functions according the role of the given orbital in a particular atom: k Gaussians are used to describe each of the inner core orbitals; and functions comprised of n and m Gaussians for the outer valence orbitals. In forming this partition of the number of functions, fewer functions are required to form an effective DZ set. This formalism may be further extended to effective triple zeta, k-nlm, basis sets and so forth in a similar manner.

The Pople basis sets, along with the majority of other basis sets, may be further modified by the inclusion of polarisation and diffusion functions. Polarisation functions, denoted in the Pople sets by one or two * symbols, e.g. 6-31G*, are added to account for the possibility of a given atomic orbital to be biased from its central position and allow for greater freedom in the shapes assumed by the orbitals. Diffusion functions, denoted in the Pople sets by one or two + symbols, e.g. 6-31+G, are highly spread functions which are of particular importance in systems with large charge re-arrangement properties e.g. anionic systems.

While it is true that an increase in the number of basis functions will increase the accuracy of a given method, it is not always straightforward to extrapolate to a complete basis set (CBS) limit using Pople basis sets based on a series of increments in the basis set size. One family of basis sets designed with this extrapolation procedure in mind is the Dunning-Huzinaga correlation-consistent - valence N-tuple zeta (cc-VNZ) family, particularly with added polarisation functions (cc-pVNZ) or polarisation and diffuse functions (*aug*-cc-pVNZ) [213]. These basis sets allow, in principle, for a systematic convergence with increasing order of N. As such, they can be utilised for obtaining a good estimate of the CBS limit of a given calculation [157, 213].

Throughout this work, we utilise the Pople and cc basis sets for all QC calculations. For each variant of calculation, it is generally necessary to experiment with the basis sets used and we shall detail these appropriately along with the corresponding

calculations.

2.3.2 Ab-initio methods

While it is true that the size of a basis set is a major factor in the accuracy of a calculation, its effect is often dependent on the calculation method employed. The first class of QC calculation methods we discuss are those known as *ab-initio* methods [135, 214–218]. These methods gain their name from being based on some form of direct approximation to the full Schrödinger equation which, upon increasing order of approximation, may be extrapolated to a full and exact solution. The original *ab-initio* method is the Hartree-Fock (HF) method [135]. This method solves the QC problem based on the Hamiltonian of Eq. 2.36 with a trial wavefunction which neglects the effects of electronic correlation. In essence, it is a mean-field representation of the molecular system.

The HF method utilises a single, N-dimensional Slater determinant representation of the molecular wavefunction, Φ_0, based on the N occupied MOs, ϕ_i [219]. This representation ensures the antisymmetry of the wavefunction under electronic exchange as is required for fermions. Denoting an electron with position $\mathbf{r}_i$ occupying the spin-orbital ϕ_j as $\phi_j(\mathbf{r}_i)$, the Slater determinant is given by:

$$\Phi_0 = \frac{1}{\sqrt{N!}} \begin{vmatrix} \phi_1(\mathbf{r}_1) & \phi_2(\mathbf{r}_1) & \dots & \phi_N(\mathbf{r}_1) \\ \phi_1(\mathbf{r}_2) & \phi_2(\mathbf{r}_2) & \dots & \phi_N(\mathbf{r}_2) \\ \dots & \dots & \dots & \dots \\ \phi_1(\mathbf{r}_N) & \phi_2(\mathbf{r}_N) & \dots & \phi_N(\mathbf{r}_N). \end{vmatrix} \tag{2.41}$$

From this, the HF algorithm is established by, through the course of utilising Lagrange multipliers, first defining the Fock operator [135] for the molecular orbital ϕ_i. Each Fock operator contributes to a matrix spanning all of the system electrons. By diagonalising the corresponding Fock matrix, the eigenfunctions of this matrix may then be used to determine a new Fock matrix which, in turn, sets up a self-consistent iterative scheme by which to solve the problem.

In utilising only a single Slater determinant, the HF approach is a mean-field approach which represents the averaged effect of electrons occupying states up to the highest occupied MO. As such, the features of electronic correlation are entirely neglected. In order to fully account for electron correlation, it is necessary to generate excited Slater determinants which take into account the possibility of occupation of molecular orbitals higher than ϕ_N. The lack of a description of electronic correlation in the HF theory generally yields a total electronic energy higher than the exact energy. As such, the HF method generally serves as a reference for more accurate descriptions of the electronic behaviour provided by *post-HF methods*.

The most straightforward of the post-HF methods is the configuration interaction (CI) [135]. This directly follows the procedure of expanding the electronic

wavefunction, denoted as Ψ_{CI}, as combination of excited Slater determinants:

$$\Psi_{CI} = a_0\Phi_0 + a_S\Phi_S + a_D\Phi_S + a_T\Phi_S + \dots . \tag{2.42}$$

In Eq. 2.42, Φ_0 represents the HF wavefunction and the subscripts S, D, etc. refer to singly, doubly, etc. excited Slater determinants. The summation over combinations of these determinants is omitted for clarity.

This forms, perhaps, the most natural expression of the electronic wavefunction and yields the advantage of being highly accurate but also the disadvantage of being computationally prohibitive for all but the smallest of systems. This is true even when truncating the expression to include only singly and doubly excited determinants.

Post-HF expansions are generally expressed as expansions similar to that of Eq. 2.42 which may then be truncated for practical use. In forming the CI expansion of Eq. 2.42, this truncation is performed across the groupings of excited Slater determinants. However, it is possible to gain significant advantages by generating different expansions which may be truncated in a manner more suitable to the given system. Two common examples of this type of method, which have been utilised in other works [93, 157, 220] to determine dihedral angle potentials and in this work to serve as reference potentials, are the Møller-Plesset perturbation theory (MP) and coupled-cluster (CC) methods which we discuss now.

Møller-Plesset perturbation theory methods

Møller-Plesset perturbation (MP) theory [135,215,216] addresses the quantum chemical problem by applying perturbation theory:

$$\hat{H} = \hat{H}_0 + \lambda\hat{V}. \tag{2.43}$$

In the context of MP theory, $\hat{H}_0$ is the 'unperturbed' Hamiltonian comprised of a sum over Fock operators [135, 215, 216]. With the perturbation, $\hat{V} \equiv \hat{H} - \hat{H}_0$, MP theory may then be formed to orders in a perturbation expansion in $\lambda\hat{V}$ which are denoted as MPn for nth-order. The resulting wavefunction, Ψ_{MPn}, is given by:

$$\Psi_{MPn} = \sum_{i=0}^{n} \lambda^i \Phi_i. \tag{2.44}$$

Again, Φ_0 is the HF wavefunction. A full, i.e. infinite, MP expansion is equivalent to the full CI. As with the CI expansion, in practice, the MP expansion is truncated only now in orders of the perturbative contributions to the system wavefunction and energy. In this formulation, the MP0 contribution returns an energy which is the sum over the energies of each occupied MO and including the MP1 corrections leads to the HF energy. The first meaningful contribution from MP theory is at second order

(MP2). Further details of this procedure may be found in references [135, 215, 216], and, for general perturbation theory, in reference [221].

The advantage of the MP expansion is that MP2, in many cases, accounts for a large fraction of the missing correlation energy. This means that MP2 is widely used across QC work generally as well as in conjugated polymers. In many cases, extending to MP3 and MP4 does not yield significantly different results though does lead to a substantial increase in computational expense. However, it has been demonstrated [93, 202, 220] that MP2 methods can also be sensitive to BSSE and, in calculating dihedral potentials for thiophene 2mers, Dubay *et al* [93] found it to require basis sets as high as quadruple-zeta.

In Section 3.1.1, we calculate dihedral potentials using MP2 as a reference for obtaining an optimal calculation method. These calculations were carried out by our collaborator Peter Repiščák using the Molpro 2012 program [222, 223].

Coupled-Cluster methods

Coupled-Cluster (CC) methods [135, 217, 218] involve expressing the system wavefunction in terms of the cluster operator $\hat{T}$ which contains the amplitudes for single, double, triple etc. excitations:

$$\hat{T} = \hat{T}_1 + \hat{T}_2 + \hat{T}_3 + \dots \tag{2.45}$$

Utilising this operator, the CC wavefunction, Ψ_{CC}, is written in terms of the HF wavefunction, Φ_0, as:

$$\Psi_{CC} = e^{\hat{T}}\Phi_0. \tag{2.46}$$

In representing the exponential operator by a Taylor expansion and grouping the orders of excitation, this method returns the full CI. In the CC representation, truncation is performed in orders of the cluster operator. For example, in the most common case this truncation is performed using only single and double excitations with Eq. 2.45 becomes $\hat{T} = \hat{T}_1 + \hat{T}_2$. This is referred to as CCSD.

This CCSD formulation of the QC problem has proven to be widely successful [218]. In particular, the CCSD(T) method, which modifies CCSD by including the effect of the $\hat{T}_3$ operator in perturbative manner, is widely utilised as a benchmarking method in the limit of a large basis set. As a notable example, this method was used by Bloom and Wheeler [157] to calculate dihedral potentials in thiophene 2mers which serve as the highest quality calculation of this potential available to date. However, even at the CCSD and CCSD(T) levels, the computational power required is often prohibitive for all but the smallest molecules. Furthermore, as has been shown in other works and discussed in Chapter 3, the CCSD(T) method is prone to BSSE and requires a large (often up to quadruple zeta) basis set to return converged

results [157, 220]. Again, this adds to the computational cost of the method and, as a result, makes it prohibitive for calculations of molecules much greater than, for example, thiophene 2mers.

Given this domain of applicability, we have utilised this method as a means of calculating dihedral energetics as a reference for other methods. As with MP2, these calculations were carried out by Peter Repiščák using Molpro 2012 [222, 223] and the results obtained are discussed in Section 3.1.1.

Local and density-fitted methods

While both MP and CC methods are advantageous over a full CI treatment of the correlated molecular system, it is still the case that these methods are computationally prohibitive for large molecular systems. Furthermore, at practical levels of theory such as MP2 and CCSD(T) with, for example, double or triple zeta basis sets, these methods are prone to BSSE in a number of systems [224] including conjugated oligomers [93,220]. However, by invoking local [224,225] and density-fitted [226–228] versions of each method (prefixed by 'L' or 'DF-'), it is possible to reduce the effect of each of these drawbacks.

Local methods, e.g. LMP2 and LCCSD(T), are based on partitioning the electronic structure into domains based on how physically relevant the correlations between electrons on different parts of the molecule are. The domains are typically generated using an algorithm such as the Boughton-Pulay algorithm [229] and threshold coefficient, c_{BP}, which determines the extent to which orbital domains extend across the entire orbital space. ($c_{BP} = 1$ defining a single, delocalised domain and, thus, the full 'canonical' version of the given method.) By enforcing a locality on the basis of a method, local methods often reduce BSSE by reducing the capability of basis functions to form stabilising superpositions across the domains imposed by the calculation. In the context of thiophene 2mer dihedrals potentials, DuBay *et al* showed that the dihedral potential calculated using LMP2/cc-pVTZ was more accurate than that calculated with MP2/cc-pVTZ [93]. Furthermore, by reducing the number of relevant excitations to be treated in a given expansion, local methods generally incur a smaller computational expense.

Density-fitted methods e.g. DF-MP2 and DF-LCCSD(T) (also known as resolution of identity (RI) methods) are primarily a means of improving the computational performance of *ab-initio* methods by approximating four-site electronic integrals by a sum over three-site integrals mediated by a residual density [228]. This approach can significantly reduce the data overhead of a calculation due to the number of combinations of three-site integrals being far smaller than that of four-site integrals.

The DF and L variants of MP2 and CCSD(T) are used as comparison methods for calculations of dihedral potentials in Section 3.1.1. As with MP2 and CCSD(T) calculations, these were carried out by Peter Repiščák using Molpro 2012. Further

details of these calculations are given along with the discussion of the results.

2.3.3 Density Functional Theory

While the *ab-initio* methods described above are capable of providing both highly accurate results and an order-extendable approximation to the full solution of the Schrödinger equation, it is often the case that they are either computationally prohibitive or unwieldy in their application to reasonably-sized conjugated systems. The bulk of the QC work we present was carried out using density functional theory (DFT) [135, 230–235]. As we shall discuss, the key success of DFT methodology is reducing the correlated electron problem from a problem of $3N$ quantum mechanical variables to a functional representation of a 3 dimensional one-particle electron density [135]. While this approach has drawbacks, particularly in losing the extensibility to a full Schrödinger equation solution, the reduction of the problem to one based on the electron density often yields results of comparable accuracy to high level MP and CC calculations with a computational expense close to that of HF methodology. Here, we shall discuss the basic outline of DFT both as a ground-state methodology and also its extension to include response theory and, in particular, the light-matter interaction in time-dependent density functional theory (TD-DFT).

Ground-state DFT

The key success of the Density Functional Theory (DFT) [230, 231] approach is to reduce a problem of $3N$ variables, the electronic co-ordinates, to one of 3 contained in the one particle electronic density. That this is possible is a result of the Hohenberg-Kohn theorem [230]. This theorem states that the total energy of any system may be expressed as a functional of the electronic density and, particularly, the density which minimises the functional is uniquely the ground-state density of the system.

Defining the single particle density, $\rho_e(\mathbf{r})$, as:

$$\rho_e(\mathbf{r}) = N \int \dots \int d^3\mathbf{r}_1 \dots d^3\mathbf{r}_N \sum_{i=1}^{N} \delta(\mathbf{r} - \mathbf{r}_i) |\psi(\mathbf{r_1}, \mathbf{r}_2, \dots, \mathbf{r}_N)|^2, \tag{2.47}$$

the energy functional is expressed as:

$$\hat{H}[\rho_e] = \hat{T}_e[\rho_e] + \hat{V}_{ee}[\rho_e] + \hat{V}_{en}[\rho_e] + \hat{V}_{nn}[\rho_e]. \tag{2.48}$$

The terms $\hat{T}_e[\rho_e]$, $\hat{V}_{ee}[\rho_e]$, and $\hat{V}_{en}[\rho_e]$ are functionals denoting the electronic kinetic energy, and the potentials for electron-electron, electron-nuclei, and nuclei-nuclei Coulomb interactions respectively. In the Born-Oppenheimer approximation, the $\hat{V}_{nn}$ term is constant for a given molecular configuration. The remaining terms follow, in principle, from the definitions given in Eq. 2.36. However, an exact,

general expression can only be formulated for the $\hat{V}_{nn}[\rho_e]$ and $\hat{V}_{en}[\rho_e]$ functionals while there are no such expressions for the $\hat{T}_e[\rho_e]$ and $\hat{V}_{ee}[\rho_e]$ functionals [135].

The typical approach to approximating the $\hat{T}_e[\rho_e]$ and $\hat{V}_{ee}[\rho_e]$ is the Kohn-Sham formalism [135, 231]. The $\hat{V}_{ee}[\rho_e]$ functional can be split into two contributions, the Coulomb part, $J[\rho_e]$ and exchange part, $K[\rho_e]$, as is the case with the HF method. The Coulomb functional has a straightforward definition:

$$J[\rho_e] = \frac{1}{2}\frac{1}{4\pi\epsilon_0}\iint d^3\mathbf{r}d^3\mathbf{r}'\frac{\rho(\mathbf{r})\rho(\mathbf{r}')}{|\mathbf{r}-\mathbf{r}'|}. \tag{2.49}$$

The exchange contribution is that which has no analytical formulation. Considering, then, $\hat{T}_e[\rho_e]$, one can define the functional $\hat{T}_S[\rho_e]$ corresponding to the exact kinetic energy functional of a system of non-interacting electrons:

$$\hat{T}_S = \frac{-\hbar^2}{2m}\sum_i^N \langle\psi_i|\nabla^2|\psi_i\rangle\,. \tag{2.50}$$

The orbitals ψ_i are the Kohn-Sham (KS) orbitals which, similarly to HF orbitals, are single particle solutions to the equivalent mean-field problem and obtained by the method of Lagrange multipliers. The difference between the KS and HF orbitals, and the key success of the DFT approach, follows from the definition of an additional functional: the exchange-correlation (XC) functional, $\hat{V}_{xc}[\rho_e]$ [135, 231]. Given that the functionals defined by Eq. 2.49 and Eq. 2.50 are both deficit in their description of the exact system (the former neglecting the exchange interaction, the latter electronic correlation in interacting electronic systems), the XC functional is formulated to compensate for these deficiencies:

$$\hat{V}_{XC}[\rho_e] = (T_e[\rho_e] - T_S[\rho_e]) + (V_e e[\rho_e] - J[\rho_e]), \tag{2.51}$$

with the the electronic energy functional of Eq. 2.48 expressed as:

$$\hat{H}[\rho_e] = \hat{T}_S[\rho_e] + \hat{J}[\rho_e] + \hat{V}_{XC}[\rho_e] + \hat{V}_{nn}[\rho_e]. \tag{2.52}$$

As such, the key success of the DFT approach is that, with a suitably defined XC functional, one can develop a theory with similar accuracy to correlation-inclusive *ab-initio* methods with close to the computational expense of the HF method [135]. However, the XC functional itself must be approximated which means that, as opposed to *ab-initio* methods, in practice it is not necessarily true that a given DFT methodology may be extrapolated to the full SE result with an infinite basis set and infinite order method. However, with the utility of modern XC functionals, as discussed at the end of this subsection, DFT has become a very widely used approach [44, 47, 75, 97, 98, 103, 140, 220, 236] and is particularly well-suited to accurate calculations of substantially large or complex molecules.

With the above in mind, the DFT method is the primary QC tool utilised in

this work. In Chapter 3, we explore the functionality of DFT as a tool for calculating dihedral potentials based on comparison to high-level, *ab-initio* calculations. In finding this correspondence, we are able to explore long (up to 16mer) conjugated molecules in optimised configurations which would be inaccessible using correlated *ab-initio* methods. In Chapter 5, we also use DFT methodology for calculating optical phenomena. This requires an extension of the DFT approach, time-dependent DFT (TD-DFT), to account for an external time-dependent optical potential.

Time-dependent DFT

Up to now, the methods described have been focused on ground-state wavefunctions and, thus, ground-state molecular geometries, energies, and electronic densities. To treat any form of excited-state phenomena, it is necessary to solve the time-dependent Schrödinger equation:

$$i\hbar\frac{\partial\Psi}{\partial t} = \hat{H}_W\Psi(\mathbf{r}_1,\ldots,\mathbf{r}_M,t), \tag{2.53}$$

where $\hat{H}_W$ is defined as the electronic Hamiltonian, $\hat{H}_e$, with an external, time-dependent potential, $\hat{W}(t)$:

$$\hat{H}_W = \hat{H}_e + \hat{W}(t). \tag{2.54}$$

At first sight, it is not straightforward to extend DFT to excited state phenomena due to its basis on the Hohenberg-Kohn theorem. However, a similar theorem - the Runge-Gross theorem [237] - exists which states that identical systems in identical initial states acted upon by different external potentials will result in two different final states. As such, the time dependent potential has a functional correspondence to the initial state which, in turn, corresponds to the ground-state density. Utilising this theorem, it is possible to determine time dependent dynamics using an algorithm similar to that of standard DFT: time-dependent DFT (TD-DFT) [232, 237–239].

One example of excited-state phenomena - which is the sole use of TD-DFT in this work - is the calculation of linear absorption behaviour. The TD-DFT approach performs such calculations by treating the optical source as a perturbing potential and utilising linear response theory [232]. This allows for the calculation of the excited state structure and the transition energies and oscillator strengths of the excitations from the ground state to the higher lying electronic states and, in turn, a determination of the spectral properties of a molecular system.

As with ground-state DFT, the advantages of TD-DFT over *ab-initio* excited-state methods are rooted in the computational affordability of the approach. In this work, particularly in Chapter 5, we are concerned with calculating absorption spectra based on numerous geometries of molecules up to 32mer in length obtained from MD simulations which would be an impractical task using other QC methods.

As with ground-state DFT, TD-DFT approaches require considerable care with regards to the choice of functional as well as basis sets and are discussed accordingly alongside each type of calculation.

DFT functionals

As we discussed above, at the core of the DFT method is the approximative XC functional. This functional is what is commonly referred to simply as the functional for a DFT calculation and must be chosen judiciously to appropriately represent the electronic physics in question.

Historically, an exact functional form of the exchange interaction in a uniform electron gas, $K_D[\rho]$, was derived by Block [135]:

$$K_D[\rho] = -\frac{e^2}{4\pi\epsilon_0}\frac{3}{4}\left(\frac{3}{\pi}\right)^{\frac{1}{3}}\int d\mathbf{r}\,[\rho(\mathbf{r})]^{\frac{4}{3}}\,. \tag{2.55}$$

Utilising the $K_D[\rho]$ functional with no correlation part does not form a valid approximation as, in particular, it cannot predict atomic bonding [135]. However, a first approximation to the DFT functional can be formed by assuming that a uniform electronic density is true over a sufficiently small domain. This approximation is known as the *local density approximation* (LDA). LDA functionals utilise the functional form of Eq. 2.55 for the exchange part of the XC functional - $E_X^{LDA}[\rho] \equiv K_D[\rho]$ - in conjunction with an appropriate interpolation formula for the correlation functional such as in the VWN [240] and PW [241] functionals.

In almost all cases, a simple LDA functional lacks sufficient accuracy. The next step in approximation is in functionals which depend on derivatives of ρ: *generalised gradient approximation* (GGA) functionals. These either form a correction to the LDA functional or have an entirely independent form. One example is the B or B88 functional of Becke [233]:

$$E_X^B[\rho] = E_X^{LDA}[\rho] - \beta\frac{e^2}{4\pi\epsilon_0}\int d\mathbf{r}\frac{\rho(\mathbf{r})^{4/3}x(\mathbf{r})^2}{1+6\beta x(\mathbf{r})\,\mathrm{arsinh}[x(\mathbf{r})]};\quad x(\mathbf{r}) \equiv \frac{|\nabla\rho|}{\rho^{4/3}}. \tag{2.56}$$

The factor $\beta = 0.0042$ is a parameter obtained by fitting to the HF exchange energies of noble gas atoms. A GGA exchange functional of this form must be used in conjunction with an appropriate correlation functional in order to generate a full XC functional. One common example is the Lee-Yang-Parr (LYP) functional [235] which is commonly used with the B functional. This combination is known as BLYP following standard naming conventions.

A further extension, which makes up the majority of modern functionals, is in forming *hybrid* functionals [234, 242–247]. Hybrid functionals further improve the functional representation by including a proportion of the exact exchange energy

calculated from the HF method. For example, the B functional is often extended to the B3 functional [234] which is of the form:

$$E_{XC}^{B3} = (1-a)E_X^{LDA} + aE_X^{HF} + bE_X^B + +cE_C^{GGA} \tag{2.57}$$

The three parameters a, b, and c are semi-empirical fitting parameters which give the B3 functional its name. In the common B3LYP functional, the E_C^{GGA} is the LYP functional.

Hybrid functionals, such as B3LYP and PBE0 [242], are widely used in current DFT calculations. In particular, much progress has been made in the theoretical understanding of conjugated polymers using these types of functionals [47, 98, 103, 236]. Recently, there has been growing use of *long-range corrected* (LC) hybrid functionals [108, 238, 243–247]. These are generally developed to address the failure of hybrid functionals to account for long range phenomena such as excitations in long chains and charge transfer states [243, 248]. One example is CAM-B3LYP, which modifies the B3LYP functional to correct for its incorrect long-range behaviour [243]. Other examples are the M06 family of functionals [244] (notably M062X) and ωB97XD [245, 246] as well as the general LC scheme of Iikura *et al* [247] which allows for the definition of functionals such as LC-BLYP.

It should also be noted that the DFT method does not natively account for dispersion interactions. While the exchange terms account for the repulsion due to neighbouring electron clouds, there is no intrinsic mechanism for the dispersion interaction to arise from a DFT-based calculation. As such, for systems where dispersion is of importance, e.g. multiple interacting molecules, an additional corrective term must be included to properly account for the attractive forces. Of the functionals listed above, the ωB97XD functional includes dispersion by default. In all other cases, dispersion forces may be included using the correction scheme defined by Grimme *et al* [249, 250] which is defined for most common functionals.

As is the case with basis sets, the appropriate functional choice is made by comparison of various possibilities with either experiment or other high level calculations. Throughout this work, we perform tests with many combinations of the functionals listed above among others. It is not always the case that one particularly good combination of functional and basis set for a particular phenomenological property is transferable to another property. As such, we detail these testing procedures throughout this work when considering particular calculations.

2.3.4 Calculation methods

Following the above outline of *ab-initio* and DFT methodology, we conclude this chapter with an outline of the use of QC calculation schemes in this work. We begin by discussing geometry optimisation and single-point (SP) energy calculations before discussing calculations of dihedral potentials, linear absorption and, finally, partial

charges.

Barring the *ab-initio* calculations detailed in Chapter 3, all QC calculations have been carried out using Gaussian 09 Revision D.01 [251]. This program suite has a wide range of functionality for DFT and TD-DFT calculations including a wide range of functionals and dispersion modifications.

Geometry optimisation and single-point energy calculations

The first step in a typical QC calculation is some form of geometry optimisation. In its usual form, the geometry optimisation procedure obtains a local minimal ground-state configuration of a molecule by considering effective forces on the nuclei due to the electronic configurations and minimising accordingly. Another similar mode of operation applies restrictions on particular degrees of freedom - known as *redundant co-ordinates* - and optimises all other degrees of freedom in the usual manner. This second mode allows for the isolation of the dependence of properties, such as the total energy or linear absorption, based on a given molecular degree of freedom.

Geometry optimisation procedures are necessary primarily to ensure a physically reasonable molecular configuration. The properties of molecules, a particular example being the total energy, are often significantly sensitive to geometrical inconsistencies. As any protocol for building configurations, such as using a molecular visualisation package, e.g. GaussView, or our own automated procedure detailed in Section 2.2.1, can only form a reasonable guess at a starting structure, the optimisation step effectively cleans up the initial geometry and removes possible inconsistencies. Furthermore, optimised geometries allow for a consistency of comparison between methods e.g other QC methods or force-field methods. This is particularly important in performing dihedral scans with redundant dihedral co-ordinates as we shall discuss shortly.

The first step of a geometry optimisation (following the Berny optimisation algorithm in Gaussian09d [251]) is forming an initial guess to the Hessian matrix of second derivatives. In simple terms, an optimisation algorithm computes forces based on the Hessian matrix, moves the nuclear co-ordinates accordingly, and recalculates the Hessian matrix until convergence criteria, such as the variation in the total energy and atomic displacements between steps and the maximum force calculated being below defined tolerances, are met. In our all of our geometry optimisations, we use the defaults of Gaussian09d for DFT calculations and, for *ab-initio* methods, the defaults of Molpro2012.

Following an optimisation procedure, the electronic total energy is obtained automatically. This energy is known as a single-point (SP) energy and is obtained directly from the calculation of the electronic wavefunction or density and, thus, can be performed independently of the geometry optimisation. This is particularly useful given that geometry optimisation, which is far more computationally demand-

ing than an SP energy calculation alone, can be performed accurately for smaller basis sets than those required for accurate SP energy calculations. As such, it is often the case that the SP energy is calculated separately based on an optimised geometry. This process is followed for all of our SP calculations and is of particular importance in determining dihedral potentials.

Dihedral scans

Dihedral scans are calculated using a two step method alluded to previously. First, we obtain optimised geometries for series of redundant dihedral co-ordinates spanning 0° to 180° with an interval of 10°. From each of the resulting geometries, an SP calculation is performed. We refer to this as the 'Scan-SP' approach. This approach is well-documented [93, 144, 157, 220] for obtaining dihedral potentials across both *ab-initio* and DFT methods.

While Gaussian09 contains functionality for performing the geometry scan step automatically based on an initial geometry at 0° or 180°, we perform scans by generating each individual geometry using the methods of Section 2.2.1. There are two main reasons for this. First, separating the geometries allows for parallelising each step of the calculation across a number of computing nodes which, when available, significantly speeds up the calculation process. Secondly, the Gaussian09 scan process optimises a geometry at one dihedral value and forms the subsequent geometry by rotating the given dihedral by its required amount. In certain cases, particularly molecules with long side-chains, this can lead to artefacts in the optimisation procedure, such as side-chains becoming tangled in unpredictable conformations, which are dependant on the direction of the scan. As such, dihedral potentials calculated in each direction do not always match. By generating separate geometries, it is possible to form a starting point for each geometry which is consistent with the other geometries and, thus, ensures reproducible results. This latter point is symptomatic of the difficulty in dealing with side-chains using optimised geometries which is discussed further in Chapter 3.

The possible inconsistency of the dihedral scan process is one reason why performing geometry optimisations at each step is important. In some works, notably that of Bhatta *et al* [140], it is argued that it is not strictly necessary to perform an optimisation at each step. Instead, they calculate dihedral potentials for thiophene oligomers based on calculating one optimised structure and performing only a simple rotation of the dihedral angle and calculating SP energies. They show that, for their choice of the 0° conformation for optimisation, that their results for thiophene 2mers correspond almost exactly to the full Scan-SP approach. This idealisation allows for a significant reduction in the computational expense and allows them to probe dihedral potentials of up to 12mer in length. However, we have found that this principle does not hold true in all cases. While computationally more expensive,

we find it necessary to perform geometry optimisations at each step and, in doing so, obtain results which contradict those of Bhatta *et al* while also being in agreement with the similar observations of Jackson *et al* [144]. Along with our dihedral potential calculations, we discuss the implications of this procedure in Chapter 3.

We utilise redundant dihedral co-ordinates to restrict the dihedral co-ordinates upon geometry optimisation. As with force-field scans (see Figure 2.5 and Section 2.1.4), four intermonomer four-atom dihedrals are available. For QC calculations, there is generally not as much sensitivity to the number of restraints imposed as there is for force-fields. As such, we use two restraints for each calculation so as to cover all six atoms at the junction.

In Chapter 3, we explore a wide variety of methods spanning *ab-initio* and DFT methodology and show that the Scan-SP approach can be optimally performed using CAM-B3LYP/6-31G* and CAM-B3LYP/cc-pVTZ for the geometry scan and SP energies respectively. Based on the results we present, we use this methodology to obtain optimised geometries and SP energies in all other contexts unless otherwise noted.

Linear absorption

In Chapter 5, we report calculations of optical linear absorption spectra. Calculations of this type are performed across an ensemble of geometries generated from MD simulations. However, we also perform these calculations for geometries optimised by DFT methods. These serve primarily as reference calculations for the features extracted from the ensemble calculations. What follows here is an overview, in the first instance, of these calculations for optimised geometries before expanding the techniques to calculations over the ensemble.

It has been demonstrated in a number of works that TD-DFT methodology can adequately describe both linear and excited state absorption properties in oligofluorenes [98, 103, 248] and oligothiophenes [47, 236] with the correct choice of functional and basis set. For all of our TD-DFT calculations, we utilise B3LYP/6-31G. This method is both computationally efficient, particularly for performing ensemble calculations over $\sim 10^2$-10^3 geometries, and has been demonstrated to be of good accuracy in oligofluorenes [98] and comparable for oligothiophenes to a number of widely-used functionals, such as PBE0 [47], which also lacks any long range corrections. We find that functionals without long-range corrections result in spectra which compare more favourably to experiment than those such as LC-BLYP, CAM-B3LYP, and M062X. Furthermore, an increase in basis set to 6-31G* offers negligible improvements and incurs a significant decrease in calculation efficiency. A full discussion of the methods we have investigated can be found in Appendix C.

From a TD-DFT calculation of a given geometry, the transition energy eigenvalues, ϵ_i and oscillator strengths f_i are calculated. We find that calculating the first

twenty of these states is sufficient for capturing the primary absorption states in all cases. We then discard states with $\epsilon > 5\,\mathrm{eV}$ so as to avoid calculating transitions which encroach upon the ionisation threshold. From the remaining set of energies and oscillator strengths, we generate continuous spectra by associating each of the n spectral lines with a Lorentzian function with a broadening parameter γ. The total spectrum for a particular geometry is then a sum over such Lorentzians:

$$S(\epsilon) = \sum_{i=1}^{n} L_i(\epsilon(i)) = \sum_{i=1}^{n} f_i \frac{\gamma}{\gamma + (\epsilon - \epsilon_i)^2}. \tag{2.58}$$

Ensemble spectra are obtained by summing over the Lorentzians, such as Eq. 2.58 associated with the spectral lines of each sampled geometry. The summation, in this instance, is both over the the number of states per frame, n, as well the number of conformations, N.

$$S(\epsilon) = \sum_{j=1}^{N} \sum_{i=1}^{n} L_i^{(j)}(\epsilon) = \sum_{j=1}^{N} \sum_{i=1}^{n} f_i^{(j)} \frac{\gamma}{\gamma + (\epsilon - \epsilon_i^{(j)})^2}. \tag{2.59}$$

This expression gives the full spectrum of a given molecule based on the range of conformations obtained from an MD simulation.

Partial charge calculations

In performing SP energy and TD-DFT calculations, the molecular electronic density is obtained by default. This density may then be used to ascertain the proportion of the electronic density associated with each atom. This is known as population analysis [252] and yields partial (net) atomic charges.

The primary use of these charges is in describing the electrostatic interactions of the molecular system in a classical force-field. As described in Section 2.1.2, classical force-fields such as OPLS describe the electrostatic interactions between electron clouds using static (i.e. geometry independent) partial charges inferred from optimised geometry electronic densities. In Chapter 5, we also use population analysis to determine excitation localisation properties based on computing the difference between partial charge distributions of ground-state and excited-state geometries (calculated using DFT and TD-DFT, respectively).

There exists a wide range of techniques for population analysis. A review of a number of methods and how they compare for calculations of water molecules can be found in reference [253]. Perhaps the most widely used techniques [46,47,93,140,141] are those which involve fitting to molecular electrostatic potential, V_{ESP} defined by [135]:

$$V_{ESP}(\mathbf{r}) = f\left(\sum_{i=1}^{N} \frac{Z_i}{|\mathbf{r} - \mathbf{R}_i|} - \int d^3\mathbf{r}' \frac{\rho_e(\mathbf{r}')}{|\mathbf{r} - \mathbf{r}'|}\right). \tag{2.60}$$

The vectors $\mathbf{R}_i$ denote the nuclear positions each of nuclear charge Z_i and ρ_e is the electronic density. Partial charges are obtained by implementing a fitting scheme to fit a coulomb potential, V_{PC}, based on partial charges, q_i, for each nuclear centre:

$$V_{PC}(\mathbf{r}) = \sum_{i=1}^{N} \frac{q_i}{|\mathbf{r} - \mathbf{R}_i|}. \tag{2.61}$$

How this fitting procedure is performed defines the method used. Perhaps the most straightforward method is the Merz-Singh-Kollman method [254], also known as simply the ESP (ElectroStatic Potential) method, which performs a least-squares fit of the partial charges. Another similar variant is the CHELPG scheme [255, 256] which differs only in how the grid points for the integration of V_{ESP} are defined. While these schemes are often useful for accurate calculations of partial charges in small molecules, for a large number of nuclei or particularly complex molecules, a straight least-squares fitting procedure can lead to poorly defined and, often, highly conformationally dependent charges [252, 253]. This latter point is a particular drawback when implementing a force-field with a static representation of partial charges such as OPLS.

A simple but substantial improvement to the basic ESP scheme comes from the introduction of a penalty function to the least-squares fitting procedure. One particularly succesful approach of this kind is the restrained-ESP (RESP) scheme, introduced by Bayly *et al* [252], which utilises a hyperbolic penalty function in the fit. This penalty function substantially improves the consistency of the fitting procedure by combatting the possibility of charges varying substantially between different least-squares minimising routes. As a result, this method yields charges which are less sensitive to conformation and representative of the molecular symmetry. Given the consistency of this scheme as well as its accuracy, RESP charges are particularly well suited to obtaining charges for force-field implementation and also for determining the variations in partial charge distributions as function of molecular environment (as we discuss in Section 3.3). We utilise this scheme for all calculations of partial charges for force-field implementation.

We obtain RESP charges using the Antechamber program within the AmberTools 14 suite [257]. As defined in Eq. 2.60, the fitting procedure requires the electronic density as input. These are obtained from SP energy calculations performed in Gaussian09 at the CAM-B3LYP/cc-pVTZ level for consistency with the SP energy calculations required for dihedral potentials. In Sections 3.3 and 4.1, we further discuss the implementation procedure of partial charges based on these calculations.

In Section 5.3, we determine the size and location of excitations on individual geometries in our ensemble calculations using population analysis methods. The scale of the molecules in question and their quantity generally restrict this to utilising

a simple ESP scheme. However, the issues raised previously of the ESP scheme in obtaining partial charges for molecular simulation are not as damaging in this context. This is primarily because we sum all charges in a monomer into a single monomer charge for these calculations. This means the possible inconsistencies in the charges do not engender the same inaccuracy as they would in an MD simulation.

2.4 Summary

Throughout this chapter, we have analysed and discussed the computational methods used in this work. First, we discussed the use of the OPLS force-field and, in turn, the limitations of classical force-fields and pair-wise long-range interactions and how these limitations can be best overcome. In doing so, we described our approach to parameterising conjugated polymers which forms the basis of the results of Chapter 3 and Section 4.1. From this, we discussed MD simulation methods within the Gromacs package from simulation building and pre-processing, through the various simulation algorithms and protocols, and how we obtain conformational results, such as those presented in Chapter 4, from simulations. Finally, we outlined a number of quantum chemical approaches ranging from *ab-initio* calculations to DFT and TD-DFT and how they are implemented for obtaining dihedral potentials and partial charges in Chapter 3, and absorption spectra and excitation localisation in Chapter 5.

Chapter 3

Quantum chemical calculations of force-field parameters

As discussed in Section 2.1.4, the aim of our parameterisation procedure is to build on a set of monomer force-field parameters by implementing an accurate representation of the inter-monomer dihedral potential and obtaining partial charges for the resulting oligomer. We aim to determine parameters which may be generalisable to any length of conjugated backbone and side-chains. In this chapter, we present the quantum chemical (QC) calculations required for these tasks. We begin by detailing a DFT based approach which is of comparable accuracy to high-level *ab-initio* calculations. We then investigate the effect of increasing backbone length and side-chains on the dihedral potentials as well as on the partial charge distributions. This investigation allows us to identify the lengths of backbone and side-chain beyond which these parameters are invariant and, as a result, generate an optimal calculation route to obtain a generally applicable force-field.

3.1 Quantifying inter-monomer dihedral potentials

The first step in our parameterisation procedure is the acquisition of accurate inter-monomer dihedral potentials which govern the rotation of one monomer with respect to its neighbour. As we discussed in Section 1.1, dihedral rotation is a key component of a conjugated molecule's optical response as it directly affects the π conjugation along the molecular backbone and, as a result, substantially modifies the electronic energy landscape. As such, it is one of the most important parameters of a conjugated molecular force-field.

Inter-monomer dihedral potentials have a similar form in the majority of conjugated oligomers which can be split in two components: a barrier resulting from the breaking of π conjugation and one or more barriers resulting from steric hindrances - the strong repulsion of atoms or groups of atoms at short separations ($\lesssim 2\,\text{Å}$ for H-H interactions and $\lesssim 3\,\text{Å}$ for heavy atom interactions). To highlight these typical features, we first present, in Figure 3.1, the dihedral potentials of 2mers of fluorene

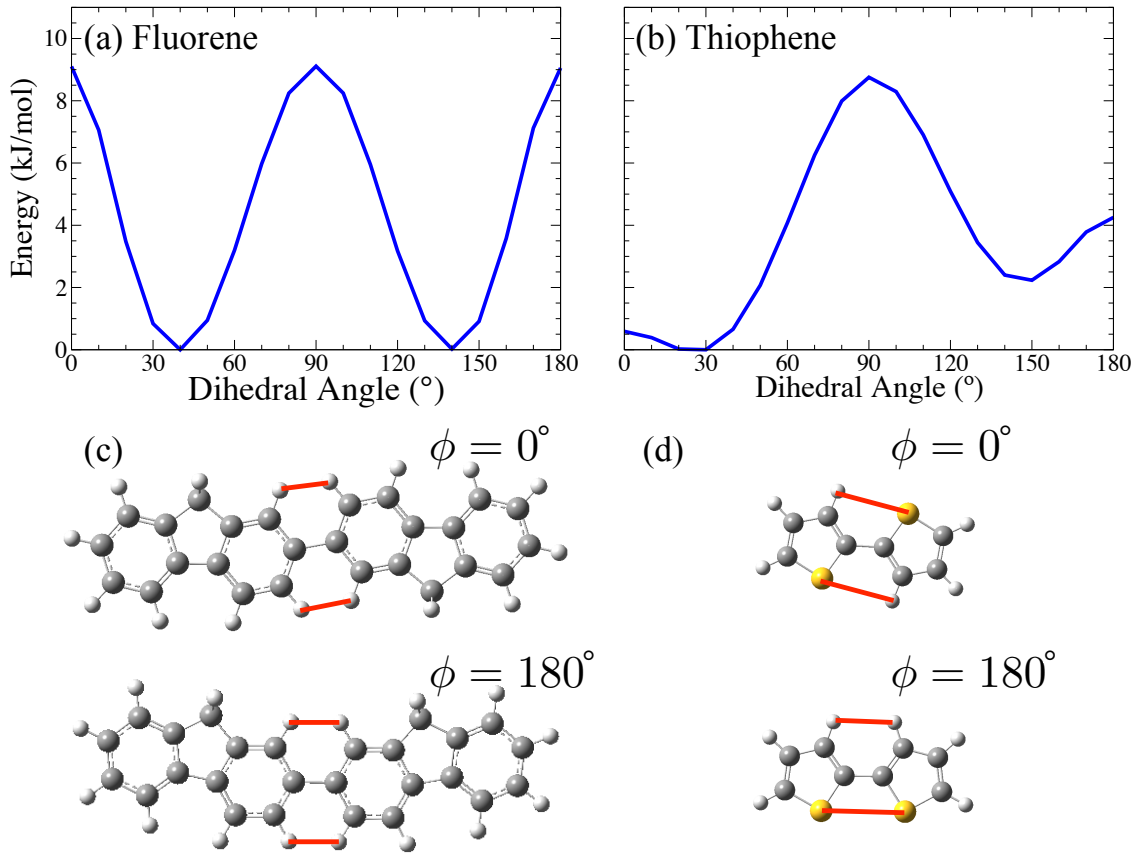

Figure 3.1: Calculated dihedral potentials of (a) fluorene and (b) thiophene 2mers respectively. (c) and (d) Schematics of the major steric barriers at each planar position.

and thiophene (Figure 3.1(a) and (b) respectively) and discuss the details of how they are calculated in the remainder of this section. Both potentials show that the effect of the competing energetic barriers results in minimal dihedral angles in the region 30-50° and 130-150°. Both molecules have a similar barrier of $\simeq 9\,\mathrm{kJ/mol}$ corresponding to breaking the favourable sp_2 hybridised conformation. Both potentials, differ, however, in their steric components. Fluorene has sharply peaked repulsion at the planar positions (0° and 180°) which are of comparable magnitude to the 90° barrier and symmetric. These are due primarily to the close contact ($\simeq 2\,\text{Å}$) of the hydrogen atoms on the opposing units which have weak dispersion but, at short separations, a high repulsive component. In contrast, the thiophene potential is asymmetric about 90° with minima which differ by $\simeq 2.5\,\mathrm{kJ/mol}$. The barrier between the *trans* minimum and 0° is $\simeq 0.5\,\mathrm{kJ/mol}$ while the *cis*-180° barrier is $\simeq 2\,\mathrm{kJ/mol}$ and both result from weaker steric repulsions than in fluorene. In the *trans*-0° case, the slight barrier results from the repulsion of distant ($\simeq 3\,\text{Å}$) sulphur and hydrogen atoms and, in the *cis*-180° case, from both the hydrogen-hydrogen (H-H) interaction (which, at a separation of $\simeq 2.5\,\text{Å}$, is weaker than that of fluorene) and the sulphur-sulphur (S-S) interaction (each separated by $\simeq 3.5\,\text{Å}$).

Numerous methods have been proposed for calculating dihedral potentials in

conjugated molecules. For instance, Raos *et al* [220] demonstrated that theoretical approaches such as DFT, MP2, CCSD(T) are capable of forming a representation of these potentials for thiophene 2mers. They also show that MP2 and CCSD(T) methods can be significantly sensitive to basis set superposition error (BSSE) and, therefore, require up to quadruple-zeta basis sets.

DuBay *et al* [93] further demonstrated the sensitivity of, in particular, MP2 to BSSE in calculating potentials for stilbenes and bithiophenes and found that using L-MP2 reduces this error. In their work, they find that the L-MP2/cc-pVTZ(-f) calculation of the bithiophene dihedral potential performs better, when compared with MP2/cc-pVQZ, than MP2/cc-pVTZ(-f) as a clear result of BSSE. As discussed in Section 2.3.2, L-MP2, as well as having this benefit over MP2, has the advantage of computational performance enhancement due to splitting the calculation into domains [225, 229]. However, the formation of these domains becomes increasingly problematic with increasing monomer size.

It has been proposed in several works [97, 132], including that of Raos *et al*, that the use of DFT methods with the B3LYP functional also yields accurate potentials in conjunction with basis sets such as 6-31G** [220] and 6-31+G** [97]. With this and the above considered, it is evident that there remains some debate as to the appropriate level of theory required for calculating dihedral potentials.

Another key point in calculating dihedral potentials for MD simulations, particularly when building models scalable to all lengths, is the effect of increasing backbone length on the dihedral potential. The use of *ab-initio* methods for this task is practically infeasible due to the difficulty of these methods for calculations of large molecules and, as such, suggests the use of accurate DFT methods. The work of Bhatta *et al* uses the combination of B3LYP/6-31G** to analyse the effect of increasing length of a thiophene oligomer on the calculated dihedral potential, finding that the 90° barrier converges for a 12mer. However, this result is produced by using non-relaxed scans (as discussed in Section 2.3.4) and both the results of this section and those of Jackson *et al* [144] suggest that these potentials are independent of backbone length.

The questions raised over the appropriate level of theory and possible dependence on backbone length of dihedral profiles of fluorene and thiophene oligomers are examined in this section. First, we detail our calculations involving several types of method spanning the DFT and *ab-initio* methods discussed in Section 2.3 as well as an analysis of several choices of basis set in the geometry optimisation and energy calculation steps of each scan. As a benchmark, we compare our results for thiophene 2mers to the CCSD(T)/CBS calculations of bithiophene performed by Bloom and Wheeler [157]. Upon establishing a suitably accurate DFT method, we proceed to examine the variations in the dihedral potentials of longer molecules. We first focus on the effect of neighbouring dihedral angles and the position of the dihedral along

the chain on the individual dihedral potentials in 4mers. This is followed by an investigation into the variations in the potentials with increasing molecule length.

3.1.1 Comparison of different quantum chemical methods

As the first step in defining our parameterisation scheme, we investigate a wide-variety of QC methods for dihedral profile calculations of thiophene 2mers. As we wish to obtain a suitable DFT methodology for extensions beyond 2mers, we have utilised numerous DFT functionals alongwith variants of MP2 and CCSD(T) using the scan-SP separation approach (detailed in Section 2.1.4). In each case, the geometries were optimised at the B3LYP/6-31+G** level as this choice has been demonstrated as sufficient for obtaining accurate geometries [93,97,140]. Each optimisation is performed with constraints on two of the four available dihedral angles. The two dihedrals used are chosen so as to ensure all six atoms at the inter-monomer junction are utilised which ensures a symmetric constraint. Any choice made in this way was found to yield effectively identical results. The dihedrals used for these and subsequent dihedral scans are those shown in Figure 2.10(a) and (b) for fluorenes and thiophenes, respectively, and their counterparts. Further single point (SP) energy calculations were performed in all cases using the cc-pVTZ basis set. Comparison is made in all cases to the result of Bloom and Wheeler [157].

Figure 3.2(a) displays the dihedral profiles obtained using MP2, Density-Fitted Local MP2 (DF-LMP2), CCSD(T), and DFT with the CAM-B3LYP functional. From these results, it can be seen that using DFT with CAM-B3LYP gives results comparable to those of MP2 and DF-LMP2; all of which are in very good agreement with CCSD(T)/CBS result. It is seen that the most significant differences between CAM-B3LYP and both the MP2-based and CCSD(T)/CBS results are in CAM-B3LYP slightly overestimating the energy difference between the *cis* and *trans* minima by $\simeq 0.5\,\mathrm{kJ/mol}$; and underestimating the *cis*-180° and *cis*-90° barriers by $\simeq 0.1\,\mathrm{kJ/mol}$ and $\simeq 0.8\,\mathrm{kJ/mol}$, respectively. Given that the these errors individually correspond to to $\simeq 0.2\,k_BT$, $\simeq 0.05\,k_BT$, and $\simeq 0.3\,k_BT$, respectively, (with $k_BT \simeq 2.5\,\mathrm{kJ/mol}$ at room T) these errors are modest.

As a brief note, DF-LMP2 calculations require a specification of orbital domains based on the proportion of the full space of basis functions included in each local portion of the calculation. These domains are determined using the Boughton-Pulay algorithm [225, 229] based on the coefficient c_{BP} which determines this proportion. Also, for consistency of comparison, these domains must be consistent for each geometry in the dihedral scan. In Molpro 2012, the MERGEDOM directive generates consistent domains by merging the domains of individual geometries which have a number of atoms in common greater than a specified number, n_{MGD}. In tests carried out by Peter Repiščák, it was found that the optimal specification for calculations of thiophene 2mers was $c_{BP} = 0.985$ and $n_{MGD} = 1$.

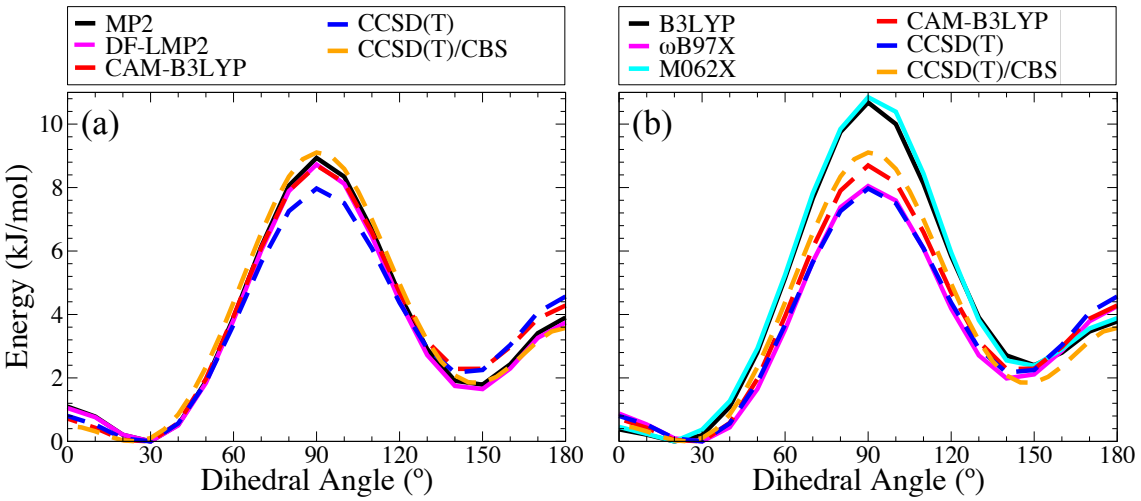

Figure 3.2: Dihedral profiles of thiophene 2mers for various choices of SP calculation methods using the cc-pVTZ basis set. In (a), results for MP2 and DF-LMP2 are presented with (b) containing results for B3LYP, ωB97X, and M062X. In each graph, results for CAM-B3LYP and CCSD(T) are also provided for comparison as well as the CCSD(T)/CBS results of Bloom and Wheeler [157].

It should also be noted that using CCSD(T) with the cc-pVTZ basis set, as opposed to a CBS extrapolation, results in a potential which is less accurate than the above methods. This, as discussed by Raos *et al* [220], is an example of the sensitivity of CCSD(T) to BSSE. Compared to CAM-B3LYP's performance, the CCSD(T)/cc-pVTZ result over-estimates the energy of the *cis* minimum to a similar extent while also underestimating the 90° barrier by $\simeq 1.3\,\mathrm{kJ/mol}$ ($\simeq 0.5\,k_BT$), leading to an overall reduction in the barrier between the *cis* conformation and the 90° point of $\simeq 2.1\,\mathrm{kJ/mol}$ ($\simeq 0.9\,k_BT$). Given the scale of this deviation, it would be expected that this would considerably affect in the resulting dynamics.

In Figure 3.2(b), the results of scans performed using a variety of hybrid DFT functionals - namely B3LYP, ωB97X, M06-2X and CAM-B3LYP are shown. We found that, of all functionals tested, CAM-B3LYP provided the best agreement with the CCSD(T)/CBS result. A number of M06 functionals were tested (M06, M06-L, M06-2X, and M06-HF) with M06-2X giving the closest agreement of all of these. We found that using B3LYP gives a result similar to that of M06-2X, both of which largely overstate the effect of the 90° barrier. Utilising ωB97X results in a profile very similar to the CCSD(T)/cc-pVTZ profile.

From the above analysis, it is evident that using CAM-B3LYP/cc-pVTZ results in dihedral profiles of comparable accuracy to MP2, DF-LMP2, and CCSDT/CBS calculations of thiophene 2mers. DFT methods allow for considerable extensions in molecular size than can be afforded by correlated *ab-initio* methods. As a particular example, it becomes problematic to perform *ab-initio* calculations, for example CCSD(T) or L-MP2, for more complex molecules such as fluorene 2mers or co-polymers (such as those discussed in Section 1.1). As such, by determining that

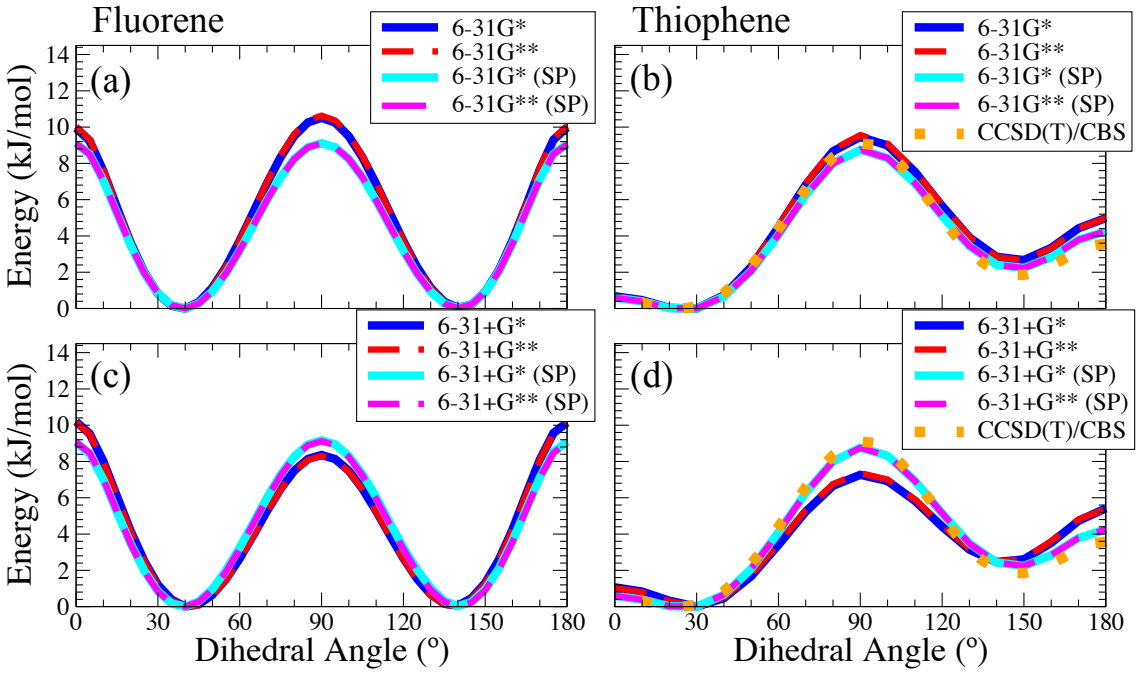

Figure 3.3: Dihedral profiles from DFT with CAM-B3LYP for various combinations of geometry optimisation basis set for 2mers of (a), (c) fluorene and (b), (d) thiophene with and without a further SP step. In (c) and (d), diffuse functions are used in the optimisation basis set and not in (b) and (c). In (b) and (d), comparison is given to the thiophene 2mer CCSD(T)/CBS result [157].

CAM-B3LYP/cc-pVTZ is a suitable functional and basis set choice for accurate calculations of dihedral potentials is one of the core results of our parameterisation procedure and allows us to examine fluorene 2mers as well as longer conjugated backbones and molecules with side-chains. We posit that this method could also be utilised to examine more complex co-polymeric systems.

3.1.2 Comparison of basis sets

Previously, we utilised B3LYP/6-31+G** to obtain geometries for dihedral scans. As mentioned, this combination has been shown to provide accurate geometries and allowed us to obtain a suitable SP calculation method. To further optimise the calculation procedure, we examine the effect on the resulting dihedral potentials of 2mers of fluorene and thiophene of reducing the number of polarisation and diffuse functions in the 6-31G-based basis set used for geometry optimisation with CAM-B3LYP. We examine the potentials obtained both directly from the scan procedure as well as with the further SP step performed using CAM-B3LYP/cc-pVTZ.

As a brief note, for these and the subsequent scan calculations, we are now using the CAM-B3LYP functional for optimisation as opposed to B3LYP as used previously. We discuss towards the end of this section that this change has no effectively no effect on the resulting potential provided that a further SP calculation is performed.

Figure 3.3 presents a series of dihedral potentials calculated using CAM-B3LYP and variants of the 6-31G basis set for the geometry scan (6-31G*, 6-31G**, 6-31+G*, and 6-31+G** as labelled) both with and without further SP calculation. In the first instance, it is seen that, for both fluorene and thiophene (Figure 3.3(a), (c) and (b), (d), respectively), the profiles obtained using the 6-31G-type basis sets are often substantially different from those calculated with a further cc-PVTZ SP calculation.

In the case of thiophene, when compared to the calculations with a further SP step and the CCSD(T)/CBS calculation, 6-31G-type basis sets which include diffuse functions (6-31+G* and 6-31+G**, Figure 3.3(d)) perform with less accuracy than those without (6-31G* and 6-31G**, Figure 3.3(b)). Using the diffuse functions, the most prominent deviation is in the *cis*-90° barrier which is underestimated by $\simeq 3\,\mathrm{kJ/mol}$ ($\simeq 1.2\,k_BT$). For fluorene, those with diffuse functions (Figure 3.3(c)) perform marginally better than those without (Figure 3.3(a)); those without most prominently over-estimating the minimum-90° barriers by $\simeq 2\,\mathrm{kJ/mol}$ ($\simeq 0.8\,k_BT$). In both cases, those with diffuse functions tend to underestimate the 90° barriers while those without tend to do the opposite. In both cases, the planar barriers are slightly overestimated.

It is clear from these results that further SP calculation is required. When comparing the effect of different choices of optimisation basis-set on the resulting SP calculation, it is seen that there is very little effect on the resulting potentials. Furthermore, we have performed calculations using cc-PVTZ for geometry optimisations and found that the dihedral profile calculated in this manner is near-identical to those calculated using cc-PVTZ only for the SP step. Additionally, the potentials calculated in the previous subsection using B3LYP/6-31+G** as the optimisation basis are also effectively identical provided the further SP step is performed. This implies that the above 6-31G-type choices for geometry optimisation provide near-identical geometries and that the accuracy of the final dihedral potential is primarily controlled by the choice of SP method. As such, we have determined that the choice of CAM-B3LYP/6-31G* and CAM-B3LYP/cc-pVTZ for scans and SP energy calculations, respectively, is an accurate and computationally optimal approach for dihedral potential calculations.

3.1.3 Variations due to backbone length

Having established the CAM-B3LYP/6-31G* scan and CAM-B3LYP/cc-pVTZ SP paired method, we explore the effect of increasing backbone length on the dihedral potentials. As a first step, we determine the effects of dihedral position and neighbouring dihedrals in 4mer molecules of fluorene and thiophene. This examination allows us to address several questions which are crucial for a force-field implementation. By determining the effect of neighbouring dihedrals, we assess the validity

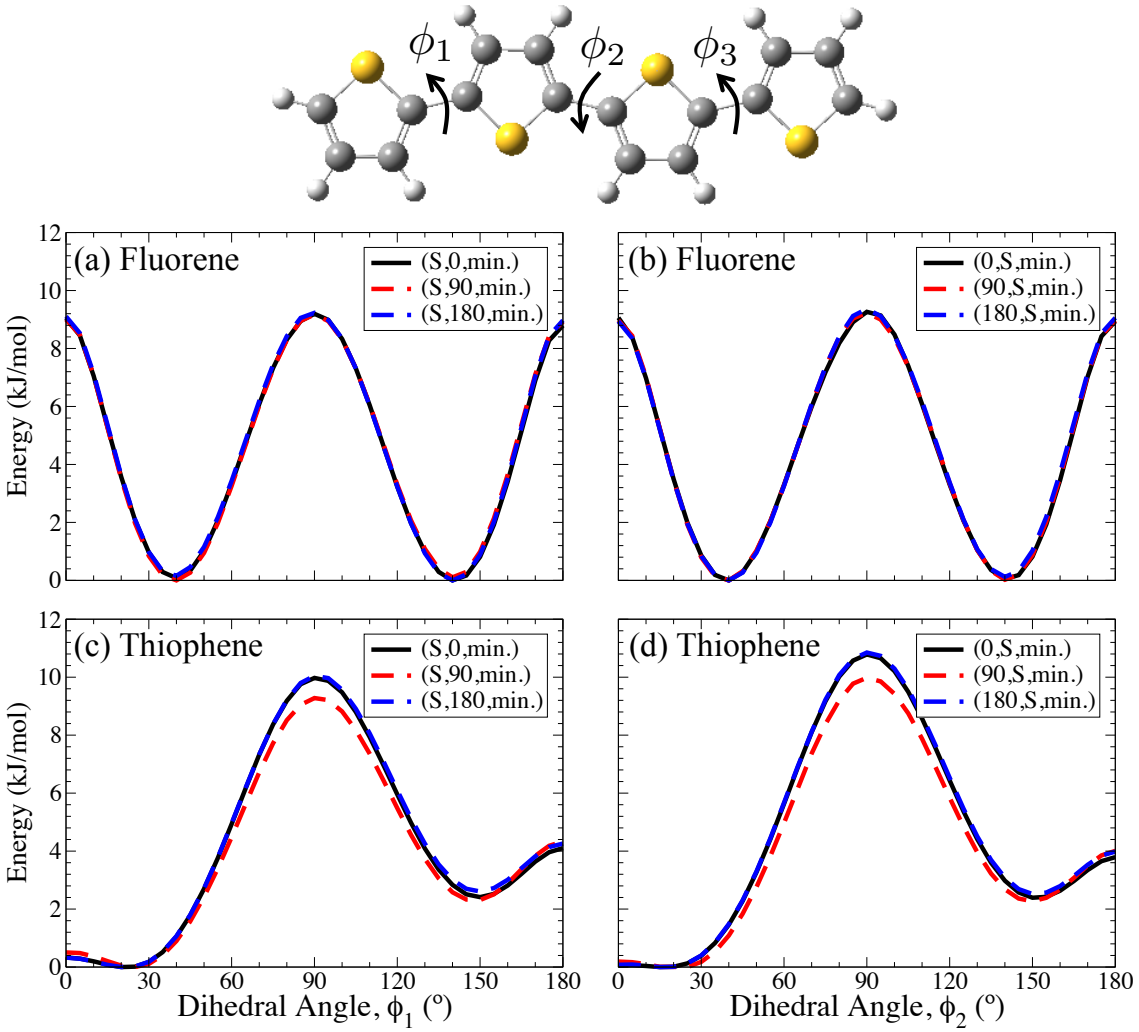

Figure 3.4: Dihedral profiles obtained from scans of 4mers of (a), (b) fluorene and (c), (d) thiophene. In each, the labelling denotes (ϕ_1, ϕ_2, ϕ_3) as shown in the thiophene 4mer above the graphs with 'S' denoting the scanned dihedral angle, 'min.' denoting the freely-optimised dihedral (ϕ_3 in all cases), and values given in degrees.

of using individual, uncorrelated potentials as a representation of the dihedral motion and, in assessing how the potential varies according to its position along the molecule, we determine whether it is the case that each molecular dihedral must be represented by entirely different potentials.

In Figure 3.4, dihedral scans are performed on 4mers of fluorene and thiophene for the end-most (ϕ_1, (a) fluorene and (c) thiophene) and central (ϕ_2, (b) fluorene and (d) thiophene) dihedrals with the either ϕ_1 or ϕ_2 fixed at 0°, 90°, or 180° and ϕ_3 free to optimise. From these calculations, we see that, for fluorene, there is no dependence of a given dihedral function on the neighbouring dihedral value. For thiophene, there is a slight decrease ($\simeq 1\,\mathrm{kJ/mol} \simeq 0.4\,k_BT$) in the 90° barrier when the neighbouring dihedral is at 90° when compared to the case of the neighbouring dihedral being in either of the planar positions.

Comparison of the potentials of different dihedral positions in each molecule reveals that the position of a given dihedral has only a negligible effect on the

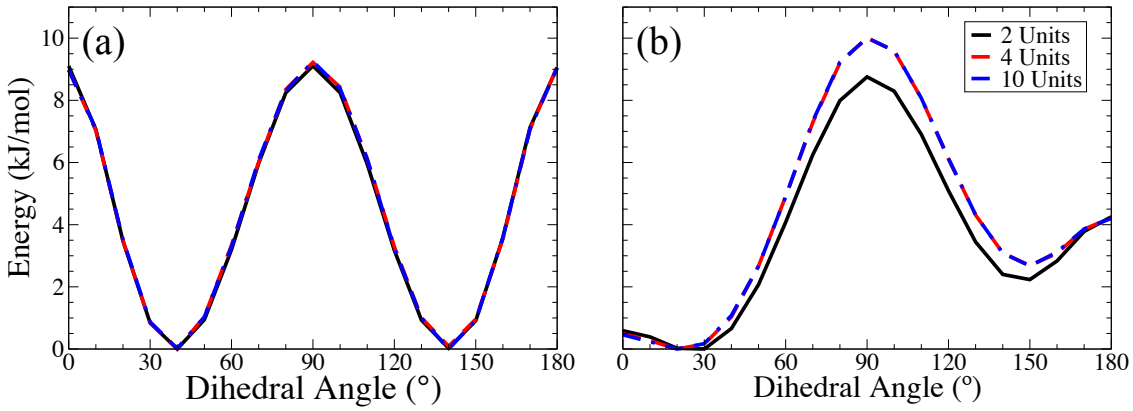

Figure 3.5: Dihedral profiles for various backbone lengths of (a) fluorene and (b) thiophene. (Legend applies to both graphs.)

corresponding potential. For fluorene, again, there is basically no difference while, in thiophene, the potential of ϕ_2 is slightly ($\simeq 0.5\,\mathrm{kJ/mol} \simeq 0.2\,k_BT$) higher in energy at the 90° points. All of the above deviations may be considered effectively negligible.

The above results indicate that the potential of a given dihedral bears little correlation with its neighbouring dihedrals and no significant dependence on its location along the chain. This is one of the key results of this chapter as we have shown that a force-field representation based on a single dihedral potential for each dihedral across a molecule of a given backbone length is valid. These facts also simplify an analysis of the effect of increasing backbone length by reducing the calculation procedure to that of one dihedral potential for each length of molecule.

We examine the effect of increasing backbone length on the dihedral potentials of oligomers of fluorene and thiophene ranging from 2 to 10 units in length by performing dihedral scans on the end-most dihedral. While the choice of the end-most dihedral will typically result in end effects, the previous results suggest that these end effects will be minimal. Additionally, obtaining energetic minima for the end-most dihedrals is typically less prone to convergence issues than central dihedrals. This is particularly relevant for increasingly complex molecules such as molecules of considerable back-bone length or with side-chains. All other dihedrals are free to optimise at each step. In the case of fluorene, Figure 3.5(a), increasing backbone length is of effectively no consequence to the dihedral potential. For thiophene, however, in increasing backbone length from 2 to 4 units, the 90° barrier increases by $\simeq 1.3\,\mathrm{kJ/mol}$. We believe this, and the slight difference observed in Figure 3.4(c) and (d), to be due to the small monomer size of thiophene amplifying nearest neighbour interactions and the effect of the terminal hydrogens. While this increase is larger than previous deviations, we deem that, given the height of the barrier ($\simeq 10\,\mathrm{kJ/mol}$) and the proportion of k_BT represented by this energy ($\simeq 0.5\,k_BT$), this deviation should not play too large a role in the dynamics resulting

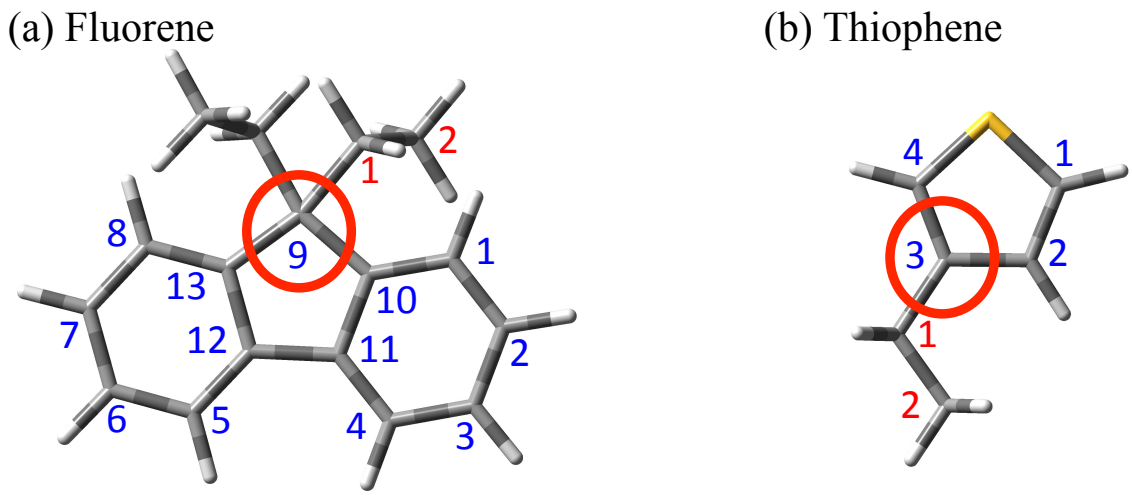

Figure 3.6: Schematic of monomers of (a) diethyl-fluorene and (b) ethyl-thiophene with the heavy-atom numbering convention used throughout this work. The red-circles indicate the carbons to which side-chains are appended.

from this potential. Additionally, the slight reduction in the *cis*-180° barrier height of 0.5 kJ/mol (0.2 k_BT) for longer molecules is similarly negligible. As such, we have shown that the dihedral potential is, to within a suitable tolerance, invariant of molecular length.

Combined with the previous results, we have now shown that dihedral potentials can be treated as invariant to neighbouring dihedrals, dihedral position, and backbone length. This forms a crucial result for our parameterisation scheme by demonstrating that one dihedral potential can be applied generally to any length of molecule and to each dihedral angle independently. Having established this, we now turn to our search for a similar invariance with respect to alkyl side length.

3.2 Dihedral potentials of molecules with side-chains

With a methodology established for calculating dihedral potentials, we now turn to cases in which alkyl side-chains are attached to the molecules and present calculations of dihedral profiles of dialkyl-fluorenes and alkyl-thiophenes using this methodology. In each molecule, side-chains are appended to their most commonly found positions (two equal side-chains at the 9 position on fluorene and one side-chain at the 3 position of thiophene, as shown in Figure 3.6).

As we discussed in Section 1.1, attaching side-chains to conjugated polymers is crucial as they facilitate solvation and, thus, solution processing meaning that they are a vital component of MD simulations. However, from the standpoint of QC calculations, alkyl side-chains typically have little effect on properties associated with conjugated orbitals such as optical absorption behaviour. (This point is discussed in greater detail in Appendix C.) This is a consequence of the different orbital hybridisation of alkyl side-chains carbons when compared to conjugated carbons. This

point typically allows a substantial decrease in the computational expense of TD-DFT calculations due to the basis functions and resulting excited states attributable to the side-chain electrons being easily discarded by removing the side-chains. This reduction in computational expense is further enhanced in geometry optimisation calculations by circumventing the need to find optimised geometries of the side-chain along with the conjugated backbone. Beyond concerns of computational expense, side-chains can also be problematic for geometry optimisations both in QC calculations as well as in the force-field calculations discussed in Section 4.1. As a side-chain has considerable flexibility and numerous local minima, optimisation procedures are highly sensitive to initial conditions - particularly when dispersion interactions are included. As such, an ideal scenario would involve removing the side-chains from dihedral potential calculations in both methods. This requires an understanding of the effect a side-chain has on the conjugated component of the dihedral rotation.

In this section, we calculate the dihedral potentials of alkyl-substituted fluorenes and thiophenes. In doing so, we examine the variations in the potentials resulting from the presence of the side-chains and, in particular, to what extent these variations result from changes in the conjugated component of the rotation. DFT methodology is particularly useful in this respect due, ironically, to it not intrinsically capturing dispersion interactions. As such, it is possible to separate the component of the dihedral potential due to the conjugated backbone orbitals and the side-chain - side-chain interactions. The latter of these is, in principle, suitably represented by the force-field. As such, we determine the effect of the side-chain on the part of the potential we are aiming to model in the force-field. We also examine the inclusion of dispersion interactions for methyl and ethyl substituted molecules in order to obtain a fuller understanding of the effect of the side-chains.

3.2.1 Variations due to the inclusion of side-chains

To investigate the influence of side-chains on the dihedral potentials, scans have been performed on 2mers of dialkyl-fluorene and alkyl-thiophene with side chains of lengths varying from C_1H_3 (methyl) to $C_{10}H_{21}$ (decyl). In the case of fluorene, initial geometries with the side-chains aligned perpendicular to the plane of the corresponding fluorene unit have been chosen while the side-chains of the thiophene molecule are aligned such that each carbon atom is in the plane of its corresponding thiophene unit.

Figure 3.7(a) gives the resulting profiles calculated for fluorene 2mers with various lengths of side-chain. In this case, the inclusion of the side-chain has effectively no influence on the dihedral profile and this remains true for increasingly long side-chains. This is one of the central results of this chapter as it shows that side-chains have no effect on the fluorene dihedral potential and, together with the length-invariance of the previous section, means that a dihedral potential calculated for a

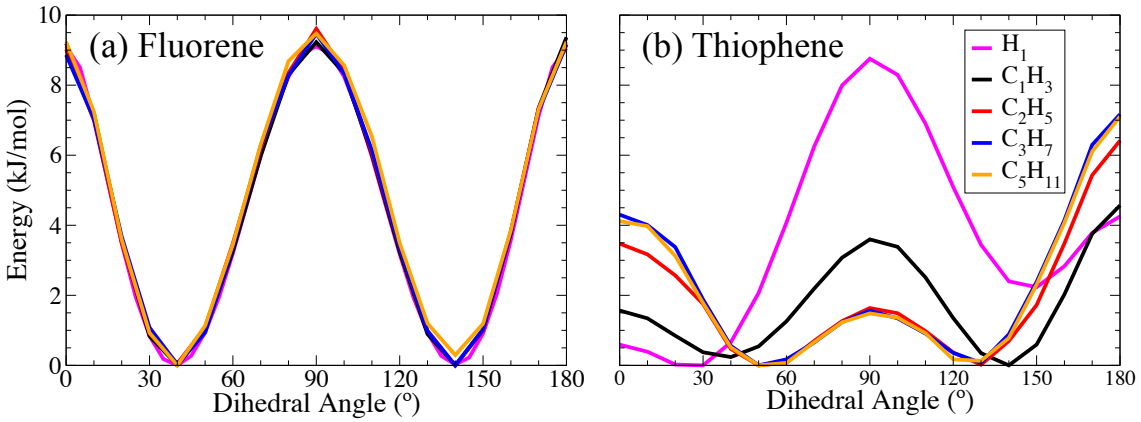

Figure 3.7: Dihedral potentials for 2mers of (a) dialkyl-fluorenes, and (b) alkyl-thiophenes of varying side-chain lengths. (Legend applies to both graphs.)

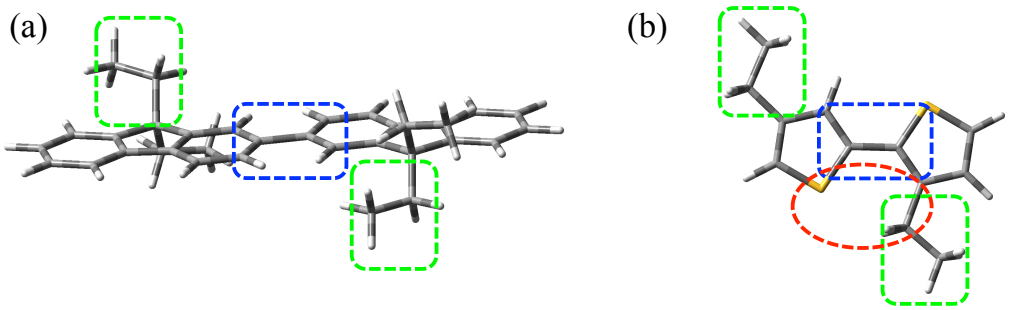

Figure 3.8: Schematic highlighting the difference in the location of the alkyl side-chains in 2mers of fluorene and thiophene. The blue area represents the location of the inter-monomer dihedral angle; the green the alkyl side-chain; and, in thiophene, the red area highlights the steric conflict involved.

fluorene 2mer is generally applicable to all backbone lengths and side-chain lengths.

In contrast to fluorene, including side-chains in thiophene (Figure 3.7(b)) has a considerable effect on the resulting dihedral profile. The inclusion of side-chains produces a large increase in the planar barriers, a decrease in the 90° barrier, and a shift in both minima towards 90°. It can also be seen that changes begin to reduce with increasing side-chains at around the C_3H_7 (propyl) side-chain length.

At a first glance, the large differences in the thiophene dihedral potentials with increasing side-chains seems to be the result of the large steric repulsion due to the close proximity of the side-chain to the dihedral. As illustrated in Figure 3.8, fluorene (Figure 3.8(a)) has side-chains much further from the centre of dihedral rotation than thiophene (Figure 3.8(b)). In thiophene, the key area of steric conflict involves the interaction of the first methylene (CH_2) group in the thiophene side-chain and the opposing sulphur (highlighted in the figure) and, in the 180° conformation (not shown in the figure), the opposing hydrogen. This difference in side-chain positioning means that the the steric and conjugated components of the dihedral rotation in thiophene cannot be decoupled so easily.

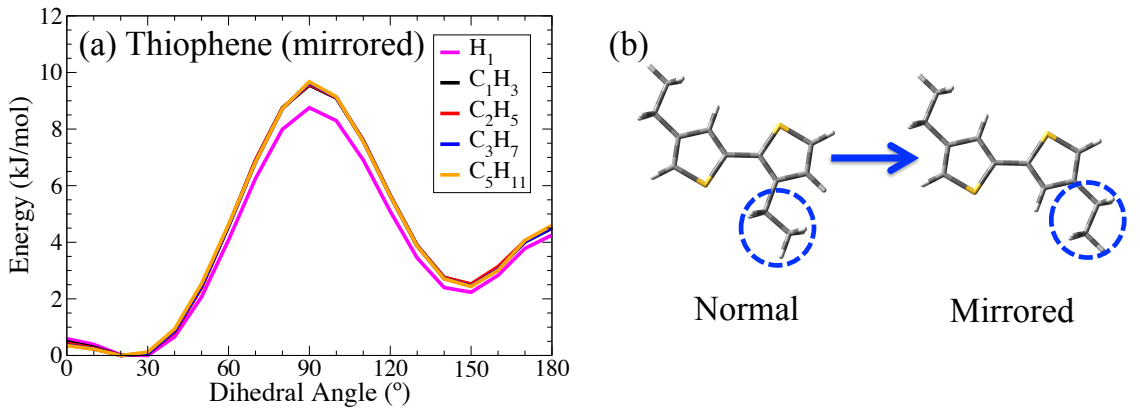

Figure 3.9: (a) Dihedral potentials of alkyl-thiophene 2mers in the 'mirrored' configuration with side-chains placed on opposing carbons. (b) Schematic comparison of the normal and mirrored thiophene 2mer configurations.

3.2.2 Nature of thiophene variations

While it is evident from Figure 3.7(b) that the side-chains have a considerable effect on the thiophene potential, it cannot be directly inferred what the full nature of the effect is. In order to further analyse its nature, we perform dihedral scans on a 'mirrored' thiophene 2mer. In the mirrored thiophene 2mer, the side-chain of one unit is moved from the 3 carbon to the 2 carbon (as shown in Figure 3.9(b)). In doing so, we effectively remove the steric contribution to the dihedral potential and analyse the conjugated orbital component. These depend on an approximation in which the effect of the side-chain on the orbital conjugation is assumed to be invariant to which of the carbons the side-chain is attached. We return to this point later in this subsection.

Figure 3.9(a) depicts the energetic profile of the mirrored thiophene 2mer. For this variant, the dihedral potential is only slightly modified by the presence of the side-chain by $\simeq 0.8\,\mathrm{kJ/mol}$ ($\simeq 0.3\,k_BT$) at the 90° barrier. This result strongly suggests that any variation in the dihedral energetics on account of the inclusion of side-chains is primarily governed by long-range, non-covalent interactions - particularly, the steric interactions shown in Figure 3.8(b).

The results of the mirrored case also support the case that conjugated orbitals are invariant to the inclusion of side-chains. As the side-chain in this scenario has little effect, it must be true that the only strong effect of the side-chain must be in its steric and dispersive contributions. This a key result as it implies, due to the inclusion of the steric and dispersive components in the force-field through the non-covalent potential terms (shown in Eq. 2.4 and discussed in Section 2.1.2), that the potential calculated for a thiophene 2mer is transferable with respect to the addition of alkyl side-chains. This transferability is explored in our discussions of dihedral potential implementation in Section 4.1.

For further insight into this feature and to our approximation, we have calculated

Table 3.1: S_0-S_1 absorption transition energies, ϵ_0, of thiophene 2mers in the three cases shown in Figure 3.10.

ϵ_0 (eV)	
None	4.563 eV
Normal	4.587 eV
Mirrored	4.543 eV

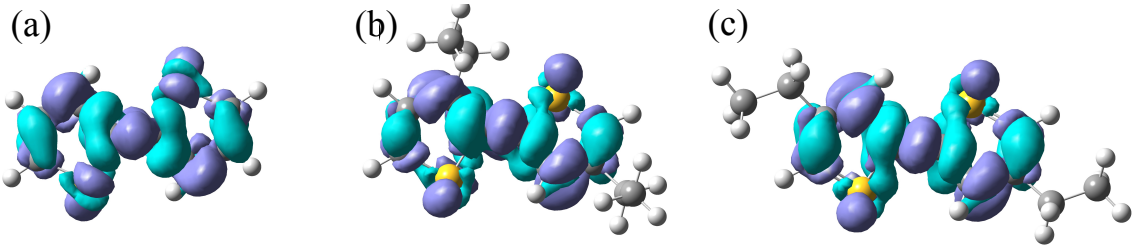

Figure 3.10: S_0-S_1 absorption differential densities of thiophene 2mers with (a) no side-chains, (b) 3-position side-chains (the normal case), and (c) 'mirrored' side-chains.

S_0-S_1 absorption differential densities (Figure 3.10) and energies (Table 3.1) for thiophene 2mers with no side-chains and with ethyl side-chains in the normal and mirrored configurations. Each calculation was performed at the CAM-B3LYP/cc-pVTZ level. Both the differential densities and energies suggest that there is very little effect on the excitations in all cases. This implies that the side-chains have little effect on the properties of the orbital conjugation along the backbone. Between the cases with side-chains and without, the transition energies differ by $\simeq 0.05\%$, and between the mirrored and normal side-chain cases, the difference is $\simeq 0.1\%$. It can be seen, also, from the differential densities that the electron density around the side-chains remains unchanged upon excitation; implying that the side-chains are not highly involved in the excitation. This is consistent with our previous discussion at the beginning of this section and a more complete discussion of this point in presented in Appendix C in the context of the results of Chapter 5.

3.2.3 Use of dispersion corrections

As mentioned previously, the dihedral potentials given so far in this chapter do not include any treatment of dispersive interactions. For cases without side-chains, this was because we found that including dispersion had no effect on the results and, for those with side-chains, inclusion of dispersion proves to yield difficulties in both computation and physical interpretation for sufficiently long chains.

For side-chains up to ethyl in length, it remains possible to obtain results using dispersion interactions. For short side-chains, the above considerations are not as applicable as the side-chains are, comparatively, less free. As such, using the dispersion correction GD3BJ [249, 250], we have calculated dihedral profiles for 2mers of

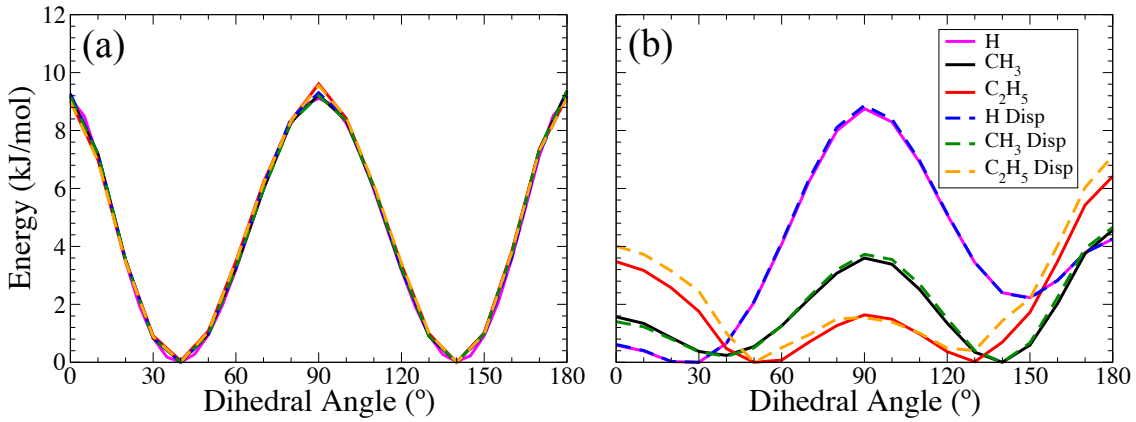

Figure 3.11: Dihedral potentials calculated using DFT with and without dispersion correction for 2mers of (a) fluorene, and (b) thiophene. For each molecule, the profile with no side-chains, with methyls, and with ethyls is given.

fluorene and thiophene up to ethyl in length and, in Figure 3.11, compared to those calculated with no dispersion correction.

As shown in Figure 3.11(a), the use of GD3BJ has no effect on the dihedral energetics of fluorene. This can be expected given the lack of a side-chain dependent component in the dihedral potential discussed above. For thiophene (Figure 3.11(b)), we find that, for 2mers with no side-chains and methyls, including dispersion interactions has, also, very little effect. With ethyls, dispersion interactions begin to play a role. Generally, there is a slight deviation in the energies at each point which, on average, is $\simeq 0.3\,\mathrm{kJ/mol}$. As with fluorene, this result is in line with the side-chain dependence of the dihedral potentials.

The potential obtained for ethyl-thiophene with dispersion is considerably less smooth than in the calculation without dispersion. This is a result of the freedom of the second carbon in the ethyl chain to adopt three minimal configurations. From the resulting geometries, the position of this carbon varies from point-to-point in the scan. The variation of the minimal state of this carbon cannot be consistently controlled by the initial conditions. This serves as an example of the inconsistency previously discussed which is only further amplified with increasing side-chain length. The only way of removing this inconsistency is to fix the position of the side-chain within the scan (as has been performed in references [93] and [140]). However, we feel it is counter-intuitive to do so as this procedure is, in essence, defining a preferential side-chain geometry which may not be preferential or especially significant in a dynamical run. However, it is clear that the ethyl side-chain profiles with and without dispersion are in good agreement and, as a result, our analysis in the previous section is justified.

The results of this section have explored the effect of the side-chains on the dihedral potentials of fluorene and thiophene and, in particular, the effect on the conjugated component of the potentials. In both cases, transferability can either be demonstrated immediately, as with fluorene, or inferred, as in thiophene. Following

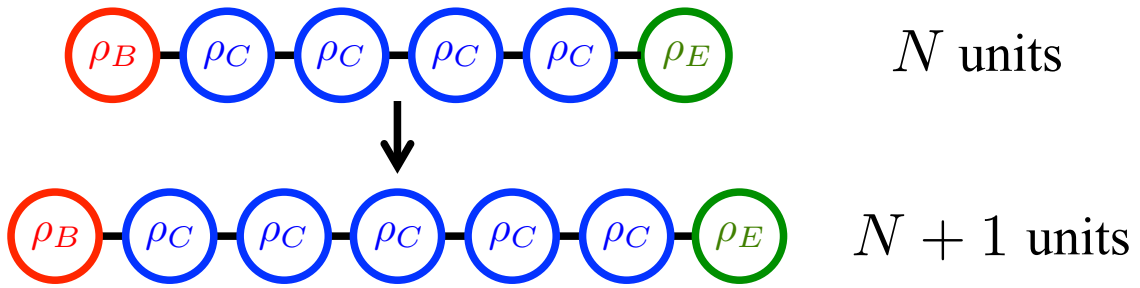

Figure 3.12: Sketch of a three residue model for a polymer system based on two end residues, ρ_E and ρ_B, and a general central residue ρ_C. For neutral molecules, the modelled molecule can be extended in length if and only if the sum of charges in ρ_C is zero. Note that, in this diagram, ρ_B and ρ_E do not necessarily span only one monomer unit.

the length invariance described in Section 3.1, the dihedral potential for fluorene of any backbone length and alkyl side-chain is appropriately modelled by that of a 2mer with no side-chains. It can be argued that this same transferability holds for thiophene though it is evident that the short separation between the side-chain and dihedral centre leads to increased complexity. We return to this point in Section 4.1. This concludes the calculations of dihedral potentials and leaves only partial charges to be obtained from QC calculations.

3.3 Obtaining partial charges for conjugated oligomers

In Section 2.1.2, we mentioned that any molecular force-field requires a set of partial charges which govern the pair-wise electrostatic interactions resulting from local pockets of electronic density. For individual molecules, these can be straightforwardly calculated using the population analysis procedures detailed in Section 2.3.4. As such, if one were to obtain partial charges for simulating a 2mer of fluorene and a 16mer of fluorene, a simple (excluding, for the time being, the computational demand) means of doing so would be to perform two SP energy calculations: one for the 2mer and one for the 16mer. This approach is often utilised in MD works of conjugated polymers [46, 132] which are only concerned with one length scale of molecule. If one goes on to consider different lengths of molecule, combinations of side-chains or multiple combinations thereof, this straightforward procedure quickly becomes infeasible.

Another approach is to define charge sets which, from biomolecular nomenclature [166], are known as ‘residues’. The natural choice of residue in the polymeric system is the set of charges corresponding to the base monomer. If one can define a set of residues which are invariant to either increasing length or to appending side-chains, one can build a wide variety of derivative molecules based on, in principle, one SP calculation.

For polymeric systems, it is typically assumed that one can build a model of

charges based on three residues: two sets, ρ_B and ρ_E, for the beginning and end unit, and one, ρ_C, for all central units. This model allows for various lengths of molecule to be generated, given the condition that both the total charge of ρ_C and the combined total charge of ρ_B and ρ_E are zero, by inserting additional ρ_C residues. This is shown schematically in Figure 3.12.

The manner in which residues are formed is not consistent in numerous other works. For example, Bhatta *et al* [140] form a similar model based on the charges of a single thiophene unit while Bockmann *et al* [47] form one based on a thiophene tetramer. However, it is not clear from either of these works whether their residues are converged with respect to molecule length and whether they can be suitably applied to thiophenes of up to 40mer and 32mer in length, respectively. As such, an investigation of the suitability of such models is required for a generalisable parameterisation scheme.

In the remainder of this section, we aim to determine a set of partial charges for a given molecule, based on a minimal quantum chemical calculation scheme, which correspond to any backbone length or alkyl side-chain combination. We utilise fluorenes, dioctyl-fluorenes, thiophenes, and hexyl-thiophenes as our test molecules for cases with no side-chains and cases with side-chains (the cases with side-chains chosen for correspondence with the common polymers PF8 and P3HT). In doing so, we assess the applicability of the three-residue model and detail a scheme for determining a converged set of partial charges.

3.3.1 Symmetry and length convergence of charge distributions

Before discussing our results regarding backbone length convergence, we first discuss how length convergence emerges from polymeric systems and the role of reflective symmetry on the charge distributions. This then allows us to determine a scheme by which to assess when a charge distribution is converged.

The first requirement of a three residue model is that the total charge of the residue ρ_C, denoted Q_C, is zero. Considering a homo-polymeric structure, such as that of fluorenes and thiophenes, of N units in length, the central $N-2$ units are identical but the two end-most units serve as boundaries and differ from the central units by an extra hydrogen atom. For sufficiently large N, such that the effect of the boundary units on the central units is effectively zero, the central units form a translationally invariant system. If we then consider an $N+1$ unit molecule, which has an additonal central unit, and note that both the N and $N+1$ unit system have a total charge of zero, it follows that the total charge of a central unit is zero. As such, the individual central units of a sufficiently long molecule will form the zero-charge ρ_C residues with ρ_B and ρ_E spanning some number of units at each end of the molecule. It follows then that determination of the total charges of the central units from a partial charge calculation is a means of determining a converged set of

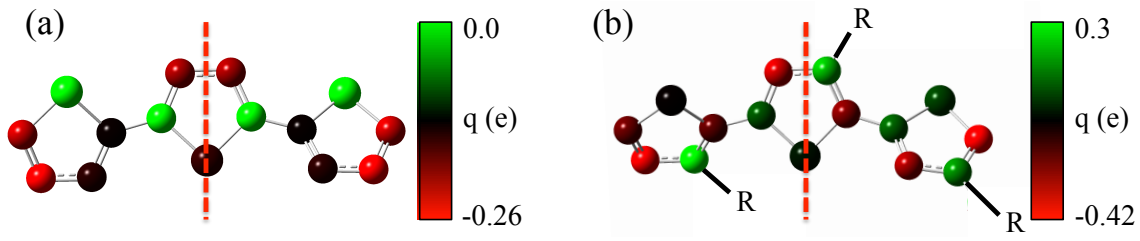

Figure 3.13: Partial charges, q, of 3mers of (a) thiophene and (b) hexyl-thiophene ($R = C_6H_{13}$). On each molecule, the axis of reflective symmetry is shown (red dashed line). In (b), this symmetry is broken as can be seen from the asymmetry of the charge distributions. Side-chains and hydrogens have been omitted for clarity.

partial charges.

With no side-chains present, the base units of oligo-fluorene and thiophene molecules are reflectively symmetric in the plane perpendicular to the axis of the molecule. With the intuitive notion of the partial charge sets obeying the symmetry of the molecule, the residue sets ρ_B and ρ_E are also reflective symmetric and each have a total charge of zero. Furthermore, given that the end-units differ only by an extra hydrogen, as opposed to another considerably bulkier or electronegative terminal group, it can also be expected that the span of ρ_B and ρ_E is small with respect to the overall size of the molecule.

In cases with side-chains, it is often the case that this reflective symmetry is broken. Of fluorenes, thiophenes, and their alkyl-substituted variants, this occurs when considering alkyl-thiophenes. While the overall translational symmetry of the middle units is preserved (as is always the case for a homo-polymer), that the side-chain is appended to the position 3 carbon (see Figure 3.6) means that the overall reflective symmetry between the ends of the molecule is broken.

This point is illustrated in Figure 3.13 which gives a representation of the charge distributions on the thiophene units of 3mers of thiophene and hexyl-thiophene. Comparing both distributions, it is evident that the symmetry is broken in the hexyl-thiophene 3mer and unbroken for thiophene. As discussed in the remainder of this section, the implication of this is that it is likely that this broken symmetry would induce an intrinsic dipole across the molecule. This then means that it can both be expected that the convergence of charge distributions would happen at longer molecular lengths and that the ρ_E and ρ_B groups would span a greater portion of the overall molecule.

3.3.2 Variations of charge distributions with backbone length

For each of our following calculations of partial charge distributions, we use electronic densities calculated with CAM-B3LYP/cc-pVTZ on geometries obtained with CAM-B3LYP/6-31G* in a manner akin to the method used for obtaining dihedral potentials. The calculated electronic densities are then fitted to partial charge dis-

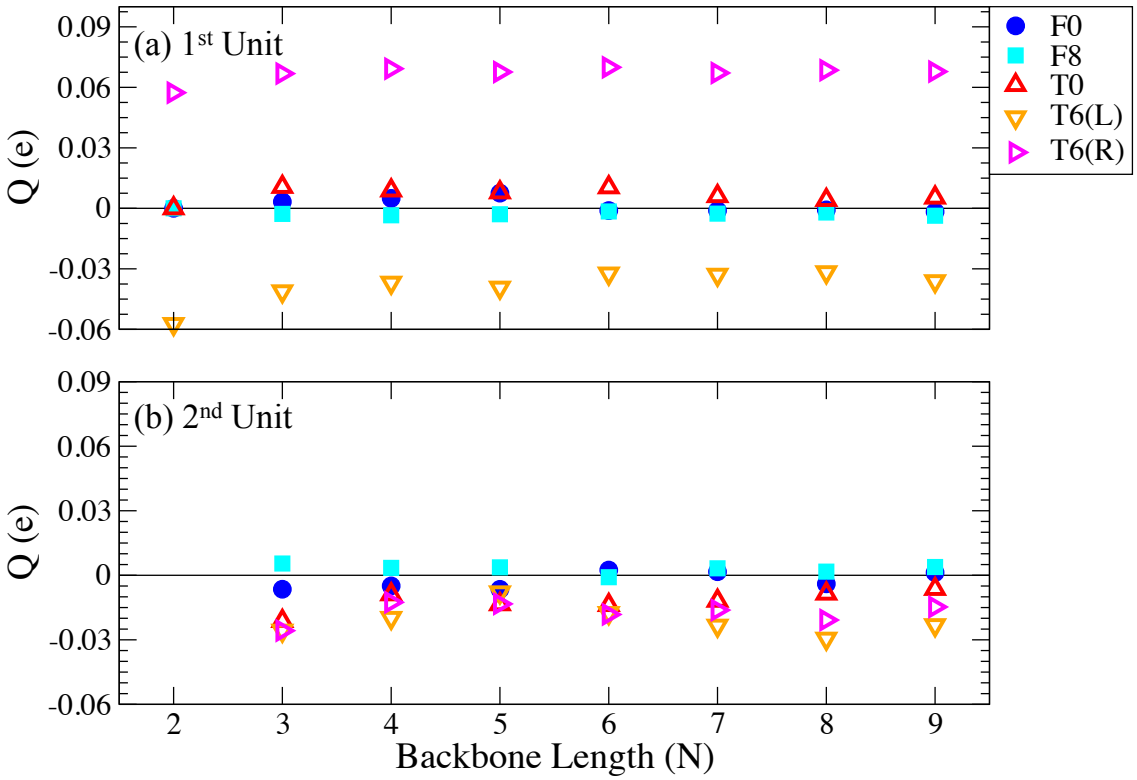

Figure 3.14: Total charges of (a) the 1st unit and (b) the 2nd unit of fluorene (F0), dioctyl-fluorene (F8), thiophene (T0), and hexyl-thiophene (T6) for varying lengths of conjugated backbone (given by the number of units, N). Due to the asymmetry, these values are plotted for both sides of the T6 molecule with the opposite side shown as T6(L) and T6(R). (Legend applies to both graphs.)

tribution using the RESP method (discussed in Chapter 2.3.4).

In observing the trend of the total charges of the first and second units of fluorene, dioctyl-fluorene, thiophene, and hexyl-thiophene, as shown in Figure 3.14, it is seen that the convergence of the total charges of the end units happens upon extending beyond the 3mer in all cases. For the symmetric molecules (both fluorene variants and thiophene without side-chains), the total charge of each of these units is effectively zero for all lengths of molecule as expected given that they are constrained to be zero in the 2mer by the symmetry considerations.

For hexyl-thiophene, the asymmetry of the molecule means that the total charges of the end units (Figure 3.14(a)) are substantial and there is a notable difference in the total charge between each end unit. The second units (Figure 3.14(b)) of hexyl-thiophene do not change appreciably beyond the 3mer (with std. deviations of $6.4 \times 10^{-3}\,e$ and $4.3 \times 10^{-3}\,e$ for the L and R units) but are significantly different from zero in charge on average (-0.017 e and 0.020 e, respectively) compared to the second units of the symmetric molecules. However, as opposed to the end units, the second units are of near-equal charge for all backbone lengths. This, along with the short convergence lengths across all molecules, suggests that the translational invariance begins for backbone lengths greater than the 3mer.

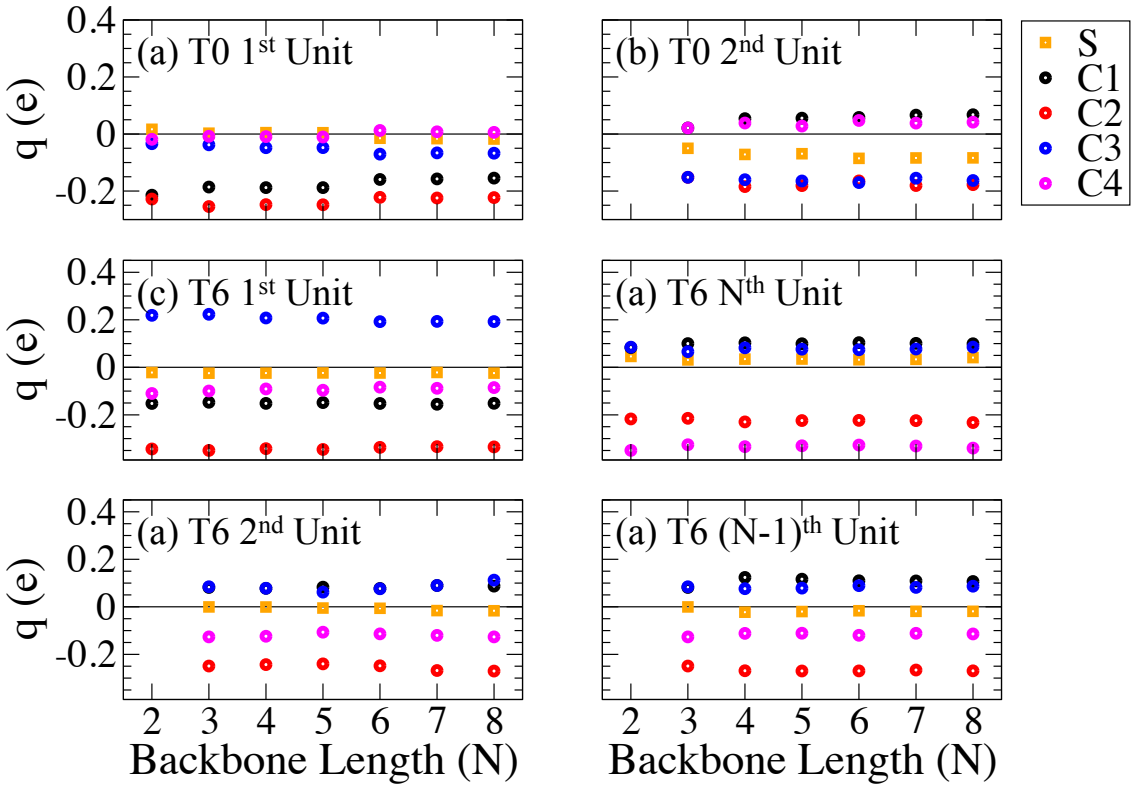

Figure 3.15: Partial charges, q, of the heavy atoms of (a) the 1st unit and (b) the 2nd unit of thiophene for varying lengths of conjugated backbone (given by N, the number of units). (c) and (d) are the partial charges of the heavy, non-side-chain atoms on the 1st unit from each end of hexyl-thiophene and (e) and (f) are those of the 2nd unit from each end. (Legend applies to all graphs.)

It is worth noting that, while there is a large charge difference in the hexyl-thiophene end units and second units relative to the other molecules, the charge difference is $\simeq$ 0.03-0.06 e. In the overall scheme of electrostatic effects, this difference is insignificant. However, charge differences on this scale are the result of large differences in the partial charge distributions within each unit. This can be seen from Figure 3.15, in which the length-dependence of the individual partial charges of each of the heavy atoms of thiophene end units and hexyl-thiophene end and second units is given. In each case, the charges are seen to be effectively constant across all lengths of backbone beyond the 3mer. However, in comparing the partial charges between different units and the two molecules, it can be seen that the distribution of the charges are significantly different. Also, the difference of the individual charges in the two end units of hexyl-thiophene is considerable compared to that of the two end units of thiophene and the two second units of hexyl-thiophene.

In all cases, it was found that the side-chains display similar behaviour to the main-units of the molecule except that the side-chain distributions are effectively constant for all lengths of molecule regardless of the symmetry considerations. A further breakdown of the partial charge distributions of all atoms (including side-chains) of each of the above molecules for a variety of lengths as well as the total

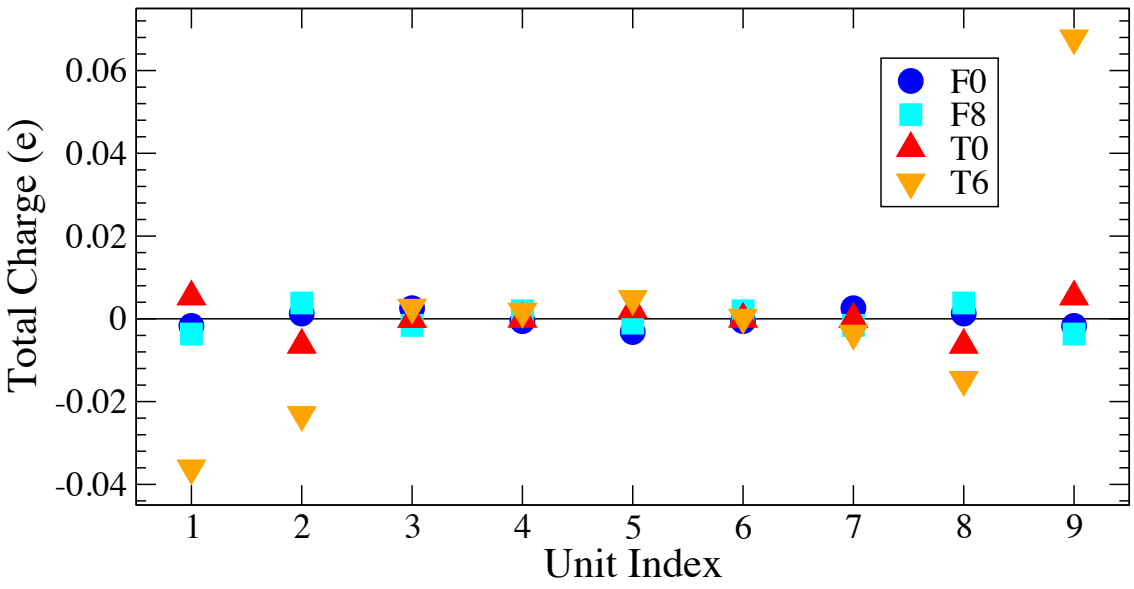

Figure 3.16: Total charges, Q, of individual units of 9mers of fluorene (F0), dioctyl-fluorene (F8), thiophene (T0), and hexyl-thiophene (T6). Molecular reflective symmetry is broken only in the hexyl-thiophene molecule. (Legend applies to both graphs.)

charge distributions for length of molecule up to 9mer can be found in Appendix A.

Figure 3.16 shows the total charges across each individual unit of 9mers of each molecule. Again, these follow the same trends described previously but also serve as confirmation of the translational invariance argument in that the central units of such a long molecule are of effectively zero total charge in both the symmetric and asymmetric cases. As discussed previously, the overall charge on the second units of hexyl-thiophene is converged beyond a 3mer. However, a 5mer is required to obtain a converged middle unit of zero total charge. As such, the distributions ρ_B and ρ_E span the two end-most units with ρ_C distribution obtained from above a 5mer. This is discussed further in Appendix A.

The convergence behaviour of the partial charge sets and its symmetry dependence form a central result of this chapter. Given the above, we determine that obtaining the three residues ρ_B, ρ_E, and ρ_C is possible by comparison of the total charges of the individual units between two lengths greater than, based on the cases considered, a 5mer. For more complicated systems e.g. with terminal units other than hydrogen or highly asymmetric systems, it follows that a fully converged set of residues would be obtained at greater lengths than those shown.

3.3.3 Attempts to obtain a fully extendable side-chain charge set

In a manner akin to the three-residue approach, we attempt to obtain a set of side-chain parameters which can be further extended to any length of side-chain. This would require determining a length of side-chain such that there exists a methylene CH_2 residue of total charge zero. This CH_2 group would then be inserted into

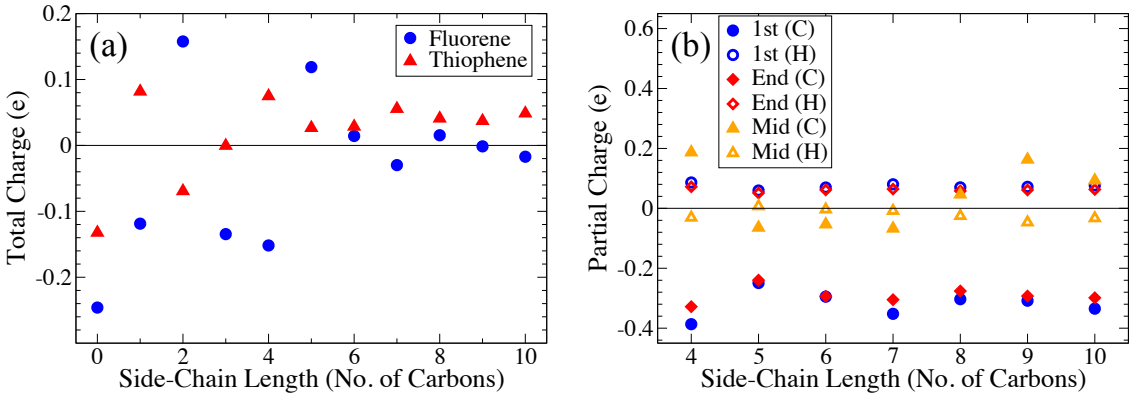

Figure 3.17: (a) Relationship of the total charge, excluding side-chains, of monomers of dialkyl-fluorenes and alkyl-thiophenes of various lengths of alkyl chain. Each display a convergence to near zero at around 6 carbons side-chain length. (b) Sample of partial charges on the C and H atoms at the beginning, middle, and end of the side-chain of alkyl-thiophene monomers of various lengths of side-chain. It is observed that, as opposed to the end groups, the charge of the carbon on the inner methylene group (gold triangles) does not converge with increased side-chain length.

the side-chain in order to extend the parameter set without modification of the remaining side-chain charges.

As a test of the possibility of this, we have computed the charge distributions of 1mers of dialkyl-fluorene (Fx) and alkyl-thiophene (Tx). Figure 3.17(a) depicts the progression of the total charge of each 1mer, excluding that of the side-chain, with increasing side-chain length. Both molecules appear to converge to total charge of $\simeq 0\ e$ and $\simeq 0.05\,e$ for the fluorenes and thiophenes, respectively, at side-chain lengths of 6 carbons.. As the total charge of the entire molecule is fixed, this implies that the overall charge of the side-chain is also converged to near-zero in both cases. As such, the three-residue principle may be applied.

It was found, however, that it is not possible to obtain a CH_2 group of zero charge for side-chain lengths of up to 12 carbons. Figure 3.17(b) gives, as an example, the charges of the carbons and hydrogens nearest to, farthest from, and half-way from the main-body of the monomer along the side-chain for increasing lengths of side-chain. While the nearest and farthest atoms display non-zero, converged charges across all lengths, it was found that the middle atoms still fluctuate greatly (from -0.05 - $0.2e$) with increasing side-chain length.

Given that large asymmetry is present between each end of the side-chain - one terminated with a hydrogen and the other terminated with the conjugated unit - and the arguments of the previous section, this lack of convergence is not surprising. Following from the previous arguments, it can be reasoned that the convergence of an individual CH_2 unit to a total charge of zero will be possible but for considerably longer side-chains than those considered. However, given that most experimentally and functionally interesting molecules rarely have side-chains greater than 12 carbons in length, we feel that this is not of practical use to our

parameterisation scheme.

To conclude this section, we have demonstrated that it is possible to build scalable charge sets for homo-polymers based on a three-residue model and have described a scheme by which to generate such sets based on partial charge calculations of two lengths of a given molecule. We find that the expected convergence length differs depending on whether or not the molecule has inversion symmetry - with the non-symmetric hexyl-thiophene molecule requiring a longer backbone length for convergence - and reason that molecules with greater degrees of asymmetry or large terminal groups may follow the same trend. While it is possible to obtain a fully-scalable set of charges for backbone length variations, side-chains can not be so simply treated due to the considerable asymmetry between the ends.

3.4 Conclusions

By exploring a number of different quantum chemical approaches, we have determined a DFT methodology for calculating dihedral potentials. We find that a combination of CAM-B3LYP/6-31G* optimised geometries with CAM-B3LYP/cc-pVTZ SP energies produces potentials which agree well with more computationally-demanding and complex methods such as L-MP2 and CBS limit CCSD(T). With this DFT methodology, we have explored the effect of increasing backbone lengths in dialkyl-fluorenes and alkyl-thiophenes and found that increasing backbone length has little effect in both molecules. In varying side-chain lengths, it was found that fluorene potentials are not affected. For thiophenes, the close-proximity of the side-chain and the centre of rotation was found to have a significant effect primarily as a result of steric repulsion.

We have also shown that, for both fluorenes and thiophenes, obtaining a three-residue set of charges is possible for short lengths of molecule. For fluorenes, dialkyl-fluorenes, and thiophenes, a three-residue set can be obtained using a 3mer while for alkyl-thiophenes, this approach requires a 5mer molecule. The difference in length scales between the former and latter is found to be the result of molecular asymmetry due to the presence of the alkyl side-chain on the thiophene unit. Similar convergence behaviour was not observed for the side-chains themselves at the lengths (up to 12 carbons) we investigated due to the considerable asymmetry between each end of the chain.

These results provide key insights into the generality of these key force-field parameters. As the partial charges are directly implemented into the force-field, building a three-residue model at the above length scales allows for a charge model which is scalable to all conjugated backbone lengths based on a relatively small calculation. The results obtained for the dihedral potentials imply that these potentials also display convergence behaviour in backbone length and side-chain. The first part of the following chapter details how this convergence translates to the force-

field regime and illustrates some of the subtleties involved in direct implementation of these calculated potentials.

Chapter 4

Force-field implementation and simulation of solvated molecules

The results of Chapter 3 have provided us with the foundational principles of a force-field parameterisation scheme for conjugated molecules. In particular, we have identified a suitable DFT methodology to obtain dihedral potentials and assessed the independence of said potentials to backbone length and side-chain length. The current chapter is comprised of two parts. First, we detail the implementation of dihedral potentials into the force-field using the subtraction procedure, detailed in Section 2.1.4, and determine the necessary refinements required in order to accurately replicate the DFT potentials. Secondly, we present MD simulations of fluorene and thiophene derivates in solution. We aim to assess the performance of our force-field with respect to measures such as dihedral angle distributions and persistence lengths. We also utilise simulations to better understand the nature of conformational properties of conjugated oligomers, the complex side-chain - solvent interactions, and how conjugation lengths emerge. These simulations form the foundations required for understanding optical phenomena and form the basis of the TD-DFT investigations detailed in Chapter 5.

4.1 Implementation and preliminary testing

The DFT calculations of Chapter 3 have provided accurate, quantitative representations of the dihedral potentials and partial charges in fluorene and thiophene and, by the same methodology, can be extended to other conjugated molecular systems. However, these results alone are not sufficient in and of themselves for use within the force-field. While partial charges are straightforward to implement, the calculated dihedral potentials are composites of a number of interactions - both covalent and non-covalent - which are already described in the force-field (such as those shown in the OPLS definition Eq. 2.4). It is therefore necessary to utilise a method of implementation which avoids double-counting these pre-existing terms.

There are numerous methods for implementing dihedral potentials in conjugated

force-fields. One which has been demonstrated successfully for conjugated molecules [132, 142, 143, 187] involves separating the contributions to the dihedral potential resulting from pre-existing terms in the force-field and generating a modified function based on the remaining contribution to the total potential. This method forms the basis of our 'subtraction' implementation procedure.

As described in Section 2.1.4, we begin by generating force terms for bonds, angles, and dispersion interactions using pre-existing values from the OPLS force-field. For both fluorene and thiophene, full sets exist for individual monomers while only fluorene has parameters for the bonds and angles around the inter-monomer junction. As they are lacking for oligo-thiophenes, the fluorene inter-monomer parameters are used for the thiophene inter-monomer junctions. The proper and improper dihedral terms are then generated for each molecule. In terms of covalently bound forces, this leaves only the four dihedral terms governing the intermonomer torsion.

In our implementation, we focus on 2mer molecules. As the force-field does not have significant contributions from long-range interactions of neighbouring monomers, we have found that the implementation for the 2mer is general to all backbone lengths. Furthermore, force-field energy minimisation for longer molecules generally requires further modifications due to the amplification of errors. By using a 2mer representation, we are required to use partial charges calculated from 2mers as opposed to three-residue models suitable for longer molecules.

In the remainder of this section, we begin by utilising the subtraction procedure to obtain dihedral potentials for fluorene and thiophene with no side-chains. When including side-chains, the close proximity of the side-chain dihedral results in problems regarding the transferability of dihedral potentials which we examine and discuss minor alterations to the OPLS force-field which allow for a better description of each of the fitted potentials. Throughout, we assess the suitability of each potential by obtaining minimal configurations of each 2mer so as to ensure that the true minima (resulting from unrestrained optimisation) are suitably accurate when compared to those obtained from DFT.

As a brief note on notation, in this section we utilise a variety of side-chains on each molecule. For clarity, we affix each of the fluorene and thiophene labels with C_x to denote side-chains of x carbons in length (e.g. C_2-thiophene denotes ethyl-thiophene and C_2-fluorene diethyl-fluorene) and fluorene and thiophene refer to unsubstituted molecules.

4.1.1 Force-field subtraction procedure

Following the scheme described in Section 2.1.4, the required force-field contribution to the dihedral potential is isolated by performing force-field scans over intervals of 10° from 0° to 180° in a manner analogous to that of the DFT scans performed in Chapter 3. Each point in the scan is initiated using the corresponding geometry

from the DFT scan calculation so as to ensure optimal correspondence between each geometry and, thus, comparability of the resulting energies. As the force-field minimisation is more sensitive to distortions in initial geometries than the DFT procedure, this measure is taken to provide greater consistency between the two procedures while also aiding the force-field minimisation in finding the correct minimum.

As we wish to isolate all interactions relevant in the dihedral rotation which are not the covalent interaction and also wish to restrain the dihedral at each value in the scan, the four covalent energetic functions at each inter-monomer juncture are free to be utilised as restraints. In order to generate an effective restraint at a given angle, ϕ_0, each of the four dihedral terms are placed under the influence of a periodic potential, V_R, given by:

$$V_R(\phi) = k_c[1 - \cos(\phi - \phi_0)]. \tag{4.1}$$

While we have found it to be sufficient to impose only two restraints on the corresponding DFT scans, we find that it is necessary to impose restraints on all four dihedral terms in the FF scan. Failure to do so results in significant deviations in the free dihedral terms ($\pm$ 5°). Deviations of this scale result in poor comparability between the force-field and DFT scans and lead to ill-fitted potentials. In turn, this leads to inconsistency between the subtraction profiles and resulting unrestrained optimisations and simulations.

In choosing the value of k_c for the periodic restraint, care must be taken so as to find a balance between forming an effective restraint without inducing any unwanted distortion in the molecule. We obtained values of k_c by a trial and error procedure of maximising k_c, for optimal correspondence of the final dihedral angle with the target dihedral angle, without risking distortions of the given molecule. For molecules with methyl or no side-chains, the choice of a large value, $k_c = 5 \times 10^4$ kJ/mol, provides a suitable restraint with very low error in the resulting dihedral values ($\pm \sim 0.25°$). In the case of ethyl-thiophene, a significant reduction to $k_c = 10^3$ kJ/mol is necessary which can be attributed to the prevalence of large forces in the side-chain - dihedral area. This reduction results in an increased error in the dihedral values ($\pm \sim 1°$) though this error is still within an acceptable tolerance. From this, the geometry is then optimised in vacuum using the conjugate-gradients minimisation algorithm within Gromacs and the total energy of each point along the scan is calculated to form the corresponding profile.

With the force-field (FF) contribution to the dihedral potential isolated, the required dihedral profile is obtained by subtracting the FF contribution from the DFT potential. The resulting 'subtracted' potential is then fitted to a 5th order

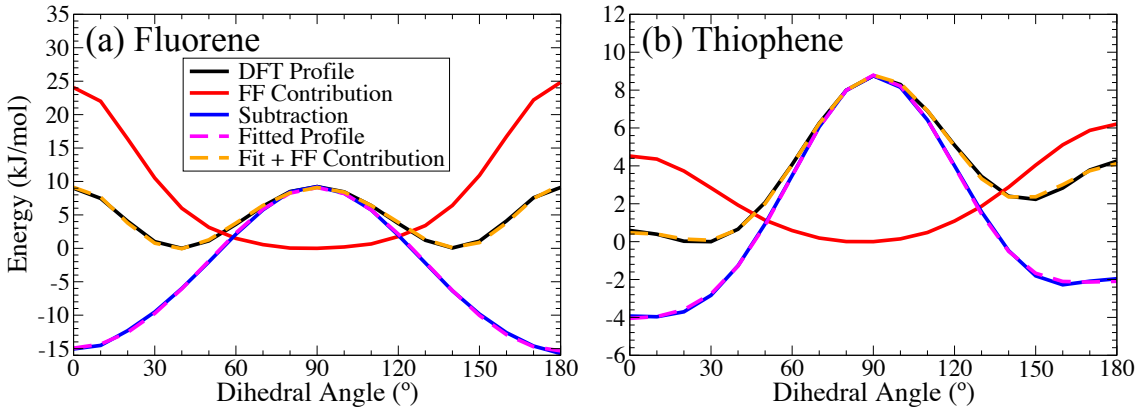

Figure 4.1: Subtraction potentials for (a) fluorene and (b) thiophene. Each figure displays the calculated DFT potential; the FF contribution; the resulting subtracted potential; the fit of the subtracted potential to a 5th order Ryckaert-Bellmans function; and the resulting effective potential given by the addition of the FF scan potential and the fitted potential. (Legend in (a) applies to both graphs.)

Ryckaert-Bellmans (RB) function:

$$V_{RB}(\phi) = \sum_{n=0}^{5} c_n [\cos(\phi)]^n. \tag{4.2}$$

In Figure 4.1, the subtraction curves and fits are shown for 2mers of fluorene and thiophene. In both cases, the fit from the RB function is accurate and the combined fit and FF contribution of each closely resembles the corresponding DFT potential.

To implement the fitted potential, we divide the potential across each of the four available four-atom dihedrals at the inter-monomer junction. This is shown schematically in Figure 4.2. As can be seen, two of the four dihedrals are in the same convention as the fitted potential (the polymer convention) with the *trans* angle set to 0° while the other two are in the *trans* = 180° convention. Given that $\cos(\phi + \pi) = -\cos(\phi)$, the potential for the latter two is expressed with alternating positive and negative coefficients as is shown.

With the potential in place in the 2mer FF, a first test is to determine the correspondence between the minima obtained from free optimisation in the FF and using DFT. For each 2mer, we have calculated the difference in energy, $\Delta E_m = E_{cis} - E_{trans}$, between the *cis* and *trans* minima of each molecule using both methods. As is shown in Table 4.1, in both cases without side-chains, the FF and DFT values are comparable to within $\simeq 0.1\,\mathrm{kJ/mol}$ ($\simeq 0.04\,k_BT$). This test demonstrates both the accuracy of the correspondence found by the fitting procedure as well as the ability of the fitted force-field to reproduce the quantum chemical minima in these examples. This point is discussed further in Section 4.1.3.

For both fluorene and thiophene, we see that this procedure is fairly straightforward and yields both accurate fits to the subtraction potentials and provides an accurate representation of the *cis* and *trans* optimal geometries. This correspon-

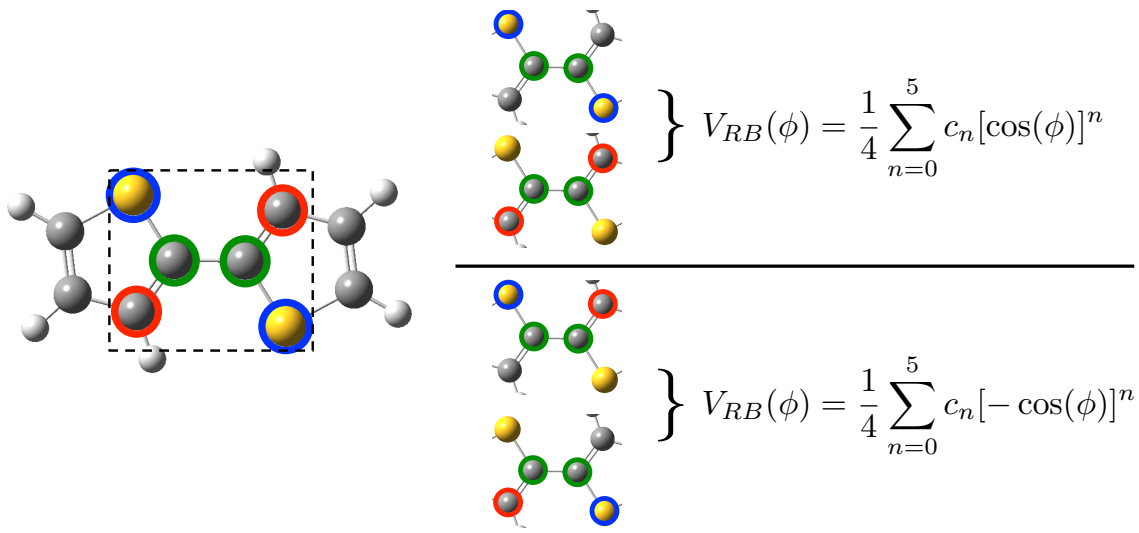

Figure 4.2: Schematic depicting the four dihedral terms at a thiophene junction and the sign convention of the RB function (Eq. 4.2) associated with it. For fluorene, this convention is followed analogously.

Table 4.1: Comparison of the difference in energy between the *cis* and *trans* minima, ΔE_m, of 2mers of fluorene, C_1-fluorene, thiophene, and C_2-thiophene calculated from DFT and from the force-field (FF).

	ΔE_m (kJ/mol)	
	DFT	FF
fluorene	0.04	0.08
C_1-fluorene	-0.05	0.05
thiophene	2.23	2.09
C_2-thiophene	0.84	0.86

dence was enhanced in both cases by modifying the equilibrium bond lengths and angles of the OPLS force-field which we shall discuss in greater detail in Section 4.1.3. For now, we proceed to apply the same procedure to fluorenes and thiophenes with side-chains.

4.1.2 Force-field subtraction with side-chains

As was the case with obtaining DFT potentials in Section 3.2, obtaining FF potentials for molecules with side-chains results in significant complications. In the particular case of thiophene, which has side-chains close to the intermonomer junction, optimisation procedures are complicated by the additional steric contributions and relative freedom of the side-chains. While we have found that differences in the dihedral potentials of thiophene resulting from the side-chains are almost entirely the result of steric contributions, which would be expected to be represented by the force-field already, it is imperative to properly examine whether this implied transferability of the potential holds.

In the first instance, we consider fluorenes with side-chains. Testing the C_1-

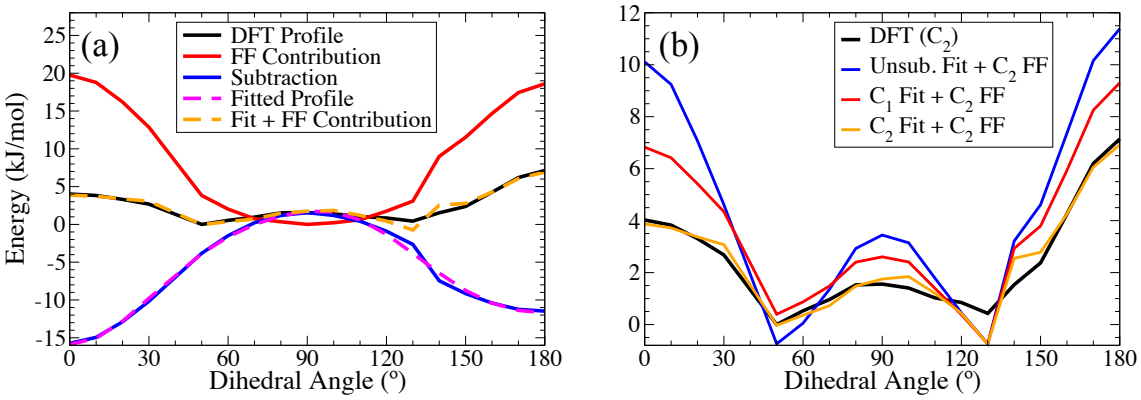

Figure 4.3: (a) Subtraction potentials for C_2-thiophene. (Labelling follows that of Figure 4.1.) (b) Total force-field potentials for C_2-thiophene comprised of the sum of the C_2-thiophene FF contribution and subtraction potentials fitted from unsubstituted (unsub.) thiophene, C_1-thiophene, and C_2-thiophene. Comparison is given to the C_2-thiophene dihedral potential.

fluorene 2mer, we found that the dihedral potential resulting from the scan is effectively identical to that of fluorene. As is seen in Table 4.1, values of ΔE_m obtained from minimisations of C_1-fluorene are in agreement with the DFT values to within 0.1 kJ/mol. Performing the same test with C_2-fluorene also showed the same behaviour. This follows as would be expected from the invariance found in performing the DFT calculations and shows that the fluorene dihedral potential is transferable to the full class of dialkyl-fluorene molecules.

For thiophenes, we have performed the subtraction procedure for C_1 and C_2-thiophene with the resulting curves for C_2-thiophene shown in Figure 4.3(a). It is noted that this procedure results in a far less smooth fit than that of thiophene shown in Figure 4.1(b). This behaviour is an example of the inconsistency in a geometry optimisation scheme which comes from the freedom of the side-chains and is amplified as side-chain length is increased. To minimise this inconsistency, taking the initial scan geometries from the DFT calculations is of particular importance. This being said, it is not the case that this measure leads to a perfect correspondence in the side-chain conformations between the DFT and FF scans. While the error in the fitting procedure impacts the direct comparison of the fit with the DFT potential, in calculating ΔE_m of the C_2-thiophene 2mer (Table 4.1), we find agreement between the DFT and our FF fit to within $\simeq 0.1$ kJ/mol.

In Section 3.1, we argued that steric interactions, responsible for large changes in dihedral potential for alkyl-thiophenes, will be incorporated by the force-field and, thus, the potential fitted from thiophene should be transferable in the same manner as with fluorene. However, the FF potential obtained from C_2-thiophene differs drastically from that obtained from thiophene. In Figure 4.3(b), we show the effective FF potential resulting from the FF contribution of C_2-thiophene and utilising the potential fit from unsubstituted and C_1-thiophene. In comparison to

Table 4.2: Energetic barriers at 0° (ΔE_0) and 180° (ΔE_{180}) of thiophene 2mers with various side-chains using fitted potentials obtained from scans using different side-chain lengths. The labels C_x (C_y) denote the energies of a 2mer with a side-chain of x carbons using the potential obtained from a fit of the 2mer with a y carbon side-chain with 'unsub.' denoting the unsubstituted case. The DFT values shown are those from the dihedral scans of the C_x-thiophene 2mer. Each barrier is calculated relative to the closest local minimum (i.e. the *trans* minimum for ΔE_0 and the *cis* minimum for ΔE_{180}).

	ΔE_0 (kJ/mol)		ΔE_{180} (kJ/mol)	
	DFT	FF	DFT	FF
unsub. (unsub.)	0.59	0.33	2.02	1.75
C_1 (unsub.)	1.20	5.35	4.65	7.21
C_1 (C_1)	1.20	1.33	4.65	5.00
C_2 (unsub.)	4.02	11.07	6.71	12.00
C_2 (C_1)	4.02	6.67	6.71	9.18
C_2 (C_2)	4.02	3.90	6.71	7.66

the expected DFT potential, we see that the assumption of transferability leads to a significant overestimation of the planar energetic barriers. Quantitatively, by defining the difference in energy between each unrestrained minimal configuration and their nearest planar configurations, defined as ΔE_0 and ΔE_{180} for the *trans* and *cis* sides respectively, we find that the error introduced in the planar barriers of C_2-thiophene from utilising the C_1-thiophene potential can be as large as $\simeq 2.5\,\mathrm{kJ/mol}$ ($\simeq k_BT$). Using the unsubstituted thiophene potential, this error increases approximately two-fold. These energies are summarised in Table 4.2. This is one of the key results of this chapter as it highlights that one cannot assume that the FF dihedral potential is transferable purely from the argument that the conjugated component of the dihedral potential is transferable (as was shown in Section 3.2.2).

One possible reason that the transferability of the dihedral potential with respect to increasing side-chain length in thiophenes implied by the DFT calculations does not hold is due to the use of the Lennard-Jones 12-6 potential in the OPLS force-field. Dubay *et al* [93], have shown that the OPLS force-field produces an overstatement of the planar barriers in C_2-thiophene and highlighted that this may be remedied, in part, by utilising a buffered 14-7 potential [173]. It may be the case that using such a potential may replicate the expected behaviour and signifies that an entirely generic force-field for conjugated polymers (e.g. one built of interchangeable conjugated moieties such as amino acids in current protein force-fields) may require such a modification. However, as it currently stands, we have shown that careful consideration of the thiophene side-chain by performing subtraction with the ethyl side-chain leads to an appropriate force-field representation of the dihedral potential without any modification to the Lennard-Jones definitions of the OPLS force-field.

Given the inconsistency observed in the C_2-thiophene fitted potential resulting from the side-chain degrees of freedom, performing similar calculations for longer side-chains becomes impractical due to increasingly noisy fits. However, as shown in Figure 3.7(b), the difference in DFT dihedral potential between C_2 and C_3-thiophene is $\simeq 0.5\,\mathrm{kJ/mol}$ ($0.2\,k_BT$) at the planar barriers which is slight compared to those between C_2 and C_1, and C_1 and the unsubstituted case. As such, we feel it is justified that the C_2-thiophene potential be used as a general potential for longer lengths of side-chain.

We have found that the subtraction procedure is capable of reproducing the expected form of the dihedral potential and respective energetic minima even for the complicated C_2-thiophene 2mer. To conclude this section, we now discuss how we modify equilibrium bond lengths and angles in order to further enhance the correspondence obtained from the subtraction procedure.

4.1.3 Modification of equilibrium bonds lengths and angles

Throughout our previous discussions of implementation by subtraction, we have utilised modified OPLS equilibrium bond lengths and angles. The first motivation for this procedure is that, while there exist parameters which govern the energetics of many individual conjugated units within the OPLS force-field, it is often necessary to essentially 'borrow' parameters for the inter-monomer junction from other conjugated molecules e.g. from fluorene for thiophene. We borrow parameters by taking the force-constants associated with the intermonomer bond and angles and modifying the equilibrium values to better represent the host molecule. However, a secondary motivation is to obtain the best possible correspondence between the geometries obtained from the force-field and from DFT. In this regard, we obtained the best results when replacing all of the available bond length and angle equilibrium values across each molecule with those obtained from DFT optimisations while keeping the original OPLS force-constants.

Equilibrium values are taken from the global minimal geometries obtained from optimisation with CAM-B3LYP/6-31G*. Table 4.3 contains a breakdown of these changes on: the energy difference between the dihedral minima, ΔE_m; the values of each dihedral minimum, $\phi_{trans,cis}$; and the end-to-end length of each minimal geometry, $l_{EE,trans,cis}$. For each molecule, we find there is either a general improvement or changes which are negligible ($\simeq 0.1\,\mathrm{kJ/mol}$, 1°, 0.1 Å in each value).

For fluorenes, we find that the only substantial improvement is in the location of ϕ_{cis} of unsubstituted fluorene in which the error reduces from 6° to 1°. In all other respects, both the original and modified parameters result in values which correspond to within acceptable tolerances of the DFT values. For thiophenes, modifying the the equilibrium values yields substantial improvements. For unsubstituted thiophene, the major improvement is in reducing the error in ΔE_m from $0.47\,\mathrm{kJ/mol}$ to

Table 4.3: Comparison of the un-modified and modified OPLS force-fields (MD_0 and MD_1 respectively) with DFT calculations for 2mers of fluorene, C_1-fluorene, thiophene, and C_2-thiophene. The properties compared are: the difference in energy between the *cis* and *trans* minima (ΔE_m); the dihedral angle of each minimum (ϕ); and the end-end length associated with each minimum (l_{EE}).

	ΔE_m (kJ/mol)			ϕ_{trans} (°)			ϕ_{cis} (°)		
	DFT	MD_0	MD_1	DFT	MD_0	MD_1	DFT	MD_0	MD_1
fluorene	0.04	0.0	0.08	39	39	40	141	135	140
C_1-fluorene	-0.05	0.03	0.04	39	41	38	141	139	142
thiophene	2.23	1.76	2.09	26	31	28	147	145	145
C_2-thiophene	0.84	1.43	0.86	45	20	50	129	129	135

	$l_{EE,trans}$ (Å)			$l_{EE,cis}$ (Å)		
	DFT	MD_0	MD_1	DFT	MD_0	MD_1
fluorene	15.3	15.2	15.4	15.1	15.0	15.2
C_1-fluorene	15.3	15.2	15.4	15.1	15.0	15.2
thiophene	6.4	6.4	6.4	6.3	6.3	6.3
C_2-thiophene	6.4	6.5	6.4	6.3	6.5	6.3

0.14 kJ/mol while also slightly improving the minimal dihedral angles. Further improvement is seen for C_2-thiophene in which the original fit yields an error in ϕ_{trans} of 25° which is reduced to 5° after modification. The value of ΔE_M also corresponds almost exactly to the DFT prediction with the modified force-field as opposed to the 0.61 kJ/mol difference seen with the original. While both dihedral minima in C_2-thiophene deviate from their DFT values by around 5°, the modified force-field results in consistency between the two. On the whole, the improvements made in C_2-thiophene are substantial and the energetic improvement significantly impacts the resulting dynamics shown throughout the subsequent sections of this chapter.

As a brief note, while this procedure is beneficial to the fluorene and thiophene force-field description, in which OPLS parameters are readily available for the individual monomers, it may also be the case that a similar procedure may have merit in monomers which have missing parameters or only have van der Waals parameters readily available. Indeed, one similar procedure has been employed by Guilbert *et al* [141] in parameterising the benzothiadiazole (BT) moiety. This procedure, dubbed the modified Badger rule, determines bond and angle force constants based on DFT optimisations of the monomers. We have considered utilising such a procedure both for comparison with the values obtained for thiophenes and fluorenes as well as for future parameterisation work e.g. for molecules such as PTB7 whose core units are not currently well represented within the OPLS force-field. However, due to its success in reducing the large errors in the thiophene geometries, particularly C_2-thiophene, we have followed our modified approach in all of our force-field parameterisation.

In this section, we have set out a scheme for implementing DFT calculated

dihedral potentials into the wider OPLS force-field and have shown its capability in formulating correspondence between the FF and DFT potentials. Additionally, we have also noted the complications which arise for molecules with side-chains close to the dihedral centres and how their treatment can be incorporated into the procedure. Built upon this implementation, the remainder of this chapter concerns the discussion of simulations of fluorenes and thiophenes in solution.

4.2 Simulations of short molecules

In the previous section, we have shown that our force-field is capable of representing the DFT dihedral potentials based on optimisations of static geometries. Full validation of the force-field requires extending and examining its applicability to the MD regime. The simplest manner of doing so is first simulating 2mer molecules. In particular, 2mers without side-chains offer a key point of verification given the basic, effectively unperturbed dependence of the dihedral angle on its core dihedral potential i.e. without any external influence from side-chains. As such, it is possible to measure the correspondence between the dynamics of the force-field and a simple Boltzmann distribution obtained from the corresponding DFT potential.

Simulations of 2mers serve two key purposes: first, they form a partial force-field validation which is completed by simulations of longer molecules; secondly, they can be utilised to probe effects such as the interactions between solvents and side-chains and the relationship between the inter-monomer bond angle and dihedral angle. Both of these points serve as foundations for interpreting the conformational dynamics of longer molecules.

4.2.1 Molecules with no side-chains

With a 2mer system in mind, but without any loss of generality, we can describe the potential energy of the system, U, as a function of the dihedral angle, ϕ, and the set of all other degrees of freedom, $\mathbf{x}$, in the form:

$$U(\phi, \mathbf{x}) = u_\phi(\phi) + u_{\mathbf{x}}(\mathbf{x}) + u_m(\phi, \mathbf{x}). \tag{4.3}$$

This expression effectively separates the general potential energy into component functions: u_ϕ and $u_{\mathbf{x}}$ being the contributions to the potential which are dependent only on ϕ or the remaining degrees of freedom independently of ϕ, respectively; and u_m which corresponds to all interactions which are dependent on correlations between ϕ and $\mathbf{x}$. As such, the probability density for ϕ is expressed as:

$$P(\phi) = \frac{1}{Z} \int d\mathbf{x} \exp\{-[u_\phi(\phi) + u_{\mathbf{x}}(\mathbf{x}) + u_m(\phi, \mathbf{x})]/k_B T\}, \tag{4.4}$$

with Z defined as the partition function of the system. If the dihedral degree of freedom is effectively independent of the other degrees of freedom, i.e. $u_m(\phi, \mathbf{x}) \approx 0$,

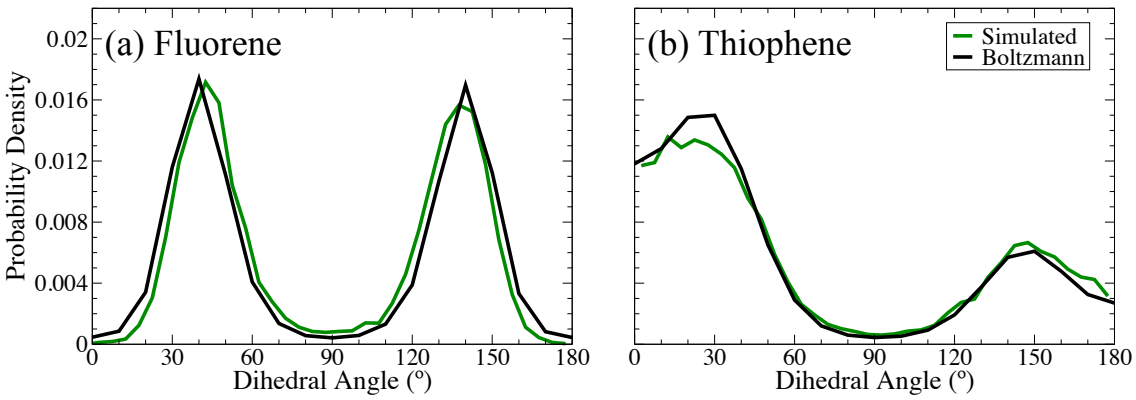

Figure 4.4: Dihedral angle distributions for (a) fluorene and (b) thiophene 2mers obtained from MD simulation in chloroform. Comparison is made to Boltzmann distributions calculated directly from the corresponding DFT potentials. Simulations were carried out over 100 ns and 10001 geometries were sampled.

Eq. 4.4 reduces to:

$$P(\phi) \approx \frac{1}{Z}\int d\mathbf{x}\exp(-u_{\mathbf{x}}(\mathbf{x})/k_BT)\exp(-u_\phi(\phi)/RT) = \frac{1}{Z_\phi}\exp(-u_\phi(\phi)/k_BT), \tag{4.5}$$

with Z_ϕ defined as the component of the partition function over ϕ:

$$Z_\phi = \int \exp(-u_\phi(\phi)/k_BT). \tag{4.6}$$

Evidently, in a system where the dihedral rotation is effectively independent of contributions from the other degrees of freedom, the probability density is that of an effectively isolated rotation governed entirely by a single potential. In systems such as fluorene and thiophene, which, when excluding side-chains, essentially consist of two rigid planes rotating about an axis, it would be expected that the contribution from $u_m(\phi, \mathbf{x})$ would be negligible and that the dihedral angle probability density would resemble that given by Eq. 4.5. This allows for a simulation-based, first verification of the parameter sets based on the correspondence of the dihedral angle distributions resulting from MD simulation and the Boltzmann distributions predicted by the DFT calculations.

In Figure 4.4, dihedral angle distributions obtained from MD simulations of fluorene and thiophene (each with no side-chains) in chloroform are shown with comparison to their respective Boltzmann distributions. In both cases, the MD distribution strongly resembles the predicted Boltzmann distribution. As such, building on the correspondence obtained from optimised geometries and scans in Section 4.1, this result confirms that the force-field implementation procedure leads to accurate thermodynamics in an MD simulation.

The MD distribution discussed above is from simulation in chloroform though

the same conclusion holds regardless of the solvent chosen. The same calculations performed in the solvents THF, toluene, methanol, and water are discussed in Appendix B.2 and show solvent independence in the fluorene and thiophene systems. Given that the solvent dependence of conformational properties is most prominent in systems with a large state space i.e. with a large number of possible, distinct configurations and, thus, possibility for greater conformational entropy, a small system such as either of the fluorene and thiophene 2mers should not exhibit any strong solvent dependence. In considerably longer systems and systems with side-chains, solvent effects often become significant and will be discussed in the following sections.

4.2.2 Solvent-dependent dynamics with the inclusion of side-chains.

The result of the previous section shows both that the implemented dihedral potential accurately represents the dihedral dynamics in 2mers with no side-chains and also that these dynamics follow a Boltzmann distribution of the corresponding potential. We omitted the inclusion of side-chains to offer a simplified picture and, thus, a first *in situ* test of our parameterisation scheme. To include side-chains in our simulations allows us to take a step towards practically realistic simulations. Particularly, the complex behaviour of long side-chains - highly-entropic appendages to the basic conjugated molecule - and their interplay with the solvent form a significant motivation for utilising MD simulations given that dynamical simulation is capable of capturing the, primarily thermodynamic, features of solvent behaviour which cannot be captured by static calculations alone. As we expect a significant amount of solvent - side-chain interaction, we investigate the role of combinations of each in 2mers. This allows us to obtain the basic dynamical principles which occur at the core of conjugated molecular dynamics i.e. below the level of effects resulting from highly-disordered oligomer or polymer systems.

As a practical motivation of this investigation, one particularly interesting feature of polyfluorenes, as discussed previously in Section 1.1, is the formation of β-phase regions characterised by highly planarised regions and a corresponding sharp, red-shifted absorption peak at $\simeq 2.8\,\text{eV}$ ($\simeq 440\,\text{nm}$). This phase, which typically occurs in systems exhibiting aggregation [52, 99, 100] - which, in turn, involves solvent dependent behaviour - has also been shown to depend on the length of side-chain. Bright *et al* have shown experimentally that the formation and stability of the β-phase is a function of two competing side-chain dependent features: significantly long side-chains such that side-chain - side-chain interactions can overcome the high energetic barriers otherwise blocking the planar fluorene conformations; and the increased entropic freedom and, therefore, instability resulting from long side-chains. As such, they find that heptyl and octyl side-chains typically afford the greatest β-phase fractions [100]. In the work of Kitts *et al*, β-phase was shown in experiment to have a clear dependence on the quality of solvent used and, in turn, confirms the

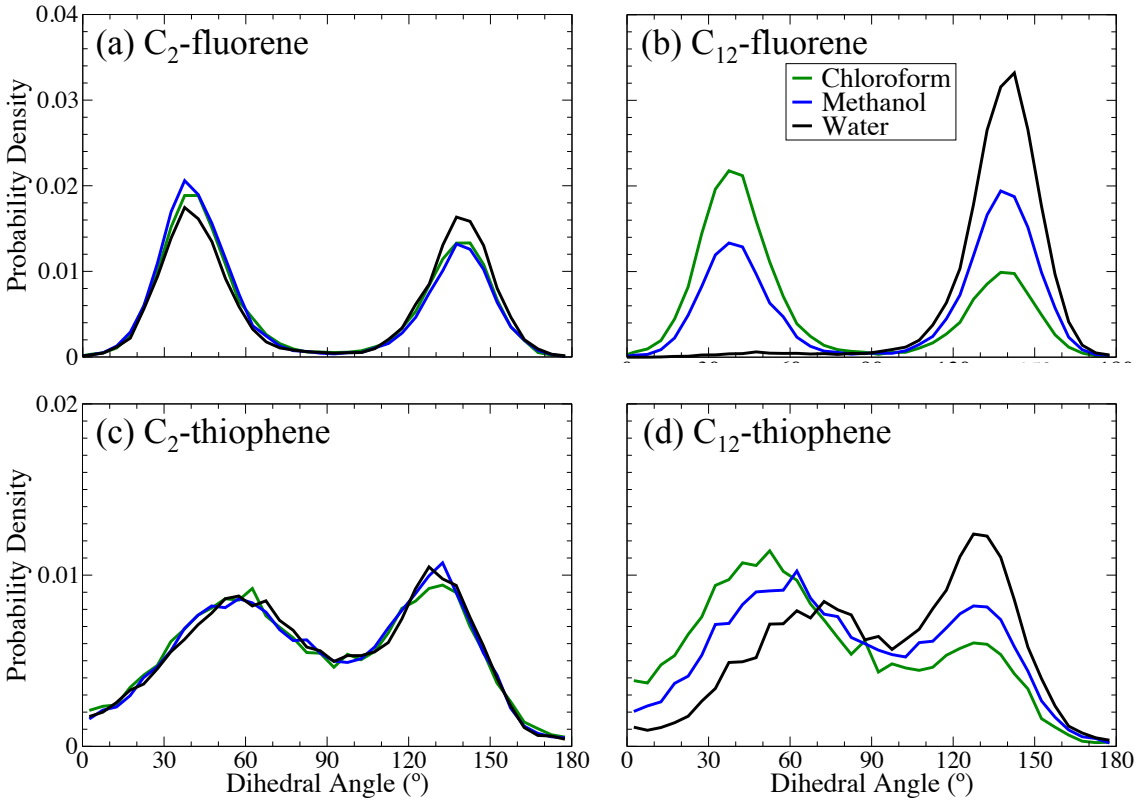

Figure 4.5: Dihedral angle distributions for (a) C_2-fluorene, (b) C_{12}-fluorene, (c) C_2-thiophene, and (d) C_{12}-thiophene. Distributions are shown for simulations in chloroform, methanol, and water.

work of Knaapila *et al* in showing, by experiment, that β-phase results from collapsed 'sheets' of polyfluorenes [52, 99]. While it is clear that the solvent-dependent emergence of β-phase arises from the solvent's effect on aggregation, the side-chain dependent dynamics should, at the small molecule level, show how the side-chains enhance this process.

To probe the interactions of side-chains with the chosen solvent, we have performed a number of simulations on 2mers of both fluorene and thiophene in a variety of solvents and with various lengths of side-chain. The solvents chosen are THF, chloroform, toluene, methanol and water. Full details of the solvent parameters used are given in Section 2.2.4. Of the five chosen, THF, chloroform, and toluene are typically 'good' solvents for conjugated polymers and are widely used in sample processing. Methanol is typically a poorer solvent than the above while still being practically capable of solvating polymer systems. Water is chosen as an exemplar poor solvent and, given that conjugated polymers are typically insoluble in water, provides extreme example of the effect of solvent choice on the molecular dynamics.

In Figure 4.5, the dihedral distributions for 2mers of C_2- and C_{12}-fluorene and C_2- and C_{12}-thiophene are shown for the solvents of chloroform, methanol, and water. Each of these examples represents a particular extreme of side-chain and solvent combinations given the relative solubilising properties of each solvent. As is seen, even with such different solvents, both C_2-fluorene and C_2-thiophene are unaffected

by the solvent choice as seen from the near-constant dihedral distributions. With C_{12}-fluorene and C_{12}-thiophene, we see that the underlying dihedral dynamics are substantially modified by the presence of the side-chain. In each of these cases, the dihedral distributions in chloroform become notably biased towards the *trans* minimum while those in water become oppositely biased. This can be rationalised by considering that a good solvent, such as chloroform, will make side-chain - side-chain interactions unfavourable while the opposite is true with a poor solvent. For a side-chain long enough such that side-chain - side-chain interactions are possible, such as the C_{12} substituted molecules, this behaviour will incur an average energy penalty against the dihedral angles which bring neighbouring side-chains closer or vice versa.

It is clear that this solvent - side-chain dependent dihedral behaviour must become significant at a critical length of side chain. To investigate this point, we have generated similar distributions for the five solvents listed above. As a quantitative measure, we have calculated the probabilities, $P_{\phi<90}$ based on the calculated probability density function, $P_\phi(\phi)$:

$$P_{\phi<90} = \int_0^{90} d\phi P_\phi(\phi) \tag{4.7}$$

The resulting probabilities are shown in Table 4.4 for each combination of solvent and side-chains labelled. The corresponding distributions for each are shown and discussed in Appendix B.2. For each combination of molecule and side-chain, the associated predictions based on a Boltzmann distribution of the corresponding DFT profile are also shown. The errors in each probability were obtained from simulations of 16mers of dioctyl-fluorene and hexyl-thiophene by obtaining the individual $P_{\phi<90}$ values for each of the 15 dihedral angles and calculating the standard deviation.

For fluorenes, the probabilities are near constant for the unsubstituted 2mer and in agreement with the Boltzmann distribution prediction. For C_2-fluorene, there is slight bias towards dihedrals with opposing side-chains though the biasing is close to the error of the calculation. For C_6-fluorene, dependence on solvent quality begins to emerge and becomes significant for C_8-fluorene and C_{12}-fluorene. In C_8-fluorene and C_{12}-fluorene, substantial biasing occurs for water with biasing in favour of neighbouring side-chains. For THF, chloroform, and toluene, similar and opposite biasing occurs though not as significantly as that in water. That this effect becomes significant at the dioctyl-fluorene level is consistent with the findings of Bright *et al* discussed above [100]. Furthermore, that poor quality solvents lead to enhanced side-chain - side-chain interactions is suggestive of a precursory solvent-dependent contribution to β-phase formation beyond that leading to polymer aggregation.

For thiophenes, dihedral biasing also occurs with increasing side-chain length though to a significantly lesser degree than for fluorenes. For unsubstituted and C_2-thiophene, the probabilities are significantly different from those of longer side-chains

Table 4.4: Probabilities of $0^\circ \leq \phi \leq 90^\circ$ of fluorene and thiophene 2mers with various combinations of side-chains and solvents. The error in each calculation is listed for each molecule. Columns with no side-chain listed denote unsubstituted molecules.

	Fluorene (± 0.07)					Thiophene (± 0.03)				
Solvent	-	C_2	C_6	C_8	C_{12}	-	C_2	C_6	C_8	C_{12}
chloroform	0.50	0.58	0.56	0.54	0.69	0.68	0.51	0.68	0.68	0.69
THF	0.53	0.59	0.68	0.58	0.68	0.69	0.52	0.67	0.68	0.67
toluene	0.49	0.61	0.51	0.61	0.61	0.74	0.53	0.71	0.71	0.71
methanol	0.51	0.61	0.53	0.54	0.41	0.71	0.52	0.65	0.64	0.58
water	0.54	0.52	0.37	0.06	0.03	0.71	0.52	0.60	0.50	0.44
Boltzmann (DFT)	0.50	0.50	0.50	0.50	0.50	0.78	0.57	0.53	0.53	0.53

which, as is seen in the Boltzmann predictions, is the result of the steric contribution of the first carbons of the side-chain to the dihedral potential. This is further shown by the lack of an effect of solvent at this level. For water, there is a notable biasing of the dihedral angle to the *cis* side - again, maximising the side-chain - side-chain interaction - though the converse effect is not seen with any significant effect. We believe that, while the thiophene unit is considerably shorter than that of the fluorene unit and, thus, should require far shorter side-chains to have a similar effect, the solvent effects in fluorenes are amplified due to the double side-chains which can more effectively form trap conformations (two side-chains effectively locked on to another one or two) than the individual side-chains in thiophenes.

From this analysis, we see that the MD simulation regime allows us to obtain significant insight into the conformational dynamics of conjugated polymers even by analysis at the 2mer level. We have found that fluorenes have the capability for significant solvent-dependence in their dihedral distributions depending on the length of side-chain used. This allows us to better understand the steps in the formation of side-chain dependent conformational phases such as the β-phase.

4.2.3 Inter-monomer bond angle distributions

While dihedral angles are of great significance to the conformational and electronic properties of conjugated molecules, the overall conformational freedom of a conjugated, or, indeed, any other, oligomer or polymer is directly related to the freedom of the inter-monomer bond angles (herein referred to simply as bond angles). Any change in the overall molecular conformation can be considered as a series of changes in individual bond angles. As such, it is useful to analyse the properties of bond angle variations at the 2mer level so as to better understand the conformational properties in extended length systems.

As has been demonstrated for fluorene in the work of Schumacher *et al* [127], optimised geometries from DFT calculations predict that the bond angles between each unit in conjugated molecules display dependence on their associated dihedral

angles. If this holds true in a dynamical system, it implies that significant biasing in the dihedral distributions would lead to two different classes of conformation. For instance, in fluorenes, the bond angle between successive units in the *trans* conformation is $\simeq 10^\circ$ while the *cis* conformations typically have bond angles of $\simeq 20^\circ$. For thiophenes, the bond angles are $\simeq 15^\circ$ and $\simeq 30^\circ$ respectively. This means that molecules which are biased strongly to the *trans* conformations will be expected to have effectively straight chains of small, alternating bond angles while those biased to *cis* conformations will adopt curved or helical conformations.

Following the method discussed in Section 2.2.6, we have generated distributions of bond angles calculated from the angles between the monomer end-to-end vectors of 2mers of C_8-fluorene and C_6-thiophene (herein referred to as fluorene and thiophene, respectively). In Figure 4.6 (a) and (c), these distributions are shown for fluorene and thiophene, respectively. For fluorene, a distinctly bimodal character is found in the distribution, which contains two distinct peaks at $\simeq 10^\circ$ and 25°. The thiophene distribution does not display this character as prominently as in fluorene in that it does not have a clearly-defined two-peak structure. The overall shape of the distribution is considerably spread and contains a plateau in the $\simeq 10^\circ$ - 35° range. This suggests that the distribution may also result from two distributions with a stronger degree of overlap.

Based on the prediction of a dependence of bond angles on dihedral angles, we split the bond angle distributions based on those which correspond to dihedral angles above (*cis*) and below (*trans*) 90° as shown in Figure 4.6 (a) and (c). In both cases, two clearly distinct distributions emerge with geometries with *trans* dihedrals having bond angles closer to 0° than the greater bond angles associated with the *cis* dihedrals. For fluorene, geometries with *trans* and *cis* dihedral angles have bond angle distributions peaked at $\simeq 10^\circ$ and 25°. For thiophene, the underlying bond angle distributions are peaked at $\simeq 15^\circ$ and 35° for *trans* and *cis* dihedrals respectively.

It must be noted that the separation of the peaks of the underlying distributions of thiophene ($\simeq 20^\circ$) is slightly greater than that of fluorene ($\simeq 15^\circ$) though the fluorene distribution has a clearer distinction between its respective peaks. From the bimodal character of each distribution, it is clear that there is a far greater overlap between the underlying distributions of thiophene than those of fluorene. This can be explained by observing the complete correspondence between the bond angle and dihedral angle. Figure 4.6 (b) and (d) show the 2-D distribution of each combination of bond angle and dihedral angle in fluorene and thiophene respectively. For thiophene, there is an evident continuity of the bond angle and dihedral angle dependence as the dihedral angle passes through 90°. As fluorenes generally have far fewer thermodynamically available conformations around 90° than thiophenes (as shown in Figure 4.5), the distribution of bond angles and dihedral angles is notably

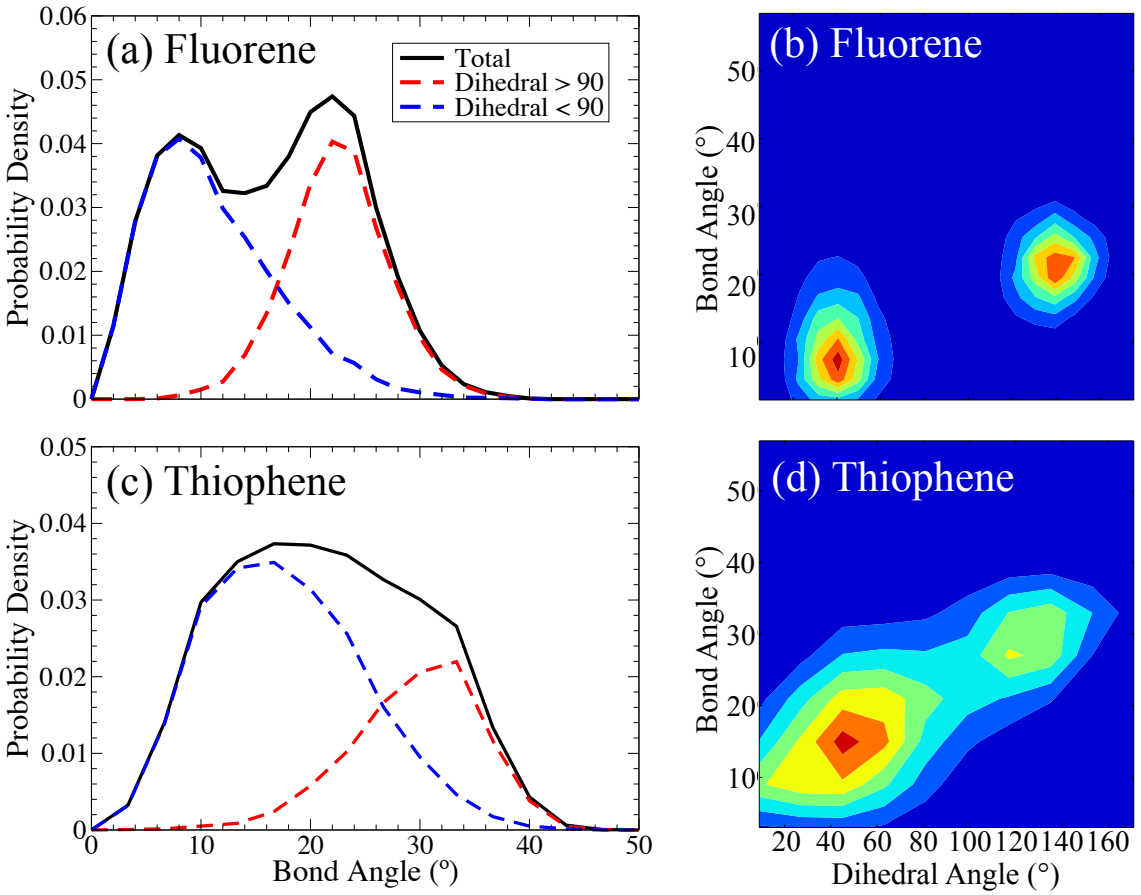

Figure 4.6: Histograms of bond angles from simulations of 2mers of C_8-fluorene (a-b) and C_6-thiophene (c-d). In (a) and (c), the respective probability densities for the bond angles are given along with those for dihedral angles above and below 90°. In (b) and (d), the relationship between the bond angle and dihedral angle is shown explicitly for the whole range of dihedral angles.

distinct between the *trans* and *cis* dihedral sections. In thiophene, the presence of near-90° dihedral angle conformations shows that the population of bond angles in this region is distributed in the region between the *trans* and *cis* peaks. This extra contribution results in the large spread of each of the bond angle distributions shown in Figure 4.6(c) and explains why the bimodal nature is smoothed over in this case and not for fluorene.

In this section, we have discussed a series of simulations of 2mer fluorenes and thiophenes and have both performed a first *in situ* validation of our dihedral potentials by showing that the obtained distributions of dihedral angles conform to Boltzmann distributions obtained from the original DFT potential. Furthermore, we have demonstrated the effect of side-chains on dihedral potentials and how this effect is mediated by solvent choice, as well as demonstrated the bimodal character of bond angle distributions with respect to the dihedral angle.

4.3 Simulations of longer molecules

From the simulations of 2mers discussed above, we now proceed to the core simulations of this work: simulations of long conjugated oligomers in solution. In this regime, we aim to understand the key conformational dynamics of each molecule. Particularly, we calculate correlation functions and end-to-end length distributions for both an understanding of the intrinsic flexibility and chain-folding at play in a well-solvated molecule as well insight into the underlying polymer behaviour in fluorene and thiophene.

The aim throughout this thesis has been in utilising MD simulations as a means of understanding optical phenomena in conjugated molecules. The results of this section delineate the underlying conformational properties of ground-state molecules. As such, we obtain distributions of geometries which underpin ground to excited state transition behaviour. These geometries may then be utilised to obtain conformational features such as persistence lengths (using tangent-correlation functions), end-to-end lengths, and conjugation lengths (based on a model of large dihedral angles serving as 'conjugation breaks'). Furthermore, the obtained geometries can be directly utilised in quantum chemical calculations of ground-to-excited state transition behaviour. This last point forms the focus of the work presented in Chapter 5.

In the remainder of this chapter, our simulations are focused on C_8-fluorene and C_6-thiophene molecules; representative of the polymers PF8 and P3HT. For simplicity of notation, these are herein referred to as fluorene and thiophene, respectively. We begin by first obtaining correlation functions for various lengths of molecule so as to understand the conformational behaviour and flexibility and determine persistence lengths. We then obtain end-to-end length distributions as a means of understanding the statistics of chain-folding and how they correspond with the semi-flexible wormlike chain distributions calculated by Wilhelm and Frey [118,119]. Finally, we conclude this chapter by building distributions of conjugation lengths based on the notion of a defined conjugation breaking dihedral angle.

4.3.1 Tangent correlation functions

As a means of determining the intrinsic flexibility of fluorene and thiophene polymers, we obtain persistence lengths, l_p, by means of calculating tangent correlation functions, $A(\Delta n)$, from simulations in chloroform. As discussed in Section 2.2.6, we obtain tangent correlation functions by ascribing unit tangent vectors to two monomers, $\mathbf{v}_n$ and $\mathbf{v}_{n+\Delta n}$ and defining the correlation function based on the average over their dot products:

$$A(\Delta n) = \langle\langle \mathbf{v}_n \cdot \mathbf{v}_{n+\Delta n} \rangle\rangle, \tag{4.8}$$

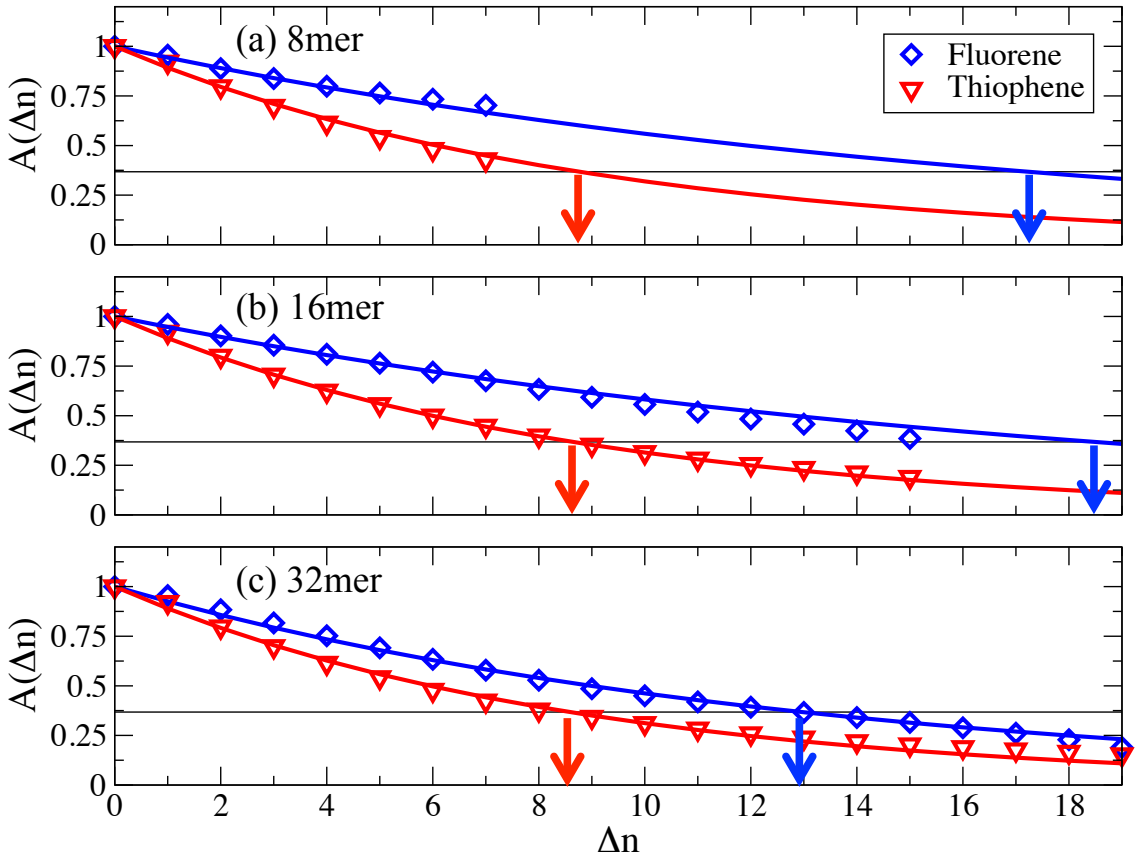

Figure 4.7: Tangent correlation functions, $A(\Delta n)$, of (a) 8mers, (b) 16mers and (c) 32mers of fluorene and thiophene obtained from simulations in chloroform. Each calculated correlation function is given along with their respective fits to Eq. 4.9 (solid lines). In each case, the persistence length, n_p, is indicated by arrows corresponding to the crossing of each fit with the $A(n_p) = e^{-1}$ line.

Table 4.5: Persistence lengths calculated from simulations of 8mers, 16mers, and 32mers of fluorene and thiophene and those obtained experimentally for the corresponding polymers, PF8 and P3HT. For each, the solvent used is either chloroform ($CHCl_3$) or THF as listed. Each persistence length is expressed both in terms of monomer units, n_p, and nm, l_p, with $l_p = ln_p$ and the monomer length, l, taken as $l = 0.832$ nm and $l = 0.397$ nm for fluorene and thiophene respectively.

Molecules	n_p	l_p (nm)
Fluorene 8mer ($CHCl_3$)	17.2	14.3
Fluorene 16mer ($CHCl_3$)	18.5	15.4
Fluorene 32mer ($CHCl_3$)	12.9	10.8
PF8 Exp. (THF) [51, 120]	9.6 ± 1.2	8.0 ± 1.0
Thiophene 8mer ($CHCl_3$)	8.8	3.5
Thiophene 16mer ($CHCl_3$)	8.6	3.4
Thiophene 32mer ($CHCl_3$)	8.5	3.4
Thiophene 32mer (THF)	7.8	3.1
P3HT Exp. (THF) [45]	6.0 ± 0.8	2.4 ± 0.3

with the double angle brackets representing an average over all n and all frames.

From simulations, we obtain correlation functions for 8mers, 16mers, and 32mers of fluorene and thiophene in chloroform with each simulation performed over 100 ns apart from the 32mer of fluorene which was performed over 50 ns. While 50 ns is not a large enough run to obtain fully converged distributions of certain properties, such as dihedral angles and, as discussed in the following subsection, end-to-end lengths, tangent correlation functions are typically well converged up to $\Delta n \simeq N/2$ across this timescale. This is due to the number of available data points for each Δn decreasing linearly with increasing Δn e.g. for one conformation of 16mer there are 15 available dot products for $\Delta n = 1$ while only one for $\Delta n = 15$.

From the correlation functions obtained, shown in Figure 4.7, there is a clear exponential decay behaviour in all cases. This corresponds to wormlike chain behaviour as discussed in Chapter 1.2.2 and, as such, permits the definition of a persistence length, labelled n_p in terms of monomer units, based on fitting to an exponential decay function:

$$A(\Delta n) \approx \exp(-\Delta n/n_p). \tag{4.9}$$

By the above argument regarding correlation function convergence, we fit only to the first $N/2$ points in each case. The persistence lengths obtained are summarised in Table 4.5. For thiophenes in chloroform, the persistence lengths are consistent across the 8mer, 16mer, and 32mer backbone lengths with the 32mer having $n_p = 8.5$. We convert this into a real-space persistence length by obtaining the combined length, l, of the thiophene unit and C-C intermonomer bond length. For thiophene, $l = 0.397$ nm. By the definition $l_p \equiv l n_p$, the persistence length of the thiophene 32mer is $l_p = 3.4$ nm. The same calculation performed for a 32mer in THF solution yields a slightly smaller persistence length of 7.8 units (3.1 nm). Given that both are good solvents, it is to be expected that there would be little significant difference between the two solvents.

For fluorene, substantially different behaviour is observed for increasing backbone lengths. For the 8mer and 16mer, n_p is calculated to be $\simeq 18$ units while, the 32mer has $n_p = 12.9$ units - a reduction by a factor of $\simeq 2/3$. This behaviour is indicative of the need to utilise molecules with $N \gg n_p$ in persistence length calculations so as to approximate polymer-like behaviour.

The persistence length of each molecule gives a crucial indicator as to the overall rigidity and, thus, provides insight into the conformational freedom in each case. Additionally, calculations of persistence length also serve as a crucial tool for experimental comparison and force-field validation. As the persistence length can be inferred from dynamic light scattering measurements of the radius of gyration of polymers in solution, it is to be expected that a simulation of a sufficiently long (i.e. $N \gg n_p$) molecule will replicate this measure. Experimental values of persistence

lengths in the polymers PF8 and P3HT are shown in Table 4.5. For PF8, the persistence length obtained by Grell *et al* for PF8 in THF is 8 ± 1 nm [51, 120], while in P3HT, $l_p = 2.4 \pm 0.3$ nm as reported by Heffner *et al* [45]. The values obtained from our simulations of 32mers are in close agreement with these experimental values. This is one of the key results of this chapter.

While the agreement between our calculations and the experiments is excellent, it must be noted that our simulations are of 32mers and, in the case of fluorene, only available in chloroform. Judging by the progression in increasing backbone length of the thiophene persistence lengths, we are confident that no significant change will occur for further elongated backbones. However, given the aforementioned problem regarding length scales in fluorene, we can only assume that utilising a 32mer is sufficiently long so as to have overcome the initial $N \simeq n_p$ problem phase and gives a persistence length close to that of a polymer-scale calculation. Due to the scale of the fluorene 32mer and, in turn, the number of chloroform molecules ($\simeq 2 \times 10^5$) required for fully-solvated simulation, we are currently practically limited to this length scale. Given also that simulations in THF incur ~ 5 times the computational expense, we have also been limited to simulations in chloroform for this system.

The persistence lengths calculated show both the differences in the flexibility and, thus, conformational freedom of both fluorene and thiophene. Furthermore, their favourable comparison to experimental values serve as a crucial point of validation of the force-field parameterisation scheme discussed in this work. As such, the conformational freedom predicted by the MD simulation regime is accurate and, in turn, the geometries resulting from simulations are expected to be representative of experimental conformations such as those probed by measurements of absorption spectra. This point is particularly crucial to the work of Chapter 5 in which we utilise the MD geometries as the basis for spectral calculations.

4.3.2 End-to-end length distributions

The persistence lengths calculated in the previous section serve only as one particular measure of conformational freedom of a single molecule. For further investigation, we have also calculated distributions of the end-to-end length for the 8mers, 16mers, and 32mers of fluorene and thiophene. As discussed in Section 1.2, the end-to-end length (Eq. 1.1) and the radius of gyration (Eq. 1.6) measurements both give insight into how folded a given conformation is. Of the two, the radius of gyration is typically more relevant to polymer-scale molecules as it implies a spherical picture of a given chain. For oligomers, the radius of gyration has a less intuitive interpretation. Instead, the end-to-end length is more conceptually suitable as a measure of chain-folding.

Figure 4.8 depicts the distributions of end-to-end lengths for 8mers and 16mers of fluorene (Figure 4.8(a)) and 8mers, 16mers, and 32mers of thiophene (Figure

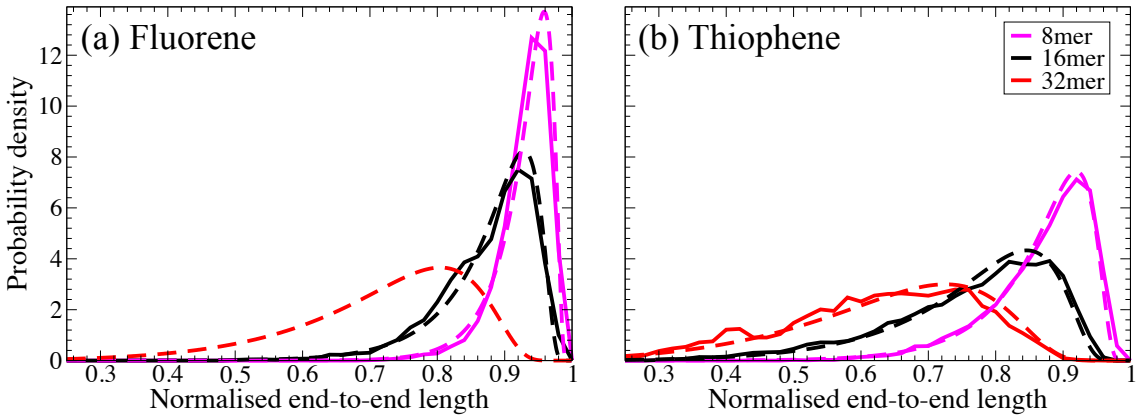

Figure 4.8: End-to-end length distributions (solid lines) of various lengths of (a) fluorene and (b) thiophene. The dashed lines given for each distribution are the calculated distributions, $r^2 P_{ee}(r)$, obtained using Eq. 4.10 [118, 119] with a curve given in (a) for a fluorene 32mer based on the calculated persistence length. The end-to-end length is scaled to give each length as a fraction of the fully extended length of each molecule. Legend in (b) applies to both graphs with the 32mer in (a) omitted.

4.8(a)) each obtained from 100 ns simulations in chloroform. In each, the end-to-end length is expressed as a fraction of the total arc length of each molecule for comparability between each length scale and molecule. While converged tangent correlation functions were obtained for the 32mer of fluorene, the distribution of the end-to-end lengths was not suitably converged over similar time-scales and has not been included.

Comparing the different lengths of each molecule, the clear progression of the distributions is towards lower values and larger ranges with increasing length. This follows intuitively given the increased conformational freedom afforded by longer chains. For thiophene, the 32mer has a much wider distribution and a lower peak length fraction ($\simeq 0.7$) than that of the 16mer which is narrower and peaked at $\simeq 0.85$. The 8mer is narrower still and peaked at $\simeq 0.9$. For fluorene, the distributions at each length scale are narrower and peaked at higher values when compared to the corresponding length of thiophene with the 16mer peaked at $\simeq 0.9$ and the 8mer peaked at $\simeq 0.95$. That the thiophene distributions are considerably broader and peaked at lower end-to-end length fractions than the corresponding lengths of fluorene is consistent with the smaller persistence lengths, and, thus, higher flexibility, of the thiophene molecules.

While experimental measurements of radii of gyration of polymers is possible - and leads to the experimental measurements of persistence length discussed previously - experimental measures of end-to-end lengths are far less available. As such, it is difficult to utilise such a measure as a means of experimental comparison. However, recent advances in utilising end-markers - functional groups generally of high fluorescent quantum yield attached to each end of the molecule - have allowed for such measurements to be possible for molecules in host polymer matrices. One

relevant example is that of Muls *et al* [116] who, using end-marked hexyl-fluorenes of $\simeq 42$ monomer units in length (with a polydispersity of 1.8) in an inert host polymer matrix, measured end-end length distributions which are centred at a length fraction (based on the fully-extended 42mer) of $\simeq 0.89$. Judging roughly by the progression of our end-to-end length distributions, it can be expected that a 42mer simulation would be peaked at a length fraction of around $\simeq$ 0.7-0.8 and indicates a more flexible fluorene molecule. Given the significantly different environments of the experiment and our solution-phase simulations, it is difficult to compare these results and we feel that the inert environment of the experiment can be expected to yield an effectively 'stiffer' molecule given the reduction of conformational freedom in going from a solution to an effectively solid phase. However, future experimental work in this spirit may yield suitable comparison.

Both the progression of the distributions and the difference in overall spread between fluorene and thiophene can be understood conceptually by considering the increase in conformational entropy with increasing length and is consistent with the persistence lengths calculated previously. One feature of the tangent correlation functions discussed previously is the clear exponential decay which is indicative of a wormlike chain (WLC). As briefly mentioned in Section 1.2.2, the WLC model can yield a number of general results using path integral approaches. (Many of these calculations and details of the method are presented in reference [119].) In particular, a general end-to-end length distribution for a WLC has been calculated by Willhelm and Frey [118]:

$$P_{ee}(r) = \mathcal{N} \sum_{k=1}^{\infty} (-1)^{k+1} k^2 \pi^2 e^{-k^2 \pi^2 \xi (1-r)}, \tag{4.10}$$

where r is the end-to-end length fraction, $\xi = l_p/L$ is the persistence length fraction, and $\mathcal{N}$ is the normalisation constant such that $\int_0^1 dr r^2 P_{ee}(r) = 1$. In their work, they found that this expression is in near-exact agreement with Monte Carlo simulations of WLCs. As such, comparison of this distribution function with our obtained distributions serves as an indicator of how much WLC behaviour is exhibited by fluorenes and thiophenes. The calculated distributions are shown as the dashed lines in Figure 4.8 with each value of ξ used taken from the values of n_p given in Table 4.5. In all cases, it is seen that there is very close agreement between the MD distributions and the distributions of Eq. 4.10. In turn, this is indicative of fluorene and thiophene exhibiting WLC behaviour in chloroform and, most probably, in other solvents of similar quality. Furthermore, as we have obtained a value of n_p for the fluorene 32mer, utilising Eq. 4.10 allows us to predict its end-to-end length distribution as shown in Figure 4.8(a).

From the above, we have seen that the end-to-end length distributions behave in a manner similar to that of a WLC based on their associated persistence lengths. As

chains get longer, more substantial folding occurs which leads to fractional end-to-end length distributions which are peaked at lower values and of significantly higher ranges. As with the persistence lengths, the additional flexibility in thiophene gives it substantially greater conformational freedom than fluorene. Potentially, this could result in significantly different spectral properties due to greater conformational distortion in thiophenes which we shall discuss further in Chapter 5.

4.3.3 Dihedral angles and conjugation lengths

As a basic means of attempting to understand the possible spectral behaviour of conjugated molecules using MD simulations alone, it is possible to determine distributions of conjugation breaks and conjugation lengths based on defining a 'break angle', ϕ_B, which 'breaks' conjugation. For such a measure, ϕ_B is often defined as 40° [88, 92, 93] due to the significant changes in the spectral properties such as a blue-shift becoming more significant for dihedral angles greater than 40°. However, the picture of chromophores as the conjugation lengths between such break angles is contested [89, 94–96] (which we discuss further in Section 5.3).

Inasmuch as there is no consensus on the strict theoretical definition of a conjugation length, so neither is there an agreed definition on a conjugation break angle. Our simulations allow us to probe the conjugation lengths obtained in these molecules based on the break angle definition. With the above in mind, we analyse the distributions and number of breaks for a variety of break angles with the aim of later inferring spectral behaviour based on these results.

In Figure 4.9, the distributions of the number of break angles, n_B, for 4mers, 8mers, and 16mers of fluorene and thiophene in chloroform are given. This number also immediately gives the number of chromophores, $n_C = n_B + 1$. For each, the distributions are given for $\phi_B = 40°$, 60°, and 80°. Comparing each set of distributions for fluorene and thiophene shows that thiophene has a substantially wider range of possible values of n_B than fluorene. This follows from the results of Section 4.2 showing that thiophene has a greater tendency towards high angle conformations than fluorene. It also follows immediately that higher ϕ_B values lead to distributions skewed more towards $n_B = 0$ than lower ϕ_B values as is observed.

To better understand the resulting shape of each distribution, we consider, as a simple model, a system of uncorrelated dihedral angles each with a probability, P_B, of breaking conjugation. In such a system, if each dihedral angle is governed by a probability density, $P_\phi(\phi)$, P_B, is defined by:

$$P_B = \int_{\phi_B}^{\pi-\phi_B} d\phi P_\phi(\phi). \tag{4.11}$$

A system of N monomers, therefore $N-1$ dihedral angles, can be described as system of $N-1$ binary links which are either broken or unbroken. Assuming no

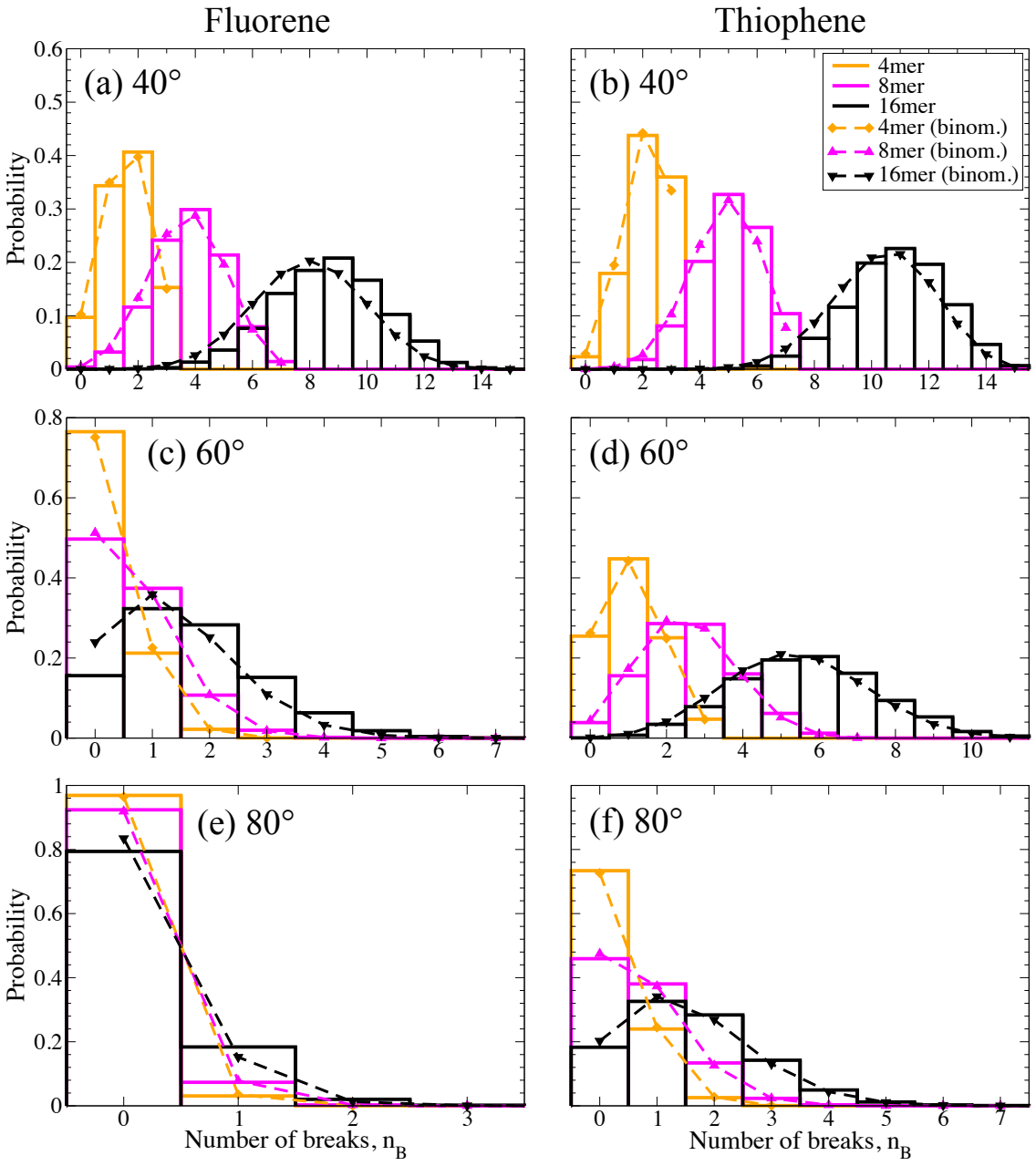

Figure 4.9: Distribution of the number of dihedrals which break conjugation, n_B, for different lengths of fluorene and thiophene. The defined break angle is labelled in each graph. For each distribution, the prediction from the binomial distribution (Eq. 4.11) is given based on the break probabilities given in Table 4.6. Legend in (b) applies to all graphs.

Table 4.6: Probabilities, P_B, of a dihedral angle breaking conjugation calculated using Eq. 4.11 based on defining break angles, ϕ_B, of 40°, 60°, and 80°. Each probability is calculated from the dihedral angle distribution functions calculated from simulations of 2mers in chloroform.

ϕ_B	Fluorene	Thiophene
40°	0.53	0.69
60°	0.09	0.36
80°	0.01	0.10

correlation between each link, the probability, $P_n(n_B)$, that the molecule will have n_B broken links is thus obtained from a binomial distribution:

$$P_n(n_B) = \binom{N-1}{n_B} (P_B)^{n_B} (1 - P_B)^{(N-1-n_B)}. \tag{4.12}$$

Utilising probabilities obtained from the 2mer distribution functions (displayed in Table 4.6), we calculate distributions from Eq. 4.12 and show them alongside those obtained directly from the MD simulation. In all cases, we see that a binomial distribution of this form suitably represents the MD distribution. Given that we have seen previously that invididual dihedral angles are effectively uncorrelated in these oligomers, this result is to be expected. It would, however, form an interesting measure in systems in which dihedral angle correlation could possibly be expected e.g. systems with long side-chains, in poor solvents, or bulk samples.

Utilising a defined conjugation break angle and, as above, an associated break probability, one can partition a given conformation into groups of monomers between a pair of conjugation breaks. As such, the number of monomers in each segment corresponds to a given conjugation length, n_c (in number of monomer units). By this method, we have generated distributions of n_c from simulations. However, the distribution of conjugation lengths alone is difficult to interpret given that it has a large contribution from very small conjugation lengths. These conjugation lengths are not expected to have a particularly notable effect on the overall spectral properties of the molecule. For greater clarity, we will instead discuss the distributions of the maximum conjugation length taken from each conformation (such that there is one conjugation length per conformation) which, as we discuss in Section 5.3.2, are the conjugation lengths typically responsible for localisation of the S_0-S_1 differential density.

From the distributions of the longest conjugation length shown in Figure 4.10, we see that, for all choices of break angle, fluorene has typically longer conjugation lengths than in thiophene. This follows from the above reasoning regarding the lower break probabilities of the corresponding 2mers (Table 4.6). Indeed, for break angles of 60° and 80°, we see that the fluorene distributions are increasingly dominated by a full molecular conjugation length while this is only true for 80° in thiophene.

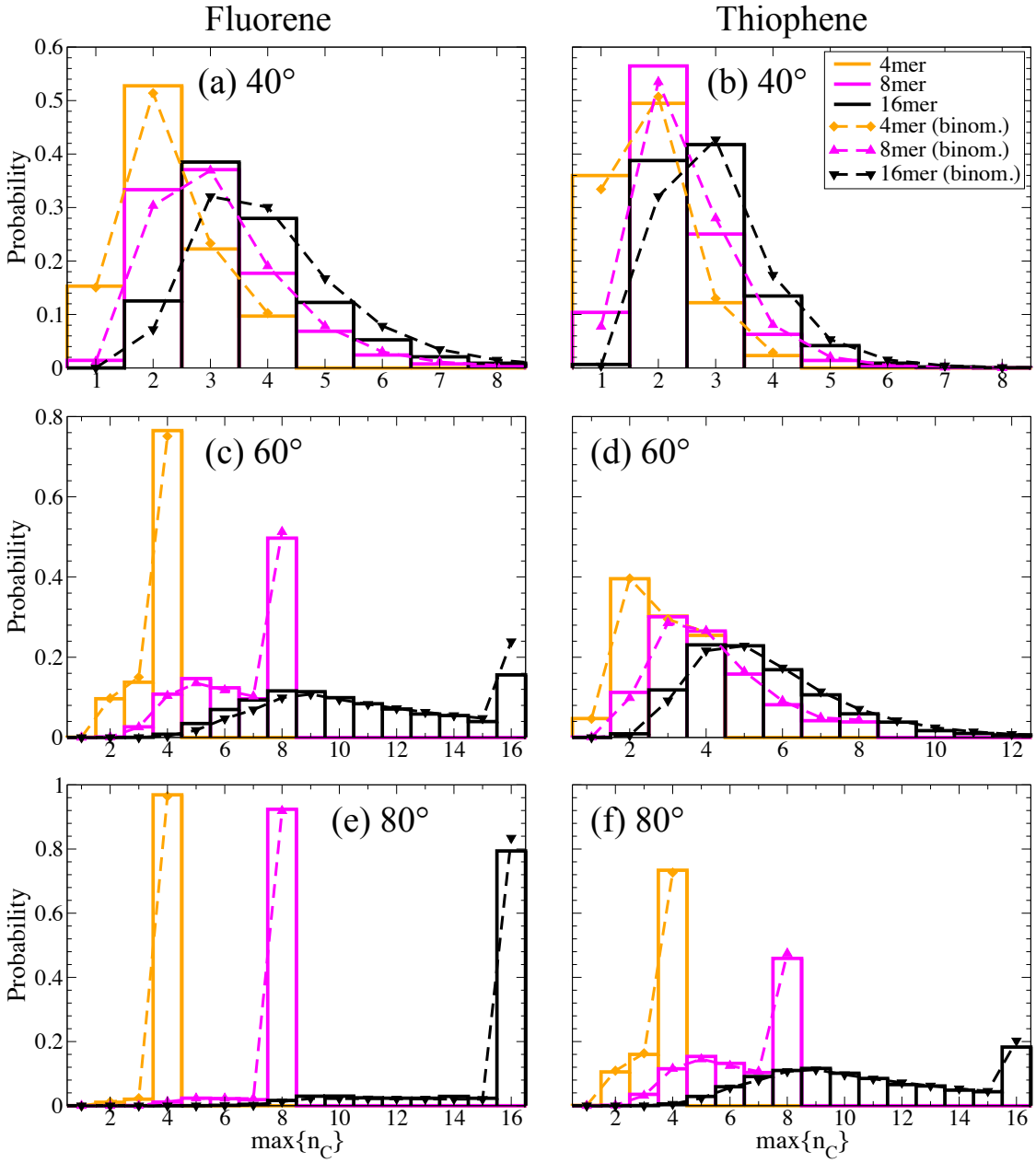

Figure 4.10: Distribution of the longest conjugation length obtained from simulations of different backbone lengths of fluorene and thiophene. The defined break angle is labelled in each graph. For each distribution, the prediction obtained numerically, based on the binomial distribution in Eq. 4.11 and the break probabilities given in Table 4.6, is given. Legend in (b) applies to all graphs.

Considering the 16mers in each case, the 16mers of fluorene have peaks in their l_c distributions at 3 units for $\phi_B = 40°$, 16 units with a secondary peak at 9 units for $\phi_B = 60°$, and 16 units for $\phi_B = 80°$. In thiophene, the distributions are peaked at 3 units, 5 units, and 16 units for $\phi_B = 40°$, 60°, and 80°, respectively, with a secondary peak at 9 units for $\phi_B = 80°$.

In each graph, numerical results based on the binomial model are shown. These are generated by generating all 2^{N-1} possible combinations of broken or unbroken links for an Nmer molecule. Each combination may be represented with an $N-1$ bit binary number such that each bit corresponds to a dihedral angle, ϕ, with a zero corresponding to $\phi < \phi_B$ and one to $\phi > \phi_B$. As such, for each combination, n_B is equivalent to the number of ones in the number, the conjugation lengths are defined by the number of zeros between two ones or a one and the end plus one, and the longest conjugation length defined by the longest unbroken string of zeros. For example, for an 8mer molecule, two example combinations are:

$$\texttt{0000100} \quad n_B = 1 \quad \max\{n_c\} = 5; \tag{4.13}$$

$$\texttt{0100100} \quad n_B = 2 \quad \max\{n_c\} = 3. \tag{4.14}$$

Each combination thus has an associated longest conjugation length and can be weighted by the probability $P_n(n_B)$ of Eq. 4.12 to build a full distribution. In Figure 4.10, it can be seen that distributions generated in this manner correspond very closely to the MD distributions which follows given the agreement of the distributions of the number of conjugation breaks obtained from simulation and from the binomial distribution shown in Figure 4.9.

The insight obtained from the above results is in showing that, in a system where a good solvent is used, if one wishes to define a conjugation length or a chromophore size by a conjugation breaking dihedral angle, it is possible to infer the distribution of such lengths by means of a simulation of a 2mer and invoking a binomial distribution. However, this analysis on its own does not illuminate the nature of chromophore formation or the value or validity of the chosen conjugation-breaking dihedral angle. To exploit the full potential of this analysis, it is necessary to better understand how optical spectra and exciton localisation occurs as a function of molecular geometry and, if possible, how applicable the concept of a conjugation break is. This line of thinking is one of the key motivations of the work presented in the coming chapter.

4.4 Conclusions

In this chapter, we have detailed and analysed the use of the subtraction method in implementing dihedral potentials for a conjugated molecular force-field and have performed a series of MD simulations ranging from small (2mer) to long (up to

32mer) oligomers of fluorene and thiophenes in solution. In doing so, we have reported a series of validations of our force-field, gained insight into how solvents affect dihedral angle dynamics via the alkyl side-chains, and calculated tangent correlation functions and persistence lengths, end-to-end length distributions, and conjugation length distributions.

Utilising a subtraction procedure to determine the force-field contribution to the dihedral potential can, with certain caveats, lead to an accurate representation of the given potential. We have determined the accuracy of this procedure by means of determining how the minimal dihedral conformations emerge from unrestrained optimisation of static geometries and by obtaining dihedral distributions from dynamical simulations - noting strong correspondence between the simulation dihedral distributions and calculated Boltzmann distributions. We have also shown that the transferability of the dihedral potential with respect to the side-chains of thiophene, predicted by DFT, does not hold in the OPLS force-field and, as such, must be implemented for molecules of ethyl side-chains or longer.

In 2mers, we have assessed the role of solvent and side-chains on the dihedral dynamics and found that the side-chains of fluorene display significant solvent-mediated interactions at octyl and above. In poor solvents, the side-chains have favourable interactions which lead to a biasing of the dihedral angles towards the *cis* conformation while the opposite is true in good solvents. In addition, we have found that the intermonomer bond angle has a notably bimodal dependence on the dihedral angle in 2mers with *cis* conformations generally being of greater angle than *trans* conformations.

For longer molecules, we have calculated tangent-correlation functions and find a near-perfect exponential decay. As such, it is possible to calculate persistence lengths based on the exponential definition and, in doing so, find values which compare favourably with experimental values. In line with the exponential decay of the correlation functions, the end-to-end length distributions follow the progression derived by Wilhelm and Frey for semi-flexible wormlike chains which, thus, suggests an overall wormlike chain nature in both fluorene and thiophene.

The above simulations have offered insight into the conformational features of oligomers in good solvents. With the force-field parameterisation scheme in place, it is possible to go on to examine many other interesting problems from an MD perspective such as aggregation behaviour in multi-molecular and polymer systems and further examinations of how solvent-dependent behaviour emerges from larger systems. Currently, we aim to utilise the conformational principles we have obtained from simulation, as well as the molecular geometries themselves, to understand optical properties. To carry out this work, we utilise TD-DFT methods on the individual geometries which we shall go on to discuss in Chapter 5.

Chapter 5

Conformational dependences in linear absorption

Classical MD simulations, while capable of obtaining conformational and thermodynamic insights, cannot be used directly to determine any quantum mechanical properties. However, the distribution of conformations generated by these simulations can be used as the basis for further calculations to determine, for instance, how the ensemble of conformations impacts the optical response. In this chapter, we employ this method to calculate optical absorption spectra from conformation ensembles in order to understand the role various conformations have on the resulting absorption spectra and how excitation densities localise along molecular chains. We begin by first calculating the conformation-dependent spectral properties of 2mers as a preliminary example of the basic concepts of dihedral angle dependence, inhomogeneous broadening, and the emergence of high energy absorption features. This is followed by calculations of absorption spectra and inhomogeneous broadening from conformation ensembles of longer oligomers and an investigation of the various contributions from individual dihedral angles in these chains. Finally, we define measures of excitation localisation and apply them to the same conformation ensembles to investigate the role of conformational distortions, such as the conjugation breaks discussed in Section 4.3.3, in disturbing the overall delocalisation of excitations.

5.1 Spectral properties of 2mer systems

As preliminary examples, 2mer systems offer a useful introduction to principles such as dihedral-dependent inhomogeneous broadening and the emergence of high-energy absorption spectral lines. The simplicity of the 2mer system allows simple analysis methods to be employed such as investigating the direct relationship between the single dihedral angle and a particular transition energy as well as building spectra based on directly calculating inhomogeneous broadening based on the dihedral dependence of the dominant, low-energy transition and the probability of a given

dihedral angle occuring. These approaches provide a testing ground for utilising ensemble geometries from MD simulations. In the following, we perform the aforementioned analyses and, in doing so, outline the primary concepts and obtain reference results which guide the interpretation of the MD ensemble spectra presented in later sections.

5.1.1 Dihedral angle dependent absorption spectra

As an investigation into the effect of conformational variation on absorption spectra, we begin by calculating absorption spectra for geometries obtained from dihedral scans such as those utilised for calculating dihedral potentials in Chapter 3. As discussed in Section 1.1.3, dihedral angle rotation has a significant effect on the π conjugation and, given also that the dihedral angle is the primary degree of freedom in the 2mer system, it is to be expected that it will be the primary source of any conformation-dependence in the absorption spectra.

To obtain absorption spectra, we calculate a set of absorption transitions using TD-DFT at the B3LYP/6-31G level with geometries, as in Chapter 3, obtained using CAM-B3LYP/6-31G*. We find that utilising long-range corrected functionals, such as CAM-B3LYP, as opposed to standard hybrid functionals, such as B3LYP, typically leads to an overestimation of the thiophene 16mer S_0-S_1 transition energy of around 0.5 eV when compared to expriment. A full discussion of this choice of TD-DFT functional and basis set is presented in Appendix C. No treatment of solvent was utilised. While we found for thiophene 2mers that utilising a polarizable continuum model (PCM) solvent led to reductions in transitions energies of $\sim$ 150 meV, for 16mers and 32mers, this reduction was $\simeq$ 40 meV. As such, we utilise no solvent correction for 2mers for consistency with the calculations performed in the following sections. Reductions in the transition energies of 16mers and 32mers due to including the PCM model with CAM-B3LYP are also of the same scale. For each geometry, we obtain the first 20 transition energies and oscillator strengths. Each geometry scan calculation is performed for dimethyl-fluorene and methyl-thiophene molecules which are referred to as fluorene and thiophene for ease of notation.

Figure 5.1 depicts the dihedral dependence of (a) the lowest (S_0-S_1) transition energy and (b) oscillator strength of fluorene and thiophene 2mers. The progression of the S_0-S_1 transition energy depicted in Figure 5.1(a) shows the expected increase in transition energy from the planar conformations to the 90° conformation. When considering inhomogeneous broadening, it is useful to consider the total variation in the S_0-S_1 transition resulting from variations in the dihedral angle defined by: $\Delta\epsilon_\phi \equiv \epsilon_{90} - \epsilon_0$, where ϵ_{90} and ϵ_0 denote the S_0-S_1 transition energy at $\phi = 0$ and $\phi = 90$, respectively. This range represents the maximum possible variation (i.e. if the oscillator strength were independent of dihedral angle and all dihedral angles were equally probable) in this transition energy resulting from variations in

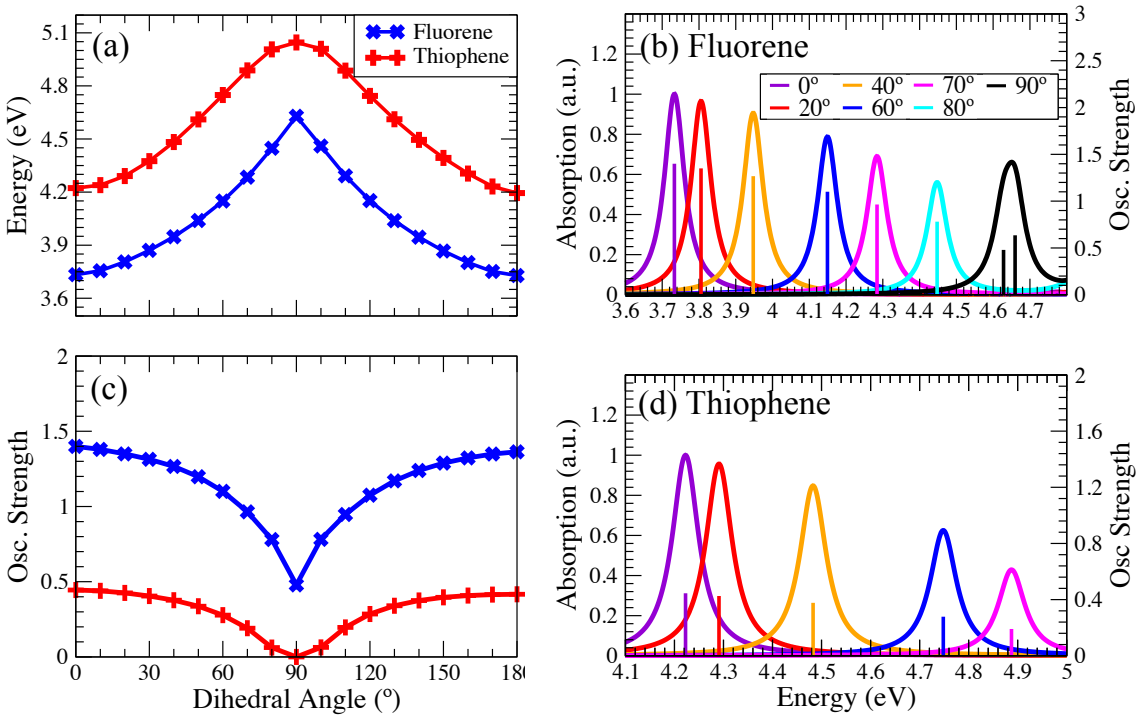

Figure 5.1: Dihedral angle dependent absorption spectra for 2mers of fluorene and thiophene. (a) and (c) are the transition energies and oscillator strengths, respectively, of the lowest transition for fluorene and thiophene. (Legend in (a) applies also to (c).) (b) and (d) depict the absorption spectra obtained for various dihedral angles for fluorene and thiophene respectively. The sticks correspond to the oscillator strengths (right axis) while the continuous spectra are given in arbitrary units (left axis) corresponding to a normalisation of the spectra to the peak of the 0° spectra. (Legend in (b) applies also to (d).)

the dihedral angle. We refer to this range throughout as the 'maximum dihedral absorption range' (MDAR). The MDARs of the fluorene and thiophene 2mers are 895 meV and 823 meV, respectively. Given that homogeneous broadening is typically $\sim$ 10 meV [76, 98], this range gives a first indication that the overall spectra of a 2mer system will be dominated by conformational broadening.

The oscillator strengths of the first transitions also display a notable dihedral dependence as shown in Figure 5.1(c). For both fluorene and thiophene, the oscillator strength of this transition decreases with increasing dihedral angle. In fluorene, the ratio of either of the planar oscillator strengths, f_0, to the 90° oscillator strength, f_{90}, is $f_0/f_{90} \simeq 3$. For thiophene, the 90° oscillator strength is close to zero. Therefore, it is to be expected that conformations with dihedral angles close to 90° shall have less prominent S_0-S_1 transitions and, thus, a lesser contribution to the conformational broadening.

So far we have discussed only the lowest energy transitions for each dihedral angle. In Figures 5.1(c) and (d), we give a representation of the resulting absorption spectra taken for the range of transitions up to 5 eV for a sample of dihedral angles (as labeled) in the scans of fluorene and thiophene. The cut-off imposed at 5 eV is to

avoid encountering problems due to the ionisation threshold. Following the scheme discussed in Chapter 2.3.4, each spectrum is generated by assigning a Lorentzian function of homogeneous broadening $\gamma = 33$ meV - chosen for consistency with MD ensemble spectra calculations to follow - to each transition energy and oscillator strength calculated for a given conformation. We note that the 'homogeneous broadening' used here is not strictly representative of the homogeneous broadening and, accordingly, does not account for any oscillator strength dependence. As will be shown later in the chapter, its function is primarily as an interpolating factor for spectra formed from MD ensemble geometries and is dominated by the resulting conformational broadening. For thiophene, the 80° and 90° conformations are omitted as their lowest states lie higher than 5 eV.

The absorption spectra show that the first transition in each case is generally the dominant transition which is often the case in conjugated polymer systems. As such, the spectra follow the progression of the transition energies and oscillator strengths. The exception to this is for the 90° conformation of fluorene. In this conformation, the primary absorption feature is comprised of two states of near-equal oscillator strength separated by $\simeq 30$ meV. This splitting behaviour is discussed further in the following subsection (Section 5.1.2).

Having established the increasing excitation energy with respect to increasing the dihedral angle, we now investigate the absorption spectra calculated from geometries taken from the MD ensemble. We calculate ensemble spectral properties of 2mer ensembles of dioctyl-fluorene and hexyl-thiophene (each referred to as fluorene and thiophene in the context of ensemble spectra unless otherwise stated) from simulations in chloroform. For fluorene, each calculation consists of 1001 geometries sampled every 100 ps of a 100 ns run, with each geometry's excited-state properties calculated using TD-DFT at the B3LYP/6-31G level. For thiophene, the same procedure is followed with 2001 geometries sampled every 50 ps. In both cases, the individual spectra are entirely uncorrelated at this level of sampling and, were it not for the computational expense of TD-DFT calculations, could be sampled at a higher rate. The sampling rates chosen were sufficiently high so as to ensure convergence of the spectra.

In Figure 5.2(a), the energies of these transitions are plotted as a function of the dihedral angle. Both the fluorene and thiophene ensembles closely follow the qualitative trend of Figure 5.1(a). Both trends, however, appear red-shifted from the DFT result by $\simeq 30$ meV and $\simeq 110$ meV in fluorene and thiophene respectively. We find that the trend in the oscillator strengths of the transition in the ensemble is comparable to that of 5.2(c).

That the qualitative trends of the optimised geometry calculations are so readily observed in the 2mer ensembles is not surprising given that the dihedral angle is the only major source of conformational disorder in the molecule. The red-shift from

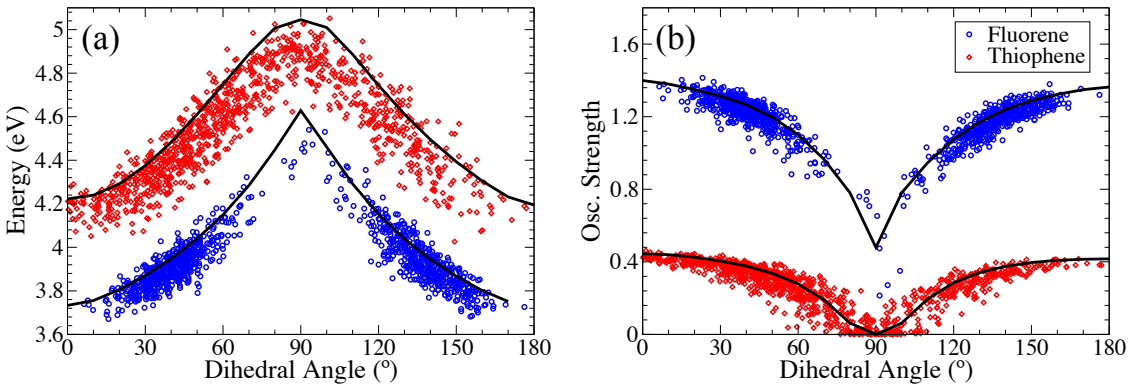

Figure 5.2: Transition energies (a) and oscillator strengths (b) of the lowest transitions of MD ensembles of fluorene and thiophene 2mers. In each case, the solid lines indicate the trends predicted from geometry scan calculations. (Legend in (b) applies to both graphs.)

the scanned geometries and the ensemble trend, however, is surprising. One possible source of this shift is the effect of slight distortions on the base monomers of each molecule which, given the size of each system, have a more significant effect than in larger molecules. The work of Jing *et al*, in calculating reorganisation energies of bacterial conjugated pigments, has noted that structural fluctuations in geometries obtained from MD runs are larger than those predicted from molecular normal modes. These inaccurate distortions are believed to be the cause of a significant overestimation of reorganisation energies from MD geometries when compared to those calculated solely from DFT [258]. Another possibility is in the sensitivity of the TD-DFT approach to error for systems of this scale.

As described in Section 2.3.4, we calculate ensemble spectra by performing a sum over Lorentzian line-shapes attributed to the transition energies, ϵ, and oscillator strengths, f. We utilise a homogeneous broadening parameter of $\gamma = 33$ meV for both fluorene and thiophene as obtained for fluorene by Denis *et al* [76]. As the inhomogeneous broadening due to conformational disorder significantly dominates the total spectral broadening, the choice of γ serves primarily as an interpolation parameter.

For the 2mers of fluorene and thiophene, the resulting spectra are shown in Figure 5.3(a) and (b) respectively. Each of the spectra displays significant inhomogeneous broadening with a half-width half-maximum (HWHM) of $\simeq 130$ meV and $\simeq 270$ meV for fluorene and thiophene respectively. While the dihedral dependence seen in the optimised geometry scans shown in Figure 5.1 predicts that both fluorene and thiophene 2mers have lowest energy transitions which span similar ranges of $\simeq 800 - 900$ meV, comparison of the broadening in Figure 5.3 shows that the resulting inhomogeneous broadening from the ensemble is substantially less than these ranges. This is easily rationalised by considering the probability distribution of each dihedral shown in Figure B.1 and discussed in Section 4.2.2 and Appendix B. The dihedral

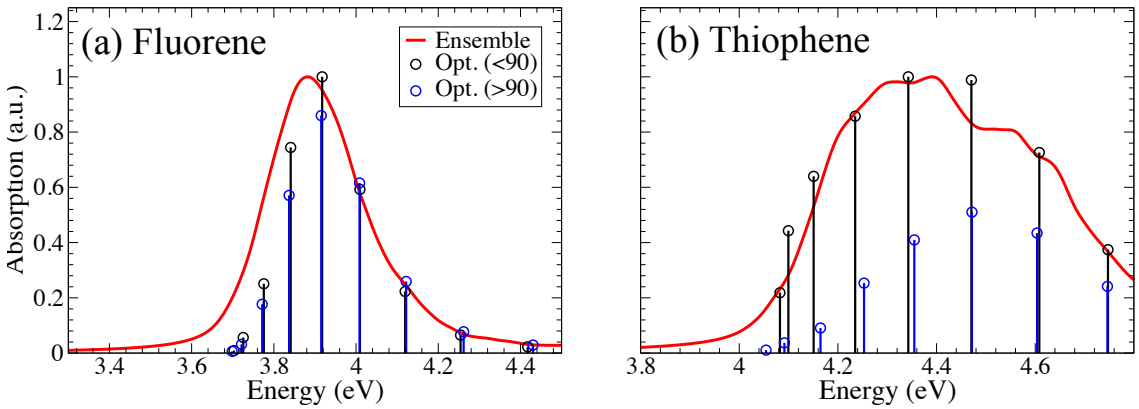

Figure 5.3: Absorption spectra (red curves) calculated from MD ensembles of fluorene (a) and thiophene (b) 2mers. In each case, the lowest transitions predicted from geometry scan calculations and weighted by the corresponding probability obtained from the MD simulation are shown as sticks. Black sticks correspond to $\phi < 90°$ and blue sticks to $\phi > 90°$. The stick spectra are corrected by a shift of 30 meV and 110 meV for fluorene and thiophene respectively. (Legend in (a) applies to both graphs.)

distribution in fluorene is limited almost entirely to the region within $\pm 20°$ of each minimal angle while that of thiophene has greater freedom to explore angles in the region of 90°. So, while the spectral ranges are similar, the proportion of this range explored by each molecule is significantly different. This is a key concept which we return to extensively throughout this chapter.

To further demonstrate this point, we build a simple model of each spectrum by taking the S_0-S_1 transition energy and oscillator strength for each point in the respective dihedral scan, $\epsilon(\phi)$ and $f(\phi)$, respectively, and generate new spectral lines by weighting the oscillator strengths by the probability, $P(\phi)\Delta\phi$, associated with that dihedral. (These probabilities are readily obtained from the MD simulation dihedral distributions discussed in Section 4.2 and Appendix B.) For reference, the weighted oscillator strengths are plotted as the stick spectra in Figure 5.3 with a correcting shift (30 meV for fluorene and 110 meV for thiophene) applied to correct for the offset observed in Figure 5.2(a). It can be seen that this simple approach yields a result in good qualitative agreement with each of the ensemble spectra calculated from the MD geometries.

5.1.2 Emergence of high-energy absorption features

In discussing the transition energies of the DFT scan geometries shown in Figure 5.1, we noted that the 90° conformation of fluorene (Figure 5.1(b)) displays a splitting feature of the lowest transitions. In the remainder of this section, we shall discuss the emergence of similar features in ensemble spectra resulting from variations in dihedral angle.

As a note on notation, in the previous examples we considered a set of tran-

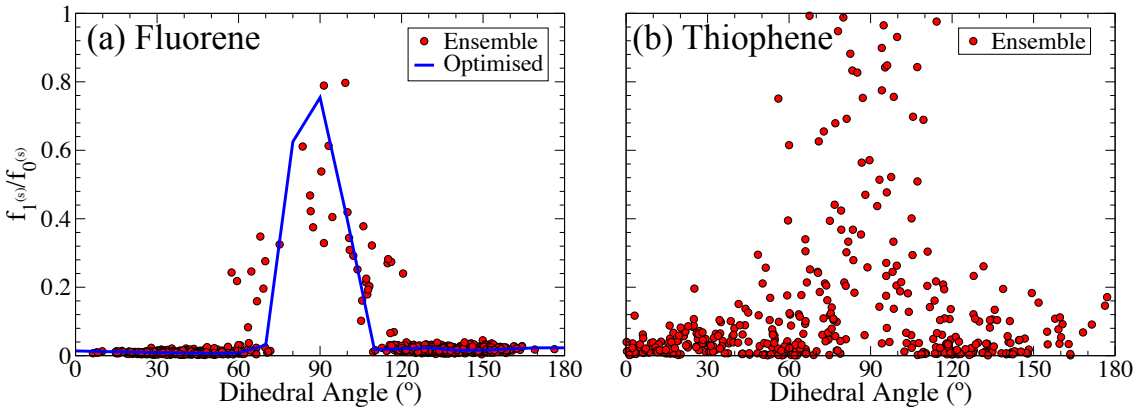

Figure 5.4: Ratios of the second largest and largest oscillator strengths, $f_{1(s)}/f_{0(s)}$, for MD ensemble conformations of fluorene (a) and thiophene (b) 2mers. In (a), the trend predicted from geometry scans is shown with the line serving as guide to the eye.

sitions for each conformation, each with energy and oscillator strengths ϵ_i and f_i, with transition $i = 0$ corresponding to the lowest energy (S_0-S_1) transition. In the following, it is convenient to sort this same set of transition in terms of descending oscillator strength with transitions in this sorting denoting by the label $i^{(s)}$ e.g. $\epsilon_{0(s)}$ refers to the energy of the transition with the greatest oscillator strength. This allows us to define the ratio of the two most significant transitions, $f_{0(s)}$ and $f_{1(s)}$, and their energetic separations by $f_{1(s)}/f_{0(s)}$ and $\Delta\epsilon_{1(s)} \equiv \epsilon_{1(s)} - \epsilon_{0(s)}$.

Figure 5.4 shows the oscillator strength ratios calculated from each conformation in MD ensembles of (a) fluorene and (b) thiophene 2mers. In both cases, notably split states ($f_{1(s)}/f_{0(s)} \geq 0.5$) are observed for dihedral angles in the region between 60° and 120° i.e. ±30° from either side of the 90° barrier. For fluorene, we also show the trend in this ratio calculated using the scan geometries which shows similar behaviour. We have not included a similar trend for thiophene due to the higher-energy states being above 5 eV in the optimised geometry calculations.

Dihedral dependence is also observed in the energetic separations, $\Delta\epsilon_{1(s)}$, as shown in Figure 5.5 for both (a) fluorene and (b) thiophene. In both cases, $\Delta\epsilon_{1(s)}$ is considerably larger ($\simeq 1$ eV and $\simeq 0.8$ eV for fluorene and thiophene respectively) for near planar geometries than for those with dihedral angles close to 90°. 90° conformations have $\Delta\epsilon_{1(s)} \simeq 0$ and, in some cases, $\Delta\epsilon_{1(s)} < 0$. The former indicates that two excited states are approaching degeneracy and, in the latter cases, that a transition other than the S_0-S_1 transition is the dominant transition. In Figure 5.4, points which have $f_{1(s)}/f_{0(s)} \geq 0.2$ are emboldened to signify transitions which may have a meaningful contribution to the absorption spectra. This shows that, while the expected trend is adhered to by the split states, there is only a very small fraction which have non-negligible spectral contributions.

The above results are consistent with considering the 90° barrier as a conjugation break. At a 90° dihedral, the π orbital overlap across the molecule is at a minimum

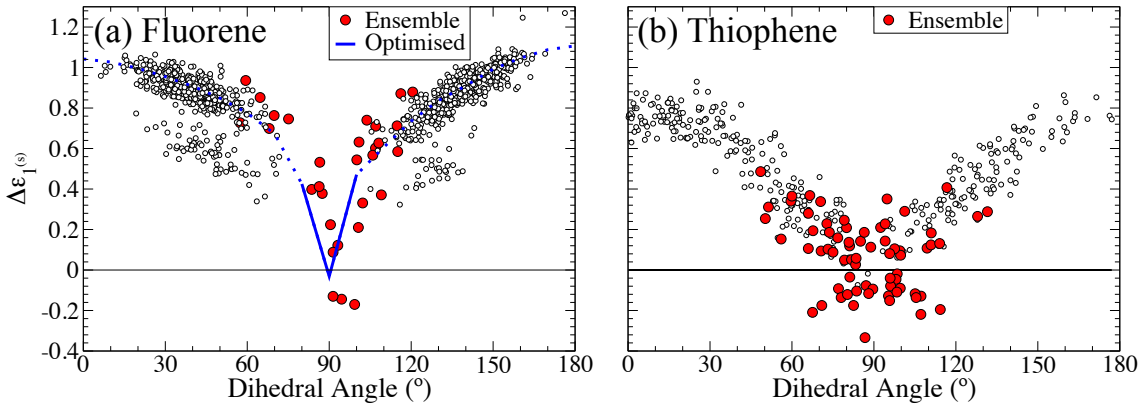

Figure 5.5: Energetic separations of the states with the second largest and largest oscillator strengths, $\Delta\epsilon_{1^{(s)}} \equiv \epsilon_{1^{(s)}} - \epsilon_{0^{(s)}}$, for MD ensemble conformations of (a) fluorene and (b) thiophene 2mers. In (a), the trend predicted from geometry scans is shown. In all cases, points which correspond to $f_{1^{(s)}}/f_{0^{(s)}} \geq 0.2$ (red dots and solid blue lines) and otherwise (white circles and dashed blue lines) are differentiated to signify states which do or do not have a non-negligible spectral contribution.

and, therefore, is the closest a 2mer system comes to resembling a system of two weakly coupled individual monomers. With no coupling between each monomer, it would be the case that each monomer would have a set of identical transitions and, as such, have degenerate primary transitions of equal oscillator strengths i.e. $\Delta\epsilon_{1^{(s)}} = 0$ and $f_{1^{(s)}}/f_{0^{(s)}} = 1$. The 90° conformation represents a weakly-coupled regime and, as such, the transitions show a near-degenerate feature which is lost as the dihedral angle is reduced to closer to planar conformations.

The results of this section have highlighted some of the key features of conformational dependence in the absorption spectra of fluorene and thiophene such as the increase in transition energies and the emergence of high energy absorption for dihedral angles approaching 90°. These effects, particularly the former, are the key sources of inhomogeneous broadening in the 2mer systems. Having established these effects, we now continue to a discussion of the effect of varying conformation in molecules longer than 2mers.

5.2 Absorption spectra of long oligomers

When considering conjugated molecules of increasing length, a well known [1, 90, 91, 98, 259, 260] feature observed in the absorption and emission spectra is a decrease in the associated transition energies. Due to the π-orbital delocalisation across the conjugated backbone, which is responsible for the dominant excitations, increasing the backbone length increases the overall orbital delocalisation and, in turn, decreases the resonant electronic energies. A simplified analogue is the particle in a box example from basic quantum mechanics in which increasing the box length decreases the energies of the eigenstates which, in turn, decreases their energetic separation. Of course, in a real molecule, such a simple model does not capture

the full qualitative behaviour. Real conjugated molecules generally have excitation energies which effectively saturate beyond a certain length. This saturation forms one possible definition of an effective conjugation length [90] in a given polymer or oligomer.

Another feature of increasing molecular length is the increase in the overall conformational freedom of the molecule. This allows conformational disorder, such as multiple large dihedral angles or strongly bent conformations, to arise. These can have implications for the spectral properties as well. As discussed in Chapters 1 and 4, large dihedral angles have the effect of sharply increasing excitation energies as well as 'breaking' conjugation with the distance between such breaks forming another, widely-used, definition of an effective conjugation length [88, 90–93]. In poor solvents and films, it is also possible to obtain highly distorted molecules and even intramolecular π-π stacking of different portions of collapsed molecules. These features often give rise to interesting optical response behaviour such as the distinct 440 nm peak of β-phase in polyfluorenes [52,100,261] and energy shifts corresponding to different types of aggregation [108, 262].

Traditionally, TD-DFT studies have often been employed to obtain insight into the excited state properties of oligomers of conjugated molecules. However, these methods are typically confined to properties of idealised, optimised conformations and the effects of conformational disorder can only be inferred either from calculations for well defined geometries or for a small sample of possible disorders [98, 103, 104]. The effects of inhomogenous broadening due to conformational disorder are typically implemented by utilising different line-shapes with broadening parameters which are fitted to experiment [76].

In the remainder of this section, we aim to obtain absorption spectra based on ensembles of geometries obtained from MD simulations in chloroform. The 2mers discussed in the previous section show a strong dependence on dihedral angle both in the inhomogenous broadening observed and the emergence of secondary absorption states. Longer oligomers have, of course, a much larger space of possible conformations and, in turn, a wider variety of possible conformational disorders. By utilising the MD simulation regime as generator of thermodynamically-accessible disordered conformations, representative of real conformational disorder in oligomer systems, we aim to identify the primary sources of inhomogeneous broadening and spectral variation. In Section 5.2.1, we generate spectra for conformation ensembles and compare these results with the spectra obtained from DFT optimised geometries. This allows us to determine the extent of conformational broadening, shifts which occur due to distortions, and the emergence of high energy absorption features not possible from a pure DFT approach. This is then followed up in Section 5.2.2 with a TD-DFT investigation of the role of the dihedral angles in shifting the transition energies in 4mers and 8mers.

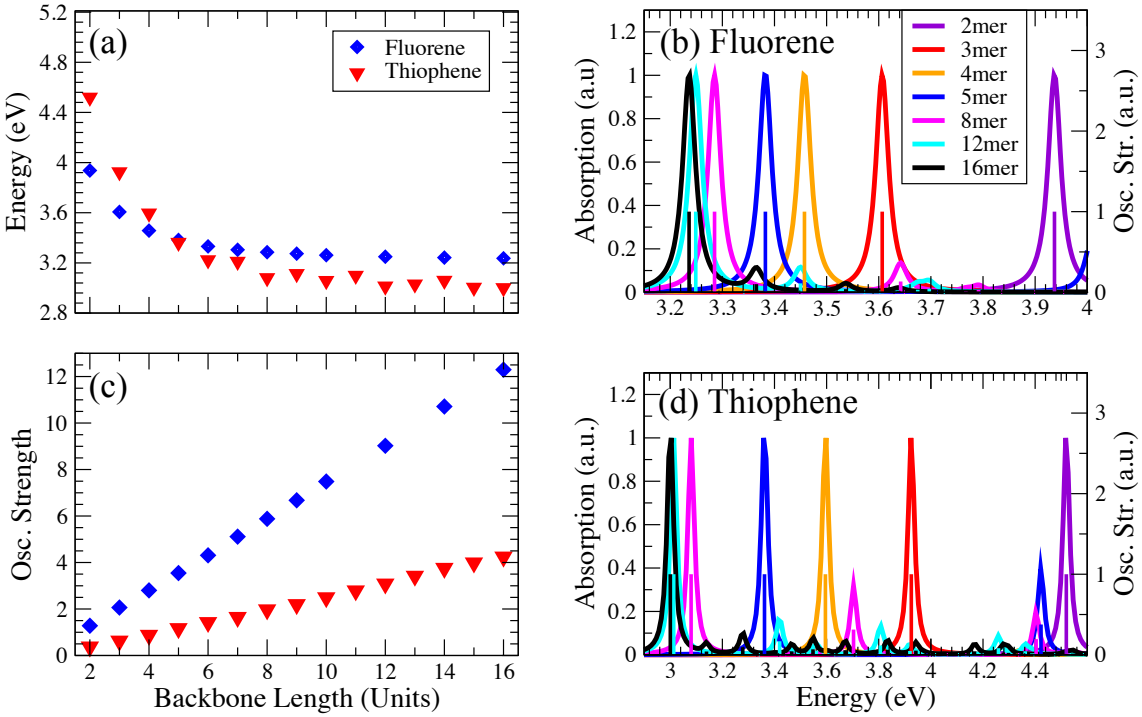

Figure 5.6: Progressions of the (a) lowest transition energies, (b), (d) spectra, and (c) lowest transition oscillator strengths for fluorene and thiophene of varying backbone lengths calculated using optimised geometries. Each the spectra and sets of oscillator strengths in (b) and (d) are normalised such that their maxima are unity. (Legends in (a) and (b) apply also to (c) and (d), respectively.)

5.2.1 Length-scale dependence in absorption spectra

For reference as well as insight, we proceed first of all by calculating the spectra, and transition energy and oscillator progressions of fluorene and thiophene oligomers ranging from 2 to 16 monomer units in length from DFT-optimised geometries. As with the 2mers discussed in Section 5.1, we perform calculations on molecules with methyls appended to the usual side-chain positions and optimise geometries at the CAM-B3LYP/6-31G* level. For fluorenes, geometries are optimised using methyls while, in order to obtain the correct dihedral minima, we utilise geometries optimised with hexyls of thiophene and replace the hexyls with methyls for subsequent calculations. This procedure is discussed in greater detail in Appendix C. TD-DFT calculations are performed at the B3LYP/6-31G level with 20 states calculated for each geometry and transitions above 5 eV discarded from analysis and generating spectra.

The convergence behaviour of absorption spectra with increasing backbone length can be seen in the optimised geometry calculations shown in Figure 5.6. Figure 5.6(a) shows that, with increasing backbone length, the lowest and dominant transition energy decreases substantially across the 2mer to 8mer range ($\simeq 0.65\,\text{eV}$ and $1.5\,\text{eV}$ overall in fluorene and thiophene, respectively) with further decreases across the 8mer to 16mer range being significantly lower ($\simeq 0.05\,\text{eV}$ and $0.08\,\text{eV}$ respec-

tively). This behaviour is also reflected in the corresponding spectra (Figure 5.6(b) and (d)) which show that, as was the case for the 2mers, the spectra are dominated by the lowest energy transition.

In contrast with the transition energies, the oscillator strengths of these transitions (Figure 5.6(c)) increase linearly with increasing length. This follows from the increasing number of monomers and, in essence, the increasing contribution to the transition amplitude of each transition.

To generate ensemble spectra, we take geometries from MD simulations of 4mers, 8mers, and 16mers of fluorene and thiophene as well as 32mers of thiophene. We omit the 32mer of fluorene due both to the lack of significant statistics in forming end-to-end length distributions (as discussed in Chapter 4) as well as due to the prohibitive computational expense of TD-DFT calculations for such large molecules ($\simeq$ 850 carbons and $\simeq$ 380 hydrogens when taken with methyl side-chains). For fluorenes, we calculate the spectra of 1001 geometries of 4mers and 8mers and 201 geometries of 16mers; the former sampled every 100 ps and the latter every 500 ps. For thiophenes, we calculate 2001 geometries of the 4mers, 8mers, and 16mers (sampled every 50 ps) and 1001 geometries of the 32mers (sampled every 100 ps). The sampling intervals chosen are not representative of the maximum sampling rate which, given the lack of correlation we found between geometries, could be considerably higher. The rate is limited by the computational expense of the calculations though we have found that these rates are sufficient to give well defined spectra. As with the 2mers, the ensemble spectrum in each case is generated following the procedure detailed in Chapter 2.3.4 in which each calculated spectral line is assigned a Lorentzian function with $\gamma = 33$ meV defining the homogeneous broadening HWHM.

At this stage, we note that our calculations do not contain any contributions from vibronic transitions which are well observed in conjugated molecules [26, 98, 108, 262]. Typically, these transitions occur in a progression of $\simeq 0.18$ eV above the dominant S_0-S_1 transition. As these transitions result from phonon coupling, they cannot be immediately extracted from TD-DFT calculations which calculate only direct transitions. Without this feature, however, it is still possible to determine the conformational broadening from the ensemble systems while noting that these additional features would yield an additional, high-energy tail to the broadening.

Absorption spectra calculated from MD ensembles display convergence behaviour similar to that of the optimised geometry spectra. For fluorene (Figure 5.7(a)), the spectral peaks closely agree with those predicted from the optimised geometry calculations with a significant amount of conformational broadening. The progression in thiophene (Figure 5.7(b)) differs significantly from that predicted from optimised geometry calculations. While the 4mer is centred near the optimised geometry energy, the 8mer and 16mer spectra are centred $\simeq 0.4$ eV higher than predicted from the DFT optimised geometries. There is very little difference ($\simeq 0.1$ eV) between the

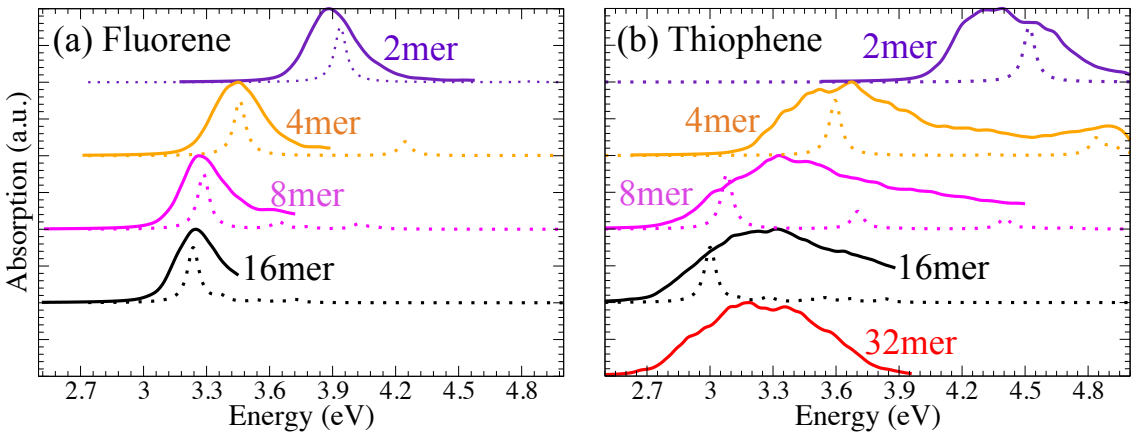

Figure 5.7: Absorption spectra of various lengths of (a) fluorene and (b) thiophene calculated from MD ensembles. For each length, the corresponding spectral profiles obtained from the optimised geometry calculation (as in Figure 5.6) are given by the dotted lines. (Note that, as opposed to the stick spectra in Figure 5.3, no shift has been applied to the optimised geometry spectra)

maxima of the 8mer, 16mer and 32mer which indicates the expected convergence behaviour.

While both displaying converged behaviour, fluorene and thiophene differ significantly in how they compare with the optimised geometry spectra. These differences form the basis of much of the proceeding discussion in this section. One possible reason is that fluorene has a much larger persistence length than thiophene over these length scales as shown in Section 4.3.1. Indeed, as we have omitted the 32mer of fluorene, the persistence lengths of the fluorenes discussed here ($\simeq$ 19 units) are larger or comparable to their molecular lengths. Thiophene, on the other hand, has a persistence length of $\simeq$ 8 units and so the longer lengths of thiophenes are far more susceptible to conformational disorder than the fluorenes. Also, the dihedral angle distributions of thiophenes have shown that near-90° conformations are present whereas they are rare in fluorenes. As shown in Section 4.3.3, any choice of conjugation breaking angle above 40° results in a smaller conjugation length in thiophene than in fluorene. Both the additional flexibility and the likelihood of large dihedral angles are significant in understanding why the convergence behaviour of thiophene is far more pronounced than that predicted solely from the optimised geometries. We discuss both of these points further in Section 5.3.

The ensemble spectra of the fluorene molecules are in good agreement with experimental results. In the work of Schumacher *et al* [98], the absorption spectra of 4mers and polymers of fluorene were shown to have peak absorption at 3.34 eV and 3.19 eV, respectively, in 2-methyl-THF solution. The ensemble peaks of 3.46 eV for the 4mer, and 3.28 eV and 3.24 eV for the 8mer and 16mer, respectively (each taken to match those of the optimised geometry predictions) calculated in this work are in good agreement with experiment. These results also compare favourably with the absorption spectra of PF8 in THF (reported by Grell *et al* to be peaked at $\simeq$ 3.3 eV

Table 5.1: Table of estimated HWHM of the MD ensemble absorption spectra shown in Figure 5.7. Each value is obtained from the difference of the peak energy and the half peak energy on the low energy side.

	Absorption HWHM (eV)	
	Fluorene	Thiophene
2mer	0.12	0.25
4mer	0.13	0.28
8mer	0.11	0.28
16mer	0.11	0.34
32mer	-	0.36

($\simeq$ 410 nm) [51]) and toluene (reported by Knaapila *et al* as peaked at $\simeq$ 3.2 eV ($\simeq$ 390 nm) [52]). To compare linewidths, we compare an equivalent HWHM (defined from the peak to the lower half-maximum due to the asymmetry of the spectra) which was reported as $\simeq$ 200 meV [51] and $\simeq$ 120 meV [52]. These linewidths are in reasonably good agreement with our spectral linewidths for fluorenes as shown in Table 5.1. As the experimental results of Schumacher *et al* were obtained at temperatures 77 K, comparison of linewidths cannot be made in this case both due to the vibronic peaks which are prominent at such low temperatures, and, otherwise, the expected temperature dependence of conformational broadening. We have not found any results for dilute solutions of chloroform though we expect that such results would be similarly comparable.

Experimental absorption spectra of P3HT in dilute solutions of good solvents e.g. chlorobenzene [263], THF [264], and chloroform [47, 265] are typically peaked in the region of $\simeq$ 2.7-3.0 eV with low-energy band edges $\simeq$ 2.3-2.4 eV and linewidths of $\simeq$ 250-450 meV. In particular, Szeremeta *et al* have found that dilute solutions of P3HT in chloroform have absorption spectra peaked at $\simeq$ 3.0 eV with a band edge at $\simeq$ 2.4 eV and a linewidth of $\simeq$ 450 meV, while Bockmann *et al* reported experimental spectra in chloroform peaked at $\simeq$ 2.8 eV with an edge at $\simeq$ 2.3 eV and a linewidth of $\simeq$ 400 meV. We are uncertain as to the nature of the discrepancy between each of these measurements though factors such as the molecular weight, preparation method, and concentration may be the cause.

The absorption spectra calculated from the ensemble of thiophene 32mers, which are to be expected to be sufficiently large as to replicate, to some extent, the spectra of the polymer scale P3HT are in reasonable but not perfect agreement with the above experiments. The overall shape of the spectrum we calculate has a maximum at $\simeq$ 3.2 eV and a band edge at $\simeq$ 2.7 eV and a linewidth of 360 meV. The difference between the peak and band edge as well as the linewidth we obtain indicate that the conformational broadening we observe is in good agreement with experiment though the overall spectrum is blue-shifted in comparison by $\simeq$ 0.2-0.4 eV. There are a number of possible factors which could contribute to this. For example, while

we have found that the inclusion of PCM solvent treatment has little effect on spectra, a more detailed solvent treatment, such as an explicit solvent treatment, may lead to a reduction of this error. However, we believe that the primary cause is the slight inaccuracy of the thiophene force-field near the minima which are 5°-10° closer to 90° in our force-field than in optimised geometries. As shown in Figure 5.1(a), the S_0-S_1 transition energy is most sensitive to variations in dihedral angles in the 30°-60° region in which the minima are.

We note that the peak of calculated spectrum obtained by Bockmann *et al* [47] using their version of this MD ensemble technique for thiophene 32mers gives better quantitative agreement with the peak of their experimental result. Their results give a spectrum peaked at 2.9 eV with a band edge at 2.1 eV compared with the experimental 2.8 eV and 2.3 eV respectively. However, we feel that this agreement is fortuitous given their methodology. The first concern is in their determination of the dihedral potential of thiophene which is performed by simply matching the height of the 90° barrier without concern for the effect of the side-chains. This is reflected in the dihedral distributions they obtain from their simulations which bear little resemblance to the qualitative predictions of the DFT potential. Furthermore, they obtain their spectrum by calculating 10 individual spectra taken from the second half of a 2 ns production run. This is in stark contrast to the 1000 individual spectra taken over a 100 ns run that we have employed and found necessary to obtain suitable statistics across all other properties such as the end-to-end length, dihedral angle distributions, and correlation functions. As such, we believe that they have notably under-sampled their simulations. This is reflected in the end-to-end length distribution they obtain, which is sharply peaked at $\simeq$ 100-105 Å with a total range of $\simeq$ 20 Å. This corresponds to an end-to-end length fraction of $\simeq$ 0.79-0.83 and a range of $\simeq$ 0.25. From our results shown in the Chapter 4, we find much smaller end-to-end length fractions and a much broader end-to-end length distribution peaked at a fraction of $\simeq$ 0.72 with a total range of $\simeq$ 0.66. By comparison, the distribution obtained in their work is far closer to that of the thiophene 16mer of this work (though still considerably narrower) and, assuming that the equation of Wilhelm and Frey (Eq. 4.10) [118] holds, this indicates a persistence length around double that calculated in this work and, thus, around double that predicted by experiment. The biasing towards longer conformations seems, to us, the reason why their result seems to give better agreement with the experiment in allowing for a larger red-shift overall. We also note that their calculations include a PCM treatment of the chloroform solvent though we have found, with ensemble spectra calculated from 16mers of thiophene using B3LYP with PCM, there is only a marginal ($\sim$ 50 meV red-shift) observed as is the case with the equivalent optimised geometries (as discussed briefly in Section 5.1.1.

One curious result regarding the ensemble spectra is that the conformational

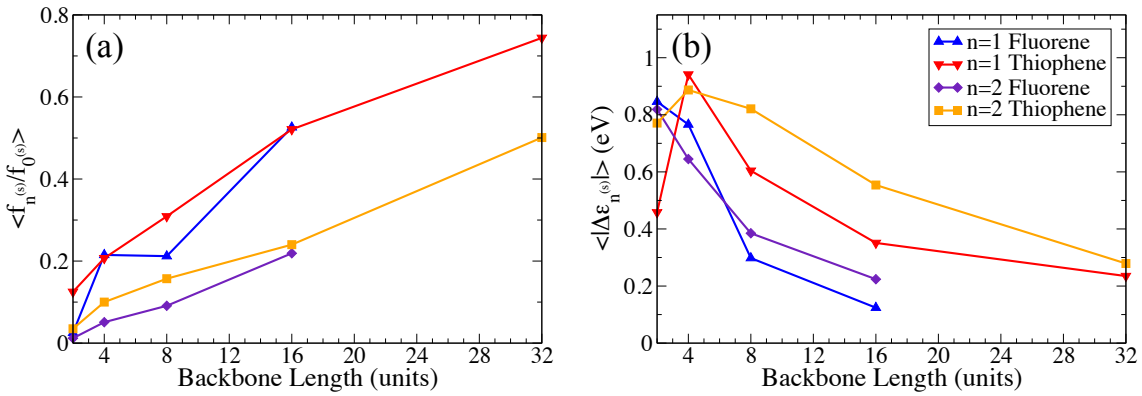

Figure 5.8: Average properties of states of second and third highest oscillator strengths ($n^{(s)}$; $n = 1$ and $n = 2$ respectively) for various lengths of fluorene and thiophene molecules obtained from MD ensembles. (a) Average ratio of oscillator strengths compared to the dominant transition $0^{(s)}$ given by $\langle f_{n^{(s)}}/f_{0^{(s)}}\rangle$. (b) Average separation given by $\langle|\Delta\epsilon_{n^{(s)}}|\rangle \equiv \langle|\epsilon_{n^{(s)}} - \epsilon_{0^{(s)}}|\rangle$. (Legend in (b) applies to both graphs. Lines are intended as a guide to the eye.)

broadening of the dominant absorption feature does not vary considerably with increasing backbone length and remains similar to that of the 2mer. In Table 5.1, estimated HWHM values of each spectrum, taken taken from the peak to band edge, are given. In fluorene, each length of molecule has a HWHM of $\simeq$ 0.1-0.12 eV while each length of thiophene has a HWHM of $\simeq 0.25 - 0.35$ eV. Naïvely, it would be expected that the dihedral broadening seen in the 2mer would progress multiplicatively with an increase in the number of dihedral centres. That this is not the case suggests that the effect of each dihedral angle cannot be equivalent to that of the of the 2mer individually. Thiophenes also have extended, high-energy tails in their spectra for lengths greater than 2mer. The tail of the 4mer has a peak associated closely with that of the optimised geometry spectrum. As such, the particularly large tail in the 8mer can be viewed as resulting from secondary features which are separated at $\simeq$ 0.6 eV (comparable to the FWHM of the dominant peak). This explanation does not, however, capture the full extent of the broadening given that this explanation cannot account for the full tail of the 4mer. As we shall discuss in the following section, both of these high energy tails can be accounted for with a better understanding of dihedral angle broadening.

The optimised geometry calculations predict transitions which are largely dominated by the S_0-S_1 transition. However, as we found with the 2mers, conformational variation in the ensemble leads to the emergence of secondary states. In Figure 5.8(a), we show the progression of the average values of the ratios of the $1^{(s)}$ and $2^{(s)}$ states to the $0^{(s)}$ states, $\langle f_{n^{(s)}}/f_{0^{(s)}}\rangle$, (again, adopting the superscript (s) to denote states sorted by descending oscillator strength) and find that both averaged ratios increase with increasing backbone length. Furthermore, the corresponding average absolute energetic separations, $\langle|\Delta\epsilon_{1^{(s)}}|\rangle \equiv \langle|\epsilon_{1^{(s)}} - \epsilon_{0^{(s)}}|\rangle$, shown in Figure 5.8(b) display a corresponding decrease with increasing backbone length. An exception to

this trend is between the 2mer and 4mer of thiophene which we believe to be an artefact of the reduction of available data points due to the imposition of the 5.0 eV spectral cut-off.

In the previous section, we found that large dihedral angles brought about this splitting behaviour by creating partitions in the molecule. That this behaviour becomes more and more prevalent in longer molecules follows from the numerous ways partitioning can occur e.g. due to the large dihedral angles or sharp bends at different sections of a given molecule.

The results of this section have illuminated key features of the spectral properties resulting from conformational variation. As expected, the general trend of the absorption spectra to progress from higher energy peaks to lower energy peaks is replicated in a conformationally disordered ensemble. Interestingly, we found that inhomogenous broadening of the S_0-S_1 transition does not increase as signficantly with increasing length as would be expected given the base dihedral broadening of the 2mer. This means that the dihedral-dependent broadening of the 2mer cannot be treated as having a multiplicative effect in molecules with more than a single dihedral angle. To better understand the mechanics of broadening due to the individual dihedral angles in longer molecules, we shall now return to a dihedral-scan based investigation for molecules longer than 2mers.

5.2.2 Dihedral broadening in oligomers

In the previous subsection, we found that the conformational broadening of the primary absorption feature does not vary significantly with increasing lengths and, in Section 5.1.1, we showed that the dihedral angle is the primary source of the conformational broadening in 2mers. To assess the role of dihedral angles in molecules longer than 2mers, we have performed similar geometry scan calculations for varying dihedral angles of 4mers. In an analogous manner, we perform geometry scans of a given dihedral, optimising at the CAM-B3LYP/6-31G* level, while fixing the remaining dihedral angles at a given value, and calculate spectra using B3LYP/6-31G.

We choose 4mer molecules so as to offer insight into both the effect of an increase in backbone length as well as the effect of neighbouring dihedral angles and the effect of the dihedral position itself on the transition energies (in a similar manner as our steps towards determining the length invariance of dihedral potentials in Section 3.1.3). Each 4mer is comprised of three dihedral angles: the end-most dihedrals, ϕ_1 and ϕ_3, and the central dihedral, ϕ_2. To assess the above effects, we have performed scans, as shown schematically in Figure 5.9, over ϕ_1 with ϕ_2 fixed at 0° and 90° and vice-versa with ϕ_3 fixed to either 0° or 90° and obtained the S_0-S_1 transition energies as a function of an individual dihedral angle for a given combination of neighbouring dihedral angles.

The trends in the lowest energy transitions of scans of fluorene 4mers are shown

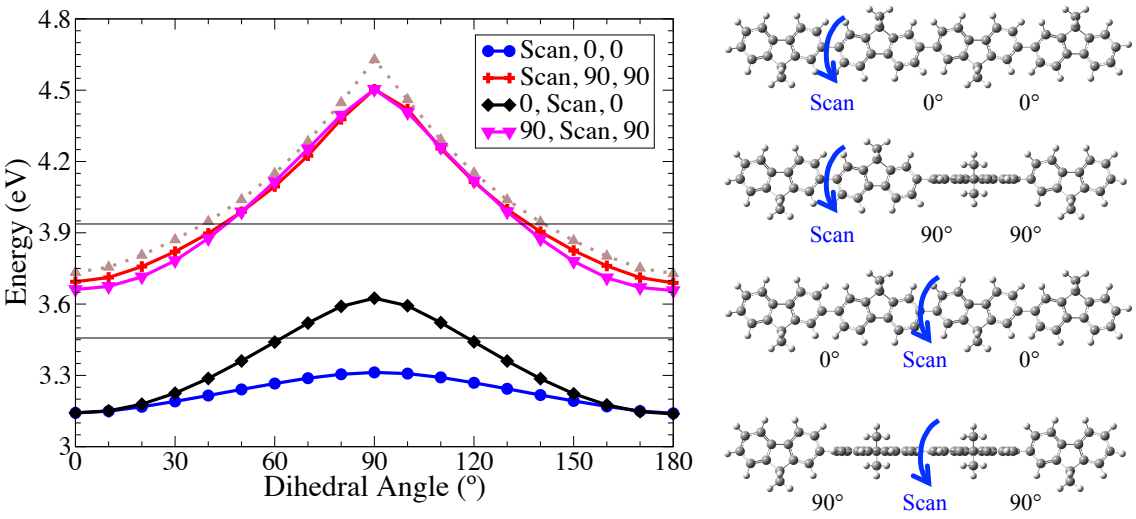

Figure 5.9: S_0-S_1 transition energies of fluorene 4mers as a function of individual dihedral angles. The diagrams on the right indicate the scanned dihedrals and the values the remaining dihedrals are fixed at. In the graph, the S_0-S_1 transition energy for the optimised 2mer and 4mer are given by the lines at 3.937 eV and 3.457 eV respectively. The dihedral trend of the transition energies of the 2mer (brown triangles) is shown for comparison.

in Figure 5.9. The four trends shown are those for scans over one end dihedral (ϕ_1) and the central dihedral (ϕ_2) with the other dihedrals fixed to 0° or 90°. Each case shows differing behaviour. Comparing the trends of the ϕ_1 and ϕ_2 scans when the other dihedrals fixed at 0°, we note that changes in ϕ_2 lead to a considerably greater increase in the S_0-S_1 transition energy than changes in ϕ_1. In contrast, when all other dihedrals are at 90°, both ϕ_1 and ϕ_2 have a similar effect on the S_0-S_1 transition energy. Interestingly, in this case, the trend is comparable to that of the 2mer molecule (as shown, for comparison, in Figure 5.9). On the other hand, when all other dihedrals are 0°, variations in both dihedrals lead to changes in the S_0-S_1 transition energies which are significantly less than that of the 2mer.

The above result demonstrates two interesting and crucial features of the dihedral angle dependence of the transition energies. First, it is possible that each of the dihedral angles in a given molecule can have differing effects on the S_0-S_1 energies. Secondly, the effect of the dihedral angles is also dependent on the values of the other dihedral angles. To further demonstrate this point, we have performed similar calculations for 8mers of fluorene with the trends shown in Figure 5.10. Again, we have considered the extreme cases in which all other dihedral angles are set to 0° or 90° (Figure 5.10(a) and (b), respectively) and, again, we see similar behaviour. When all other dihedral angles are set to 0°, each dihedral angle has a differing effect on the S_0-S_1 transition energy with the end-most dihedral angles having less of an effect than the central dihedrals. It can be seen from these trends that each dihedral angle has more of an effect the closer it is to the centre. However, as was the case in the 4mer, when all other dihedral angles are 90°, each dihedral angle has a similar

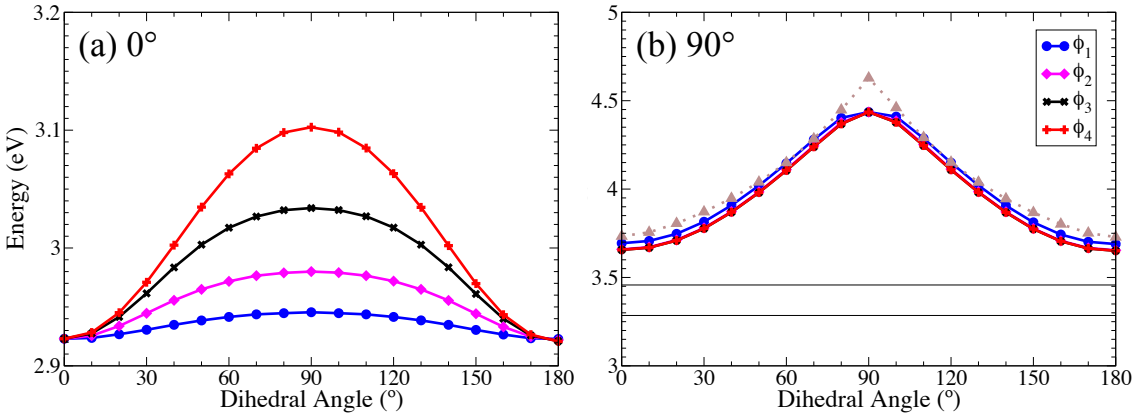

Figure 5.10: S_0-S_1 transition energies of fluorene 8mers as a function of four dihedral angles with all other dihedral angles set to (a) 0° and (b) 90°. In (b), the lowest transition energy for the optimised 4mer and 8mer are given by the lines at 3.457 eV and 3.285 eV, respectively, and the dihedral trend of the transition energies of the 2mer is also shown (brown triangles). Note the different energy scales in each graph.

Table 5.2: Maximum dihedral absorption ranges (MDARs), $\Delta\epsilon_{90} \equiv \epsilon_{90} - \epsilon_0$, of 4mers and 8mers of fluorene and thiophene. For each scanned dihedral, the range is given for all other dihedrals fixed to 0° and 90° as labelled on the left.

MDAR, $\Delta\epsilon_{90}$, of 4mers and 8mers (meV)												
	Fluorene						Thiophene					
	4mer		8mer				4mer		8mer			
	ϕ_1	ϕ_2	ϕ_1	ϕ_2	ϕ_3	ϕ_4	ϕ_1	ϕ_2	ϕ_1	ϕ_2	ϕ_3	ϕ_4
0°	170	483	22	57	111	180	346	734	72	187	348	522
90°	810	842	742	777	779	780	711	817	632	757	780	786

effect on the transition energy and, again, this effect is similar in magnitude to the 2mer.

As with the 2mers, it is convenient to quantify the range of S_0-S_1 energies covered by each dihedral angle. To do so, we use the 'maximum dihedral absorption range' (MDAR) measure defined in Section 5.1.1 by $\Delta\epsilon_\phi \equiv \epsilon_{90} - \epsilon_0$. In Table 5.2, MDARs are given for 4mers and 8mer of fluorene and thiophene. Considering the 0° dihedral cases, the MDAR values further demonstrate that the central dihedrals have a larger effect on the S_0-S_1 transitions than the outer dihedrals in both fluorene and thiophene. For the fluorene 8mer, the MDAR of the central dihedral, ϕ_4, is a factor of $\simeq 8$ greater than that of the end-most dihedral, ϕ_1, and this same factor $\simeq 7$ for the thiophene 8mer.

When compared to the 2mer, the 0° cases of fluorene 8mers have MDARs which are substantially less than that of the 2mer ($\Delta\epsilon_\phi = 895$ meV) even for the central dihedral. For thiophene, this is also true but to a considerably lesser extent. This follows given that thiophene units are a factor of $\simeq 2$ smaller than fluorene units. However, in the 90° cases, the MDARs of both molecules are comparable to the corresponding 2mer MDAR.

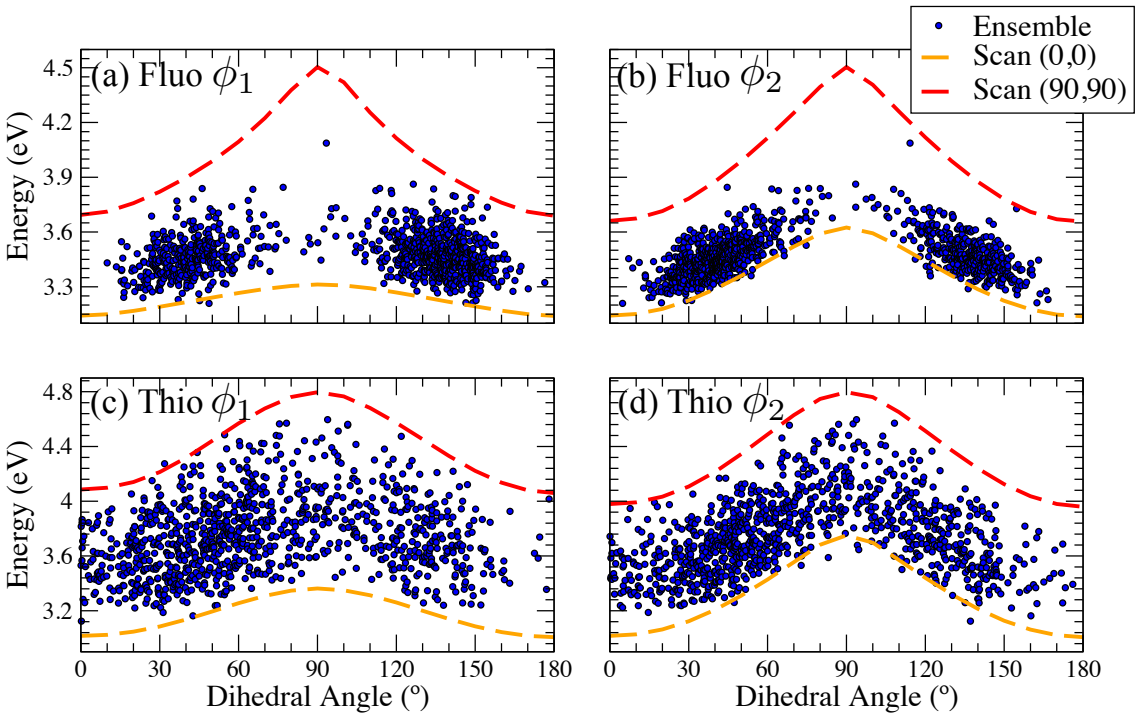

Figure 5.11: S_0-S_1 transition energies of (a)-(b) fluorene, (c)-(d) thiophene 4mers as a function of ((a), (c)) the end-most dihedral, ϕ_1, and ((b), (d)) the central dihedral, ϕ_2. The legend in (b) applies to all graphs where the 'Scan' corresponds to the labelled dihedral of that graph and the remaining values corresponding to the fixed values (ϕ_2, ϕ_3) or (ϕ_1, ϕ_2), accordingly.

These results have significant implications for the expected broadening in each molecule. It is clear that the dihedral angles each have differing effects which are highly dependent on the neighbouring dihedrals. In addition, in planar configurations, each dihedral angle has a significantly lesser effect than the individual dihedral angles in primarily 90° configurations. Essentially, as the 90° configurations recover a 2mer-like range of transition energies, the overall broadening would, perhaps, be expected to be greater than that of the 2mer; a feature not observed in the ensemble spectra of Figure 5.7. However, when one considers the probability of the 2mer-like dihedral angle dependence i.e. the probability of all but one dihedral angle being at 90°, this 2mer-like broadening will become increasingly unlikely for longer length scales. Thus, the broadening is determined by the planar-like ranges which, individually, are far less than that of the 2mer. This forms the key point of this subsection: that broadening is near constant with increasing length scales due to the weakening of the effect of individual dihedral angles.

In order to demonstrate the above point, we present the S_0-S_1 transition energies as a function of the end-most (ϕ_1) and central (ϕ_2) dihedrals of ensembles of fluorene and thiophene 4mers in Figure 5.11. The spread of these energies is consistent with the results of the DFT scan calculations in that, in both cases, the transition energies display greater correlation with ϕ_2 than ϕ_1 - thus indicating that the effect of ϕ_2 is more significant. In each example, the trends of the transition energies with respect

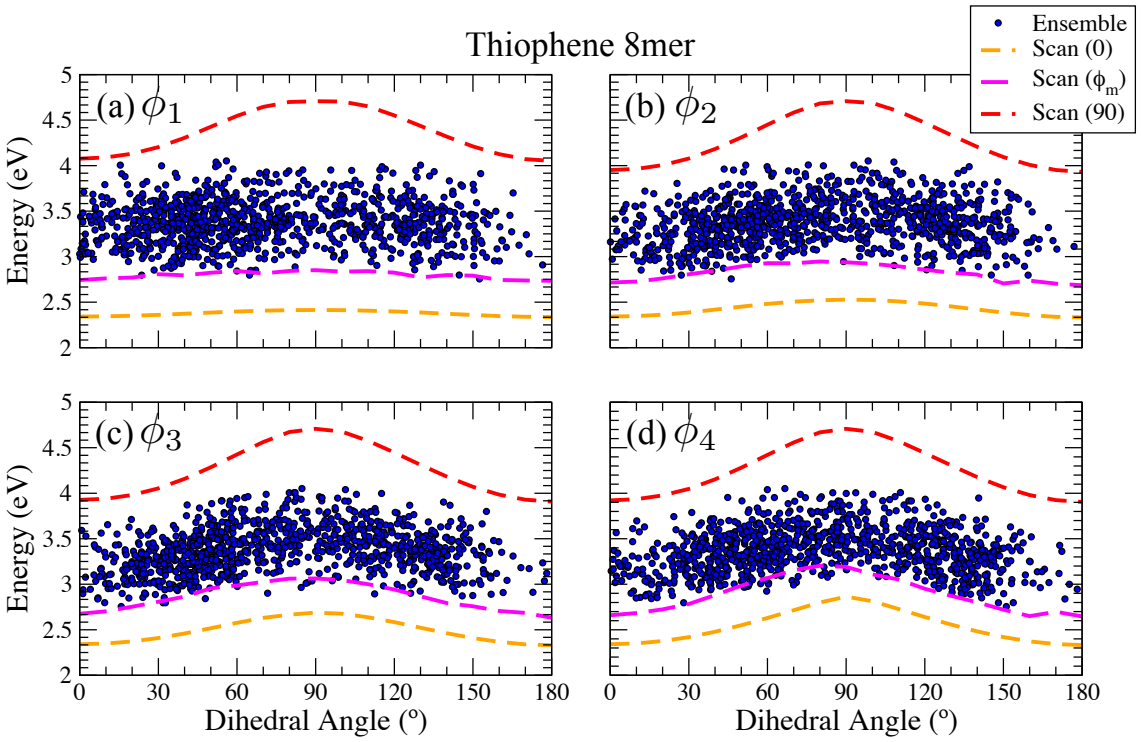

Figure 5.12: S_0-S_1 transition energies of 8mers of thiophene obtained from ensemble geometries. In each panel, the energies are plotted as a function of a particular dihedral angle with comparison to the prediction from dihedral scans with all other dihedrals set to either 0° or 90°, or free to optimise (ϕ_m). Legend in (b) applies to all graphs.

to dihedral rotation for the planar and 90° cases are given. These trends indicate the predicted lower and upper bounds, respectively, in each case and, thus, the available range of transition energies. For fluorene (Figure 5.11(a) and (b)), the transition energies occupy only the low energy region of this range, while those of thiophene (Figure 5.11(c) and (d)) are well spread across it. As follows from the dihedral angle distributions discussed in Section 4.2.2, the lack of near-90° conformations is responsible for the lack of higher S_0-S_1 transitions in fluorene.

It is clear that, as would be expected, the large broadening associated with configurations of many near-90° dihedrals is not observed in fluorene. Instead, what occurs is the lower scale of dihedral broadening associated with the lower dihedral angles. Thus, the lack of any notable increase or decrease in broadening with increasing length is the result of each increase in length scale resulting in a sum of changes which, loosely, equates to that of the 2mer ensemble. In thiophene, the distribution of transition energies occupies some of the near-90° broadening range. For 8mers, however, this is no longer the case. In Figure 5.12, the transition energies no longer occupy both the lower and higher energy regions of the available range. While the probability of large dihedral angles is much larger in thiophene than fluorene, the probability of conformations comprised solely of large dihedral angle decays exponentially in the number of units. As such, the full range of tran-

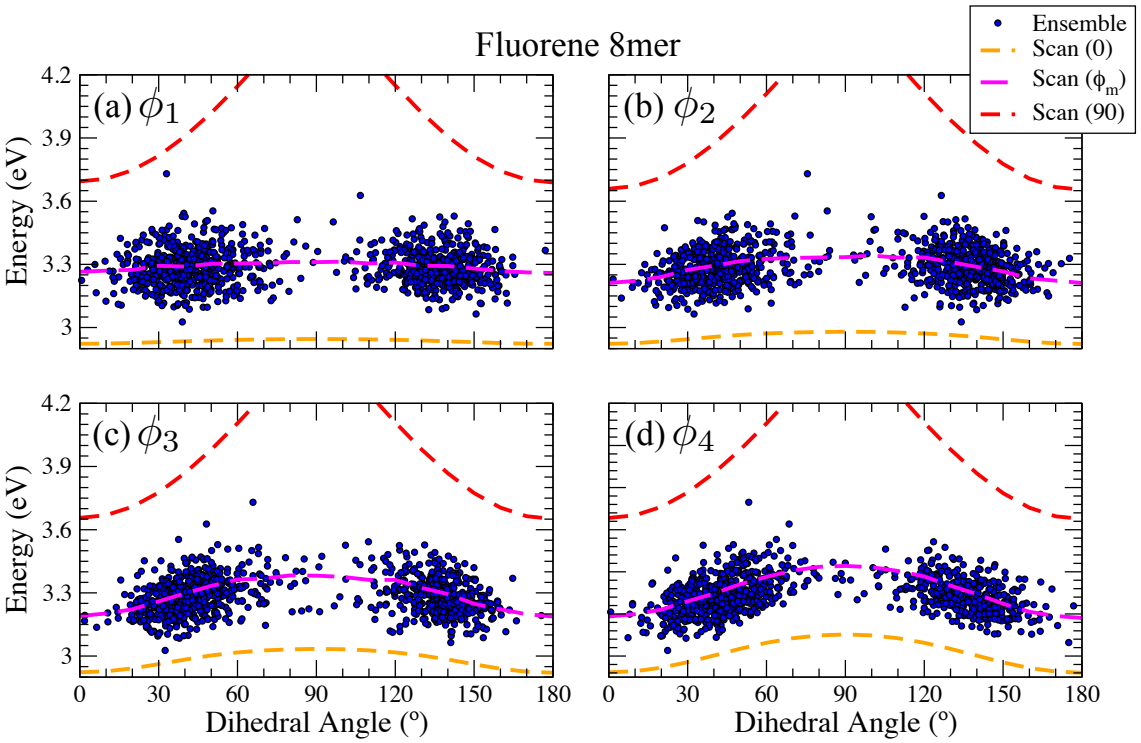

Figure 5.13: S_0-S_1 transition energies of 8mers of fluorene obtained from ensemble geometries. In each panel, the energies are plotted as a function of a particular dihedral angle with comparison to the prediction from dihedral scans with all other dihedrals set to either 0° or 90°, or free to optimise (ϕ_m). Legend in (b) applies to all graphs.

sition energies available to an 8mer of thiophene is unlikely to be fully explored by the thermodynamically available conformations.

Comparing the 8mers to the 4mers, the correlation of the S_0-S_1 energies with the central and most significant dihedral is reduced. This is observed both in thiophene as well as for fluorene (Figure 5.13). While in both cases the transition energies show greater correlation with ϕ_4, the central dihedral, than ϕ_1, the end-most dihedral, the correlation is still weak compared with the overall spread of energies. This results from the reduction in the significance of the central dihedral in the 8mers when compared to, for example, the next-from-centre dihedral, ϕ_3. This further demonstrates that broadening is the result of the cumulative effect of each dihedral angle with each individual contribution reduced for increasing lengths of molecule.

It is clear then that the role of dihedral angles in absorption spectral broadening is complex. We have shown so far that that the effect of dihedral angles in longer molecules is dependent both on molecular length but also on the other dihedral angles in the molecule. Particularly, we noted that in configurations with large dihedral angles, the range of available S_0-S_1 energies becomes comparable to that of a 2mer. As we go on to discuss in the following, a great number of the above features are linked to excitation localisation due to conformational disorder.

5.3 Conjugation breaks and excitation localisation

The ensemble spectra and their dihedral dependent properties shown in the previous section display a number of peculiar properties. First of all, in thiophenes, there is a significant blue-shift of the ensemble spectra with respect to that of the optimised geometry predictions when considering molecules $\gtrsim 8$ units in length. Also, the behaviour of the transition energies with respect to dihedral angles suggests that it is often the case that central dihedral variations produce the greatest variations in energy but, in certain cases, variations in other angles can lead to large changes in the overall excitation energies. As we alluded to in our previous discussions, these effects can be understood by considering how optically formed excitations localise with respect to various areas of the molecule.

A principle advantage of the MD ensemble approach is that it allows us to tackle the problem of understanding excitation localisation resulting from thermodynamically generated distortions. With an ensemble of geometries, each with an associated differential density, utilising a suitable measure allows us to ascertain the spatial extent of a given excitation and its location along the molecule. In essence, we can utilise this technique to give a new definition of an effective conjugation length based on the actual, calculated delocalisation across the molecule as opposed to the assumption of an arbitrarily large dihedral angle or a perfectly undisturbed system previously used [90, 91].

In the remainder of this section, we present a measure of delocalisation across molecules based on utilising partial charges obtained from the ground-state, S_0, and unrelaxed excited-state, S_1^*, electronic densities - a measure which may be readily applied to any linear polymer. The measure employed operates as an extension of the 'radius of gyration' approach utilised by Makhov and Barford [89,95] in conjunction with density-matrix renormalisation group DMRG calculations to determine exciton delocalisation. We introduce this measure and a definition of an excitation centre in the following subsection (Section 5.3.1) and determine trends with increasing molecular length both from optimised geometries - which represent the idealised, near-fully delocalised systems - and from the ensemble - where conformational disorder is seen to have a significantly localising effect. From this, we again utilise the examples of 4mers and 8mers from optimised dihedral scans to understand how dihedral angles mediate excitation localisation. These results offer insight into a wide variety of future applications and a foundational understanding of localisation phenomena in larger, considerably more distorted, molecules.

5.3.1 Excitation localisation

In order to investigate the location and spread of differential density, we first calculate the component of the differential density associated with each atom by cal-

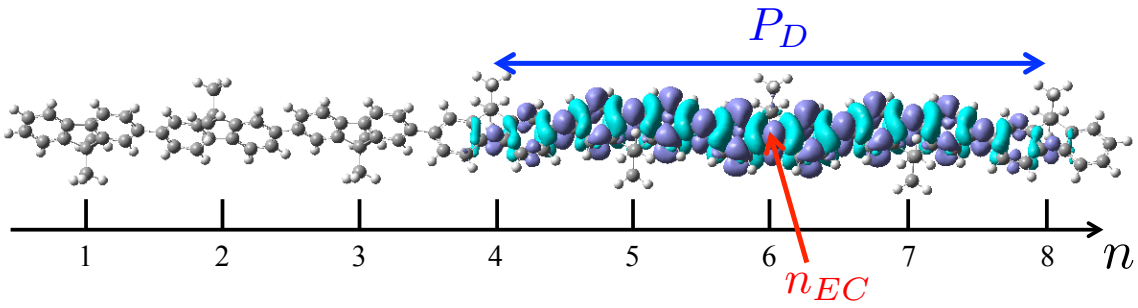

Figure 5.14: Illustration of the delocalisation, P_D, and excitation centre, n_{EC}, measures and their interpretation for an absorption excitation in an 8mer of fluorene. In this example, $P_D \simeq 4$ and $n_{EC} \simeq 6$.

culating ESP atomic charges (see Chapter 2.3.4) for both the ground and excited state electronic densities, $q_i^{(S_0)}$ and $q_i^{(S_1^*)}$ respectively for an atom i. We then sum over the absolute values of their differences for all m atoms in a given monomer, n, to a from a total monomer absolute charge difference, Q_n:

$$Q_n \equiv \sum_{i=1}^{m} \Delta q_i \equiv \sum_{i=1}^{m} |q_i^{(S1)} - q_i^{(S0)}|. \tag{5.1}$$

We form this definition using absolute values as the following approach requires the use of, essentially mass-like, positive values. This requires taking either all positive values, all negative values, or absolute values. For the following calculations, we have found that any choice of the three is valid and gives essentially the same information. We choose absolute values so as to maximise the number of data points and, thus, reduce the overall error in generating sums over all atoms in the monomer.

Each value of Q_n forms a representation of the S_0-S_1^* differential density on its corresponding monomer. This can be used to define an effective centre of the excitation in a manner similar to that of a centre-of-mass. We denote these 'excitation centres' by n_{EC}. This definition then allows for the definition of the distance (in monomer units), Δn, between a given monomer, n and the excitation centre, n_{EC}:

$$\Delta n \equiv n - n_{EC}; \qquad n_{EC} \equiv \frac{\sum_{n=1}^{N} Q_n n}{\sum_{n=1}^{N} Q_n}. \tag{5.2}$$

In the following analyses, we are concerned with the localisation and delocalisation of the excitation along the axis of the chain and, in particular, where it is situated with respect to the constituent monomers. As such, in the above, we have reduced the dimensions of the monomer positions and, thus, n_{EC} to those of individual monomers. As such, n_{EC} and Δn are dimensionless.

In defining a n_{EC}, we can study the delocalisation of the excited state differential density along the axis of the molecule. A simple means of doing so is invoking a delocalisation measure, P_D:

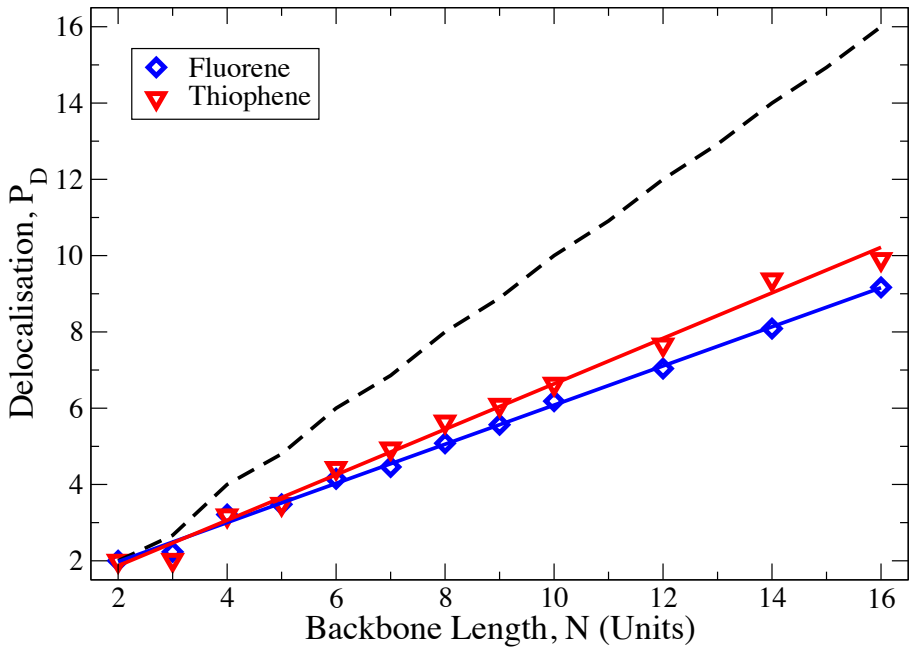

Figure 5.15: Delocalisation, P_D (Eq. 5.3), for DFT optimised geometries of fluorene and thiophene of increasing length. For each molecule, a linear line of best fit is given with a gradient of 0.513 and 0.596 for fluorene and thiophene, respectively. The black dashed line represents a perfectly delocalised system, $P_D = N$ and $P_D = N - 1/N$ for N even and odd, respectively, of each length

$$P_D \equiv 4\frac{\sum_{n=1}^{N} Q_n|\Delta n|}{\sum_{n=1}^{N} Q_n}. \tag{5.3}$$

As is discussed in greater detail in Appendix C, this measure gives a value of $P_D = N$ and $P_D = N - 1/N$ for a uniformly delocalised system (i.e. $Q_n = Q \,\forall\, n$) of N units with N even and odd, respectively, while also weighting and normalising each monomer by its respective charge.

For reference, Figure 5.14 contains an example excitation in an 8mer of fluorene. In this example, the excitation is spread over approximately four units (three full units and two half units) and is centred at unit six. These observations are reflected in the calculated values of P_D and n_{EC}. Thus, P_D is simply interpreted as a measure of the delocalisation of an excitation corresponding to the number of units an excitation is spread over and n_{EC} gives the location of the excitation along the chain axis.

As a reference prediction, we have calculated the delocalisation of the differential densities of optimised geometries of fluorene and thiophene and find a linearly increasing trend of delocalisation with increasing backbone length. The trends for each are shown in Figure 5.15 and compared to the trend of evenly delocalised systems. For both molecules, the gradient of the increase is less than that of the evenly delocalised measure which is representative of the differential densities being localised more towards the centre of each molecule than the ends. As the optimised

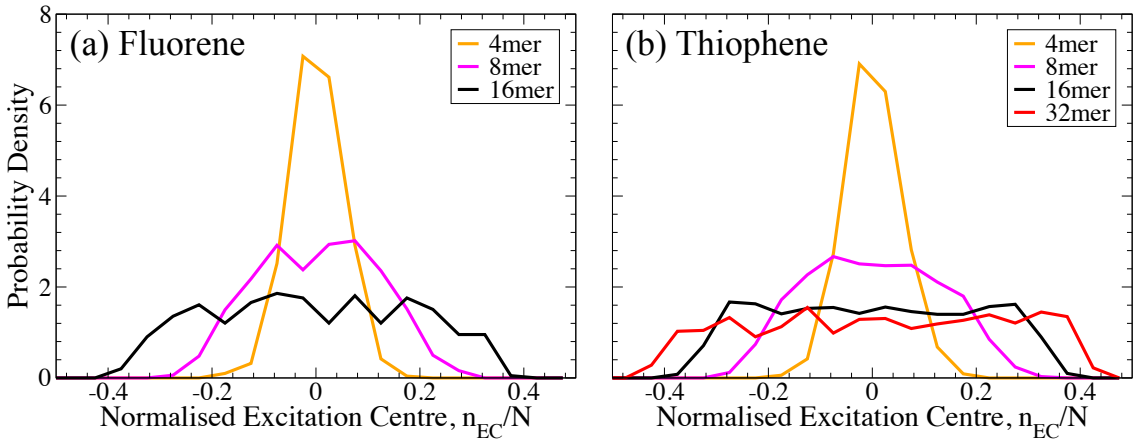

Figure 5.16: Distributions of normalised excitation centres obtained for ensembles of various lengths of (a) fluorene and (b) thiophene. The normalisation is such that the excitation centres, n_{EC}, range from -0.5 to 0.5 with the centre of the molecule at 0.

geometries are perfectly straight, these calculations offer a reference in terms of monomer units for the delocalisation of differential densities for distorted ensemble geometries.

The centres of charge for each excitation in the optimised cases are almost entirely in line with their corresponding centres of mass (with a RMS deviation of 3% and 5% for fluorene and thiophene respectively). This follows immediately from the rodlike, symmetric geometries considered.

Both the results for the calculated delocalisation and excitation centres give an idealised picture of systems with effectively no conformational disorder and show that excitation density will spread out increasingly and evenly along the molecular axis without any local disorder to inhibit it. This shows that while the optimised geometry calculation regime is capable of accurately representing the optical response of these molecules (provided that inhomogeneous broadening is accounted for phenomenologically), the well observed and discussed [90, 91, 103] notions of exciton localisation and effective conjugation lengths are not captured by these calculations alone. This type of analysis lends itself to the use of the MD simulation regime so as to capture the effect of real conformational disorder and, in turn, its effect on excitation localisation.

In the same manner as with the above optimised geometry calculations, we calculate both the excitation centres and delocalisations for each geometry for the MD ensembles of fluorene and thiophene of various lengths. The distributions of excitation centres are shown in Figure 5.16. For clarity of comparison, the excitation centres are shown as a fraction of the molecular length ranging from -0.5 to 0.5. The distributions of excitation centres of the 2mers (omitted from the figures) are sharply peaked at 0 as would be expected. With increasing length, the distributions become increasingly broad with the excitation centres being located up to 40% of

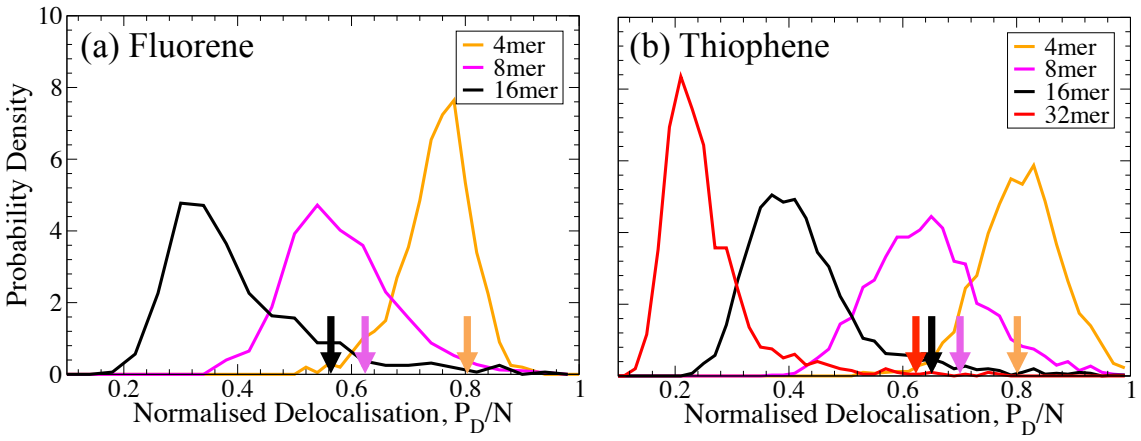

Figure 5.17: Distributions of normalised delocalisations, P_D/N obtained for ensembles of various lengths of (a) fluorene and (b) thiophene.

the molecule away from the molecular midpoint in the 16mers and up 45% in the 32mer of thiophene. This shows that there is a strong tendency towards excitation localisation for increasingly long and disordered molecules.

The shape of the distributions for the 8mer and above show an almost even spread of the probability of the excitation centre being located across the molecule within a given range. In absolute terms, the ranges are consistently up to $\simeq 2$ units from each end of the molecule. This indicates that the inner units are more preferential for forming excitations than the outer four. However, the shape of the distributions also indicates that, beyond these outer units, there is no overall preference to any particular region of a molecule.

In Figure 5.17, the distributions of the normalised delocalisation, P_D/N, are given. For comparison, the associated values of P_D/N obtained from the corresponding optimised geometries are highlighted. It can be seen that the progressions of the delocalisation peaks of the ensemble distributions differ considerably from the linear trends predicted from the optimised geometries with the peaks of the ensemble distributions following a logarithmic progression. This progression indicates that the increase in backbone length and the available conformational disorder are responsible for forming substantially localised excitations. In addition, the spread of the P_D/N distributions is near constant with increasing length. This corresponds to an effectively linear increase in the spread of the absolute delocalisation distributions and, thus, the range of molecular lengths over which excitations are typically delocalised.

In both fluorene and thiophene, the delocalisation of 4mers is close to that of the optimised geometries and typically covers the majority of the molecule. While the optimised geometry prediction for both molecules is effectively the same for the 4mer, thiophene is skewed more towards $P_D/N = 1$ than fluorene. This is due to the higher probability of split excitation densities resulting from near 90° central dihedrals which we discuss in the following section. Both 8mers typically

have excitations which are spread across more than half of the molecule while in 16mers and, for thiophene, 32mers become notably localised ($P_D/N < 1/2$).

Comparing the distributions of n_{EC} and P_D of fluorene and thiophene shows the two to have similar delocalisation features. This is somewhat surprising given the difference in the dihedral angle distributions, and thus in their tendency to form chromophores based on conjugation breaks, and their persistence lengths. In comparison to the persistence lengths, n_p = 18.5, 8.6, and 8.5 units for the fluorene 16mer, and thiophene 16mer and 32mer, respectively, the peak delocalisations, $\simeq$ 4.8, 6.3, and 6.4 for the above, respectively, are smaller in all cases. Also, the delocalisation for fluorene is less than that of both thiophenes while the persistence length is more than double those of the thiophenes. This forms a significant conclusion with regards to the spectral properties in that excitation localisation cannot solely be the result of conjugation-breaking dihedral angles or, in the good solvent regime, the result of chain-flexibility. This is one of the central results of this chapter.

From the above, we have ascertained statistical distributions pertaining to the localisation and spreading of excitations formed by absorption processes. As expected, conformational disorder plays a key role in excitation localisation. The result and the manner in which it is obtained is a key result as it both sets out an original method in analysing excitation formation and offers quantitative insight into the effect of disorder on these processes. This type of analysis is also easily generalisable to any number of polymer systems. With this scheme and the above results discussed, we now aim to understand exactly how conformational disorder leads to localisation and, particularly, which forms of disorder leads to preferential regions for the differential density.

5.3.2 Influence of dihedral angles on excitation localisation

Localisation phenomena across any system are typically the result of a region of a system having a some favourable property which distinguishes it from other regions. In other words, localisation is generally the result of some symmetry being broken. A particularly clear example of this behaviour was shown by Montgomery *et al* [103, 104] in star-shaped oligofluorene-truxene conjugated complexes in which slight distortions in any of the three oligofluorene arms cause excitations to localise on or avoid a particular arm. Also, the concept of the conjugation break and conjugation length widely utilised in rationalising the formation of chromophores on conjugated molecules [90,91] is generally considered to be a dihedral angle dependent behaviour. The results of the previous section show that conformational disorder leads to the localisation of formed excitations upon absorption. To better understand how this occurs, in this section we present calculations of the delocalisation properties of DFT optimised geometries of 4mer and 8mer molecules of varying dihedral angles. In the same manner as in Section 5.2.2, we use the results obtained from these

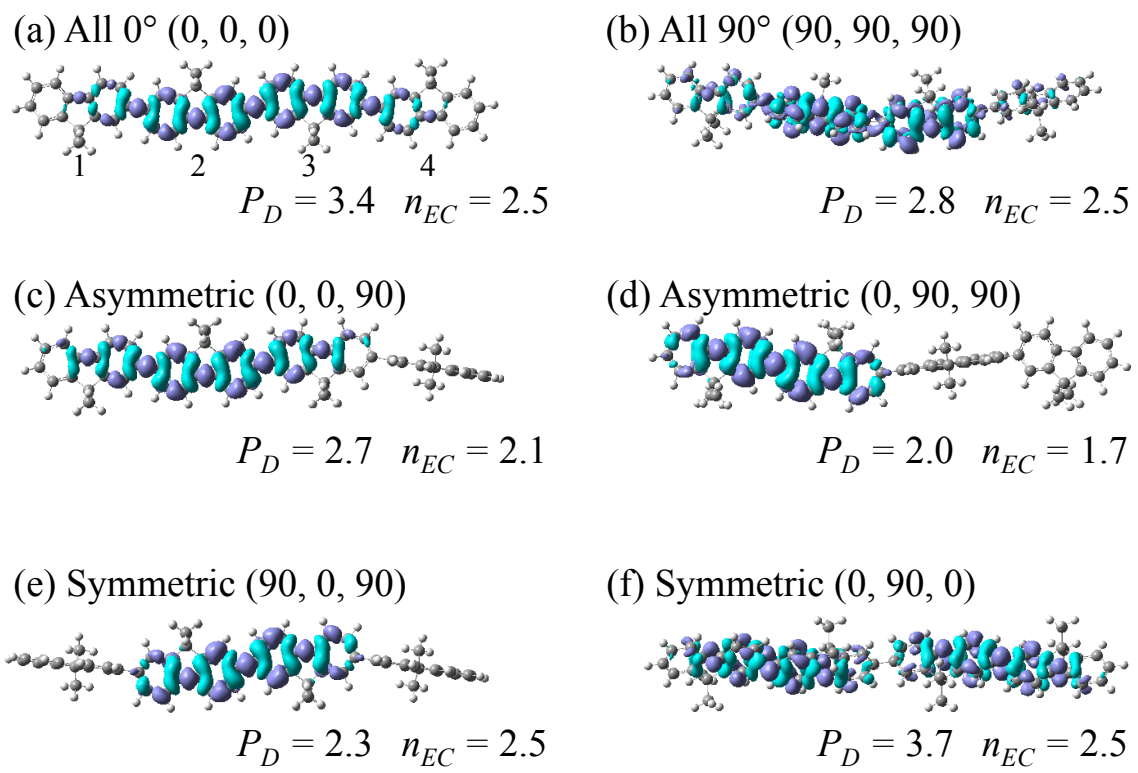

Figure 5.18: Differential densities and corresponding delocalisation, P_D, and excitation centre, n_{EC}, measures of DFT optimised fluorene 4mers. Each case is labelled according to the value of the three dihedral angles (given in brackets) and a label used in the main text. In (a), the monomer indexing (in which n_{EC} is expressed) is given and applies to each case. Note that $n_{EC} = 2.5$ represents a perfectly centred excitation density.

reduced examples to develop an understanding of the phenomena seen from the MD ensemble calculations.

In the following, we present a series of delocalisation measures and excitation centres, P_D and n_{EC}, respectively, as defined in the previous section for a number of cases of DFT optimised fluorene 4mers. With these calculations, we aim to assess the effect of large dihedral angles on the localisation behaviour of excitations. We present only calculations for fluorenes for brevity. We have performed the same calculations with thiophene and the conclusions drawn from them are effectively identical. In Figure 5.18, differential densities and the corresponding delocalisations and excitation centres are shown for six fluorene 4mer examples. Figure 5.18(a) and (b) correspond to 4mers in which all dihedral angles are 0° (all-0°) and 90° (all-90°) , respectively. In the all-0° example, the excitation is centred at the middle of the molecule ($n_{EC} = 2.5$) and is delocalised across the majority of the molecule ($P_D = 3.4$ equivalent to a spread over 3.4 monomers). However, in the all-90° case, the result is similar with a slight reduction in the delocalisation to just less than 3 monomers. This result suggests that the localising effect of 90° dihedral angles is hindered when the overall symmetry of the molecule is preserved. It must be noted that, due to the static nature of the calculation, this case with all three dihedrals at

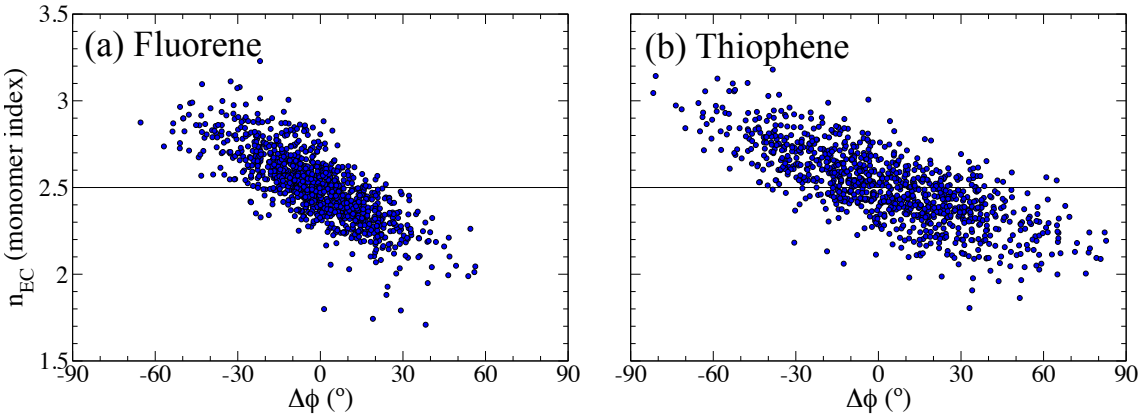

Figure 5.19: Excitation centres, n_{EC}, of geometries of (a) fluorene and (b) thiophene 4mers plotted with respect to $\Delta\phi \equiv \phi_3^{(90)} - \phi_1^{(90)}$ with $\phi_i^{(90)} \equiv 90 - |\phi_i - 90|$. The axis of the excitation centres ranges from one end unit, $n_{EC} = 1$, to the other, $n_{EC} = 4$, with the centre line at $n_{EC} = 2.5$ denoting the centre of each molecule.

exactly 90° is artificially symmetric and physically unlikely. However, as we discuss in the following, this case serves as an instructive example for understanding the effect of asymmetry on delocalisation.

In the remaining examples in Figure 5.18, all but one of the dihedral angles differs from the others. In all of these examples, the excitation density is indeed centred around the regions with dihedral angles at 0° and avoids the 90° angles. In Figure 5.18(e), when the central dihedral is 0° and the outer dihedrals are 90°, the excitation density is split due to the symmetry of each end. This then leads to the greatest delocalisation ($P_D = 3.7$) of all the cases presented. This large delocalisation is dependent on the exact symmetry between the end-most dihedral angles and it would be expected that slight changes in either of these dihedral angles would result in significant reductions in the corresponding delocalisation measures.

It is clear then that large dihedral angles do lead to localisation behaviour in these molecules. However, these examples present extreme cases of asymmetry between dihedral angles of either 90° and 0°. As shown by the asymmetric cases in Figure 5.18(c) and (d), localisation follows the trend of avoiding 90° dihedrals in favour of 0° angles as is quantified by the corresponding P_D values. These examples are notable due to the shift in the excitation centre which is an immediate consequence of the asymmetric localisation. Due to the simplicity of the 4mer, molecular asymmetry is a function of the two end dihedrals alone (as before, assuming that no other conformational distortions play any significant role). Thus, we can utilise the MD ensemble geometries to gauge the effect of asymmetry on excitation localisation.

In Figure 5.19, we show the trend in excitation centres as a function of the difference in dihedral angle between each end dihedral, ϕ_1 and ϕ_3. As dihedral angles, in this context, are considered large when they are 90°, we use a modified difference measure $\Delta\phi \equiv \phi_3^{(90)} - \phi_1^{(90)}$ in which $\phi_i^{(90)}$ is equivalent to a mapping of dihedrals $\phi_i > 90$ to $\phi_i^{(90)} = 180 - \phi_i$. (As a note, this is performed using the

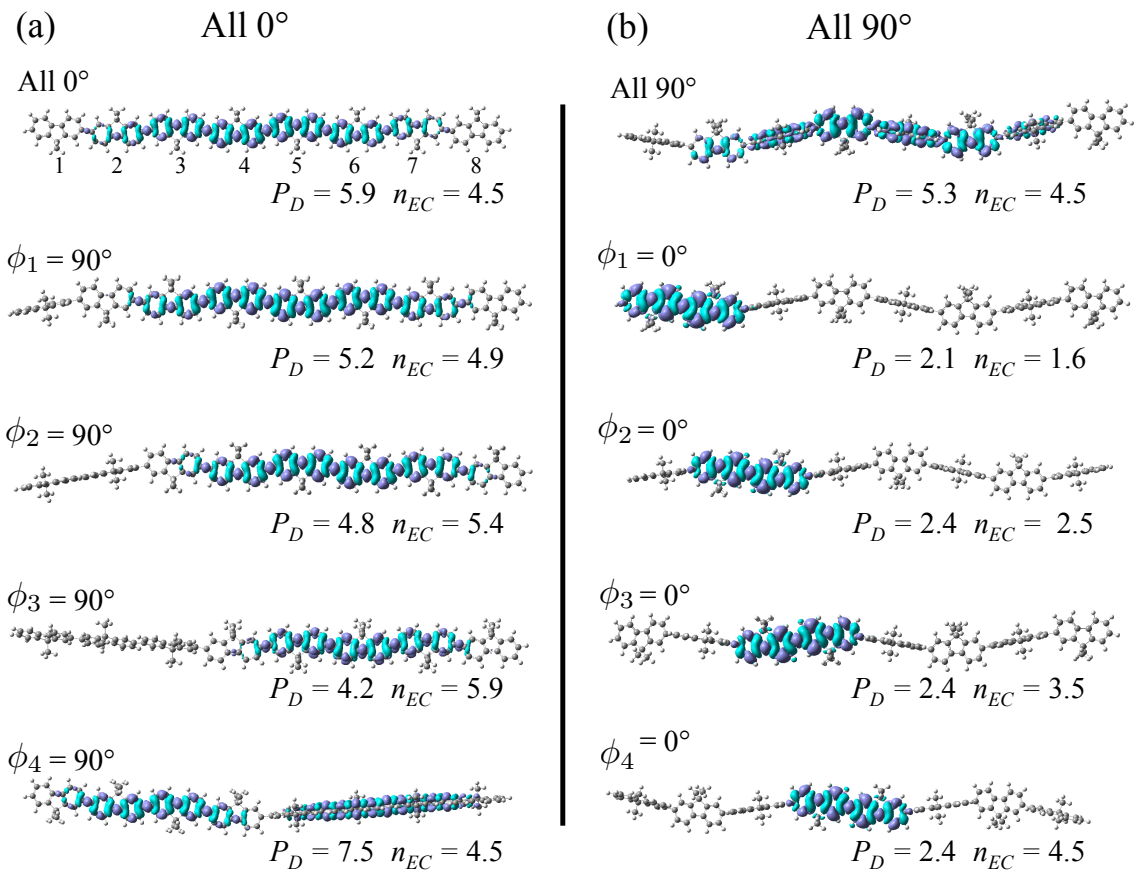

Figure 5.20: Differential densities and corresponding delocalisation, P_D, and excitation centre, n_{EC}, measures of DFT optimised fluorene 8mers. (a) Fluorene 8mers with all dihedrals set to 0° except where noted ('All 0°' cases). (a) Fluorene 8mers with all dihedrals set to 90° except where noted ('All 90°' cases). In the top molecule of (a), the monomer indexing (in which n_{EC} is expressed) is given and applies to each case.

relationship $\phi_i^{(90)} \equiv 90 - |\phi_i - 90|$.) For fluorene and thiophene (Figure 5.11(a) and (b), respectively), there is an effectively linear relationship between the asymmetry between these dihedrals and the centre of charge. In addition, we found that this trend was independent of the central dihedral even for large dihedral angles.

When considering the absorption spectral properties of 4mers discussed in Section 5.2.2, we note that there is an interesting correlation between the delocalisation behaviour and the trends in transition energies. From the results shown in Figure 5.9, we observed that changes in transition energies with respect to dihedral angle variations were considerably more pronounced when all other dihedral angles were 90° than when all other dihedrals were 0°. In these cases, the transition energy trends were comparable to that of the equivalent 2mer. This correlates clearly with the delocalisation of $P_D \simeq 2$ for each of these cases shown in Figure 5.18(d) and (e). In these conformations, the localisation is 2mer-like and, as a result, the dependence of the transition energies on the remaining dihedral angle is also 2mer-like. Additionally, if we consider the case where all dihedral angles are 0° in Figure 5.9, the delocalisation behaviour corresponding to each trend starts from that of Figure

5.18(a) in both cases and, upon increasing ϕ_1, the excitation density becomes that of Figure 5.18(c) and, upon increasing ϕ_2, becomes that of Figure 5.18(f). The point to note is that in the previous cases, with 2mer-like transition energy versus dihedral angle dependences, the excitation is concentrated closely around the varied dihedral angle while in the latter cases, the excitation is spread further from the increased dihedral. As such, the significant orbital contributions in the more spread out cases are further from the dihedral in question and, thus, the dihedral has less of an effect on the transition energy. These points show that the differing dihedral broadening effects observed in the 4mer are strongly dependent on the delocalised character of the transition orbitals. This is the key result of this section.

To further demonstrate the above point, Figure 5.20 shows the differential densities and corresponding delocalisation measures and excitation centres for fluorene 8mers with the majority of dihedral angles set to 0°, Figure 5.20(a), or set to 90°, Figure 5.20(b). The results observed follow the same trend as for the 4mers. First, we note that when all dihedrals are 0° or 90°, there is an overall delocalisation of the excitation which spans the majority of the molecule. Secondly, when one dihedral is set to 90° while all others are 0°, the excitation will localise away from this dihedral. We see in these cases that localisation occurs on the longer portion of the molecule. Again, when the central dihedral is set to 90°, the excitation is split along the molecule due to the symmetry and delocalisation is maximised though, as with the 4mers, this effect is the result of the artificiality of such a symmetric conformation. Thirdly, when all dihedrals are set to 90° except one which is set to 0°, excitations become localised around the 0° dihedral and are delocalised over $\simeq$ 2 units. We see again that this behaviour is consistent with the trends observed in the dihedral dependence of the transition energies shown in Figure 5.10.

The results discussed here demonstrate some of the basic principles behind excitation localisation and how it relates to the varying dihedral broadening discussed in Section 5.2.2. In addition, the simple case of the 4mer allows for an illustration of how excitations are positioned along the molecule as a function of the asymmetry between the dihedral angles. While we have shown that large, conjugation breaking dihedral angles do have a significant effect on excitation localisation, we posit, based on the results of the previous section, that asymmetry is also of key significance. Furthermore, we note that is may be possible to build a model of the ensemble spectra similar to that which we presented for the 2mer in Figure 5.3 based on the dihedral angle probability densities and fuller, quantitative knowledge of the link between delocalisation and dihedral broadening. As such, the work we have presented in this section has served to illuminate the foundational principles of this behaviour to be expanded upon in future developments.

5.4 Conclusions

As well as being a useful tool for understanding the properties and statistical mechanics of conformational disorder, we have shown in this chapter the applicability of MD simulations in generating realistic ensembles of molecular geometries for use in quantum mechanical calculations. We have thereby calculated linear absorption spectra which, by the nature of the calculation, have conformational inhomogeneous broadening embedded within them, and analysed the localisation of a given excitation across the set of geometries.

Using the simulation geometries for a variety of molecular lengths of fluorene and thiophene, we have found that both molecules have absorption spectra which are inhomogeneously broadened to an extent almost independent of length-scales. We have also demonstrated the emergence of high-energy absorption features with increasing molecule lengths. To understand the role of dihedral angles in broadening in molecules longer than 2mers, we have employed a TD-DFT study of a variety of geometry scans and found that it is often the case that more central dihedrals have a significantly larger effect on the transition energies. Furthermore, we have found that the individual broadening effect of dihedral angles generally decreases with molecular length and is strongly dependent on the overall molecular conformation. The result of this behaviour explains the near-constant broadening observed in the ensemble absorption spectra.

We have also developed a novel means of calculating excitation localisation in polymeric structures based on calculations of partial charges and employing a delocalisation measure, P_D. Utilising this measure, we have generated distributions of excitation centres and delocalisations for fluorenes and thiophenes of varying lengths and found that each display similar behaviour. Given the greater tendency towards large dihedral angles in thiophenes than in fluorenes, as demonstrated in Section 4.3.3, this suggests that the notion of conjugation lengths based solely on large dihedral angles forming conjugation breaks is insufficient for understanding how localisation occurs. By analysing geometries obtained from TD-DFT scans, we have found that conjugation breaking angles do contribute substantially to localisation in long (8mer) molecules but localisation behaviour also results from asymmetry in the dihedral angles. These results are consistent with the 2mer-like broadening observable in systems with large dihedral angles.

The analyses performed here are across relatively short molecules. At the polymer scale, many of the features of dihedral angle dependence will only be true over given coherence lengths in the molecule. As discussed above, it would be an interesting point of study to build on the analysis and techniques presented here for considerably larger systems where several sections of a given molecule can be deemed as effectively independent of other sections. As such, the work we have provided here forms a foundation of the principles which may guide future work in this area.

Chapter 6

Conclusions and Future Work

To conclude this thesis, we summarise the key results and perspectives gained from the preceeding chapters and discuss a number of possible avenues of future work which serve as a direct continuation of this work.

6.1 Conclusions

In Chapter 1, we presented a discussion of the role of morphology in organic semiconducting systems; the basic principles of polymer statistical mechanics; and the utility of MD simulation for the study of conjugated polymers. We discussed the potential of organic semiconductors for realising a new generation of flexible and light-weight devices amenable to low-cost, large-area fabrication. By discussing both the complexity which arises from both the discrete molecular nature of these materials as well as the material design required for their optimisation, we have shown that further progress in the field is dependant on better understanding of the microscopic nature of molecular and solvent behaviour. For the study of such behaviour, classical MD simulation is a promising theoretical tool given its ability to simulate $\sim 10^6$ atoms over $\sim \mu$s timescales. Additionally, the resulting molecular conformations of MD simulation can be mapped to quantum mechanical calculations. This allows for the unique opportunity to understand the role of conformational defects in ground-to-excited state transitions. However, the method of formulating the simulation framework - the classical force-field - for conjugated polymers requires optimisation in order to account for the many material design variables - e.g. side-chains, and backbone lengths and units - in as simple a manner as possible.

This work contained three key parts: first, developing an optimal quantum chemical calculation framework for obtaining force-field parameters for conjugated molecules which, where possible, accounts for the need to implement side-chains and utilise various lengths of conjugated backbone; secondly, developing methods for implementing and testing calculated parameters both self-consistently and by experimental comparison and, after doing so, exploring the microscopic details of polymer solution conformations through simulation; thirdly, utilising quantum chemical cal-

culations based on MD simulation geometries to probe the effect of conformational disorder on linear absorption spectra and the role conformational variations play in forming localised excitations upon absorption.

In Chapter 2, we presented a discussion of molecular dynamics and quantum chemical methods and detailed the necessary steps for carrying out this work.

In Chapter 3, we reported our exploration of the validity of DFT approaches, when compared to high-level *ab-initio* calculations, for obtaining intermonomer dihedral potentials of conjugated molecules. We established that a two step geometry optimisation and single point (SP) energy scan method based on DFT with CAM-B3LYP/6-31G* and CAM-B3LYP/cc-pVTZ, respectively, gives an accurate representation of potentials of fluorene and thiophene calculated using MP2 and CBS limit CCSD(T) methods. This allowed us to carry out an investigation of the role of alkyl side-chains and increasing conjugated backbone length on the dihedral potentials. In both fluorene and thiophene, increasing conjugated backbone length has no significant effect. Side-chains were shown to have a significant effect only in thiophene which we determined to be the result of steric contributions as opposed to significant changes in the π-orbital structure of the conjugated backbone. In investigating partial charge distributions, we found that convergence in distributions with increasing backbone length occurs in fluorene, thiophene, and their side-chain branched analogues. However, the length at which convergence occurs differs for alkyl-thiophenes due to the breaking of molecular symmetry when side-chains are present. We also found that it is not possible to obtain similarly converged charge distributions for extending side-chains for side-chains up to 12 carbons in length.

These results are of key importance in developing a general force-field parameterisation scheme for conjugated materials. In determining the backbone length convergence of dihedral potentials and partial charge distributions, we have shown the minimal calculation required in each case. These calculations serve as a guiding tool for parameterisations of other conjugated molecules which we expect to follow a similar phenomenology. This, coupled with obtaining a suitable DFT methodology, is a crucial step towards optimising force-field parameterisation and, thus, the applicability of MD simulation to organic semiconductors.

Based on a force-field subtraction method, we formulated an implementation scheme for dihedral potentials in Chapter 4. We explored the consistency of this procedure in generating force-field dihedral potentials capable of reproducing those of the input DFT potentials as well as reproducing the molecular geometries of the energetic minima and found good agreement between the two in most cases. For alkyl-thiophenes, we found that the OPLS force-field does not always reproduce the expected steric behaviour of the side-chains near the dihedral centre of rotation. In this case, we found that the subtraction procedure must be performed with ethyl side-chains so as to properly account for this behaviour. Following implementation,

we tested the force-field for agreement between the resulting dihedral distributions and a Boltzmann distribution of the DFT potential for 2mers with no side chains and found excellent agreement. This correspondence also lead us to explore how side-chain interactions are affected by solvent choice and found that poor solvents can greatly influence dihedral rotation via side-chain trapping. We followed these 2mer simulations by simulations of molecules up to 32mer in length. This allowed us to obtain tangent-correlation functions which are well-characterised by exponential decay functions. The resulting persistence lengths for dioctyl-fluorene and hexyl-thiophene 32mers correspond closely to experimental obtained values for the polymers PF8 and P3HT, respectively. This provides an experimental validation of the accuracy of our force-field. Furthermore, we found that end-to-end length distributions of various lengths of each molecule are well described by a worm-like chain model.

By utilising the geometries obtained from MD simulations in TD-DFT calculations, we performed an investigation of conformational broadening and excitation localisation of ensembles of fluorene and thiophene molecules of varying lengths in a good solvent. We found that conformational broadening of the low energy absorption states in both molecules is nearly constant with increasing backbone length. Following an investigation on optimised geometries, we found that this results from the decreasing influence of individual dihedral angles on spectral shifts with increasing lengths of backbone. The ensemble absorption spectra are in good agreement with experimental absorption spectra. We have also developed a novel method for investigating excitation localisation based on obtaining partial charges for the ground and excited states. Using this approach, we found that fully delocalised excitations are significantly hindered in molecules of increasing length and, with recourse to optimised geometry calculations, found that localisation phenomena result both from large dihedral angles - akin to conjugation breaks - but also from slight asymmetry in dihedral angles along the backbone.

6.2 Future work

Given the proven validity of the force-field parameterisation scheme we have developed, an interesting first continuation of this work would be in further exploring the role of solvent, side-chains, and conjugated structures to obtain further insight into the conformational properties of conjugated polymers in solution. Based on the existing parameters for fluorene and thiophene, it would be interesting to explore the solvent and side-chain interplay for molecules longer than 2mers as well as the role of poor solvents in molecules of lengths greater than their respective persistence lengths. Particularly, experimenting with solvent additives, such as DIO or phenyl-napthalene, as well as applying our parameterisation scheme to co-polymers such as PTB7 [57–59] or PffBT4T-2OD [80, 81] could offer insight into the solution

aggregation behaviour which has made both of these such promising OPV materials.

Another route, which is the primary goal of our future development of this work, is in simulating multi-molecular systems in solution and in solid state formations. This is would begin with investigating solution aggregation behaviour. It would be interesting to observe how aggregation occurs with respect to solvent and additives as well as how backbone length and side-chain length enhances or hinders these processes. This could then be expanded to incorporate fullerene-type (PCBM) molecules to study selective solvation processes. Ultimately, one could imagine modelling evaporation processes by, at least in the first instance, a method of gradually removing solvent molecules from the system, and observing the packing formations which occur.

Multi-molecular simulation would also be of particular importance for further validation and development of our force-field parameterisation scheme by leading to calculations of properties, such as densities, which depend both on the possible dihedral disorder as well as the strength of the conjugated backbone π-stacking interactions. While we have shown the validity of a force-field with respect to conformational properties, further validation and improvement of parameterisation approaches is crucial to unlocking the full scope of these methods for studies of conjugated molecular systems.

Further exploration of the behaviours of absorption and other transition behaviour based on the methods employed here could also shed more light on the role of conformational disorder. As above, utilising poorly-solvated systems, alternative molecules, or aggregates as input for quantum chemical calculations could be interesting both in further generalising the conclusions we have drawn for well-solvated fluorenes and thiophenes as well as uncovering the effects of other sources of disorder such as intermolecular interactions and packing. Also, calculations of additional ground-to-excited state properties utilising the geometries obtained here is possible. One such example is calculations of ionisation energies for which preliminary calculations have been performed.

To go beyond ground-to-excited state transitions, it would also be worthwhile exploring the use of *ab-initio* MD methods which are currently applicable at the short ($L \lesssim l_p$) molecule scale. Further development of these methods (as well as available computational power) will surely be of great importance in understanding excited-state relaxation processes such as exciton formation and transfer. Additionally, it would also be interesting, from the perspective of classical force-field validation, to develop something akin to a subtraction procedure based on comparing calculations of e.g. potentials of mean force for various fixed dihedrals in the *ab-initio* MD and classical MD regimes as opposed to static quantum chemical and force-field scans. This could allow a more definite correspondence of dynamical methods and, in principle, a more realistic classical force-field description.

It is clear that this work can be the beginning of much interesting research at the heart of organic semiconductor theory as well as into the general applicability of MD simulations for these materials. The results we have obtained so far and the methods we have developed can surely serve as foundational blocks for further investigations of these principles and, thus, the development of a better understanding of the physics of conjugated material conformation and morphology.

Appendix A

Length variations of partial charges

In this appendix, we provide full details of partial charge convergence following the overview presented in Section 3.3. We begin by demonstrating the progression of total monomer charges for increasing backbone lengths. This is followed by a discussion of charge convergence at the individual atom level.

A.1 Total atomic charge convergence

In Figure A.1, the total monomeric charges, Q, of each unit of fluorene, dioctyl-fluorene, thiophene, and hexyl-thiophene molecules is shown for backbone lengths ranging from 2mer to 9mer. The three symmetric molecules (those other than hexyl-thiophene) have monomers which have zero total charge for a 2mer and only slight ($\simeq 0.02e$) fluctuations about zero charge in individual Q values with increasing length. Hexyl-thiophene, on the other hand, has total charges which are consistently greater than zero charge near the molecular end-points while zero charge units only appear at the 5mer scale. While the absolute value of the non-zero charges on the end units is small ($\sim 0.05e$), these are representative of significant differences in the individual atomic charge distributions (as we discuss in the following section). As such, it follows that a molecule of at least a 5mer backbone length is necessary to obtain a set of converged hexyl-thiophene charges.

A.2 Individual atomic charge convergence

As we discuss in Section 3.3 and in the previous section, convergence in total charges is directly representative of convergence in individual atomic charges. In this section, we demonstrate this explicitly by plotting the length dependence of the individual atomic charges of fluorene, dioctyl-fluorene, thiophene, and hexyl-thiophene. The atomic labelling convention used throughout is shown in Figure A.2.

In accordance with the molecular symmetry of both fluorene and dioctyl-fluorene,

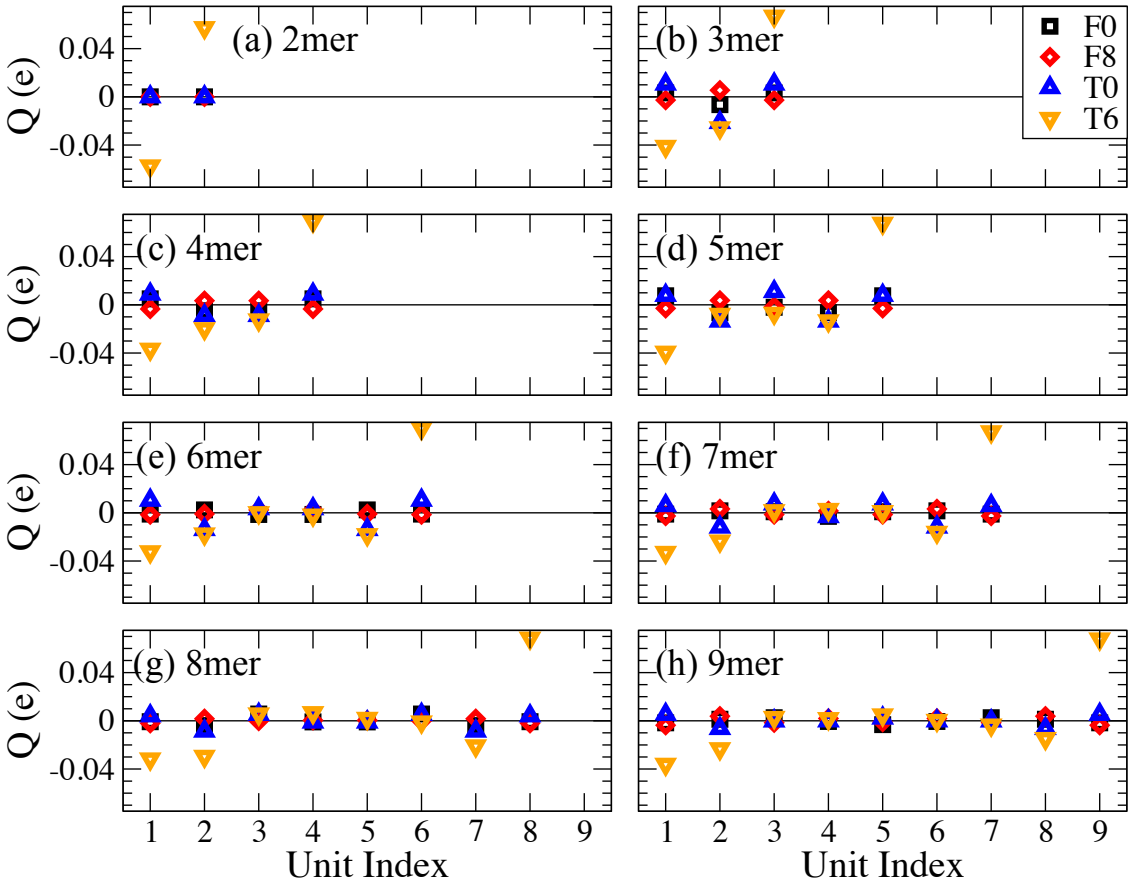

Figure A.1: Total charge, Q, per unit for varying backbone lengths of fluorene (F0), dioctyl-fluorene (F8), thiophene (T0), and hexyl-thiophene (T6).

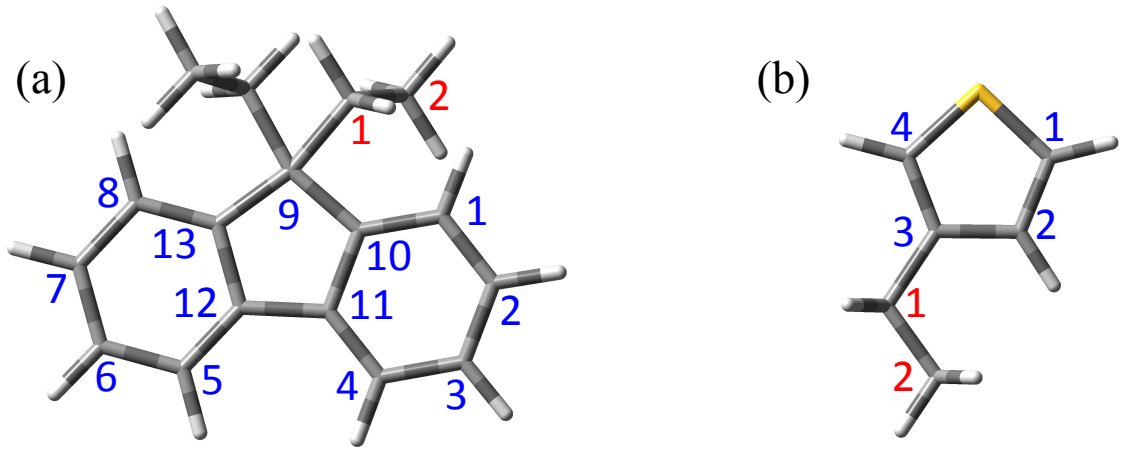

Figure A.2: Atom labelling convention used throughout for atomic partial charges for dialkyl-fluorenes, (a), and alkyl-thiophenes, (b). For mainbody carbons (shown in blue), for label X, the carbon and hydrogen labels will be 'CX' and 'HX' respectively. This follows also for side-chain carbon labels (shown in red).

individual partial charges are effectively constant with increasing backbone length. While the total charges shown in Figure A.1 show that outer units and inner units have near zero charge, it can be seen that the distributions of each are significantly different (Figures A.3(a)-(b) and A.4(a)-(b) for outer units, and Figures A.3(c)-(i) and A.4(c)-(i) for inner units). This results from the extra terminal hydrogen atom on the outer units. However, charge distributions between outer unit side-chains and those of the inner units are near identical (Figure A.5).

We note that the convergence behaviour of the outer units in going from a 2mer to a 3mer is slightly more significant for fluorene (Figure A.3(a)-(b)) than for dioctyl-flurene (Figure A.4(a)-(b)). With side-chains present, and thus a significantly greater number of atoms per unit, the effect of the terminal hydrogen is reduced. As this is the only asymmetry between the outer and inner fluorene units, it follows that this slightly enhanced convergence behaviour exists for the case with side-chains. For all fluorenes, the individual charges are converged to within a tolerence of $\pm 0.03e$ for backbone lengths of $>$ 3mer.

The lack of reflection symmetry in hexyl-thiophene leads to a considerable asymmetry in the resulting individual charge distributions of the end units (Figure A.8(a) and (b)) which is not observed for those of thiophene without sidechains (Figure A.6(a) and (b)). Also, while each of the second units have similar charge distributions (Figure A.8(c) and (d)), comparison of either with the other inner units (Figure A.9) shows a significant difference. Again, we note that this is not the case in thiophene without side-chains (Figure A.7). This difference also appears in the progression of total monomer charges in Figure A.1. As such, this confirms that converged non-zero total monomer charges can, indeed, represent significantly different charge distributions.

For thiophene with no side-chains, the charge distributions of the end units display minor convergence features (Figure A.6(a) and (b)). As above with fluorene, this results from the extra hydrogen atom on the end units having greater effect on the relatively small thiophene unit. As before, comparing the same feature between thiophene and hexyl-thiophene shows the effect is reduced when side-chains are present.

The hexyl side-chains of hexyl-thiophenes are effectively consistent across different units (Figures A.10 and A.11). However, there is noisy behaviour in the individual trends. We believe this is the result of the difficulties incurred in treating the side-chains of thiophene using optimisation algorithms.

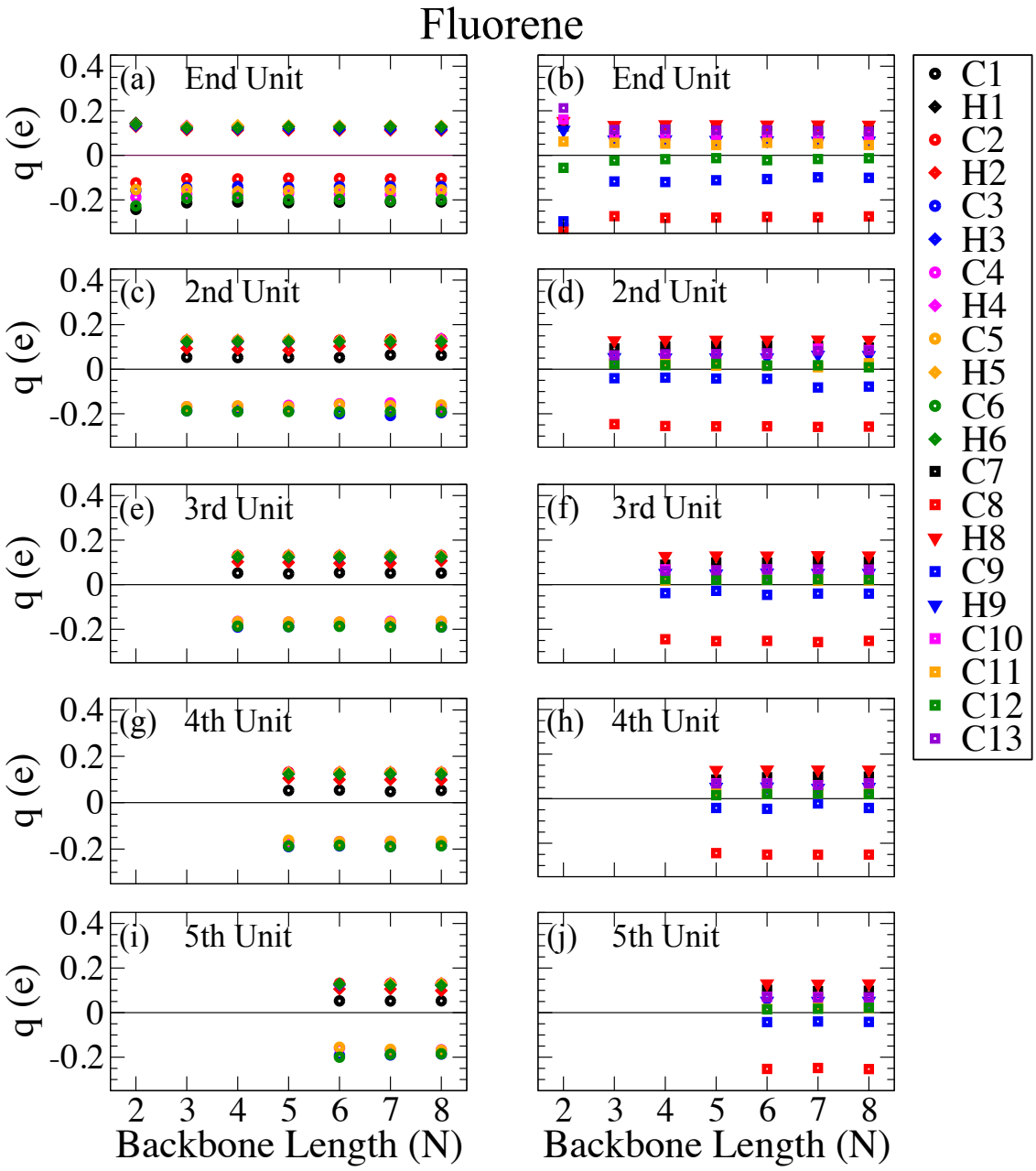

Figure A.3: Individual atomic charges of fluorenes of various backbone lengths. The graphs are the charges of the outer units, (a) and (b), second units, (c) and (d), third units, (e) and (f), fourth units, (g) and (h) and fifth units, (i) and (j). Graphs on the left are of the charges of C1-C6 and the right C7-C13 with each including the corresponding H atoms.

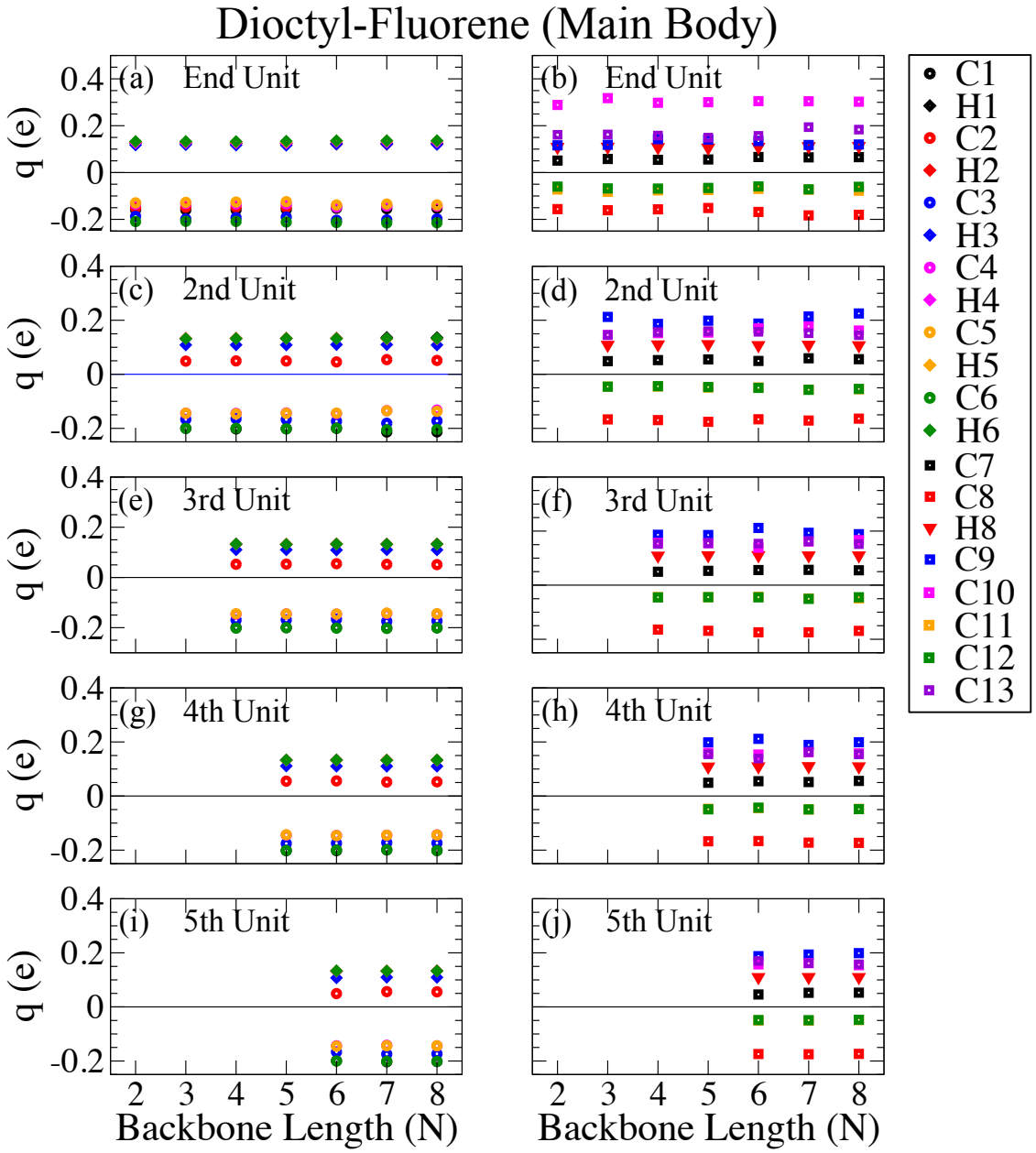

Figure A.4: Individual atomic charges on the conjugated fluorene backbone of dioctyl-fluorenes of various backbone lengths. The graphs are the charges of the outer units, (a) and (b), second units, (c) and (d), third units, (e) and (f), fourth units, (g) and (h) and fifth units, (i) and (j). Graphs on the left are of the charges of C1-C6 and the right C7-C13 with each including the corresponding H atoms.

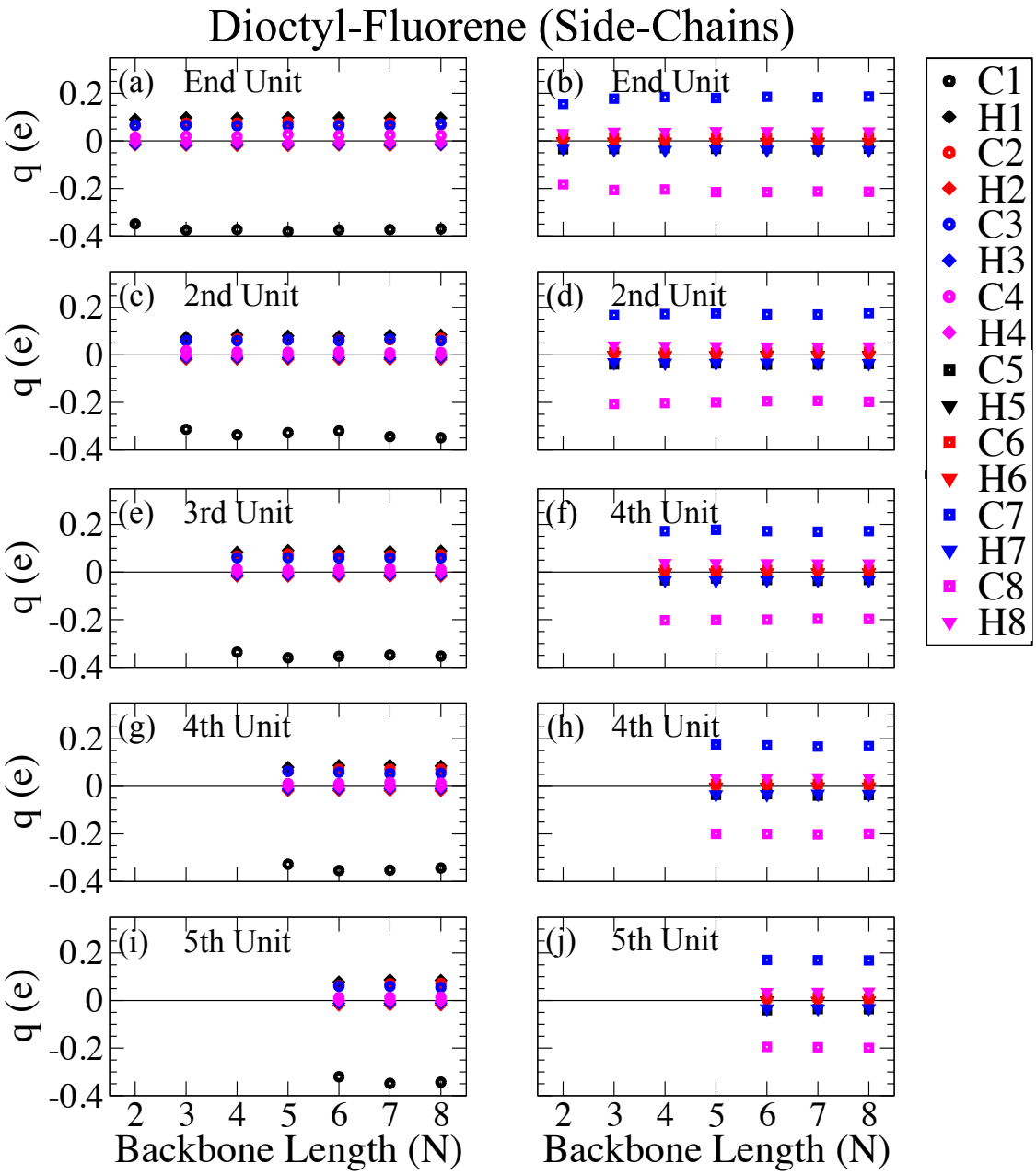

Figure A.5: Individual atomic charges on the octyl side-chains of dioctyl-fluorenes of various backbone lengths. The graphs are the charges of the outer units, (a) and (b), second units, (c) and (d), third units, (e) and (f), fourth units, (g) and (h) and fifth units, (i) and (j). Graphs on the left are of the inner four CH_2 groups and the right the outer four.

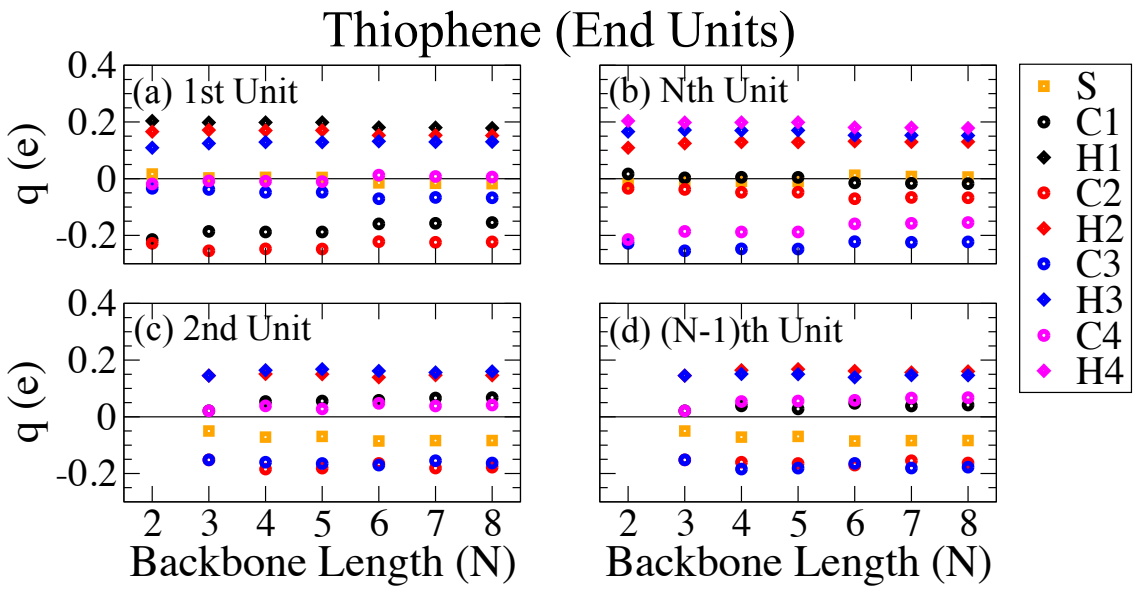

Figure A.6: Individual atomic charges of the (a) and (b) outer units and (c) and (d) second units of thiophenes of various backbone lengths. Each pair is taken from opposing ends of the molecule.

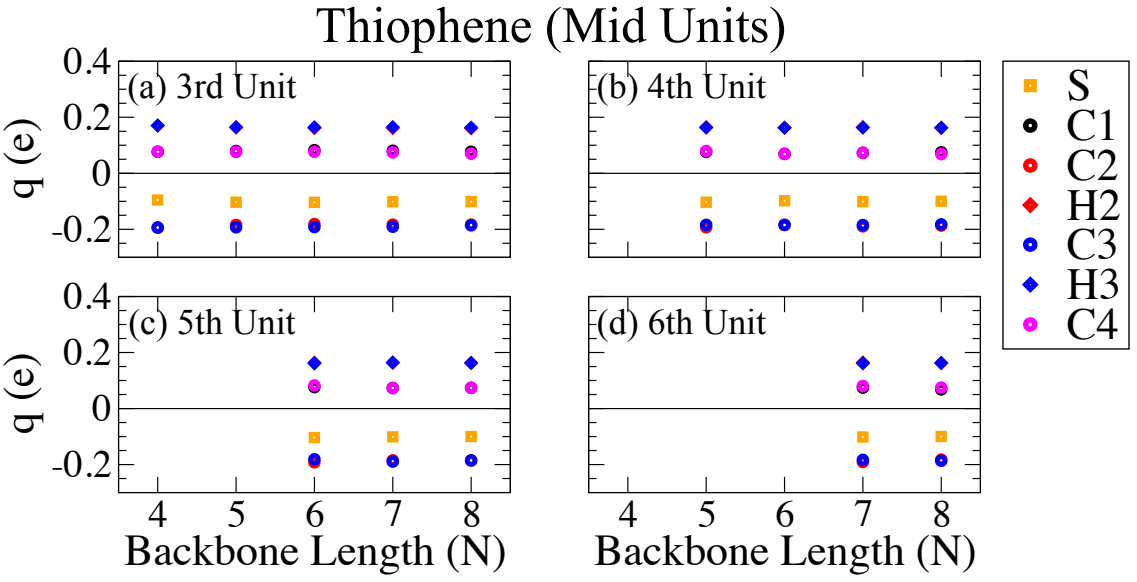

Figure A.7: Individual atomic charges of the third through sixth units ((a) through (d) respectively) of thiophenes of various backbone lengths.

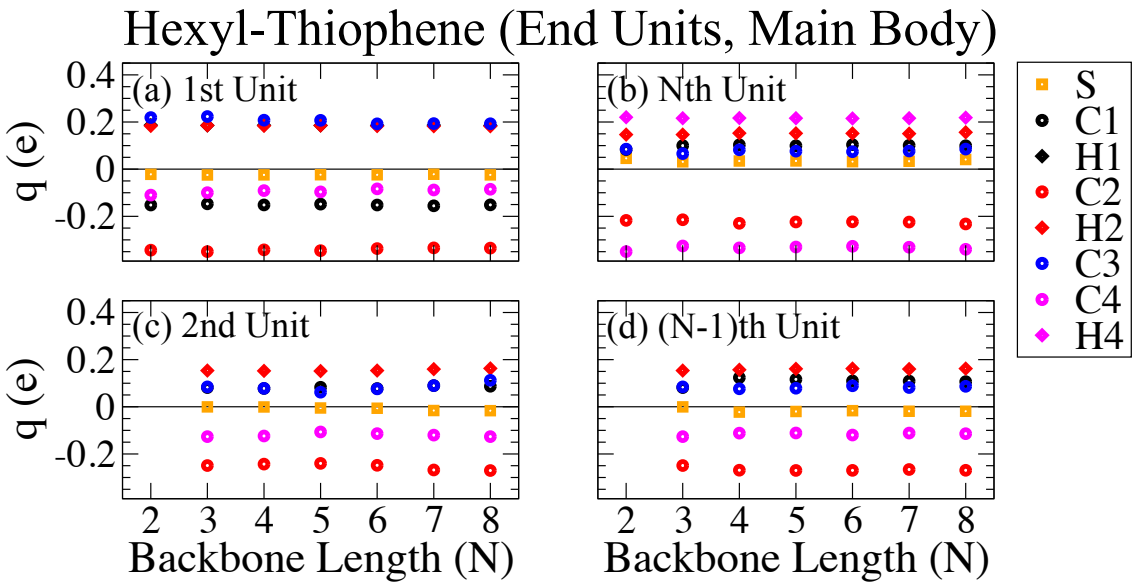

Figure A.8: Individual atomic charges of the conjugated thiophene backbone atoms of the (a) and (b) outer units and (c) and (d) second units of hexyl-thiophenes of various backbone lengths. Each pair is taken from opposing ends of the molecule.

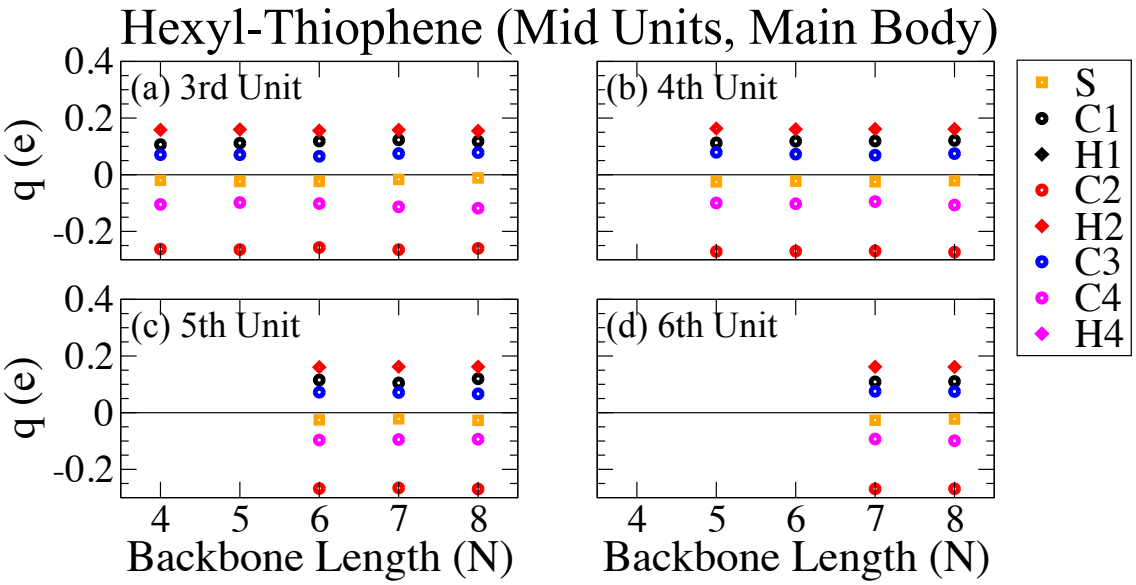

Figure A.9: Individual atomic charges of the conjugated thiophene backbone atoms of the third through sixth units ((a) through (d) respectively) of hexyl-thiophenes of various backbone lengths.

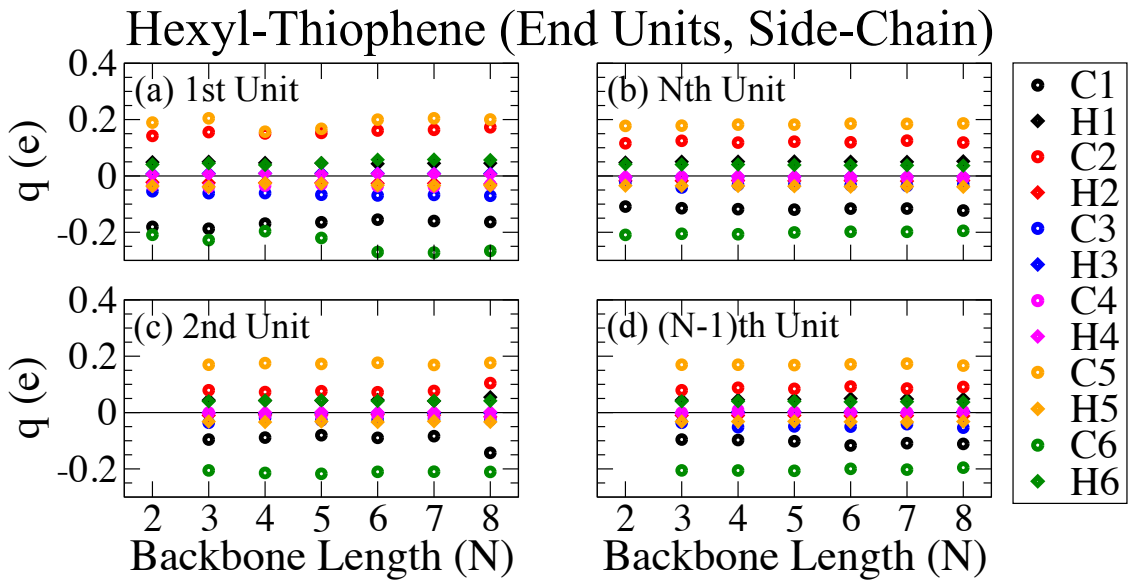

Figure A.10: Individual atomic charges of the side-chain atoms of the (a) and (b) outer units and (c) and (d) second units of hexyl-thiophenes of various backbone lengths. Each pair is taken from opposing ends of the molecule.

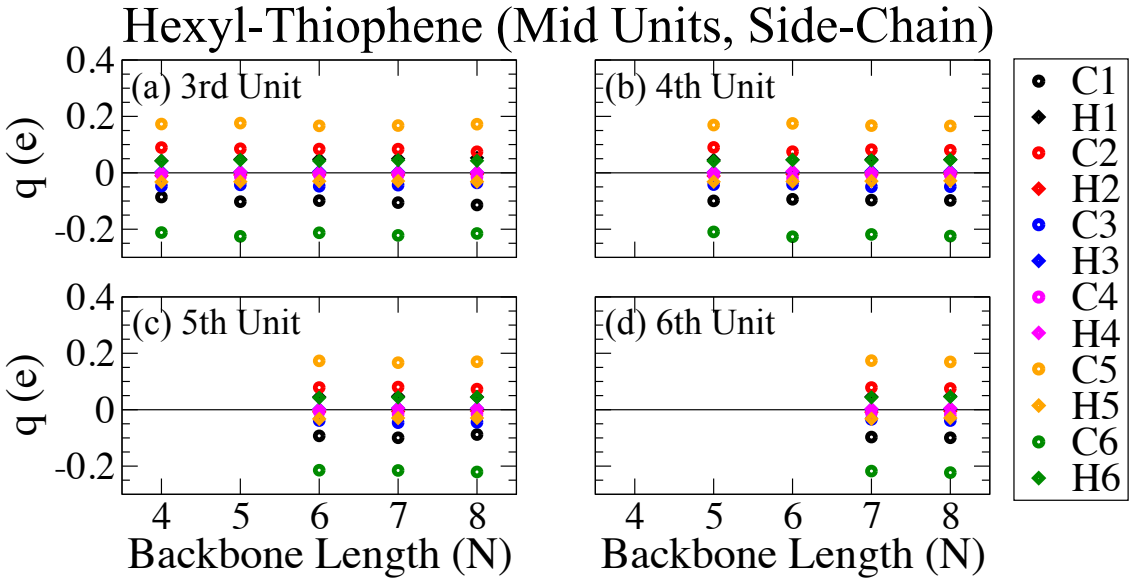

Figure A.11: Individual atomic charges of the side-chain atoms of the third through sixth units ((a) through (d) respectively) of hexyl-thiophenes of various backbone lengths.

Appendix B

Notes on molecular dynamics simulations

In this appendix, we provide additional details regarding the MD simulations presented in the Chapter 4. First, we discuss the tests we have performed of alternative methods for maintaining temperature and pressure (following the discussion of Section 2.2.2) and treating long-range electrostatic effects (following the discussion of Section 2.1.3). We then provide plots of dihedral distributions of 2mers of fluorene and thiophene of varying side-chain lengths and solvents in addition to the probabilities calculated in Section 4.2.2.

B.1 Comparison of simulation methods

Throughout this work, we have used the velocity-rescale (VR) thermostat, the Berendsen (B) barostat, and the Reaction-Field (RF) method for maintaining temperature, maintaining pressure, and accounting for long-range electrostatics, respectively. These options typically optimise simulation run-times with regards to other methods. As we discussed in Section 2.1.3 (long-range electrostatics) and Section 2.2.2 (temperature and pressure scaling), there are alternatives to these procedures which are often utilised in other MD works. In this section, we provide details of the tests we have performed of each of these protocols.

We have tested the Nosé-Hoover (NH) thermostat and Parrinello-Rahman (PR) barostat as alternatives to the VR-B thermostat-barostat scheme. As we discussed in Section 2.2.2, these methods allow for a more accurate treatment of fluctuations in each quantity. We have found, as is stated in the Gromacs manual [166], that these methods lead to instability and simulation break-down in the equilibration phase and, therefore, are only suitable for well equilibrated systems. As such, we test their applicability based on systems equilibrated using VR-B scheme. Tests based on full simulation runs of dioctyl-fluorene 2mers, hexyl-thiophene 2mers, and 16mers of hexyl-thiophene (each in chloroform) have all shown essentially identical results (in terms of dihedral distributions for the 2mers and persistence lengths for

Table B.1: Probabilities of $0° \leq \phi \leq 90°$ of dioctyl-fluorene 2mers in various solvents utilising the Reaction-Field (RF) and Particle-Mesh Ewald (PME) long-range electrostatics schemes. The error in each value is $\pm$ 0.06.

	chloroform	THF	toluene	methanol	water
RF	0.54	0.58	0.61	0.54	0.06
PME	0.56	0.69	0.48	0.47	0.07

the 16mer) for each combination of thermostat and barostat with agreement in the biasing probabilities (see Section 4.2.2) in the 2mers within the error tolerances provided in Table 4.4 and 16mer persistence lengths corresponding to within 2%. As such, we utilise the VR-B thermostat so as to simplify simulations and optimise performance.

For long-range electrostatics, we have tested the applicability of the RF scheme against the Particle-Mesh Ewald (PME) scheme. As we discussed in Section 2.1.3, it is often contested which of these methods is most suitable though it is also widely known that the RF scheme offers significant advantages in simulation run-time. The differences between systems, with regards to these algorithms, are based on the overall dielectric behaviour and, thus, the charges and polarity of the media. As such, it may be expected that the choice of the most appropriate method may be sensitive to the solvent chosen. As dioctyl-fluorene has a considerable solvent dependence in the dihedral distributions (discussed in Section 4.2.2), it follows that this is an ideal test system for gauging this effect.

In Table B.1, the probabilities of $0° \leq \phi \leq 90°$ - obtained following the procedure discussed in Chapter 4.2.2 - are shown for dioctyl-fluorene 2mers in different solvents utilising both RF and PME. THF and toluene show the most significant deviations ($\simeq 0.1$) though, in all other cases, the deviations are within the error of the calculation (± 0.06)

Given that the length of one side of the simulation box of the fluorene 2mers is $\simeq 5$ times the cut-off radius, we would expect that the correspondence obtained for these systems will also be true for greater systems. We have, however, tested both the RF and PME schemes for 16mers of hexyl-thiophene in chloroform and found good agreement in persistence lengths (to within 3%). As such, it appears that the RF scheme is generally suitable for the simulations we have performed.

B.2 Side-chain dependent dihedral distributions

In Section 4.2.2, we provided calculations of the biasing of the dihedral distributions of fluorene and thiophene 2mers with respect to variations in side-chain length and solvent choice. In Figure B.1, we display the calculated distributions from which the probabilities shown in Table 4.4 are calculated.

For fluorene (the left panels of Figure B.1), each distribution has distinct peaks

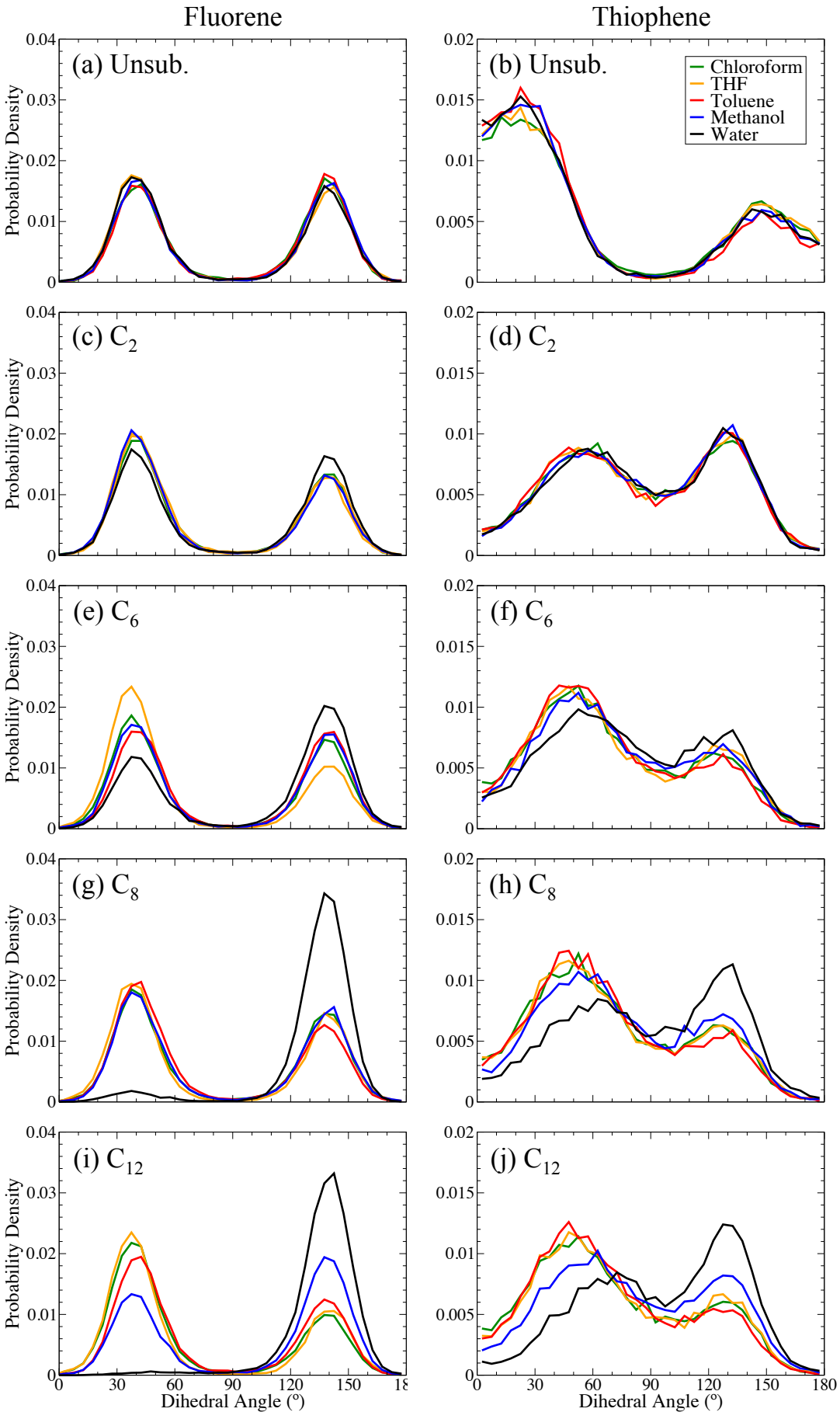

Figure B.1: Dihedral distributions of 2mers of fluorene and thiophene with side-chains of various lengths (as labelled). Legend in (b) applies to all graphs.

at $\simeq 40^\circ$ and $\simeq 140^\circ$ which remain irrespective of the solvent and side-chain choices. For the unsubstituted fluorene 2mer, (a). and C_2-fluorene, (c), the dihedral rotation is independent of the side-chain choice while C_{12}-fluorene, (e), and C_8-fluorene, (g), show very slight biasing towards the 40° minimum for the good solvents - chloroform, toluene, and THF - and towards the 140° minimum in water. This agrees with the interpretation that sufficiently long side-chains will interact and, thus, generally repel in good solvents and attract in poor solvents, and this effect is most prominent in C_{12}-fluorene (i). For methanol, a poorer solvent than the above good solvents, there is only slight biasing towards the 140° region for C_{12}-fluorene.

Between unsubstituted thiophene and C_2-thiophene ((b) and (d) respectively), there is a significant change in the qualitative form of the distributions due to the steric contribution from side-chains near the intermonomer junction. With no side-chains present, the distributions are peaked at $\simeq 30^\circ$ and $\simeq 150^\circ$ which shift to $\simeq 50^\circ$ and $\simeq 130^\circ$, respectively, for C_2-thiophene. Also, 90° conformations are highly improbable when no side-chains are present though they become significant in all cases with side-chains. These change follows from the qualitative change in the structure of the basic potential (shown in Figure 3.7(b)). Between C_{12}-thiophene and C_6-thiophene (f), there is only a slight difference in the form of the distributions with C_6-thiophene having a larger contribution near the 50° minimum. Also, slight solvent effects can be seen for water solvated 2mers which, as with fluorene, lead to a slight biasing towards the 130° minimum. Again, increasing side-chain length further compounds this effect though, in comparison to fluorene, the biasing is typically weaker. Due to the relative freedom of the distributions around 90° of thiophenes with respect to fluorenes, dihedral biasing also has the effect of slightly shifting the distribution peaks. This is seen most prominently with C_{12}-thiophene in water (j) in which the 50° peak is shifted towards $\simeq 70^\circ$.

Appendix C

Notes on time-dependent DFT calculations

In Chapter 5, we make extensive use of time-dependent density functional theory (TD-DFT) calculations to calculate linear absorption spectra and excitation delocalisation for ensembles of MD geometries. This appendix discusses the methodological details pertaining to these calculations. We first discuss the effect of removing side-chains from molecules so as to improve calculation efficiency. This is followed by tests of a number of functional and basis set combinations and how these each affect the absorption and delocalisation calculations. Finally, we give a more detailed rationale of our delocalisation measure, P_D, and other measures which could be applied to similar problems.

C.1 Influence of side-chains on absorption calculations

We have investigated the effect of side-chains on calculations of absorption spectra and delocalisation by performing calculations of each for optimised fluorene and thiophene 8mers with varying side-chains. The results of these calculations are shown in Table C.1. In order to maintain consistency in each molecular configuration (particularly, with respect to the dihedral angles), in each case all optimised geometries are taken from a single calculation with side-chains either removed or appended. In all cases, side-chains are not re-optimised upon either truncation or elongation. For the fluorenes, we appended side-chains to an unsubstituted fluorene 8mer. For thiophenes, we have both appended side-chains to an unsubstituted thiophene 8mer as well as removed them from a hexyl-thiophene 8mer. These are labelled as T_0 and T_6, respectively, in Table C.1. For fluorene, such a procedure has little effect due to the dihedral minima being independent of side-chains. For thiophene, this is not the case and, as such, there is a significant difference between the dihedral minima for side-chains less than propyl. This is reflected in the $\simeq 0.5$ eV difference between the S_0-S_1 transition energies between the T_6 and T_0 cases. However, this difference is seen to have little effect on the delocalisation.

Table C.1: S_0-S_1 transition energies (ϵ_0) and delocalisations (P_D) of optimised fluorene (F) and thiophene (T) 8mers with different side-chains. Each set of thiophene results is given for geometries optimised with hexyl side-chains (which have side-chains subsequently removed) or no side-chains (which have side-chains subsequently appended). These are labelled as T_6 and T_0, respectively. Fluorenes are independent of this choice and have been optimised with no side-chains with side-chains subsequently appended. Absolute (Δ) and percentage (Δ (%)) deviations are taken with respect to the molecule with butyl side-chains in each case.

	S_0-S_1 transition energies, ϵ_0 (eV)											
	None			C_1			C_2			C_3		
	ϵ_0	Δ	(%)	ϵ_0	Δ	(%))	ϵ_0	Δ	(%)	ϵ_0	Δ	(%)
F	3.33	0.08	3	3.29	0.04	1	3.25	0.01	0	3.25	0.0	0
T_6	3.09	0.03	1	3.08	0.03	1	3.06	0.01	0	3.06	0.00	0
T_0	2.55	0.07	3	2.52	0.03	1	2.49	0.00	0	2.49	0.00	0
	Delocalisations, P_D											
	None			C_1			C_2			C_3		
	P_D	Δ	(%)	P_D	Δ	(%)	P_D	Δ	(%)	P_D	Δ	(%)
F	6.0	0.9	18	5.2	0.1	2	5.1	0.0	0	5.1	0.0	0
T_6	5.5	0.3	6	5.7	0.2	3	5.7	0.1	2	5.9	0.0	0
T_0	5.8	0.1	3	5.8	0.2	4	5.6	0.1	1	5.6	0.0	0

In all cases, both transition energies and delocalisations are effectively converged with propyl side-chains when compared to cases with butyl side-chains (which, in turn, are converged with respect to up to hexyl side-chains in both cases). However, there is a loss of accuracy in both cases for shorter side-chains. With no side-chains, delocalisation measures are typically $\simeq$ 3-6% inaccurate and transition energies are $\simeq$ 1-3% innacurate. One exception is in the delocalisation in fluorene with a no side-chains, for which a near 20% error was observed. Going from no side-chain to methyls, the errors for both fluorene and thiophene are reduced to $\simeq$ 3-4% and $\simeq$ 1% for the delocalisation and transition energies, respectively.

In our TD-DFT calculations, we choose to use methyl side-chains so as to effect a balance between accuracy and computational expense. For thiophene MD ensemble calculations, all of which are based on hexyl-thiophenes, this means stripping the hexyl side-chain to methyl before each calculation. For thiophene freely-optimised geometry calculations (such as those presented above and in Section 5.2.1), it is neccesary to utilise hexyl or, at least, propyl side-chains so as to replicate the appropriate dihedral minima. As with MD calculations, these side-chains are then removed for TD-DFT calculations. For restrained optimisations of thiophenes (such as the geometry scans dicussed throughout Chapter 5), in which dihedral angles are fixed, this step is not necessary as the effect of the side-chain is muted by restraining the dihedral angle.

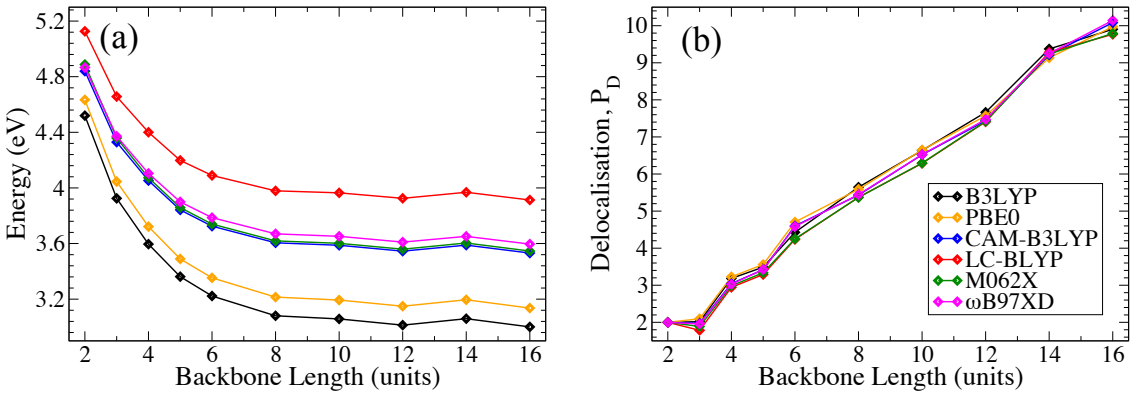

Figure C.1: (a) S_0-S_1 transition energies and delocalisation (b) for optimised geometries of thiophene obtained using different functionals in conjunction with the basis set 6-31G. Lines are intended as a guide to the eye.

C.2 Tests of functionals and basis sets

To test TD-DFT methods, we have repeated the calculations of S_0-S_1 absorption energies and delocalisation of optimised geometries of methyl-thiophene (shown in Figures 5.6 and 5.15, respectively). Methyl-thiophene geometries are obtained from optimised hexyl-thiophene geometries. We have tested the functionals B3LYP, PBE0, CAM-B3LYP, LC-BLYP, ωB97XD, and M062X along with the basis sets 6-31G and 6-31G*. Of the functionals, only B3LYP and PBE0 do not have any long-range correction (LRC) terms. For fluorene, B3LYP/6-31G has been shown by Schumacher *et al* [98] to lead to absorption energies in close correspondence with experimental results. Also, using basis sets larger than 6-31G* is computationally prohibitive for the ensemble spectra we present in Section 5.2 (based on up to 2000 individual calculations of geometries up to 32mer in length). As discussed in Section 5.1.1, we have not included any solvent treatment in these calculations as we found that, for B3LYP and CAMB3LYP, there was little effect (a reduction of $\simeq 50$ meV in the transition energies) in both cases when a PCM model chloroform was used.

In Figure C.1(a), we show the S_0-S_1 transition energy, ϵ_0 for various choices of functional and the basis set 6-31G. For each functional, the qualitative progression in backbone length is similar though there are slight differences in difference between the 2mer and effective converged energies. For LRC functionals (CAM-B3LYP, LC-BLYP, ωB97XD, and M062X), the difference between the 2mer transition energy and the 16mer is $\simeq 1.2$ eV while this difference for non-LRC functionals (B3LYP and PBE0) is $\simeq 1.6$ eV. Also, the transition energies for LRC functionals are far greater than non-LRC functionals as can be seen for the 16mers in Table C.2. Between LC-BLYP and B3LYP 16mers, the difference in transition energies is $\simeq 0.9$ eV and, between the other LRC functionals and B3LYP, is $\simeq 0.55$ eV. These differences are similar for the 6-31G* basis set. Utilising 6-31G* results in a shift of the transition energies of $\simeq 0.07$ eV with respect to the corresponding functional with 6-31G. This

Table C.2: S_0-S_1 transition energies (ϵ_0) and delocalisations (P_D) of optimised thiophene 16mers obtained with different functionals and basis sets.

Functional	B3LYP		PBE0		CAM-B3LYP	
Basis	6-31G	6-31G*	6-31G	6-31G*	6-31G	6-31G*
ϵ_0	3.001	2.936	3.136	3.062	3.532	3.446
P_D	9.90	10.06	9.97	10.05	10.08	10.16
Functional	LC-BLYP		M062X		ωB97XD	
Basis	6-31G	6-31G*	6-31G	6-31G*	6-31G	6-31G*
ϵ_0	3.913	3.813	3.546	3.471	3.596	3.500
P_D	9.77	9.83	9.79	9.82	10.14	10.22

shift is effectively constant with increasing length.

For each choice of functional, the delocalisation measure, P_D, (discussed in Section 5.3 and the following section of this appendix) is found to be effectively independent of functional choice as shown in Figure C.1(b). Also, utilising 6-31G* has no significant effect also. This can be seen for the 16mers in Table C.2.

As such, we conclude that the transition energies display a significant dependence on functional choice while the delocalisation properties do not. As such, we base our choice of functional on the spectral properties alone. As we discussed in Section 5.2.1, the absorption spectra of P3HT in good solvents are typically peaked at around 2.8-3.0 eV. This, in addition to its accuracy in describing fluorene spectra, leads to B3LYP being our functional of choice. Given the only slight improvement of the accuracy (based on the 16mer transition energies) obtained using 6-31G* compared to the computational expense entailed (which is amplified significantly given the number of MD geometries we consider), we deem that 6-31G is the most suitable choice of basis set.

C.3 Measures of delocalisation and effective conjugation lengths

In Section 5.3, we make extensive use of definitions of an excitation centre, n_{EC}, and a delocalisation measure, P_D, along the axis of the molecule. In this section, we give details regarding the choice of the P_D measure and possible alternative measures which may find applicability in future works.

C.3.1 The P_D delocalisation measure

We define the delocalisation using the P_D measure:

$$P_D \equiv 4\frac{\sum_{n=1}^{N} Q_n|\Delta n|}{\sum_{n=1}^{N} Q_M}, \tag{C.1}$$

in which n refers to monomer n and Q_n is the sum of the absolute charge differences on each atom between the ground (S_0) and excited (S_1^*) states. The factor of 4 is

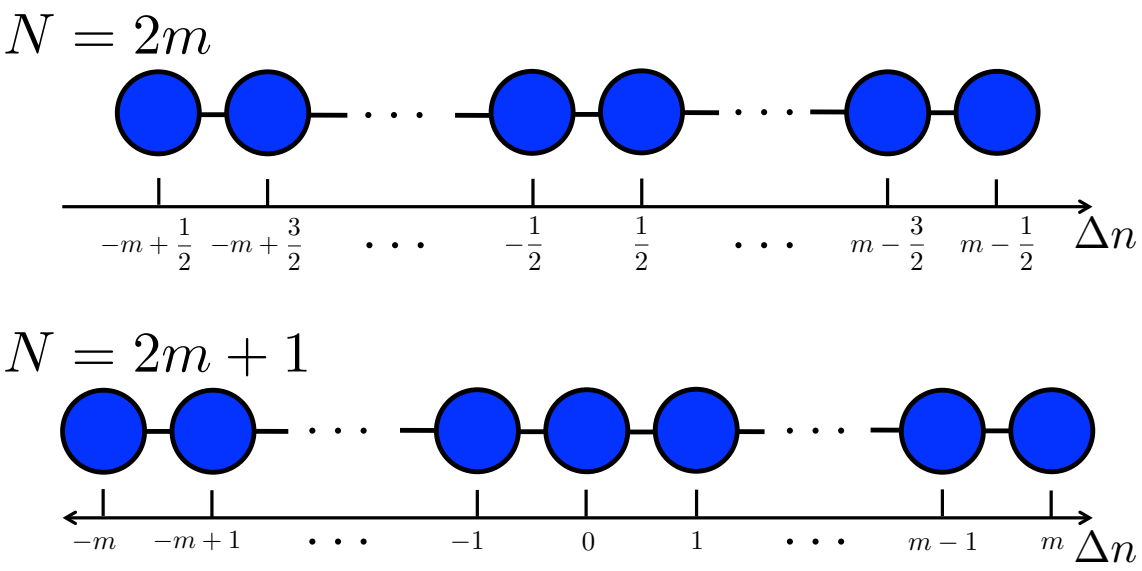

Figure C.2: Schematic of the basic test system of a linear chain of sites of even (upper) or odd (lower) units each with equal charge.

implemented so that an evenly delocalised system of N has a P_D value $\simeq N$ as will be discussed shortly. The P_D measure involves the definition of an excitation centre, n_{EC} similar to that of a centre-of-mass and a separation, Δn, between a monomer n and n_{EC}:

$$\Delta n \equiv n - n_{EC}; \qquad n_{EC} \equiv \frac{\sum_{n=1}^{N} Q_n n}{\sum_{n=1}^{N} Q_n.} \tag{C.2}$$

These measures consider only the charges on the monomer units and is a measure of delocalisation mapped to the axis of the molecular backbone. Essentially, this is a reduction of each molecular conformation to one dimension. The advantage of this reduction, for the work presented here, is that this allows for us to define the excitation centre, n_{EC}, in a manner which returns a value corresponding to an actual point along the molecular chain. This allows us to probe the effects of distortions on excitation localisation along the chain in a straightforward manner. A full three dimensional measure, such as a radius of gyration, will not be so easily mapped on to a particular segment of the molecule. Furthermore, a real-space measure has embedded in it the molecular conformation itself. While this may be useful for certain properties, for instance approximating the size of an exciton, when considering conformationally dependent localisation, we feel it is advantageous to have a conformation independent measure whose values may then be expressed as a function of conformational properties. We shall give a brief discussion of real-space measures in Appendix C.3.2.

The measure P_D was chosen for its ease of computation and its ability to effectively replicate evenly-delocalised test systems in which each monomer has a total charge $Q_M = Q$. In Figure C.2, schematics are given of such systems with even and odd numbers of units, N, with the molecular centre at $\Delta n = 0$. This means that

the values of Δn corresponding to the individual monomers differ for even and odd N: For even N, $\Delta n = m - 1/2$ with $m : \mathbb{Z} \in [-(N/2-1), N/2]$, and for odd N, $\Delta n = m$ with $m : \mathbb{Z} \in [-(N-1)/2, (N-1)/2]$.

Let us express the P_D for the even case by exploiting the symmetry about $\Delta n = 0$:

$$P_D = 4\frac{\sum_{n=1}^{N} Q_n|\Delta n|}{\sum_{n=1}^{N} Q_n} = \frac{4Q}{NQ}\sum_{i=1}^{N/2}(2i-1). \tag{C.3}$$

The factor of 2 emerges from double counting over either side of $\Delta n = 0$. Using the defintion of the sum over integers, $\sum_{i=1}^{n} i = (1/2)(n+1)n$, this reduces to:

$$P_D = \frac{4}{N}\left(\frac{N}{2}\left(\frac{N}{2}+1\right) - \frac{N}{2}\right) = \frac{4}{N}\frac{N^2}{4} = N. \tag{C.4}$$

Similarly, for odd N, P_D is expressed as:

$$P_D = 4\frac{\sum_{n=1}^{N} Q_n|\Delta n|}{\sum_{n=1}^{N} Q_n} = \frac{4Q}{NQ}\sum_{i=1}^{(N-1)/2} 2i. \tag{C.5}$$

Again, using the sum over integers, this reduces to:

$$P_D = \frac{4}{N}\frac{(N-1)}{2}\frac{(N+1)}{2} = \frac{4}{N}\frac{(N^2-1)}{4} = N - \frac{1}{N}. \tag{C.6}$$

As such, for the test system, the P_D delocalisation measure agrees closely with the expected value N. For odd N, the error term $1/N$ will become significantly small with increasing N e.g. for $N = 5$, the fractional error is $1/5^2 = 0.04$. Also, because each monomer contribution is normalised by its charge component, if one considers a system of N units with perfect, even localisation across M units and $Q_n = 0$ for all other units, the measure is unaffected by the presence of the extra units and returns an identical value. Thus, the P_D measure allows for comparison to be drawn between molecules of different length without further, length-scale dependent adjustments. For the purposes of the work presented in Section 5.3, this measure is ideal in its simplicity and interpretation.

C.3.2 Alternative delocalisation measures

The measure, P_D, is of course not a unique measure for interpreting delocalisation. Following the same principles detailed above, there are effectively an infinite number of potential delocalisation measures available. One such alternative measure, which we shall call R_D^2, can be formulated based on using squares of Δr_M as opposed to

absolute values:

$$R_D^2 \equiv 12 \frac{\sum_{M=1}^{N} Q_M \Delta r_M^2}{\sum_{M=1}^{N} Q_M}. \tag{C.7}$$

The notation R_D^2 is reflective of this measure being a direct analogue of the radius of gyration, R_G.

For the test examples given above, with N even, R_D^2 is expressed by:

$$R_D^2 = \frac{24Q}{NQ} \sum_{i=1}^{(N/2)} \left(i - \frac{1}{2} \right)^2 = \frac{6}{N} \sum_{i=1}^{N/2} (4i^2 - 4i + 1). \tag{C.8}$$

By invoking both the sum of integers and the sum over squares:

$$\sum_{i=1}^{N} i^2 = N^3/3 + N^2/2 + N/6, \tag{C.9}$$

this reduces to:

$$R_D^2 = \frac{6}{N} \left(\frac{N^3}{6} + \frac{N^2}{2} + \frac{N}{3} - \frac{N^2}{2} - N + \frac{N}{2} \right) = \frac{6}{N} \frac{(N^3 - N)}{6} = N^2 - 1. \tag{C.10}$$

For odd N, R_D^2 is similarly expressed as:

$$R_D^2 = \frac{24}{N} \sum_{i=1}^{(N-1)/2} i^2. \tag{C.11}$$

Again, using the sum over squares, this reduces to:

$$R_D^2 = \frac{24}{N} \left(\frac{(N-1)^3}{24} + \frac{(N-1)^2}{8} + \frac{N-1}{12} \right) = N^2 - 1. \tag{C.12}$$

For both cases, taking the square root, the R_D measure thus gives:

$$R_D = N \left(1 - \frac{1}{N^2} \right)^{\frac{1}{2}}. \tag{C.13}$$

The R_D measure thus gives a similar value as a the P_D measure with an error factor of $\sqrt{1 - 1/N^2}$. Clearly, this measure would also be suitable as a measure of delocalisation. The reason we have chosen to use P_D is that that the dependence on the distance from the excitation centre is linear as opposed to harmonic. The linear dependence allows for weighting of all terms with respect to charge without increasing the weighting for further monomers. We have performed brief tests and found that there are differences in the values returned for each measure but their interpretation with regards to a reference geometry (i.e. the DFT optimised geometry) is effectively the same. We reason, thus, that the measures are essentially interchangeable for our purposes. However, it may be the case if one were to use

these delocalisation measures as input for further calculations of physical processes, as opposed to being purely measures, that one measure may be more appropriate than the other.

The R_D example is, as with P_D, a 1-D, dimensionless measure of delocalisation and, in removing the explicit conformational dependence, is not strictly a measure of a real space delocalisation. While we have discussed that this is beneficial for our purposes of understanding the effect of conformational disorder and on-chain localisation, it is also true that a real-space measure may be more useful for purposes such as estimating the size of a formed exciton. One simple measure for this purpose is an analogous radius of gyration, R_G:

$$R_G^2 \equiv \frac{\sum_{i=1}^{N} q_i |\Delta \mathbf{r}_i|^2}{\sum_{i=1}^{N} q_i}. \tag{C.14}$$

Here, we define q_i as the absolute difference between the S_0 and S_1^* charges:

$$q_i \equiv |q_i^{(S_1^*)} - q_i^{(S_0)}|, \tag{C.15}$$

and $\Delta \mathbf{r}_i$ is the difference between the atomic position, $\mathbf{r}_i$ and the real-space excitation centre, $\mathbf{r}_{EC}$:

$$\Delta \mathbf{r}_i \equiv \mathbf{r}_i - \mathbf{r}_{EC}; \qquad \mathbf{r}_{EC} \equiv \frac{\sum_{i=1}^{N} q_i \mathbf{r}_i}{\sum_{i=1}^{N} q_i}. \tag{C.16}$$

As mentioned previously, the interpretation of $\mathbf{r}_{EC}$ is less well defined in a polymer in solution than the dimensionless n_{EC} given that $\mathbf{r}_{EC}$ may be located anywhere in space and may not be well mapped to a particular point on the molecule. This may be a more useful measure in close-packed systems such as polymers in poor solvents or films where excitations may be spread over two or more neighbouring chromophores.

Bibliography

[1] W. Brütting, ed., *Physics of Organic Semiconductors*. Wiley-VCH, 2005.

[2] C. Kittel, *Introduction to Solid State Physics*. Wiley, 2005.

[3] C. F. Klingshirn, *Semiconductor Optics*. Springer, 1997.

[4] J. M. Shaw and P. F. Siedler, "Organic electronics: Introduction," *IBM J. Res. Dev.*, vol. 45, no. 1, pp. 3–9, 2001.

[5] J.-H. Park and T. Sudarshan, eds., *Chemical Vapour Deposition*. ASM, 2001.

[6] A. Facchetti, "π-conjugated polymers for organic electronics and photovoltaic cell applications," *Chem. Mater.*, vol. 23, no. 3, pp. 733–758, 2011.

[7] A. J. Heeger, "Nobel lecture: Semiconducting and metallic polymers: The fourth generation of polymeric materials," *Rev. Mod. Phys.*, vol. 73, pp. 681–700, 2001.

[8] H. Bässler and A. Köhler, *Charge Transport in Organic Semiconductors*, pp. 1–65. Berlin, Heidelberg: Springer Berlin Heidelberg, 2012.

[9] S. Roth and D. Carroll, *One-Dimensional Metals: Conjugated Polymers, Organic Crystals, Carbon Nanotubes*. Wiley, 2006.

[10] H. Kallmann and M. Pope, "Bulk conductivity in organic crystals," *Nature*, vol. 186, no. 4718, pp. 31–33, 1960.

[11] H. Kallmann and M. Pope, "Positive hole injection into organic crystals," *J. Chem. Phys.*, vol. 32, no. 1, pp. 300–301, 1960.

[12] M. Sano, M. Pope, and H. Kallmann, "Electroluminescence and band gap in anthracene," *J. Chem. Phys.*, vol. 43, no. 8, pp. 2920–2921, 1965.

[13] C. K. Chiang, C. R. Fincher, Y. W. Park, A. J. Heeger, H. Shirakawa, E. J. Louis, S. C. Gau, and A. G. MacDiarmid, "Electrical conductivity in doped polyacetylene," *Phys. Rev. Lett*, vol. 39, no. 17, pp. 1098–1101, 1977.

[14] H. Shirakawa, E. J. Louis, A. G. MacDiarmid, C. K. Chiang, and A. J. Heeger, "Synthesis of electrically conducting organic polymers: halogen derivatives of polyacetylene, (CH)," *J. Chem. Soc., Chem. Commun.*, pp. 578–580, 1977.

[15] P. J. Flory, *Statistical Mechanics of Chain Molecules*. Wiley (Interscience), New York, 1969.

[16] P. G. de Gennes, *Scaling Concepts in Polymer Physics*. Cornell University Press, 1979.

[17] J. des Cloizeaux and G. Jannink, *Polymers in Solution: Their Modelling and Structure*. Clarendon Press, 1990.

[18] R. Partridge, "Electroluminescence from polyvinylcarbazole films: 1. carbazole cations," *Polymer*, vol. 24, no. 6, pp. 733 – 738, 1983.

[19] R. Partridge, "Electroluminescence from polyvinylcarbazole films: 2. polyvinylcarbazole films containing antimony pentachloride," *Polymer*, vol. 24, no. 6, pp. 739 – 747, 1983.

[20] R. Partridge, "Electroluminescence from polyvinylcarbazole films: 3. electroluminescent devices," *Polymer*, vol. 24, no. 6, pp. 748 – 754, 1983.

[21] R. Partridge, "Electroluminescence from polyvinylcarbazole films: 4. electroluminescence using higher work function cathodes," *Polymer*, vol. 24, no. 6, pp. 755 – 762, 1983.

[22] C. W. Tang and S. A. VanSlyke, "Organic electroluminescent diodes," *Appl. Phys. Lett.*, vol. 51, no. 12, pp. 913–915, 1987.

[23] J. H. Burroughes, D. D. C. Bradley, A. R. Brown, R. N. Marks, K. Mackay, R. H. Friend, P. L. Burns, and A. B. Holmes, "Light-emitting diodes based on conjugated polymers," *Nature*, vol. 347, no. 6293, pp. 539–541, 1990.

[24] C. W. Tang, "Two-layer organic photovoltaic cell," *Appl. Phys. Lett.*, vol. 48, no. 2, pp. 183–185, 1986.

[25] H. Koezuka, A. Tsumura, and T. Ando, "Field-effect transistor with polythiophene thin film," *Synth. Met.*, vol. 18, no. 1, pp. 699 – 704, 1987.

[26] W. Barford, *Electronic and Optical Properties of Conjugated Polymers*. International Series of Monographs on Physics, OUP Oxford, 2005.

[27] M. Smith and J. March, *March's Advanced Organic Chemistry: Reactions, Mechanisms, and Structure*. Wiley, 2007.

[28] G. Karagounis, *Introductory Organic Quantum Chemistry*. Academic Press, 1962.

[29] J. Slater, *Quantum Theory of Matter*. International series in pure and applied physics, McGraw-Hill, 1968.

[30] Wikimedia Commons. http://commons.wikimedia.org.

[31] Sigma-Aldrich. http://www.sigmaaldrich.com.

[32] C. Sekine, Y. Tsubata, T. Yamada, M. Kitano, and S. Doi, "Recent progress of high performance polymer OLED and OPV materials for organic printed electronics," *Sci. Technol. Adv. Mater.*, vol. 15, no. 3, pp. 034203–034217, 2014.

[33] K. S. Yook and J. Y. Lee, "Small molecule host materials for solution processed phosphorescent organic light-emitting diodes," *Adv. Mater.*, vol. 26, no. 25, pp. 4218–4233, 2014.

[34] M. Zhu and C. Yang, "Blue fluorescent emitters: design tactics and applications in organic light-emitting diodes," *Chem. Soc. Rev.*, vol. 42, pp. 4963–4976, 2013.

[35] Y. Yuan, G. Giri, A. L. Ayzner, A. P. Zoombelt, S. C. B. Mannsfeld, J. Chen, D. Nordlund, M. F. Toney, J. Huang, and Z. Bao, "Ultra-high mobility transparent organic thin film transistors grown by an off-centre spin-coating method," *Nat. Commun.*, vol. 5, p. 3005, 2014.

[36] B. Kraabel, C. Lee, D. McBranch, D. Moses, N. Sariciftci, and A. Heeger, "Ultrafast photoinduced electron transfer in conducting polymerbuckminsterfullerene composites," *Chem. Phys. Lett.*, vol. 213, no. 3, pp. 389 – 394, 1993.

[37] S. H. Park, A. Roy, S. Beaupre, S. Cho, N. Coates, J. S. Moon, D. Moses, M. Leclerc, K. Lee, and A. J. Heeger, "Bulk heterojunction solar cells with internal quantum efficiency approaching 100%," *Nat. Photonics*, vol. 3, no. 5, pp. 297–302, 2009.

[38] A. Fruchtman, R. Gómez-Bombarelli, B. W. Lovett, and E. M. Gauger, "Photocell optimization using dark state protection," *Phys. Rev. Lett.*, vol. 117, p. 203603, 2016.

[39] D. Moses, "High quantum efficiency luminescence from a conducting polymer in solution: A novel polymer laser dye," *Appl. Phys. Lett.*, vol. 60, no. 26, pp. 3215–3216, 1992.

[40] L. Claes, J.-P. François, and M. S. Deleuze, "Molecular packing of oligomer chains of poly(p-phenylene vinylene)," *Chem. Phys. Lett.*, vol. 339, pp. 216–222, 2001.

[41] J. K. J. van Duren, X. Yang, J. Loos, C. W. T. Bulle-Lieuwma, Z. B. Sieval, J. C. Hummelen, and R. A. J. Janssen, "Relating the morphology of poly(p-phenylene vinylene)/methanofullenerene blends to solar-cell performance," *Adv. Funct. Mater.*, vol. 14, no. 5, pp. 425–433, 2004.

[42] A. Lukyanov, A. Malafeev, V. Ivanov, H.-L. Chen, K. Kremer, and D. Andrienko, "Solvated poly-(phenylene vinylene) derivatives: conformational structure and aggregation behaviour," *J. Mater. Chem*, vol. 20, pp. 10475 – 10485, 2010.

[43] L. C. P. Almeida, V. Zucolotto, R. A. Domingues, T. D. Z. Atvars, and A. F. Noguiera, "Photoelectrochemical, photophysical and morphological studies of electrostatic layer-by-layer thin films based on poly(p-phenylenevinylene) and single-walled carbon nanotubes," *Photochem. Photobiol. Sci.*, vol. 10, pp. 1766–1772, 2011.

[44] S. Kilina, N. Dandu, E. R. Batista, A. Saxena, R. L. Martin, D. L. Smith, and S. Tretiak, "Effect of packing on formation of deep carrier traps in amorphous conjugated polymers," *J. Phys. Chem. Lett.*, vol. 4, pp. 1453 – 1459, 2013.

[45] G. W. Heffner and D. S. Pearson, "Molecular characterization of poly(3-hexylthiophene)," *Macromolecules*, vol. 24, no. 23, pp. 6295–6299, 1991.

[46] D. L. Cheung, D. P. McMahon, and A. Troisi, "Computational study of the structure and charge transfer parameters in low-molecular-mass P3HT," *J. Phys. Chem. B*, vol. 113, pp. 9393–9401, 2009.

[47] M. Bockmann, T. Schemme, D. H. de Jong, C. Denz, A. Heuer, and N. L. Doltsinis, "Structure of P3HT crystals, thin films, and solutions by UV/Vis spectral analysis," *Phys. Chem. Chem. Phys.*, vol. 17, pp. 28616–28625, 2015.

[48] U. Mehmood, A. Al-Ahmed, and I. A. Hussein, "Review on recent advances in polythiophene based photovoltaic devices," *Renew. Sustainable Energy Rev.*, vol. 57, pp. 550 – 561, 2016.

[49] A. Monkman, C. Rothe, S. King, and F. Dias, *Polyfluorene Photophysics*. Berlin, Heidelberg: Springer Berlin Heidelberg, 2008.

[50] D. D. C. Bradley, M. Grell, X. Long, H. Mellor, A. W. Grice, M. Inbasekaran, and E. P. Woo, "Influence of aggregation on the optical properties of a polyfluorene," *Proc. SPIE*, vol. 3145, pp. 254–259, 1997.

[51] M. Grell, D. Bradley, X. Long, T. Chamberlain, M. Inbasekaran, E. Woo, and M. Soliman, "Chain geometry, solution aggregation and enhanced dichroism in the liquidcrystalline conjugated polymer poly(9,9-dioctylfluorene)," *Acta Polym.*, vol. 49, no. 8, pp. 439–444, 1998.

[52] M. Knaapila, V. M. Garamus, F. B. Dias, L. Almsy, F. Galbrecht, A. Charas, J. Morgado, H. D. Burrows, U. Scherf, and A. P. Monkman, "Influence of solvent quality on the self-organization of archetypical hairy rods-branched and linear side chain polyfluorenes: Rodlike chains versus "beta-sheets" in solution," *Macromolecules*, vol. 39, no. 19, pp. 6505–6512, 2006.

[53] K.-H. Weinfurtner, H. Fujikawa, S. Tokito, and Y. Taga, "Highly efficient pure blue electroluminescence from polyfluorene: Influence of the molecular weight distribution on the aggregation tendency," *Appl. Phys. Lett.*, vol. 76, no. 18, pp. 2502–2504, 2000.

[54] Y. He, S. Gong, R. Hattori, and J. Kanicki, "High performance organic polymer light-emitting heterostructure devices," *Appl. Phys. Lett.*, vol. 74, no. 16, pp. 2265–2267, 1999.

[55] A. C. Arias, J. D. MacKenzie, R. Stevenson, J. J. M. Halls, M. Inbasekaran, E. P. Woo, D. Richards, and R. H. Friend, "Photovoltaic performance and morphology of polyfluorene blends: a combined microscopic and photovoltaic investigation," *Macromolecules*, vol. 34, no. 17, pp. 6005–6013, 2001.

[56] H. J. Snaith, A. C. Arias, A. C. Morteani, C. Silva, and R. H. Friend, "Charge generation kinetics and transport mechanisms in blended polyfluorene photovoltaic devices," *Nano Lett.*, vol. 2, no. 12, pp. 1353–1357, 2002.

[57] G. J. Hedley, A. J. Ward, A. Alekseev, C. T. Howells, E. R. Martins, L. A. Serrano, G. Cooke, A. Ruseckas, and I. D. W. Samuel, "Deteriming the optimum morphology in high-performance polymer-fullerene organic photovoltaic cells," *Nat. Commun.*, vol. 4, p. 2867, 2013.

[58] S. Guo, E. M. Herzig, A. Naumann, G. Tainter, J. Perlich, and P. Müller-Buschbaum, "Influence of solvent and solvent additive on the morphology of PTB7 films probed via X-ray scattering," *J. Phys. Chem. B*, vol. 118, no. 1, pp. 344–350, 2014.

[59] C. Gu, Y. Chen, Z. Zhang, S. Xue, S. Sun, C. Zhong, H. Zhang, Y. Lv, F. Li, F. Huang, and Y. Ma, "Achieving high efficiency of PTB7-based polymer solar cells via integrated optimization of both anode and cathode interlayers," *Adv. Energy Mater.*, vol. 4, no. 8, p. 1301771, 2014. 1301771.

[60] P. M. Beaujuge, C. M. Amb, and J. R. Reynolds, "Spectral engineering in π-conjugated polymers with intramolecular donor-acceptor interactions," *Acc. Chem. Res.*, vol. 43, no. 11, pp. 1396–1407, 2010.

[61] J. Mei and Z. Bao, "Side chain engineering in solution-processable conjugated polymers," *Chem. Mater.*, vol. 26, no. 1, pp. 604–615, 2014.

[62] V. Vohra, K. Kawashima, T. Kakara, T. Koganezawa, I. Osaka, K. Takimiya, and H. Murata, "Efficient inverted polymer solar cells employing favourable molecular orientation," *Nat Photon*, vol. 9, no. 6, pp. 403–408, 2015.

[63] A. J. Heeger, "25th anniversary article: Bulk heterojunction solar cells: Understanding the mechanism of operation," *Adv. Mater.*, vol. 26, no. 1, pp. 10–28, 2014.

[64] Y. Yamashita, "Organic semiconductors for organic field-effect transistors," *Sci. Tech. Adv. Mater.*, vol. 10, no. 2, p. 024313, 2009.

[65] T. Hasegawa and J. Takeya, "Organic field-effect transistors using single crystals," *Sci. Tech. Adv. Mater.*, vol. 10, no. 2, p. 024314, 2009.

[66] J. Locklin and Z. Bao, "Effect of morphology on organic thin film transistor sensors," *Anal. Bioanal. Chem.*, vol. 384, no. 2, pp. 336–342, 2006.

[67] R. Tempelaar, A. Stradomska, J. Knoester, and F. C. Spano, "Circularly polarized luminescence as a probe for long-range interactions in molecular aggregates," *J. Phys. Chem. B*, vol. 115, no. 36, pp. 10592–10603, 2011.

[68] J. Lakowicz, *Principles of Fluorescence Spectroscopy*. Springer US, 2007.

[69] D. Beljonne, Z. Shuai, G. Pourtois, and J. L. Bredas, "Spin-orbit coupling and intersystem crossing in conjugated polymers: a configuration interaction description," *J. Phys. Chem. A*, vol. 105, no. 15, pp. 3899–3907, 2001.

[70] A. Rao, P. C. Y. Chow, S. Gelinas, C. W. Schlenker, C.-Z. Li, H.-L. Yip, A. K. Y. Jen, D. S. Ginger, and R. H. Friend, "The role of spin in the kinetic control of recombination in organic photovoltaics," *Nature*, vol. 500, no. 7463, pp. 435–439, 2013.

[71] A. J. Heeger, S. Kivelson, J. R. Schrieffer, and W. P. Su, "Solitons in conducting polymers," *Rev. Mod. Phys.*, vol. 60, pp. 781–850, 1988.

[72] X. Guo, M. Baumgarten, and K. Müllen, "Designing π-conjugated polymers for organic electronics," *Prog. Polym. Sci.*, vol. 38, no. 12, pp. 1832–1908, 2013.

[73] T. Förster, "Zwischenmolekulare energiewanderung und fluoreszenz," *Ann. Phys.*, vol. 437, pp. 55–75, 1948.

[74] D. L. Dexter, "A theory of sensitized luminescence in solids," *J. Chem. Phys.*, vol. 21, pp. 836 – 850, 1953.

[75] J.-C. Denis, S. Schumacher, and I. Galbraith, "Quantitative description of interactions between organic chromophores," *J. Chem. Phys.*, vol. 137, p. 224102, 2012.

[76] J.-C. Denis, S. Schumacher, G. J. Hedley, A. Ruseckas, P. O. Morawska, Y. Wang, S. Allard, U. Scherf, G. A. Turnbull, I. D. W. Samuel, and I. Galbraith, "Subpicosecond exciton dynamics in polyfluorene films from experiment and microscopic theory," *J. Phys. Chem. C*, vol. 119, no. 18, pp. 9734–9744, 2015.

[77] A. Köhler and H. Bässler, "What controls triplet exciton transfer in organic semiconductors?," *J. Mater. Chem.*, vol. 21, pp. 4003–4011, 2011.

[78] R. R. Lunt, N. C. Giebink, A. A. Belak, J. B. Benziger, and S. R. Forrest, "Exciton diffusion lengths of organic semiconductor thin films measured by spectrally resolved photoluminescence quenching," *J. Appl. Phys.*, vol. 105, no. 5, 2009.

[79] S. Baranovski and O. Rubel, *Description of Charge Transport in Amorphous Semiconductors*, pp. 49–96. John Wiley & Sons, Ltd, 2006.

[80] Y. Liu, J. Zhao, Z. Li, C. Mu, W. Ma, H. Hu, K. Jiang, H. Lin, H. Ade, and H. Yan, "Aggregation and morphology control enables multiple cases of high-efficiency polymer solar cells," *Nat. Commun.*, vol. 5, p. 5293, 2014.

[81] J. Zhao, Y. Li, G. Yang, K. Jiang, H. Lin, H. Ade, W. Ma, and H. Yan, "Efficient organic solar cells processed from hydrocarbon solvents," *Nat. Energy*, vol. 1, p. 15027, 2016.

[82] D. Vacar, E. S. Maniloff, D. W. McBranch, and A. J. Heeger, "Charge-transfer range for photoexcitations in conjugated polymer/fullerene bilayers and blends," *Phys. Rev. B*, vol. 56, pp. 4573–4577, 1997.

[83] B. P. Lyons and A. P. Monkman, "The role of exciton diffusion in energy transfer between polyfluorene and tetraphenyl porphyrin," *Phys. Rev. B*, vol. 71, p. 235201, 2005.

[84] P. E. Shaw, A. Ruseckas, and I. D. W. Samuel, "Exciton diffusion measurements in poly(3-hexylthiophene)," *Adv. Mater.*, vol. 20, no. 18, pp. 3516–3520, 2008.

[85] A. Bruno, L. X. Reynolds, C. Dyer-Smith, J. Nelson, and S. A. Haque, "Determining the exciton diffusion length in a polyfluorene from ultrafast fluorescence measurements of polymer/fullerene blend films," *J. Phys. Chem. C*, vol. 117, no. 39, pp. 19832–19838, 2013.

[86] J. Peet, J. Y. Kim, N. E. Coates, W. L. Ma, D. Moses, A. J. Heeger, and G. C. Bazan, "Efficiency enhancement in low-bandgap polymer solar cells by processing with alkane dithiols," *Nat. Mater.*, vol. 6, no. 7, pp. 497–500, 2007.

[87] J. K. Lee, W. L. Ma, C. J. Brabec, J. Yuen, J. S. Moon, J. Y. Kim, K. Lee, G. C. Bazan, and A. J. Heeger, "Processing additives for improved efficiency from bulk heterojunction solar cells," *J. Am. Chem. Soc.*, vol. 130, no. 11, pp. 3619–3623, 2008.

[88] J. L. Brédas, G. B. Street, B. Thémans, and J. M. André, "Organic polymers based on aromatic rings (polyparaphenylene, polypyrrole, polythiophene): Evolution of the electronic properties as a function of the torsion angle between adjacent rings," *J. Chem. Phys.*, vol. 83, no. 3, pp. 1323–1329, 1985.

[89] W. Barford, D. G. Lidzey, D. V. Makhov, and A. J. H. Meijer, "Exciton localization in disordered poly(3-hexylthiophene)," *J. Chem. Phys.*, vol. 133, no. 4, 2010.

[90] B. J. Schwartz, "Conjugated polymers: What makes a chromophore?," *Nat. Mater.*, vol. 7, no. 6, pp. 427–428, 2008.

[91] R. Milad, J. Shi, A. Aguirre, A. Cardone, B. Milian-Medina, G. M. Farinola, M. Abderrabba, and J. Gierschner, "Effective conjugation in conjugated polymers with strongly twisted backbones: a case study on fluorinated MEHPPV," *J. Mater. Chem. C*, vol. 4, pp. 6900–6906, 2016.

[92] M. Bernardi, M. Giulianini, and J. C. Grossman, "Self-assembly and its impact on interfacial charge transfer in carbon nanotube/P3HT solar cells," *ACS Nano*, vol. 4, no. 11, pp. 6599–6606, 2010.

[93] K. H. DuBay, M. L. Hall, T. F. Hughes, C. Wu, D. R. Reichman, and R. A. Friesner, "Accurate force field development for modeling conjugated polymers," *J. Chem. Theory Comput.*, vol. 8, pp. 4556–4569, 2012.

[94] K. Becker, E. Da Como, J. Feldmann, F. Scheliga, E. Thorn Csnyi, S. Tretiak, and J. M. Lupton, "How chromophore shape determines the spectroscopy of phenylenevinylenes: origin of spectral broadening in the absence of aggregation," *J. Phys. Chem. B*, vol. 112, no. 16, pp. 4859–4864, 2008.

[95] D. V. Makhov and W. Barford, "Local exciton ground states in disordered polymers," *Phys. Rev. B*, vol. 81, p. 165201, 2010.

[96] W. Barford, "Excitons in conjugated polymers: A tale of two particles," *J. Phys. Chem. A*, vol. 117, no. 13, pp. 2665–2671, 2013.

[97] R. S. Bhatta, Y. Y. Yimer, M. Tsige, and D. S. Perry, "Conformations and torsional potentials of poly(3-hexylthiophene) oligomers: Density functional calculations up to the dodecamer," *Comput. Theor. Chem.*, vol. 995, pp. 36–42, 2012.

[98] S. Schumacher, A. Ruseckas, N. A. Montgomery, P. J. Skabara, A. L. Kanibolotsky, M. J. Paterson, I. Galbraith, G. A. Turnbull, and I. D. W. Samuel, "Effect of exciton self-trapping and molecular conformation on photophysical properties of oligofluorenes," *J. Chem. Phys.*, vol. 131, no. 15, pp. 154906–154913, 2009.

[99] C. C. Kitts and D. A. Vanden Bout, "The effect of solvent quality on the chain morphology in solution of poly(9,9'-dioctylfluorene)," *Polymer*, vol. 48, pp. 2322–2330, 2007.

[100] D. W. Bright, F. B. Dias, F. Galbrecht, U. Scherf, and A. P. Monkman, "The influence of alkyl-chain length on beta-phase formation in polyfluorenes," *Adv. Funct. Mater.*, vol. 19, no. 1, pp. 67–73, 2009.

[101] M. N. Kobrak and E. R. Bittner, "A dynamic model for exciton self-trapping in conjugated polymers. i. theory," *J. Chem. Phys.*, vol. 112, no. 12, pp. 5399–5409, 2000.

[102] M. N. Kobrak and E. R. Bittner, "A quantum molecular dynamics study of exciton self-trapping in conjugated polymers: Temperature dependence and spectroscopy," *J. Chem. Phys.*, vol. 112, no. 17, pp. 7684–7692, 2000.

[103] N. A. Montgomery, J.-C. Denis, S. Schumacher, A. Ruseckas, P. J. Skabara, A. Kanibolotsky, M. J. Paterson, I. Galbraith, G. A. Turnbull, and I. D. W. Samuel, "Optical excitations in star-shaped fluorene molecules," *J. Phys. Chem. A*, vol. 115, no. 14, pp. 2913–2919, 2011.

[104] N. A. Montgomery, G. J. Hedley, A. Ruseckas, J.-C. Denis, S. Schumacher, A. L. Kanibolotsky, P. J. Skabara, I. Galbraith, G. A. Turnbull, and I. D. W. Samuel, "Dynamics of fluorescence depolarisation in star-shaped oligofluorene-truxene molecules," *Phys. Chem. Chem. Phys.*, vol. 14, pp. 9176–9184, 2012.

[105] A. Thiessen, D. Würsch, S.-S. Jester, A. V. Aggarwal, A. Idelson, S. Bange, J. Vogelsang, S. Höger, and J. M. Lupton, "Exciton localization in extended -electron systems: Comparison of linear and cyclic structures," *J. Phys. Chem. B*, vol. 119, no. 30, pp. 9949–9958, 2015.

[106] R. Franklin-Mergarejo, D. O. Alvarez, S. Tretiak, and S. Fernandez-Alberti, "Carbon nanorings with inserted acenes: breaking symmetry in excited state dynamics," *Sci. Rep.*, vol. 6, p. 31253, 2016.

[107] N. E. Jackson, B. M. Savoie, T. J. Marks, L. X. Chen, and M. A. Ratner, "The next breakthrough for organic photovoltaics?," *J. Phys. Chem. Lett.*, vol. 6, no. 1, pp. 77–84, 2015.

[108] M. Reichenberger, J. A. Love, A. Rudnick, S. Bagnich, F. Panzer, A. Stradomska, G. C. Bazan, T.-Q. Nguyen, and A. Köhler, "The effect of intermolecular interaction on excited states in p - DTS(FBTTH2)2," *J. Chem. Phys.*, vol. 144, no. 7, p. 074904, 2016.

[109] D. Alberga, A. Perrier, I. Ciofini, G. F. Mangiatordi, G. Lattanzi, and C. Adamo, "Morphological and charge transport properties of amorphous and crystalline P3HT and PBTTT: insights from theory," *Phys. Chem. Chem. Phys.*, vol. 17, pp. 18742–18750, 2015.

[110] A. Zusan, B. Gieseking, M. Zerson, V. Dyakonov, R. Magerle, and C. Deibel, "The effect of diiodooctane on the charge carrier generation in organic solar cells based on the copolymer PBDTTT-C," *Sci. Rep.*, vol. 5, p. 8286, 2015.

[111] W. Kim, J. K. Kim, E. Kim, T. K. Ahn, D. H. Wang, and J. H. Park, "Conflicted effects of a solvent additive on PTB7:PC71BM bulk heterojunction solar cells," *J. Phys. Chem. C*, vol. 119, no. 11, pp. 5954–5961, 2015.

[112] O. Kratky and G. Porod, "Röntgenuntersuchung gelöster fadenmoleküle," *Recl. Trav. Chim. Pays-Bas*, vol. 68, no. 12, pp. 1106–1122, 1949.

[113] K. Huang, *Statistical mechanics*. Wiley, 1963.

[114] V. N. Pokrovskii, *The Mesoscopic Theory of Polymer Dynamics*. Springer, 2010.

[115] M. Doi and S. F. Edwards, *The Theory of Polymer Dynamics*. Clarendon, Oxford University Press, New York, 1986.

[116] B. Muls, H. Uji-i, S. Melnikov, A. Moussa, W. Verheijen, J.-P. Soumillion, J. Josemon, K. Müllen, and J. Hofkens, "Direct measurement of the end-to-end distance of individual polyfluorene polymer chains," *ChemPhysChem*, vol. 6, no. 11, pp. 2286–2294, 2005.

[117] J. F. Marko and E. D. Siggia, "Stretching DNA," *Macromolecules*, vol. 28, no. 26, pp. 8759–8770, 1995.

[118] J. Wilhelm and E. Frey, "Radial distribution function of semiflexible polymers," *Phys. Rev. Lett.*, vol. 77, pp. 2581–2584, 1996.

[119] H. Kleinert, *Path Integrals in Quantum Mechanics, Statistics, Polymer Physics, and Financial Markets*. Singapore: World Scientific, 5th ed., 2012.

[120] G. Fytas, H. G. Nothofer, U. Scherf, D. Vlassopoulos, and G. Meier, "Structure and dynamics of nondilute polyfluorene solutions," *Macromolecules*, vol. 35, no. 2, pp. 481–488, 2002.

[121] L. Wu, T. Sato, H.-Z. Tang, and M. Fujiki, "Conformation of a polyfluorene derivative in solution," *Macromolecules*, vol. 37, no. 16, pp. 6183–6188, 2004.

[122] L. J. Lapidus, P. J. Steinbach, W. A. Eaton, A. Szabo, and J. Hofrichter, "Effects of chain stiffness on the dynamics of loop formation in polypeptides. appendix: testing a 1-dimensional diffusion model for peptide dynamics," *J. Phys. Chem. B*, vol. 106, no. 44, pp. 11628–11640, 2002.

[123] D. Meimaroglou and C. Kiparissides, "Review of Monte Carlo methods for the prediction of distributed molecular and morphological polymer properties," *Ind. Eng. Chem. Res.*, vol. 53, no. 22, pp. 8963–8979, 2014.

[124] P. J. Flory, "Thermodynamics of high polymer solutions," *J. Chem. Phys.*, vol. 10, no. 1, pp. 51–61, 1942.

[125] S. Kouijzer, J. J. Michels, M. van den Berg, V. S. Gevaerts, M. Turbiez, M. M. Wienk, and R. A. J. Janssen, "Predicting morphologies of solution processed polymer:fullerene blends," *J. Am. Chem. Soc.*, vol. 135, no. 32, pp. 12057–12067, 2013.

[126] J. L. Bredas, R. Silbey, D. S. Bourdreaux, and R. R. Chance, "Chain-length dependence of electronic and electrochemical properties of conjugated systems: Polyacetylene, polyphenylene, polythiophene, and polypyrrole," *J. Am. Chem. Soc.*, vol. 105, pp. 6555 – 6559, 1983.

[127] S. Schumacher, I. Galbraith, A. Ruseckas, G. A. Turnbull, and I. D. W. Samuel, "Dynamics of photoexcitation and stimulated optical emission in conjugated polymers: A multiscale quantum-chemistry and Maxwell-Bloch-equations approach," *Phys. Rev. B*, vol. 81, pp. 245407–245417, 2010.

[128] J. J. Kwiatkowski, J. Nelson, H. Li, J. L. Bredas, W. Wenzel, and C. Lennartz, "Simulating charge transport in tris(8-hydroxyquinoline) aluminium (Alq3)," *Phys. Chem. Chem. Phys.*, vol. 10, pp. 1852–1858, 2008.

[129] J. J. Kwiatkowski, J. M. Frost, and J. Nelson, "The effect of morphology on electron field-effect mobility in disordered C60 thin films," *Nano Lett.*, vol. 9, no. 3, pp. 1085–1090, 2009.

[130] R. C. I. MacKenzie, J. M. Frost, and J. Nelson, "A numerical study of mobility in thin films of fullerene derivatives," *J. Chem. Phys.*, vol. 132, no. 6, p. 064904, 2010.

[131] J. M. Frost, F. Cheynis, S. M. Tuladhar, and J. Nelson, "Influence of polymer-blend morphology on charge transport and photocurrent generation in donor-acceptor polymer blends," *Nano Lett.*, vol. 6, no. 8, pp. 1674–1681, 2006.

[132] V. Marcon, N. van der Vegt, G. Wegner, and G. Raos, "Modeling of molecular packing and conformation in oligofluorenes," *J. Phys. Chem. B*, vol. 110, pp. 5253–5261, 2006.

[133] T. Costa, D. De Azevedo, B. Stewart, M. Knaapila, A. J. Valente, M. Kraft, U. Scherf, and H. D. Burrows, "Interactions of a zwitterionic thiophene-based conjugated polymer with surfactants," *Polym. Chem.*, vol. 6, no. 46, pp. 8036–8046, 2015.

[134] J. M. Frost, J. Kirkpatrick, T. Kirchartz, and J. Nelson, "Parameter free calculation of the subgap density of states in poly(3-hexylthiophene)," *Faraday Discuss.*, vol. 174, pp. 255–266, 2014.

[135] F. Jensen, *Introduction to Computational Chemistry*. Wiley, 1999.

[136] W. K. Hastings, "Monte Carlo sampling methods using Markov chains and their applications," *Biometrika*, vol. 57, no. 1, pp. 97–109, 1970.

[137] J. P. Ulmschneider, M. B. Ulmschneider, and A. Di Nola, "Monte Carlo vs molecular dynamics for all-atom polypeptide folding simulations," *J. Phys. Chem. B*, vol. 110, no. 33, pp. 16733–16742, 2006.

[138] T. Nelson, S. Fernandez-Alberti, V. Chernyak, A. E. Roitberg, and S. Tretiak, "Nonadiabatic excited-state molecular dynamics modeling of photoinduced dynamics in conjugated molecules," *J. Phys. Chem. B*, vol. 115, no. 18, pp. 5402–5414, 2011.

[139] J. Clark, T. Nelson, S. Tretiak, G. Cirmi, and G. Lanzani, "Femtosecond torsional relaxation," *Nature Phys.*, vol. 8, no. 3, pp. 225–231, 2012.

[140] R. S. Bhatta, Y. Y. Yimer, D. S. Perry, and M. Tsige, "Improved force field for molecular modeling of poly(3-hexylthiophene)," *J. Phys. Chem. B*, vol. 117, pp. 10035–10045, 2013.

[141] A. A. Y. Guilbert, J. M. Frost, T. Agostinelli, E. Pires, S. Lilliu, J. E. Macdonald, and J. Nelson, "Influence of bridging atom and side chains on the structure and crystallinity of cyclopentadithiophene-benzothiadiazole polymers," *Chem. Mater.*, vol. 26, no. 2, pp. 1226–1233, 2014.

[142] F. Haverkort, A. Stradomska, A. H. de Vries, and J. Knoester, "Investigating the structure of aggregates of an amphiphilic cyanine dye with molecular dynamics simulations," *J. Phys. Chem. B*, vol. 117, no. 19, pp. 5857–5867, 2013.

[143] F. Haverkort, A. Stradomska, and J. Knoester, "First-principles simulations of the initial phase of self-aggregation of a cyanine dye: Structure and optical spectra," *J. Phys. Chem. B*, vol. 118, no. 29, pp. 8877–8890, 2014.

[144] N. E. Jackson, K. L. Kohlstedt, B. M. Savoie, M. O. de la Cruz, G. C. Schatz, L. X. Chen, and M. A. Ratner, "Conformational order in aggregates of conjugated polymers," *J. Am. Chem. Soc.*, vol. 137, no. 19, pp. 6254–6262, 2015.

[145] N. R. Tummala, C. Sutton, S. G. Aziz, M. F. Toney, C. Risko, and J.-L. Bredas, "Effect of solvent additives on the solution aggregation of phenyl-C61-butyl acid methyl ester (PCBM)," *Chem. Mater.*, vol. 27, no. 24, pp. 8261–8272, 2015.

[146] C. G. Ricci, A. S. C. de Andrade, M. Mottin, and P. A. Netz, "Molecular dynamics of DNA: Comparison of force fields and terminal nucleotide definitions," *J. Phys. Chem. B*, vol. 114, no. 30, pp. 9882–9893, 2010.

[147] W. L. Jorgensen, D. S. Maxwell, and J. Tirado-Rives, "Development and testing of the OPLS all-atom force field on conformational energetics and properties of organic liquids," *J. Am. Chem. Soc.*, vol. 118, no. 45, pp. 11225–11236, 1996.

[148] W. L. Jorgensen and N. A. McDonald, "Development of an all-atom force field for heterocycles. properties of liquid pyridine and diazenes," *J. Mol. Struct.: THEOCHEM*, vol. 424, no. 1, pp. 145–155, 1998.

[149] N. A. McDonald and W. L. Jorgensen, "Development of an all-atom force field for heterocycles. properties of liquid pyrrole, furan, diazoles, and oxazoles," *J. Phys. Chem. B*, vol. 102, no. 41, pp. 8049–8059, 1998.

[150] R. C. Rizzo and W. L. Jorgensen, "OPLS all-atom model for amines: Resolution of the amine hydration problem," *J. Am. Chem. Soc.*, vol. 121, no. 20, pp. 4827–4836, 1999.

[151] M. L. P. Price, D. Ostrovsky, and W. L. Jorgensen, "Gas-phase and liquid-state properties of esters, nitriles, and nitro compounds with the OPLS-aa force field," *J. Comput. Chem.*, vol. 22, no. 13, pp. 1340–1352, 2001.

[152] E. K. Watkins and W. L. Jorgensen, "Perfluoroalkanes: Conformational analysis and liquid-state properties from ab initio and Monte Carlo calculations," *J. Phys. Chem. A*, vol. 105, no. 16, pp. 4118–4125, 2001.

[153] G. A. Kaminski, R. A. Friesner, J. Tirado-Rives, and W. L. Jorgensen, "Evaluation and reparametrization of the OPLS-aa force field for proteins via comparison with accurate quantum chemical calculations on peptides," *J. Phys. Chem. B*, vol. 105, no. 28, pp. 6474–6487, 2001.

[154] C. Oostenbrink, A. Villa, A. E. Mark, and W. F. Van Gunsteren, "A biomolecular force field based on the free enthalpy of hydration and solvation: The GROMOS force-field parameter sets 53A5 and 53A6," *J. Comput. Chem.*, vol. 25, no. 13, pp. 1656–1676, 2004.

[155] N. V. Dokholyan, S. V. Buldyrev, H. E. Stanley, and E. I. Shakhnovich, "Identifying the portein folding nucleus using molecular dynamics," *J. Mol. Biol.*, vol. 296, no. 5, pp. 1183–1188, 2000.

[156] C. Ho Choi, M. Kertesz, and A. Karpfen, "The effects of electron correlation on the degree of bond alternation and electronic structure of oligomers of polyacetylene," *J. Chem. Phys.*, vol. 107, no. 17, pp. 6712–6721, 1997.

[157] J. W. G. Bloom and S. E. Wheeler, "Benchmark torsional potentials of building blocks for conjugated materials: Bifuran, bithiophene, and biselenophene," *J. Chem. Theory Comput.*, vol. 10, no. 9, pp. 3647–3655, 2014.

[158] R. Gomez-Bombarelli, J. Aguilera-Iparraguirre, T. D. Hirzel, D. Duvenaud, D. Maclaurin, M. A. Blood-Forsythe, H. S. Chae, M. Einzinger, D.-G. Ha, T. Wu, G. Markopoulos, S. Jeon, H. Kang, H. Miyazaki, M. Numata, S. Kim, W. Huang, S. I. Hong, M. Baldo, R. P. Adams, and A. Aspuru-Guzik, "Design of efficient molecular organic light-emitting diodes by a high-throughput virtual screening and experimental approach," *Nat. Mater.*, vol. 15, no. 10, pp. 1120–1127, 2016.

[159] S. B. Darling and M. Sternberg, "Importance of side chains and backbone length in defect modeling of poly(3-alkylthiophenes)," *J. Phys. Chem. B*, vol. 113, no. 18, pp. 6215–6218, 2009.

[160] J. W. Ponder and D. A. Case, "Force fields for protein simulations.," *Adv. Prot. Chem*, vol. 66, pp. 27–85, 2003.

[161] N. L. Allinger, Y. H. Yuh, and J. H. Lii, "Molecular mechanics. the MM3 force field for hydrocarbons. 1," *J. Am. Chem. Soc.*, vol. 111, no. 23, pp. 8551–8566, 1989.

[162] W. L. Jorgensen and J. Tirado-Rives, "The OPLS potential functions for proteins, energy minimizations for crystals of cyclic peptides and crambin," *J. Am. Chem. Soc.*, vol. 110, no. 6, pp. 1657–1666, 1988.

[163] J. A. Maier, C. Martinez, K. Kasavajhala, L. Wickstrom, K. E. Hauser, and C. Simmerling, "ff14SB: Improving the accuracy of protein side chain and backbone parameters from ff99SB," *J. Chem. Theory Comput.*, vol. 11, no. 8, pp. 3696–3713, 2015.

[164] M. Knaapila, S. M. Fonseca, B. Stewart, M. Torkkeli, J. Perlich, S. Pradhan, U. Scherf, R. A. E. Castro, and H. D. Burrows, "Nanostructuring of the conjugated polyelectrolyte poly[9,9-bis(4-sulfonylbutoxyphenyl)fluorene-2,7-diyl-2,2'-bithiophene] in liquid crystalline C12E4 in bulk water and aligned thin films," *Soft Matter*, vol. 10, pp. 3103–3111, 2014.

[165] P. M. Morse, "Diatomic molecules according to the wave mechanics. ii. vibrational levels," *Phys. Rev.*, vol. 34, pp. 57–64, 1929.

[166] D. van der Spoel, E. Lindahl, B. Hess, A. R. van Buuren, E. Apol, P. J. Meulenhoff, D. P. Tieleman, A. L. T. M. Sijbers, K. A. Feenstra, R. van Drunen, and H. J. C. Berendsen, *Gromacs User Manual version 4.5.6.* www.gromacs.org, 2010.

[167] B. Hess, H. Bekker, H. J. C. Berendsen, and J. G. E. M. Fraaije, "LINCS: A linear constraint solver for molecular simulations," *J. Comput. Chem.*, vol. 18, no. 12, pp. 1463–1472, 1997.

[168] B. Hess, "P-LINCS: a parallel linear constraint solver for molecular simulation," *J. Chem. Theory Comput.*, vol. 4, no. 1, pp. 116–122, 2008.

[169] F. London, "Zur theorie und systematik der molekularkräfte," *Z. Phys.*, vol. 63, no. 3, pp. 245–279, 1930.

[170] J. E. Jones, "On the determination of molecular fields. ii. from the equation of state of a gas," *Proc. R. Soc. A*, vol. 106, no. 738, pp. 463–477, 1924.

[171] R. A. Buckingham, "The classical equation of state of gaseous helium, neon and argon," *Proc. R. Soc. A*, vol. 168, no. 933, pp. 264–283, 1938.

[172] F. Archambault, C. Chipot, I. Soteras, F. J. Luque, K. Schulten, and F. Dehez, "Polarizable intermolecular potentials for water and benzene interacting with halide and metal ions," *J. Chem. Theory Comput.*, vol. 5, no. 11, pp. 3022–3031, 2009.

[173] T. A. Halgren, "The representation of van der Waals (vdW) interactions in molecular mechanics force fields: potential form, combination rules, and vdW parameters," *J. Am. Chem. Soc.*, vol. 114, no. 20, pp. 7827–7843, 1992.

[174] Y. Shi, Z. Xia, J. Zhang, R. Best, C. Wu, J. W. Ponder, and P. Ren, "Polarizable atomic multipole-based amoeba force field for proteins," *J. Chem. Theory Comput.*, vol. 9, no. 9, pp. 4046–4063, 2013.

[175] J. Zhang, B. Tuguldur, and D. van der Spoel, "Force field benchmark of organic liquids. 2. Gibbs energy of solvation," *J. Chem. Inf. Model.*, vol. 55, no. 6, pp. 1192–1201, 2015.

[176] M. Battaglia, A. Buckingham, and J. Williams, "The electric quadrupole moments of benzene and hexafluorobenzene," *Chem. Phys. Lett.*, vol. 78, no. 3, pp. 421 – 423, 1981.

[177] M. O. Sinnokrot, E. F. Valeev, and C. D. Sherrill, "Estimates of the ab initio limit for interactions: the benzene dimer," *J. Am. Chem. Soc.*, vol. 124, no. 36, pp. 10887–10893, 2002.

[178] L. Verlet, "Computer "experiments" on classical fluids. i. thermodynamical properties of Lennard-Jones molecules," *Phys. Rev.*, vol. 159, pp. 98–103, 1967.

[179] J. Barker and R. Watts, "Monte Carlo studies of the dielectric properties of water-like models," *Mol. Phys.*, vol. 26, no. 3, pp. 789–792, 1973.

[180] P. P. Ewald, "Die berechnung optischer und elektrostatischer gitterpotentiale," *Ann. Phys.*, vol. 369, no. 3, pp. 253–287, 1921.

[181] T. Darden, D. York, and L. Pedersen, "Particle mesh Ewald: An Nlog(N) method for Ewald sums in large systems," *J. Chem. Phys.*, vol. 98, no. 12, pp. 10089–10092, 1993.

[182] M. Nina and T. Simonson, "Molecular dynamics of the tRNA(Ala) acceptor stem: comparison between continuum reaction field and particle-mesh Ewald electrostatic treatments," *J. Phys. Chem. B*, vol. 106, no. 14, pp. 3696–3705, 2002.

[183] R. Schulz, B. Lindner, L. Petridis, and J. C. Smith, "Scaling of multimillion-atom biological molecular dynamics simulation on a petascale supercomputer," *J. Chem. Theory Comput.*, vol. 5, no. 10, pp. 2798–2808, 2009.

[184] O. F. Lange, D. van der Spoel, and B. L. de Groot, "Scrutinizing molecular mechanics force fields on the submicrosecond timescale with NMR data," *Biophys. J.*, vol. 99, no. 2, pp. 647 – 655, 2010.

[185] C. Caleman, P. J. van Maaren, M. Hong, J. S. Hub, L. T. Costa, and D. van der Spoel, "Force field benchmark of organic liquids: Density, enthalpy of vaporization, heat capacities, surface tension, isothermal compressibility, volumetric expansion coefficient, and dielectric constant," *J. Chem. Theory Comput.*, vol. 8, no. 1, pp. 61–74, 2012.

[186] D. van der Spoel, P. J. van Maaren, and C. Caleman, "Gromacs molecule & liquid database," *Bioinformatics*, vol. 28, no. 5, pp. 752–753, 2012.

[187] V. Marcon and G. Raos, "Molecular modeling of crystalline oligothiophenes: testing and development of improved force fields," *J. Phys. Chem. B*, vol. 108, no. 46, pp. 18053–18064, 2004.

[188] D. Van Der Spoel, E. Lindahl, B. Hess, G. Groenhof, A. E. Mark, and H. J. C. Berendsen, "Gromacs: Fast, flexible, and free," *J. Comput. Chem.*, vol. 26, no. 16, pp. 1701–1718, 2005.

[189] B. Hess, C. Kutzner, D. van der Spoel, and E. Lindahl, "Gromacs 4: algorithms for highly efficient, load-balanced, and scalable molecular simulation," *J. Chem. Theory Comput.*, vol. 4, no. 3, pp. 435–447, 2008.

[190] X. Yuan, W. Zhang, L.-H. Xie, J. Ma, W. Huang, and W. Liu, "Role of planar conformations in aggregation induced spectral shifts of supermolecular oligofluorenols in solutions and films: A combined experimental and MD/TD-DFT study," *J. Phys. Chem. B*, vol. 119, no. 32, pp. 10316–10333, 2015.

[191] R. Hockney, S. Goel, and J. Eastwood, "Quiet high-resolution computer models of a plasma," *J. Comput. Phys.*, vol. 14, no. 2, pp. 148 – 158, 1974.

[192] W. C. Swope, H. C. Andersen, P. H. Berens, and K. R. Wilson, "A computer simulation method for the calculation of equilibrium constants for the formation of physical clusters of molecules: Application to small water clusters," *J. Chem. Phys.*, vol. 76, no. 1, pp. 637–649, 1982.

[193] Z. Guo, D. Lee, Y. Liu, F. Sun, A. Sliwinski, H. Gao, P. C. Burns, L. Huang, and T. Luo, "Tuning the thermal conductivity of solar cell polymers through side chain engineering," *Phys. Chem. Chem. Phys.*, pp. 7764–7771, 2014.

[194] H. J. C. Berendsen, J. P. M. Postma, W. F. van Gunsteren, A. DiNola, and J. R. Haak, "Molecular dynamics with coupling to an external bath," *J. Chem. Phys.*, vol. 81, no. 8, pp. 3684–3690, 1984.

[195] G. Bussi, D. Donadio, and M. Parrinello, "Canonical sampling through velocity rescaling," *J. Chem. Phys.*, vol. 126, no. 1, 2007.

[196] S. Nosé, "A molecular dynamics method for simulations in the canonical ensemble," *Mol. Phys.*, vol. 52, no. 2, pp. 255–268, 1984.

[197] W. G. Hoover, "Canonical dynamics: Equilibrium phase-space distributions," *Phys. Rev. A*, vol. 31, pp. 1695–1697, 1985.

[198] H. C. Andersen, "Molecular dynamics simulations at constant pressure and/or temperature," *J. Chem. Phys.*, vol. 72, no. 4, pp. 2384–2393, 1980.

[199] M. Parrinello and A. Rahman, "Polymorphic transitions in single crystals: A new molecular dynamics method," *J. Appl. Phys.*, vol. 52, no. 12, pp. 7182–7190, 1981.

[200] S. Nos and M. Klein, "Constant pressure molecular dynamics for molecular systems," *Mol. Phys.*, vol. 50, no. 5, pp. 1055–1076, 1983.

[201] C. L. Yaws, *Yaws' Handbook of Thermodynamic and Physical Properties of Chemical Compounds*. Knovel, 2003.

[202] R. Crespo-Otero, L. A. Montero, W.-D. Stohrer, and J. M. Garca de la Vega, "Basis set superposition error in MP2 and density-functional theory: A case of methane-nitric oxide association," *J. Chem. Phys.*, vol. 123, no. 13, 2005.

[203] R. Ditchfield, W. J. Hehre, and J. A. Pople, "Self-consistent molecular orbital methods. ix. an extended gaussian-type basis for molecular-orbital studies of organic molecules," *J. Chem. Phys.*, vol. 54, no. 2, pp. 724–728, 1971.

[204] W. J. Hehre, R. Ditchfield, and J. A. Pople, "Self-consistent molecular orbital methods. xii. further extensions of gaussian-type basis sets for use in molecular orbital studies of organic molecules," *J. Chem. Phys.*, vol. 56, no. 5, pp. 2257–2261, 1972.

[205] P. Hariharan and J. Pople, "The influence of polarization functions on molecular orbital hydrogenation energies," *Theor. Chem. Acc.*, vol. 28, no. 3, pp. 213–222, 1973.

[206] P. Hariharan and J. Pople, "Accuracy of AHn equilibrium geometries by single determinant molecular orbital theory," *Mol. Phys.*, vol. 27, no. 1, pp. 209–214, 1974.

[207] M. S. Gordon, "The isomers of silacyclopropane," *Chem. Phys. Lett.*, vol. 76, no. 1, pp. 163–168, 1980.

[208] M. M. Francl, W. J. Pietro, W. J. Hehre, J. S. Binkley, M. S. Gordon, D. J. DeFrees, and J. A. Pople, "Self-consistent molecular orbital methods. xxiii. a polarization-type basis set for second-row elements," *J. Chem. Phys.*, vol. 77, no. 7, pp. 3654–3665, 1982.

[209] R. C. Binning and L. A. Curtiss, "Compact contracted basis sets for third-row atoms: Ga-Kr," *J. Comput. Chem.*, vol. 11, no. 10, pp. 1206–1216, 1990.

[210] J.-P. Blaudeau, M. P. McGrath, L. A. Curtiss, and L. Radom, "Extension of gaussian-2 (g2) theory to molecules containing third-row atoms K and Ca," *J. Chem. Phys.*, vol. 107, no. 13, pp. 5016–5021, 1997.

[211] V. A. Rassolov, J. A. Pople, M. A. Ratner, and T. L. Windus, "6-31g* basis set for atoms K through Zn," *J. Chem. Phys.*, vol. 109, no. 4, pp. 1223–1229, 1998.

[212] V. A. Rassolov, M. A. Ratner, J. A. Pople, P. C. Redfern, and L. A. Curtiss, "6-31g* basis set for third-row atoms," *J. Comput. Chem.*, vol. 22, no. 9, pp. 976–984, 2001.

[213] T. H. Dunning, "Gaussian basis sets for use in correlated molecular calculations. i. the atoms boron through neon and hydrogen.," *J. Chem. Phys.*, vol. 90, no. 2, pp. 1007–1023, 1989.

[214] R. A. Friesner, "Ab initio quantum chemistry: Methodology and applications," *Proc. Natl. Acad. Sci. U.S.A.*, vol. 102, no. 19, pp. 6648–6653, 2005.

[215] C. Møller and M. S. Plesset, "Note on an approximation treatment for many-electron systems," *Phys. Rev.*, vol. 46, pp. 618–622, 1934.

[216] D. Cremer, "Møller-Plesset perturbation theory: from small molecule methods to methods for thousands of atoms," *Wiley Interdiscip. Rev. Comput. Mol. Sci.*, vol. 1, no. 4, pp. 509–530, 2011.

[217] J. Čızek, "On the correlation problem in atomic and molecular systems. calculation of wavefunction components in Ursell-type expansion using quantum-field theoretical methods," *J. Chem. Phys.*, vol. 45, no. 11, pp. 4256–4266, 1966.

[218] R. J. Bartlett and M. Musiał, "Coupled-cluster theory in quantum chemistry," *Rev. Mod. Phys.*, vol. 79, pp. 291–352, 2007.

[219] J. C. Slater, "The theory of complex spectra," *Phys. Rev.*, vol. 34, pp. 1293–1322, 1929.

[220] G. Raos, A. Famulari, and V. Marcon, "Computational reinvestigation of the bithiophene torsion potential," *Chem. Phys. Lett.*, vol. 379, no. 34, pp. 364 – 372, 2003.

[221] A. Messiah, *Quantum Mechanics*. Dover books on physics, Dover Publications, 1961.

[222] H.-J. Werner, P. J. Knowles, G. Knizia, F. R. Manby, and M. Schütz, "Molpro: a general-purpose quantum chemistry program package," *Wiley Interdiscip. Rev. Comput. Mol. Sci.*, vol. 2, pp. 242–253, 2012.

[223] H.-J. Werner, P. J. Knowles, G. Knizia, F. R. Manby, M. Schütz, P. Celani, T. Korona, R. Lindh, A. Mitrushenkov, G. Rauhut, K. R. Shamasundar, T. B.

Adler, R. D. Amos, A. Bernhardsson, A. Berning, D. L. Cooper, M. J. O. Deegan, A. J. Dobbyn, F. Eckert, E. Goll, C. Hampel, A. Hesselmann, G. Hetzer, T. Hrenar, G. Jansen, C. Köppl, Y. Liu, A. W. Lloyd, R. A. Mata, A. J. May, S. J. McNicholas, W. Meyer, M. E. Mura, A. Nicklass, D. P. O'Neill, P. Palmieri, D. Peng, K. Pflüger, R. Pitzer, M. Reiher, T. Shiozaki, H. Stoll, A. J. Stone, R. Tarroni, T. Thorsteinsson, and M. Wang, "Molpro, version 2012.1, a package of ab initio programs," 2012. see http://www.molpro.net.

[224] M. Schütz, G. Hetzer, and H.-J. Werner, "Low-order scaling local electron correlation methods. i. linear scaling local MP2," *J. Chem. Phys.*, vol. 111, no. 13, pp. 5691–5705, 1999.

[225] C. Hampel and H.-J. Werner, "Local treatment of electron correlation in coupled cluster theory," *J. Chem. Phys.*, vol. 104, no. 16, pp. 6286–6297, 1996.

[226] M. Feyereisen, G. Fitzgerald, and A. Komornicki, "Use of approximate integrals in ab initio theory. an application in MP2 energy calculations," *Chem. Phys. Lett.*, vol. 208, no. 5, pp. 359 – 363, 1993.

[227] O. Vahtras, J. Almlöf, and M. Feyereisen, "Integral approximations for LCAO-SCF calculations," *Chem. Phys. Lett.*, vol. 213, no. 5, pp. 514 – 518, 1993.

[228] F. Weigend, M. Häser, H. Patzelt, and R. Ahlrichs, "RI-MP2: optimized auxiliary basis sets and demonstration of efficiency," *Chem. Phys. Lett.*, vol. 294, no. 13, pp. 143 – 152, 1998.

[229] J. W. Boughton and P. Pulay, "Comparison of the Boys and Pipek-Mezey localizations in the local correlation approach and automatic virtual basis selection," *J. Comput. Chem.*, vol. 14, no. 6, pp. 736–740, 1993.

[230] P. Hohenberg and W. Kohn, "Inhomogeneous electron gas," *Phys. Rev.*, vol. 136, pp. B864–B871, 1964.

[231] W. Kohn and L. J. Sham, "Self-consistent equations including exchange and correlation effects," *Phys. Rev.*, vol. 140, pp. A1133–A1138, 1965.

[232] C. A. Ullrich and Z.-H. Yang, "A brief compendium of time-dependent density functional theory," *Braz. J. Phys.*, vol. 44, no. 1, pp. 154–188, 2014.

[233] A. D. Becke, "Density-functional exchange-energy approximation with correct asymptotic behavior," *Phys. Rev. A*, vol. 38, pp. 3098–3100, 1988.

[234] A. D. Becke, "A new mixing of Hartree-Fock and local density-functional theories," *J. Chem. Phys.*, vol. 98, no. 2, pp. 1372–1377, 1993.

[235] C. Lee, W. Yang, and R. G. Parr, "Development of the Colle-Salvetti correlation-energy formula into a functional of the electron density," *Phys. Rev. B*, vol. 37, pp. 785–789, 1988.

[236] R. Schueppel, K. Schmidt, C. Uhrich, K. Schulze, D. Wynands, J. L. Brédas, E. Brier, E. Reinold, H.-B. Bu, P. Baeuerle, B. Maennig, M. Pfeiffer, and K. Leo, "Optimizing organic photovoltaics using tailored heterojunctions: A photoinduced absorption study of oligothiophenes with low band gaps," *Phys. Rev. B*, vol. 77, p. 085311, 2008.

[237] E. Runge and E. K. U. Gross, "Density-functional theory for time-dependent systems," *Phys. Rev. Lett.*, vol. 52, pp. 997–1000, 1984.

[238] D. Jacquemin, E. A. Perpte, G. E. Scuseria, I. Ciofini, and C. Adamo, "TD-DFT performance for the visible absorption spectra of organic dyes: conventional versus long-range hybrids," *J. Chem. Theory Comput.*, vol. 4, no. 1, pp. 123–135, 2008.

[239] A. D. Laurent and D. Jacquemin, "TD-DFT benchmarks: A review," *Int. J. Quantum. Chem.*, vol. 113, no. 17, pp. 2019–2039, 2013.

[240] S. H. Vosko, L. Wilk, and M. Nusair, "Accurate spin-dependent electron liquid correlation energies for local spin density calculations: a critical analysis," *Can. J. Phys.*, vol. 58, no. 8, pp. 1200–1211, 1980.

[241] J. P. Perdew and Y. Wang, "Accurate and simple analytic representation of the electron-gas correlation energy," *Phys. Rev. B*, vol. 45, pp. 13244–13249, 1992.

[242] J. P. Perdew, M. Ernzerhof, and K. Burke, "Rationale for mixing exact exchange with density functional approximations," *J. Chem. Phys.*, vol. 105, no. 22, pp. 9982–9985, 1996.

[243] T. Yanai, D. P. Tew, and N. C. Handy, "A new hybrid exchange-correlation functional using the Coulomb-attenuating method (CAM-B3LYP)," *Chem. Phys. Lett.*, vol. 393, no. 1–3, pp. 51–57, 2004.

[244] Y. Zhao and D. G. Truhlar, "The M06 suite of density functionals for main group thermochemistry, thermochemical kinetics, noncovalent interactions, excited states, and transition elements: two new functionals and systematic testing of four M06-class functionals and 12 other functionals," *Theor. Chem. Acc.*, vol. 120, no. 1, pp. 215–241, 2008.

[245] J.-D. Chai and M. Head-Gordon, "Systematic optimization of long-range corrected hybrid density functionals," *J. Chem. Phys.*, vol. 128, no. 8, 2008.

[246] J.-D. Chai and M. Head-Gordon, "Long-range corrected hybrid density functionals with damped atom-atom dispersion corrections," *Phys. Chem. Chem. Phys.*, vol. 10, pp. 6615–6620, 2008.

[247] H. Iikura, T. Tsuneda, T. Yanai, and K. Hirao, "A long-range correction scheme for generalized-gradient-approximation exchange functionals," *J. Chem. Phys.*, vol. 115, no. 8, pp. 3540–3544, 2001.

[248] S. Ling, S. Schumacher, I. Galbraith, and M. J. Paterson, "Excited-state absorption of conjugated polymers in the near-infrared and visible: A computational study of oligofluorenes," *J. Phys. Chem. C*, vol. 117, no. 13, pp. 6889–6895, 2013.

[249] S. Grimme, "Semiempirical GGA-type density functional constructed with a long-range dispersion correction," *J. Comput. Chem.*, vol. 27, no. 15, pp. 1787–1799, 2006.

[250] S. Grimme, S. Ehrlich, and L. Goerigk, "Effect of the damping function in dispersion corrected density functional theory," *J. Comput. Chem.*, vol. 32, no. 7, pp. 1456–1465, 2011.

[251] M. J. Frisch, G. W. Trucks, H. B. Schlegel, G. E. Scuseria, M. A. Robb, J. R. Cheeseman, G. Scalmani, V. Barone, B. Mennucci, G. A. Petersson, H. Nakatsuji, M. Caricato, X. Li, H. P. Hratchian, A. F. Izmaylov, J. Bloino, G. Zheng, J. L. Sonnenberg, M. Hada, M. Ehara, K. Toyota, R. Fukuda, J. Hasegawa, M. Ishida, T. Nakajima, Y. Honda, O. Kitao, H. Nakai, T. Vreven, J. A. Montgomery, Jr., J. E. Peralta, F. Ogliaro, M. Bearpark, J. J. Heyd, E. Brothers, K. N. Kudin, V. N. Staroverov, R. Kobayashi, J. Normand, K. Raghavachari, A. Rendell, J. C. Burant, S. S. Iyengar, J. Tomasi, M. Cossi, N. Rega, J. M. Millam, M. Klene, J. E. Knox, J. B. Cross, V. Bakken, C. Adamo, J. Jaramillo, R. Gomperts, R. E. Stratmann, O. Yazyev, A. J. Austin, R. Cammi, C. Pomelli, J. W. Ochterski, R. L. Martin, K. Morokuma, V. G. Zakrzewski, G. A. Voth, P. Salvador, J. J. Dannenberg, S. Dapprich, A. D. Daniels, O. Farkas, J. B. Foresman, J. V. Ortiz, J. Cioslowski, and D. J. Fox, "Gaussian09 Revision D.01." Gaussian Inc. Wallingford CT 2009.

[252] C. I. Bayly, P. Cieplak, W. Cornell, and P. A. Kollman, "A well-behaved electrostatic potential based method using charge restraints for deriving atomic charges: the RESP model," *J. Phys. Chem.*, vol. 97, no. 40, pp. 10269–10280, 1993.

[253] F. Martin and H. Zipse, "Charge distribution in the water molecule - a comparison of methods," *J. Comput. Chem.*, vol. 26, no. 1, pp. 97–105, 2005.

[254] U. C. Singh and P. A. Kollman, "An approach to computing electrostatic charges for molecules," *J. Comput. Chem.*, vol. 5, no. 2, pp. 129–145, 1984.

[255] L. E. Chirlian and M. M. Francl, "Atomic charges derived from electrostatic potentials: A detailed study," *J. Comput. Chem.*, vol. 8, no. 6, pp. 894–905, 1987.

[256] C. M. Breneman and K. B. Wiberg, "Determining atom-centered monopoles from molecular electrostatic potentials. the need for high sampling density in formamide conformational analysis," *J. Comput. Chem.*, vol. 11, no. 3, pp. 361–373, 1990.

[257] D. A. Case, T. A. Darden, T. E. Cheatham, C. L. Simmerling, J. Wang, R. E. Duke, R. Luo, R. C. Walker, W. Zhang, K. M. Merz, B. Roberts, S. Hayik, A. Roitberg, G. Seabra, J. Swails, A. W. Goetz, I. Kolossváry, K. F. Wong, F. Paesani, J. Vanicek, R. M. Wolf, J. Liu, X. Wu, S. R. Brozell, T. Steinbrecher, H. Gohlke, Q. Cai, X. Ye, J. Wang, M. J. Hsieh, G. Cui, D. R. Roe, D. H. Mathews, M. G. Seetin, R. Salomon-Ferrer, C. Sagui, V. Babin, T. Luchko, S. Gusarov, A. Kovalenko, and P. A. Kollman, "Amber 14," 2014. University of California, San Francisco.

[258] Y. Jing, R. Zheng, H.-X. Li, and Q. Shi, "Theoretical study of the electronicvibrational coupling in the Qy states of the photosynthetic reaction center in purple bacteria," *J. Phys. Chem. B*, vol. 116, no. 3, pp. 1164–1171, 2012.

[259] J. Cornil, D. Beljonne, and J. L. Brédas, "Nature of optical transitions in conjugated oligomers. i. theoretical characterization of neutral and doped oligo(phenylenevinylene)s," *J. Chem. Phys.*, vol. 103, no. 2, pp. 834–841, 1995.

[260] J. Cornil, D. Beljonne, and J. L. Brédas, "Nature of optical transitions in conjugated oligomers. ii. theoretical characterization of neutral and doped oligothiophenes," *J. Chem. Phys.*, vol. 103, no. 2, pp. 842–849, 1995.

[261] M. J. Winokur, J. Slinker, and D. L. Huber, "Structure, photophysics, and the order-disorder transition to the β phase in poly(9,9-(di-n, n-octyl)fluorene)," *Phys. Rev. B*, vol. 67, p. 184106, 2003.

[262] R. Tempelaar, A. Stradomska, J. Knoester, and F. C. Spano, "Anatomy of an exciton: Vibrational distortion and exciton coherence in H- and J-aggregates," *J. Phys. Chem. B*, vol. 117, no. 1, pp. 457–466, 2013.

[263] N. Banerji, S. Cowan, E. Vauthey, and A. J. Heeger, "Ultrafast relaxation of the poly(3-hexylthiophene) emission spectrum," *J. Phys. Chem. C*, vol. 115, no. 19, pp. 9726–9739, 2011.

[264] S. Hotta, S. D. D. V. Rughooputh, A. J. Heeger, and F. Wudl, "Spectroscopic studies of soluble poly(3-alkylthienylenes)," *Macromolecules*, vol. 20, no. 1, pp. 212–215, 1987.

[265] J. Szeremeta, R. Kolkowski, M. Nyk, and M. Samoc, "Wavelength dependence of the complex third-order nonlinear optical susceptibility of poly(3-hexylthiophene) studied by femtosecond Z-scan in solution and thin film," *J. Phys. Chem. C*, vol. 117, no. 49, pp. 26197–26203, 2013.